YEAR 4 REVIEW

INTEGRATED DIAGNOSTICS

June 1, 1998 - May 31, 1999

FOR
Office of Naval Research
800 N. Quincy Street
Arlington, VA 22217-5660

PREPARED BY
Richard S. Cowan, Program Manager
Ward O. Winer, Principal Investigator
Georgia Institute of Technology
MULTIUNIVERSITY CENTER FOR INTEGRATED DIAGNOSTICS
Woodruff School of Mechanical Engineering
Atlanta, GA 30332-0405
Ph: 404-894-3200

SUBGRANTEES
Northwestern University
Jan D. Achenbach, Director
Center for Quality Engineering and Failure Prevention
Ph: 847-491-5527

University of Minnesota
Dennis Polla, Professor
Department of Electrical Engineering
Ph: 612-626-2753
S. Ramalingam, Professor
Department of Mechanical Engineering
Ph: 612-625-4017

19990524 074

TABLE OF CONTENTS

Office of Naval Research (ONR) Grant N00014-95-1-0539, *Integrated Diagnostics*, was initiated on March 1, 1995, following approval of a research proposal submitted to the Department of Defense Multidisciplinary Research Program of the University Research Initiative (M-URI). To accomplish the objectives set forth by the M-URI program, the MULTIUNIVERSITY CENTER FOR INTEGRATED DIAGNOSTICS was formed, supported by faculty and staff from the Georgia Institute of Technology, University of Minnesota, and Northwestern University.

PROGRAM OBJECTIVE

America's military machines (e.g., ships, aircraft, and land vehicles) are growing old. Many of the mechanical systems that are confidently relied upon today were designed and built twenty and thirty years ago. Given the present economic climate, replacement with next generation equipment can no longer be taken for granted. Hence, an expectation of keeping aging machines in service well into the next century has emerged, elevating concern that poor performance, inadequate safety, and increasingly expensive maintenance will result.

To respond to this technological challenge, pending failures need to be identified before disastrous consequences occur. Incipient failures, however, are hard to locate, and current maintenance systems have limited capabilities to do so. Today's systems rely mainly on time-based inspection, which requires that parts be inspected at specified intervals, and be replaced when deemed unfit for service. A potentially more effective and efficient alternative to time-based inspection is to continuously monitor critical components. This necessitates an understanding of *Integrated Diagnostics*, a term associated with the technologies and methodologies used to determine how mechanical failures occur, and how they can be detected, predicted, and diagnosed in real-time.

As shown in Fig. 1, a systematic approach has been implemented to enable innovative ideas to be developed and mature with respect to mechanical system diagnostics and prognostics. Provided funding through the Department of Defense M-URI for a basic period of three years with an option for two additional years, a technical organization has been built to facilitate and combine the various disciplines required to perform the basic research needed to develop a system capable of being used on a commercial or defense service vehicle. Researchers, representing a variety of engineering disciplines at the Georgia Institute of Technology, Northwestern University, and the University of Minnesota have been assembled, offering expertise in material fatigue, fracture, nondestructive testing, sensors, and signal processing. To gain first-hand knowledge of the problems that maintenance personnel face, engineering support has been obtained through the CHERRY POINT NAVAL AVIATION DEPOT. Additional experience has been made available through industrial partnerships.

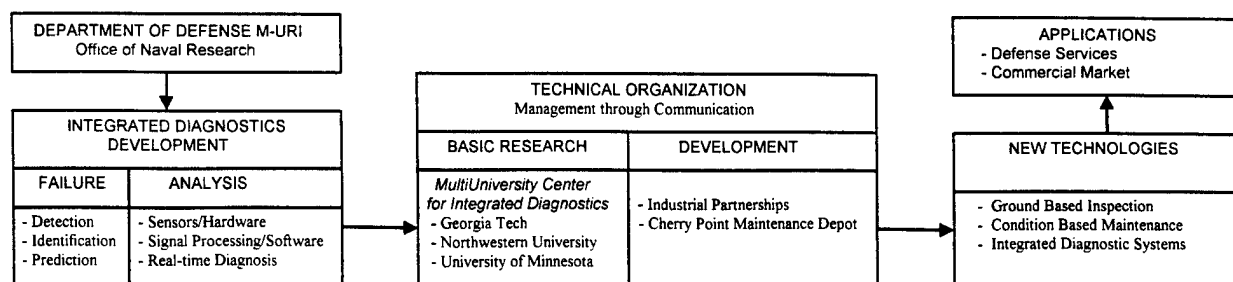| DEPARTMENT OF DEFENSE M-URI Office of Naval Research		TECHNICAL ORGANIZATION Management through Communication		APPLICATIONS - Defense Services - Commercial Market
INTEGRATED DIAGNOSTICS DEVELOPMENT		BASIC RESEARCH	DEVELOPMENT	NEW TECHNOLOGIES
FAILURE	ANALYSIS	*MultiUniversity Center for Integrated Diagnostics*		
- Detection - Identification - Prediction	- Sensors/Hardware - Signal Processing/Software - Real-time Diagnosis	- Georgia Tech - Northwestern University - University of Minnesota	- Industrial Partnerships - Cherry Point Maintenance Depot	- Ground Based Inspection - Condition Based Maintenance - Integrated Diagnostic Systems

Figure 1. Technology Delivery

The MULTIUNIVERSITY CENTER FOR INTEGRATED DIAGNOSTICS is committed to perform basic research studies associated with three major Integrated Diagnostic needs: the need to monitor the condition of a component or mechanical system in real-time, the need to reliably predict the occurrence of failures, and the need to detect and identify incipient failures. Organizationally, this has led to the formation of three research thrust areas, the objectives of which are defined below.

I. **Mechanical System Health Monitoring** (Direct Sensing, Analysis, Real-time Diagnosis)
perform studies with respect to the responses of signals early in fault inception, including research on sensors that can be placed at critical sites on mechanical systems for responses to change in variables of state or vibration.

II. **Nondestructive Evaluation** (Failure Detection and Identification)
perform studies pertaining to deterioration mechanisms and techniques for detecting the initiation of fractures or other failures.

III. **Failure Characterization and Prediction Methodology**
perform studies pertaining to the methodology for failure prediction in real-time, including modeling fault initiation and failure signatures, and observing the propagation and fracture phases of fatigue-based failure.

PROGRAM ORGANIZATION

A technical organization has been formed to facilitate and combine the various disciplines required to develop the needed scientific and engineering foundation outlined above. The participating faculty and staff, identified in Appendix A, are recognized for their significant research contributions with respect to structural fatigue, fracture, nondestructive testing, acoustics, ultrasonics, sensors, and signal processing. Integrated Diagnostics research is presently being addressed by nineteen (19) faculty associated with four schools from the Georgia Tech College of Engineering, three (3) faculty from Northwestern University, and ten (10) faculty from the University of Minnesota. In addition, during this reporting period, the program has accommodated two (2) post-doctoral researchers, three (3) visiting researchers, forty (40) graduate students, and six (6) advanced undergraduate students.

ONR PROGRAM REVIEW

In this fourth year of M-URI funding, studies continue with respect to understanding the mechanisms of failure (through detection, identification, and prediction) and the means to detect, identify and analyze them (through sensors/hardware, signal processing/software, and real-time diagnosis). To facilitate an OFFICE OF NAVAL RESEARCH Program Review of these activities, this publication was created, providing a synopsis of each sponsored research project.

1.1 *INTEGRATED MICROSENSORS FOR AIRCRAFT FATIGUE AND FAILURE WARNING*

Lead Investigator: Dennis L. Polla (University of Minnesota)
M-URI Year 4 Funding Allocation: 34.2%

PROJECT OVERVIEW

Four principal activities have taken place with the goal of developing miniature structural health monitoring systems and their related signal processing. These include 1) wideband acoustic emission sensors, 2) vibration monitors, 3) sensor interface circuits, and 4) signal processing methods.

The technical approach taken in this work is largely based on the use of piezoelectric materials and MEMS processing methods. As early as 1992, it was believed that piezoelectric (PZT) MEMS would be attractive for integrated diagnostic monitoring devices due to its inherent high sensitivity, low electrical noise, and low power dissipation. The main technical challenges however of microfabrication complexity, reproducibility, and integration with electronics represent the challenges of PZT MEMS. Prior to the start of this program no structural health monitoring devices had been made. Some preliminary data on microphones and related pressure sensors did however did indicate promise for integrated diagnostics applications. While other technologies have been developed since 1992, the use of piezoelectric MEMS is still compelling for structural health monitoring applications.

The main M-URI year 4 accomplishments for each of these activities are briefly summarized below:

- Integrated acoustic emission microsensors and associated packaging methods have been developed for the detection of fatigue-induced microcracking.
- Piezoelectric microcantilever vibration monitors have been designed and fabricated for the detection of abnormal mechanical vibration signatures in rotating machinery.
- Wideband piezoelectric charge amplifiers have been designed as custom interface circuits for AE microsensors.
- Signal processing methods have been developed for analyzing crack signatures in helicopter components.

The overall goal of this project is to realize a smart structural health-monitoring coupon consisting of sensors, electronics, and signal processing methods. Figure 1 shows the overall systems objective of this project.

1.1.1 WIDEBAND INTEGRATED ACOUSTIC EMISSION MICROSENSOR

Co-investigators: William P. Robbins, Lorraine Francis, and Ramesh Harjani
Students: J. Plummer, D. Drinkwater, and K. Nair

DoD NEED

The real-time detection of the precursor signatures leading to material failure is critical to a variety of defense needs. This is particularly relevant to helicopters where fatigue-related crack formation can lead to catastrophic component failure. Real-time detection of crack formation is also important in routine maintenance of aircraft components and ship machinery where materials are often unnecessarily replaced or serviced even though they are structurally healthy.

PROJECT MISSION

One of the major objectives of the Integrated Diagnostics effort has been to enable acoustic emission (AE) sensors to be of use in monitoring microcrack development in the critical components of a mechanical system (e.g., helicopter), while the component is in service. The system would be taken out
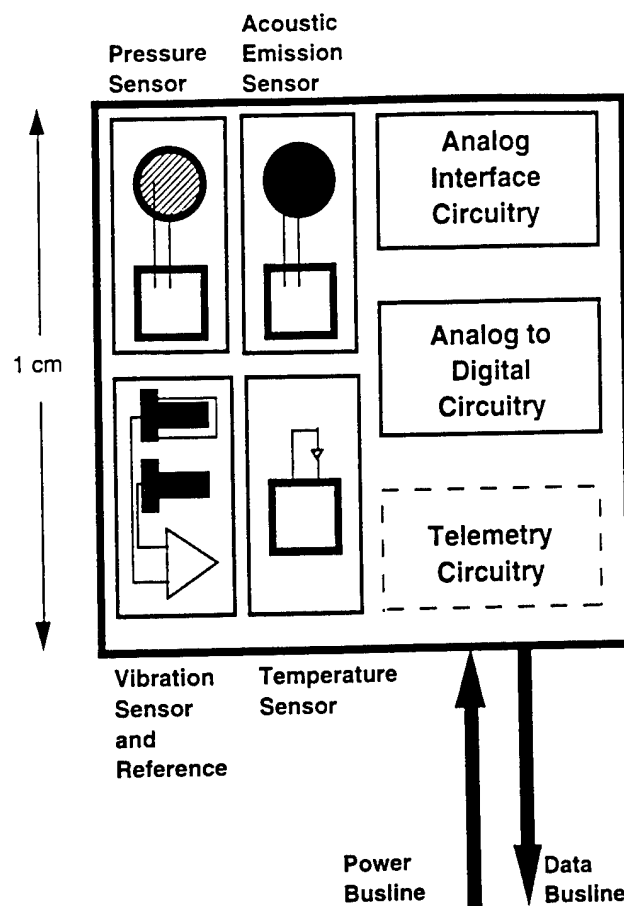
Figure 1. Smart structural monitoring coupon systems concept.

of service only when microcracks reach a predetermined threshold, and maintenance time and expense can be minimized. This would maximize the availability of the system for mission assignments.

The goal of this task is to develop a microsensor of a small size (packaged sensor dimensions having a lateral footprint of a few mm on a side and a few mm vertical height) and capable of wideband (50 kHz to 1 MHz) operation. A charge amplifier made as in integrated circuit chip is to be included in the packaged sensor to achieve good sensitivity.

TECHNICAL PERSPECTIVE

Acoustic emission sensors available during this program's inception in 1995 were unsuitable for a real-time monitoring application. Commercially available wideband (50 kHz - 1 MHz) acoustic emission sensors were too large (typically 1-2 cm in diameter and 2 cm tall), too heavy (tens of grams), too expensive ($200-$400 each), and required 40-60 db of external amplification. This integrated AE microsensor project was initiated to overcome these limitations.

RESEARCH ACCOMPLISHMENTS

During the first three years of the project, several generations of hybrid AE sensors have been fabricated and tested. The term hybrid refers to the on-board charge amplifier being fabricated with discrete surface mount components and positioned on a circuit board. The hybrid sensors had a twofold purpose: 1) to demonstrate that reductions in PZT sensor sensitivity (because of PZT size reductions) could be compensated for by means of onboard amplification, and 2) to develop an optimum circuit design for onboard amplification. The details of the hybrid AE sensor were reported in the *M-URI Year 3 Annual Report.*

MECHANICAL SYSTEM HEALTH MONITORING

During the past year (M-URI year 4), efforts have been concentrated on developing the integrated AE microsensor. An integrated circuit chip containing the charge amplifier has been designed and fabricated. Testing of the chips from the first fabrication run indicates successful operation with a bandwidth of 1 kHz to 1 MHz, gains of 40 db, and a dc power requirement (brought in on the same two interconnect leads that the amplified signal to the external world) of less than one milliwatt. A system level diagram of the IC chip is shown in Fig. 2. The overall size of the chip is 2.2-mm square and 0.5-mm thick.

A package for the integrated AE sensor has been designed and fabricated. A sketch of the package is shown in Fig. 3. The overall package size is 6-mm by 6-mm lateral footprint and 6-mm tall. Placement of the PZT sensor and IC chip in the package was just beginning at the end of M-URI year 4.

The integrated AE sensor with onboard amplification represents a significant advance in the state of the art of AE sensors. The integrated sensor is smaller than commercially available AE sensors, which do not have internal amplification, and has a bandwidth that exceeds that of most AE sensors. The cost of the integrated sensor is expected to be considerably less than present commercially available sensors if the integrated sensor is designed for mass production.
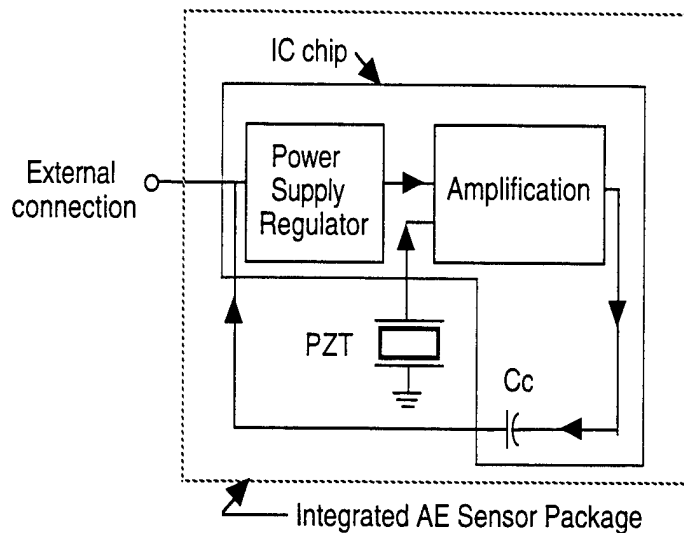

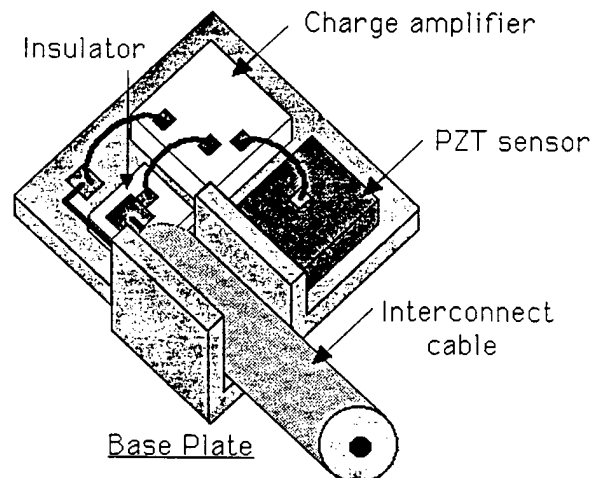**Figure 2.** System diagram of an integrated AE microsensor system.

Figure 3. Packaging of the integrated AE sensor. Overall size (with cover plate, not shown) is 6mm x 6mm x 6mm.

RESEARCH PLANS

During the first quarter of M-URI year 5, four (number of available IC chips) integrated AE sensors will be fabricated and tested. Testing will be a joint effort between the University of Minnesota and Georgia Tech. A second fabrication run of IC chips will be made in order to correct some design errors and to make available a sufficient number of sensors for all interested participants in the program. The second run of IC circuits should be available by June 1999, and completed sensors available by September 1999. The possibility of a third fabrication run in December 1999 will be considered if either more chips are needed or if additional design changes become desirable. A paper describing the fabrication and testing of the integrated AE sensor will be submitted for publication.

1.1.2 VIBRATION SENSOR
Co-investigator: Dennis Polla and Lorraine F. Francis
Students: Y. Nam, L. Zhang, D. E. Drinkwater, and C. R. Cho

DoD NEED

One of the goals of structural health monitoring is to detect the onset of unusual vibration characteristics prior to component or bearing failure. This is desirable for reasons of both preventing major systems damage and providing timely information in regularly scheduled maintenance. Most mechanical vibrations present on either helicopters or ships have fundamental movements at frequencies below 10 kHz. This presents a challenge for both silicon microsensors and signal processing due to the high 1/f electrical noise and parasitic signal losses.

PROJECT MISSION

Given the selection of piezoelectric sensors for AE sensing, the primary approach taken in this task is to apply similar microfabrication processing and electronics integration methods for both a vibration sensor and an AE sensor with the goal of possibly merging these functions on common chipsets. Preliminary success in the development of microfabrication methods for piezoelectric thin film microsensors based on 0.5 μm-thick PZT was achieved in year 3 of this program. While basic functionality was demonstrated, microsensor response characteristics (sensitivity and frequency response) were non-optimal. Activity during M-URI year 4 has included process refinement and microfabrication, electrical characterization, and hybrid amplifier integration.

TECHNICAL PERSPECTIVE

At the inception of this M-URI program, MEMS-based vibration sensors for structural health monitoring had not been reported in the technical literature. A variety of solid-state accelerometers had been commercially realized using either piezoresistive or capacitive sensing principles. These approaches however had significant barriers of high electrical power dissipation and need for precision micromachining methods with on-chip electronics.

Given the selection of piezoelectric sensors for AE sensing, the primary approach taken in this project is to apply similar microfabrication processing and electronics integration methods for both the vibration sensor and AE sensor with the goal of possibly merging these functions on common chipsets. A secondary back-up approach for the vibration sensor has been realized using very recent Analog Devices dual-axis MEMS comb-drive oscillators. These oscillators consist of two right-angle MEMS micro-fabricated electrostatic combs. An electronic circuit approach has been developed to simultaneously process changes in these oscillator characteristics in the presence of mechanical vibrations.

RESEARCH ACCOMPLISHMENTS

Several microfabrication runs were carried out this past year to optimize both the processing and responsivity of piezoelectric cantilever vibration monitors. These composite structures are based on the deposition of lead-zirconate-titanate (PZT) thin films of approximately 0.5 μm-thickness on top of a silicon nitride support structure. Figure 4 shows the main fabrication steps used in realizing the microcantilever vibration sensors. Figure 5 describes the geometry of the MEMS microcantilever. A scanning electron micrograph of a representative finished device is shown in Fig. 6. The overall device dimensions are approximately 4.5 μm-thick, 300-μm wide, and 1000 μm long.

The electrical and mechanical responses of the microcantilever beams were tested using conventional impedance analyzers, spectrum analyzers, atomic force microscopes, and a mechanical shake table. The piezoelectric coefficient Fig. 7 shows the deflection of the microcantilever beam under an applied voltage. Such a measurement based on the converse piezoelectric effect is necessary to assess the material quality of the piezoelectric thin film. The resulting measurement is used to calculate the piezoelectric coefficient of the PZT material, which in this case was determined to be –40 pC/N, which is approximately 30% of the value reported in bulk-grown PZT.

The frequency response of the PZT microcantilever under variable mechanical shake frequency was used to determine its acceleration responsivity to vibrations. The measured unamplified value at 1 kHz is approximately 0.11 pC/g based on the spectral data shown in Fig. 8. The response of the device was found to decrease significantly at lower frequencies (less than 1 kHz) presumably due to charge leakage effects (dc charges do not persist across piezoelectric capacitors). This has been identified to be one of the limitations of this type of vibration sensor, particularly for the detection of very low frequencies in systems such as mechanical pumps.

Due to the microcantilever roll-off at low frequencies and the high interest in usable devices at frequencies below 200 Hz, a piezoelectric CMOS signal conditioning process is currently under development. Successful development of a piezoelectric CMOS process could potentially 1) reduce parasitic interconnection losses, 2) provide signal amplification, and 3) implement filtering to both reject noise and linearize responsivity. Figure 9 shows the CMOS microchip currently under fabrication. This fabrication is being co-funded through this contract, DARPA, and the State of Minnesota. It is expected that the chip will be ready for testing in May 1999.

RESEARCH PLANS

Completion of the piezoelectric CMOS amplifier process and testing will take place beginning in May 1999. Vibration monitoring arrays demonstrated in M-URI year 4 will be put into specifically designed packages to produce a "smart coupon". IC chip amplifiers incorporating differential-pair cancellation technique methods will be included in the package to improve the information processing of the sensor. Integration of the vibration monitoring approach with the other hardware components of the program will be carried out.

M-URI PUBLICATIONS

D. L. Polla and L. F. Francis, "Processing and Characterization of Piezoelectric Materials and Integration in Micromechanical Systems," *Ann. Rev. Mater. Sci.,* V. 28, 1998, pp. 563-597.

C. R. Cho, D. E. Drinkwater, L. F. Francis, and D. L. Polla, "Properties of Nb-doped Lead Scandium Titanate Thin Films Prepared by Sol-Gel Method," Materials Letters, V. 38, 1999, pp. 136-140.

C. R. Cho, L. F. Francis, and D. L. Polla, "Ferroelectric Properties of Sol-Gel Deposited Pb(Zr,Ti)O$_3$/LaNiO$_3$ Thin Film on Single Crystal and Platinized-Si Substrates," Materials Letters, V. 38, 1999, pp. 125-130.

1. Etch Trench in Silicon Wafer

2. Planarize a Layer of PSG and deposit a layer of Oxide

3. Deposit a Layer of Low Stress LPCVD Nitride

4. Pattern the LPCVD Nitride and Remove the PSG

5. Deposit a layer of LTO to Seal the LPCVD Nitride Etch Holes

6. Deposit and Pattern the bottom electrode (Pt/Ti), PZT and top electrode (Pt)

7. Deposit and Pattern a layer of PECVD oxide for electrical isolation

8. Deposit and Pattern a layer of Aluminum for the bonding pads
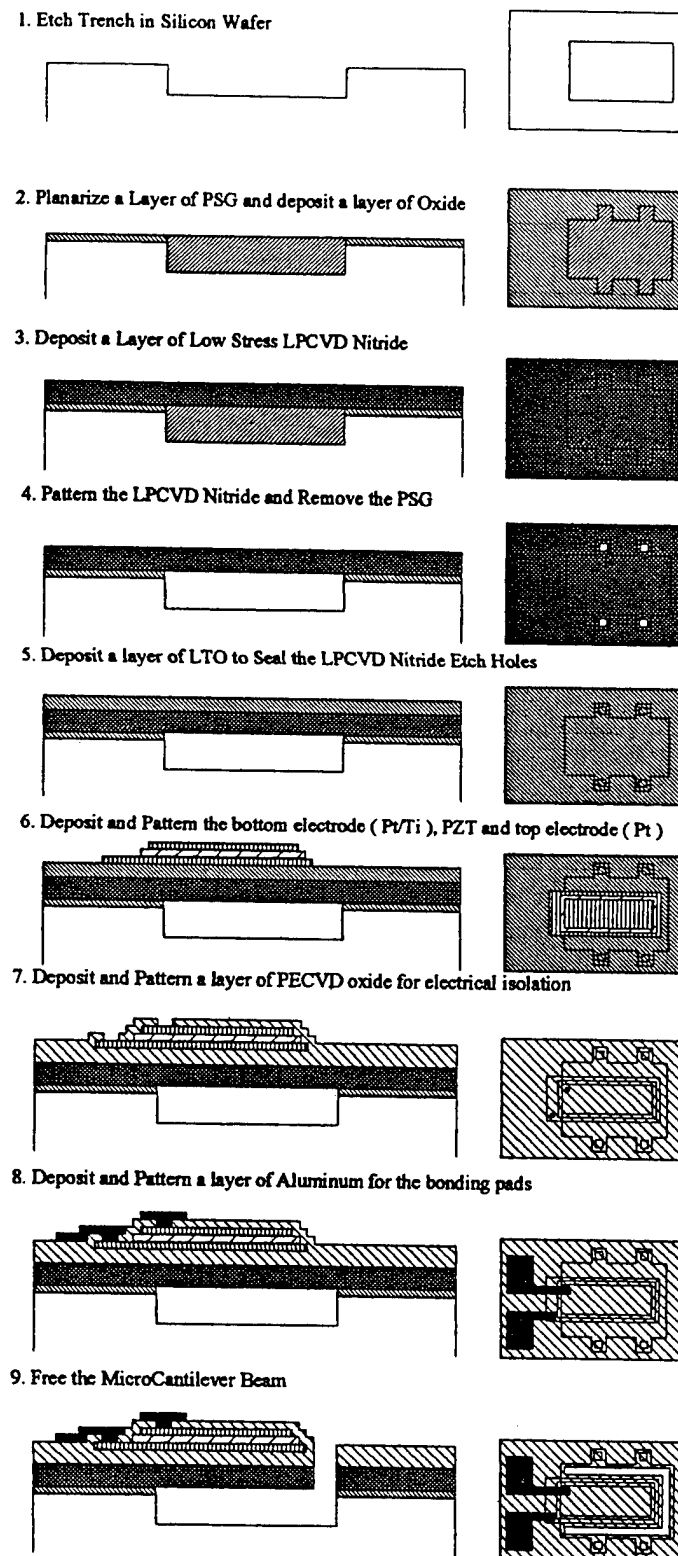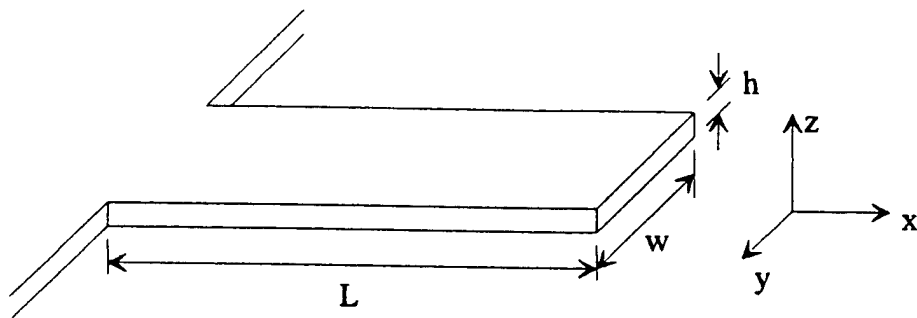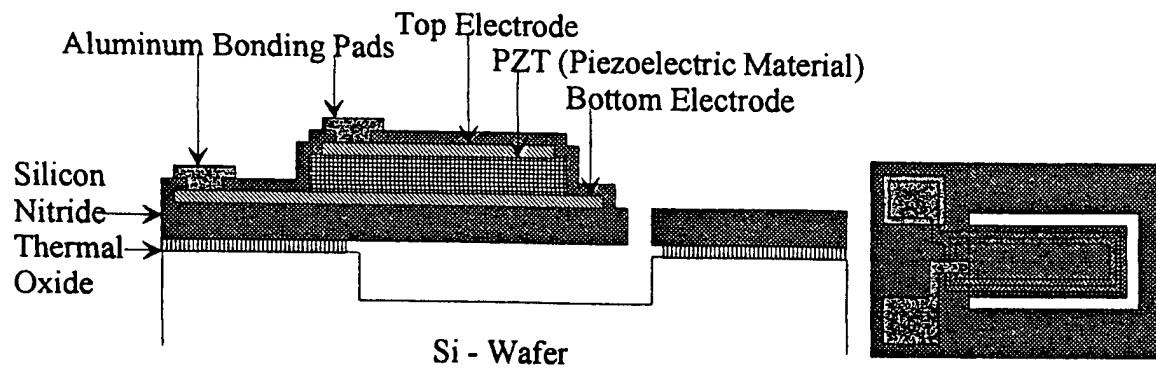
9. Free the MicroCantilever Beam

Figure 4. Main processing steps used in realizing microfabricated piezoelectric vibration sensors.

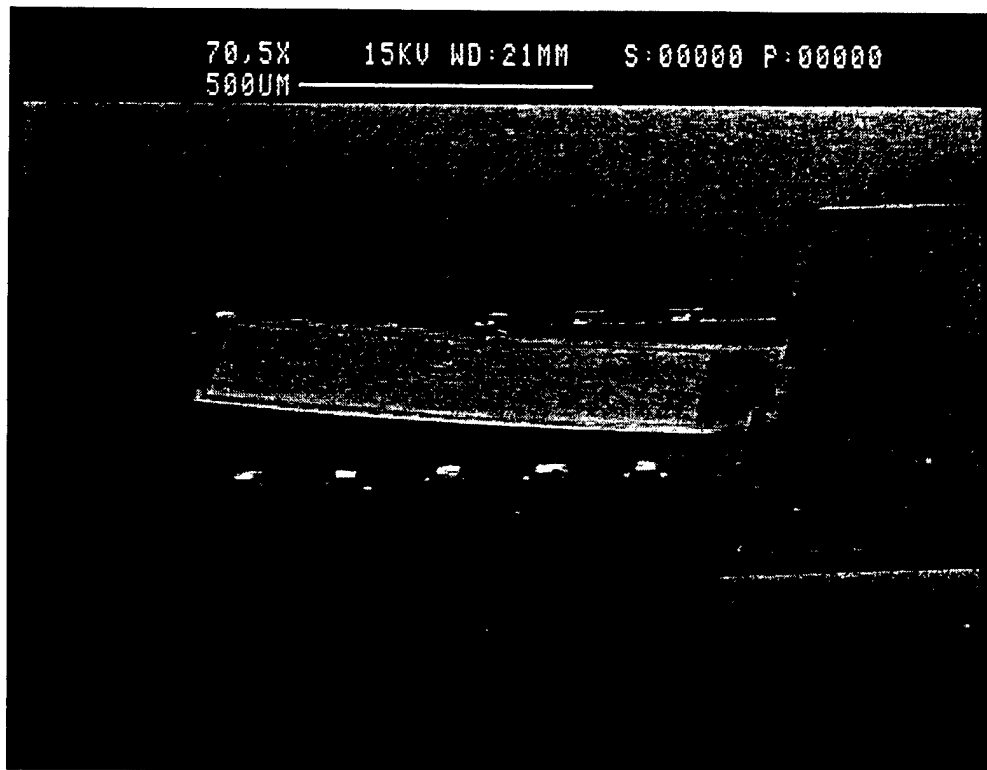Figure 5. Cross section of a surface-machined PZT microcantilever.

Figure 6. Scanning electron micrograph of a finished PZT microcantilever vibration sensor
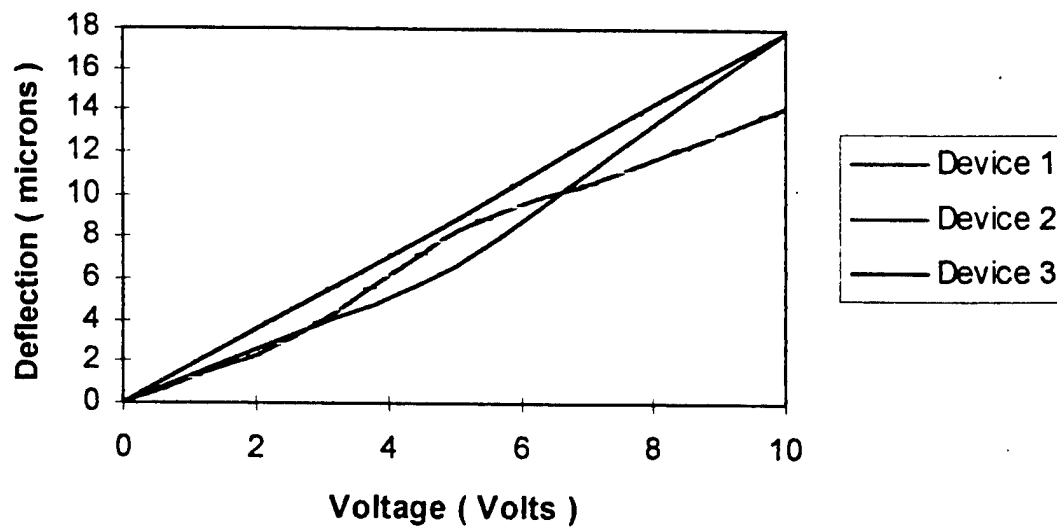
Figure 7. Measured voltage versus tip deflection characteristics obtained for three identical PZT microcantilever beams. These measurements are used in determining the piezoelectric coefficient d_{31} of the material. The measured value is -40 pC/N.

100   **1000**   **3000**

Figure 8. Electrical responsivity of a PZT microcantilever beam when mechanically excited by a shaker table. The frequency range is 100 Hz to 3 kHz.

Figure 9. Die photograph of a CMOS signal conditioning microchip (near completion) in fabrication.

1.1.3 PRESSURE SENSOR

Co-investigator: Dennis Polla

Students: X. Li, J. Ye

DoD NEED

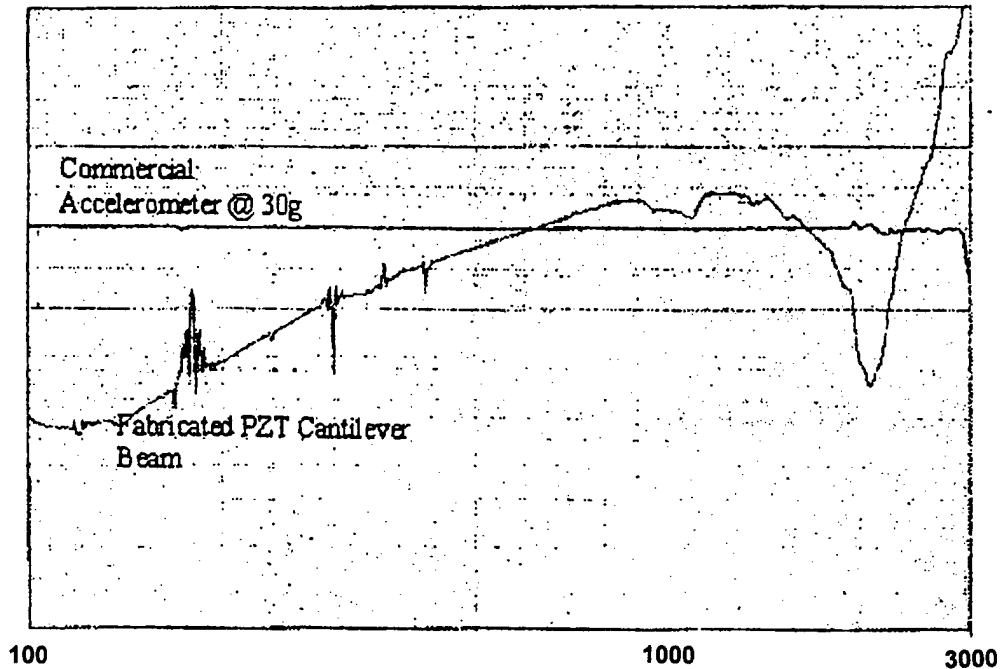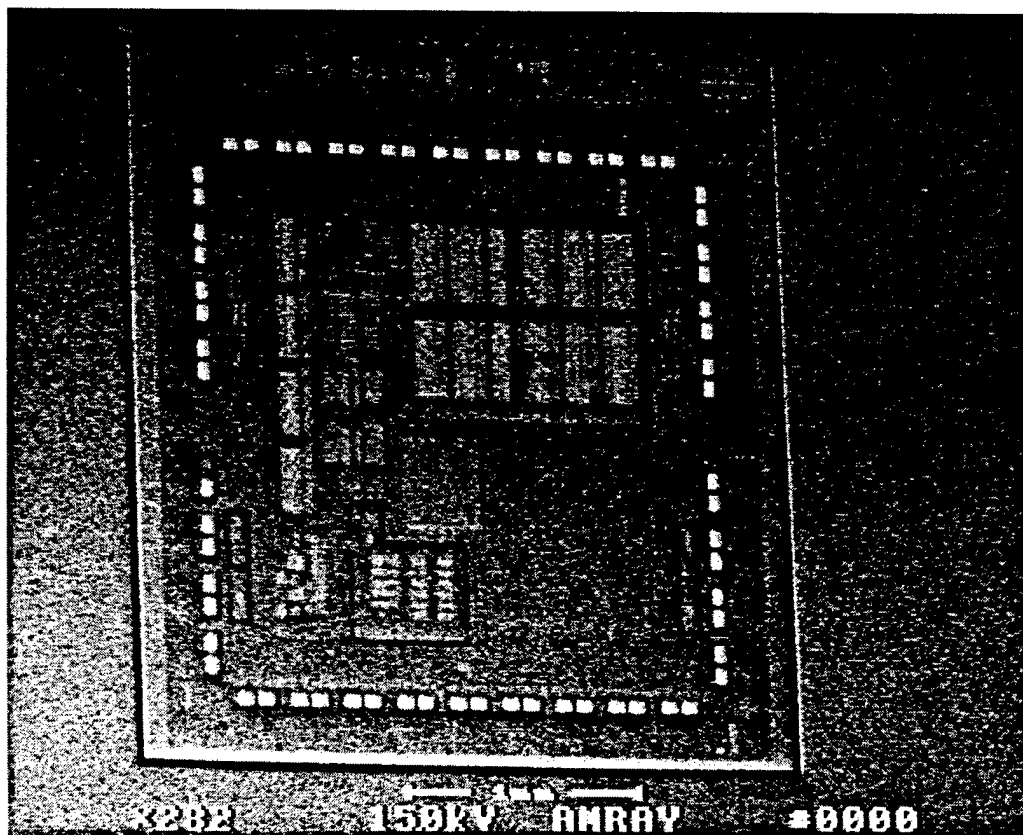Reference pressure sensors, as originally summarized in the *M-URI Year 1 Annual Report* (in addition to the temperature reference sensors developed in M-URI year 2 of this program), may be needed for signal referencing, particularly for systems such as helicopters and motors where environmental conditions might alter the response of the primary AE and vibration sensors.

PROJECT MISSION

The goal of this project is to realize a simple reference pressure sensor that has the properties of being compatible with the other components in the smart structural monitoring coupon and have low power dissipation. The technical approach selected is based on realizing a simple piezoresistive pressure sensor. When operated at a low duty cycle typical for most structural health monitoring applications, this type of device exhibits extremely low energy consumption.

RESEARCH ACCOMPLISHMENTS

Surface-micromachined piezoresistive pressure sensors were designed, fabricated and tested. Figure 10 shows a cross section for a surface-micromachined pressure sensor. A representative 1000 µm-dia. polysilicon piezoeresitive pressure sensor is shown in Fig. 11. The measured response of the device as characterized under partial vacuum conditions is shown in Fig. 12. The successful fabrication of this device represents a usable technology for an integrated multi-functional smart coupon to be realized in M-URI year 5.

RESEARCH PLANS

No further development plans are in place for the piezoresistive pressure sensor. This device can simply be inserted into the smart coupon to be assembled in M-URI year 5.
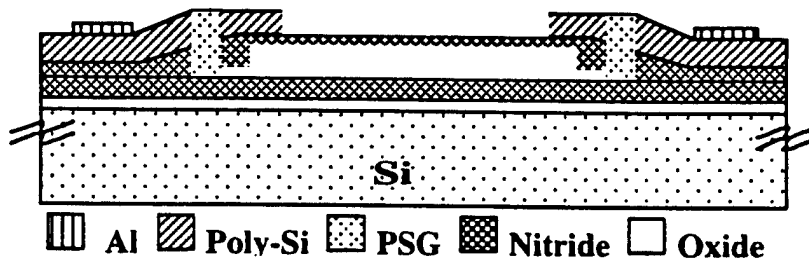
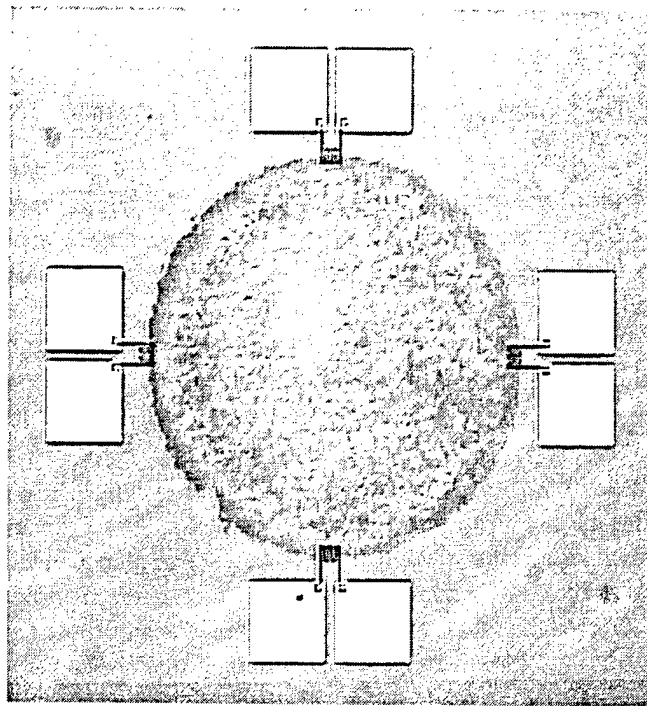**Figure 10.** Cross-section design of a piezoresistive pressure sensor.

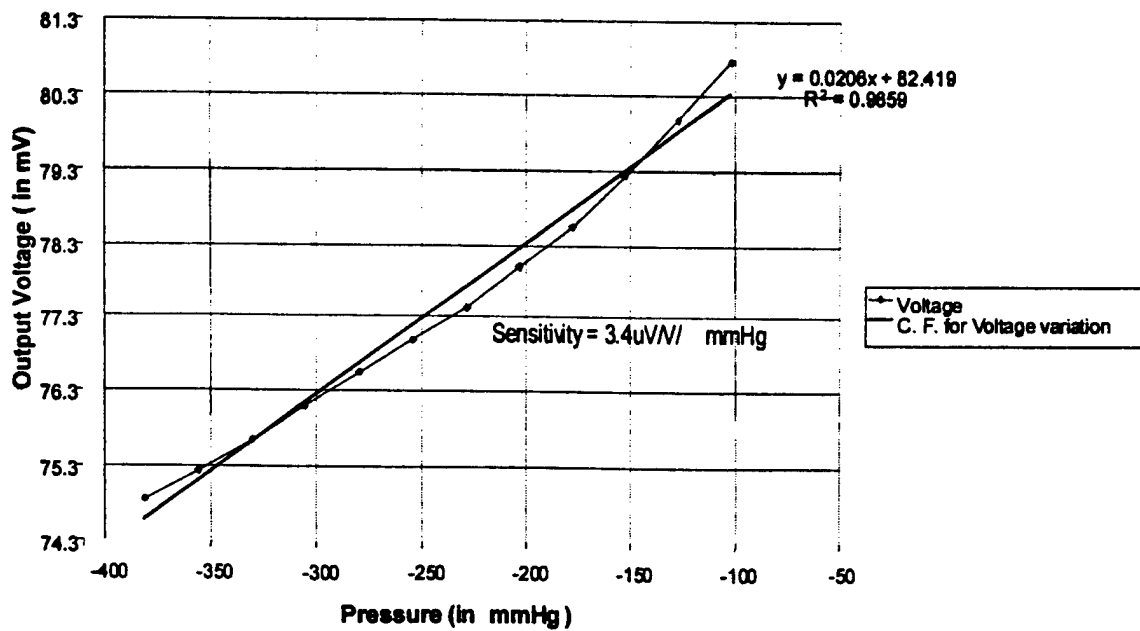**Figure 11.** Optical photograph of a representative 1000 μm-dia. polysilicon piezoresistive pressure sensor.

Figure 12. Measured responsivity of a MEMS piezoresistive pressure sensor.

1.1.4 SIGNAL PROCESSING FOR INTEGRATED DIAGNOSTICS

Co-investigators: M. Kaveh and A. H. Tewfik
Students: G. Venkatesan, D. Zhang, P. Andersson, and H. Sun

DoD NEED

Automatic monitoring techniques are a means to safely relax and simplify preventive maintenance and inspection procedures that are expensive and necessitate substantial down time in expensive machinery. Such monitoring may also be used to provide warning of possible catastrophic failures in such systems as aging helicopters and aircraft. Acoustic emissions (AEs), which are ultrasonic waves emanating from the formation or propagation of a crack in a material due, for example fatigue, provide a possible signal with informative signature which may be used for such monitoring.

PROJECT MISSION

Though the characteristics of AEs have been extensively studied, most of the work has been done under controlled laboratory conditions at very low noise levels. In operating machinery, such as a helicopter, however, the AEs are buried in a wide variety of strong interference and noise. These arise due to a number of factors that, other than low-frequency vibration, may include fretting, hydraulic noise and electromagnetic interference. Most of these noise events are transient and not unlike AE signals. In consequence, the detection and isolation of AE events from the measured data is not a trivial task and requires understanding of signal and noise characteristics and the development of intelligent multichannel space-time-frequency signal processing algorithms. The development of such analysis tools and systems form the primary mission of the signal processing effort.

TECHNICAL PERSPECTIVE

The primary impact of the signal processing research has been in the understanding of waveform and time-frequency characterizations of relevant AE signals and expected interferences, and the development of a suite of algorithms for the detection of such signals in an interference-rich environment. This stands in contrast with what was the state of the art in AE-based tools at the inception of this project in 1995, which depended primarily on the frequency of events in clean laboratory tests, and were primarily used for the understanding of various material properties and mechanical phenomena. The data used in this research has ranged from controlled, multichannel lab-based signals to on-ground and in-flight helicopter data. This data has complemented theoretical and algorithmic developments to provide a suite of analysis and detection/classification algorithms using time, frequency and spatial features for the discrimination of crack-generated AEs from other transient interference for low false-alarm rate operation.

RESEARCH ACCOMPLISHMENTS

Blind Deconvolution

Development of algorithms for the recovery of source waveform from noisy measurements by multiple sensors has continued in M-URI year 4. The aim of this work has been to attempt estimating AE signal characteristics at the point of generation from measurements by sensors following propagation in a dispersive medium. A number of fundamental results have been established in non-supervised transient signal recovery for both pole-zero (IIR) and all-zero (FIR) propagation channel models. The techniques have been applied to 3-channel nano-indentation laboratory data with mixed results. The complexity of this propagation channel, involving many boundary reflection components, was deemed too high for effective deconvolution.

In-Flight Data Analysis

The Rotor Acoustic Monitoring System (RAMS) developed by HONEYWELL was flight-tested at PATUXENT RIVER NAVAL BASE from August 28 to September 18, 1997. More than 16 hours of flight data was recorded from 8 on-rotor acoustic sensors. Honeywell provided us with a digitized set of data from the level flight segment of the test. The data included the recordings at all eight sensors for all eight permutations of pinger ON/OFF and pinger excitation 100V, 48V, 20V and 10V cases. However the digitization of the data for the different channels of observation was not synchronous, i.e. the data digitized at different channels were all from different time segments. The duration of each digitized segment of data was about 2 seconds at a sampling frequency of 2MHz (12 bit A/D accuracy). A typical high signal-to-noise ratio data record from sensor 2 is shown in Figure 13a.

Analysis of the data indicated a number of general characteristics and also discovered several sources of degradation in the measured data. The background noise was clearly observed to be nonstationary. The nonstationarity is affected by, for example, the helicopter's maneuvers. The spectral contents and transient nature of interfering signals are similar to the pinger-generated acoustic emission. Some of these transients have periodicity of the rotor, which may help in their mitigation. However, the broadband nature of many of the interfering transients is cause for concern in the effectiveness of potential low false-alarm AE detectors/classifiers. Additionally, harmonic components at 330 kHz and 660 kHz, apparently attributed to the switching power supply in the data acquisition system, were discovered as shown in Figure 13b. These interfering components and aliasing considerations led us to use data only up to 500 kHz with a notch filter around 330 kHz.

As the observations given above indicate, effective classifiers following in-band detection are required. Work has begun on a self-organizing map neural network to carry out such a classification. This network has been trained on time-frequency features of the Honeywell pinger data and tested on other data records involving pinger signals (AE simulation) and other transients. The performance of the network has shown some promise so far, with perfect detection and about a 5% false alarm. This false alarm rate is too high for our purposes and indicates the need for training with a larger database.

(a)   (b)
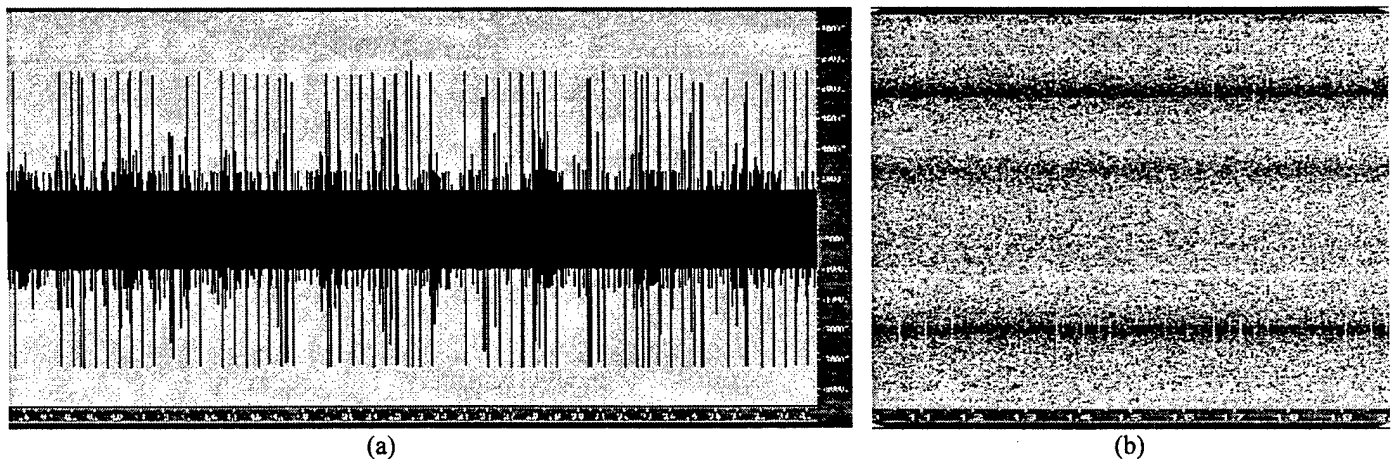
Figure 13. Typical sensor 2 data from Honeywell flight test. **(a)** Time domain record; **(b)** Time frequency spectrum over 0 - 1 MHz.

Fatigue Test Data Analysis

Experimental data were obtained from extensive fatigue test conducted at Georgia Tech. Four sensors mounted on a notched thin metal specimen simultaneously recorded the data, i.e. the data digitized at four channels were all from the same time segment at a sampling frequency of 25MHz. In contrast with the Honeywell in-flight data, the laboratory data provided multi-sensor information such as

relative time-of-arrival and average frequency. Analysis of this data, thus far, has not revealed a great deal of difference in the main frequency components at different stages of the fatigue test. Principal Component Analysis was used to delineate the key features of the data across the different stages. It was observed that signal energy, rather than other time-frequency features were a more reliable feature in separating the different stages of crack formation. This was most evident in separating stage 1 into two distinct periods, for example, as shown in Figure 14. Further work is continuing in PCA for dimensionality reduction and for characterization of the different AE signals. Cross-correlation techniques are also under development for differential time-of arrival estimation to eliminate signals from the "hot-spot" areas. These methods will be applied to new data, which is expected to include fretting fatigue-generated signals for the purposes of classification.

(a) Without Normalization   (b) With Normalization
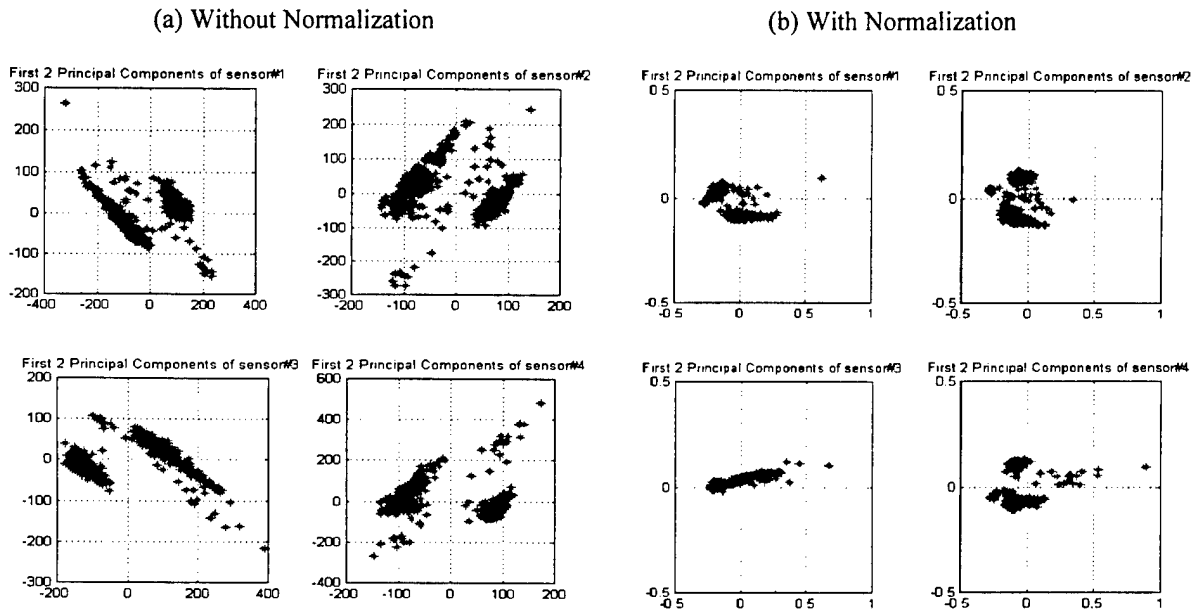
Figure 14. Clustering of the first two principal components for two time segments of stage 1 in the Georgia Tech fatigue test.

Signal Modeling and Detection

Transients have been modeled as a combination of decaying sinusoidal waveforms. In specific cases, however, depending on the material geometry and characteristics, it might be possible to predict the range of decay rates as well as the range of frequencies exhibited by the crack AE transient. This model initiated our work on a new detection scheme based on the linear model residual. In this scheme, the signal model parameters are not known a priori, but are estimated. The decision is made on the thresholding of the ratio of the residual energy in fitting the parameterized model to the total signal energy. This method was shown, theoretically, to have constant false alarm in the presence of white noise. The method was applied to a number of experimental data sets. In the case of the helicopter data, the nonstationarity and non-white nature of the noise resulted in the adaptation of the detector to the noise model. Accordingly, for such data, a simpler detector based on multiband decomposition of the data was implemented.

Classification

A Self-Organizing Map (SOM) neural network has been employed to detect crack-related AE signals because of its ability to map high-dimensional time-frequency distribution data into a low-dimensional SOM codebook. The concept of SOM was introduced by Kohonen in early 1981. Each neuron or group of neighboring neurons in SOM responds to a particular kind of input pattern. After the competitive learning process, different types of transient signals will activate neurons in different locations within the same codebook. Therefore, the index sequence of active neurons can be used on each input data set to discriminate between crack-related AE and other transients. Figure 15 gives the block diagram of such a network, which uses time-frequency vectors as input.

In this study, in-flight helicopter data from one sensor has been used to test the ability of an SOM to detect crack related AE signals. A 6x6 SOM successfully differentiated between transients due to the pinger and other interference transients. These interference transients are very similar to the transients created by the pinger in both the frequency and time domains. Signals due to the pinger were used in training the network. After training, the SOM became ordered. When test data was fed into this SOM, the neuron with the maximum output response to the current input was recorded as the active neuron. We found that only transients due to the pinger activated neuron 3, and only neuron 3 responded to transients due to the pinger. Other transients activated many other neurons. Figures 16a and 16b give the respective time distributions of the active neurons for segments of the data, which includes a sample from the AE transient (for which characteristics the network is trained) and interference transient. Therefore, a majority rule over an appropriate time window determined the effective class neuron resulting in a very high correct classification performance, but with still an unacceptable level of false alarm. Further refinement of this classifier, based on multi-sensor data, is planned.
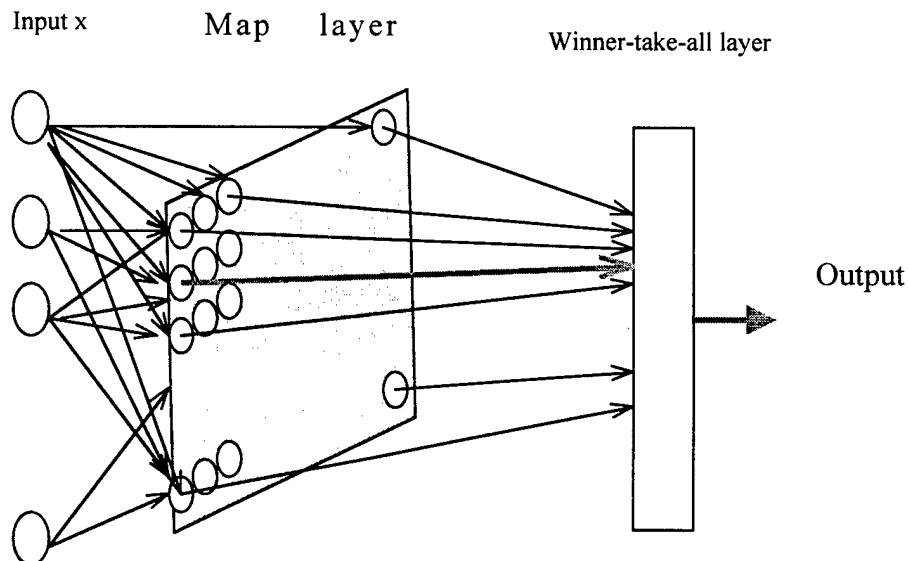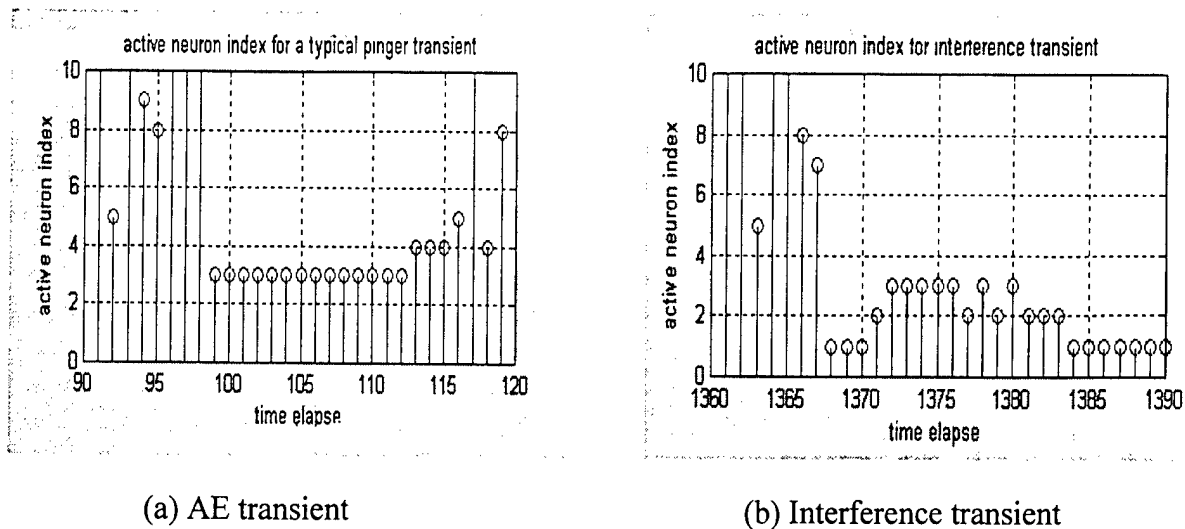

Figure 15. Self-Organizing Map network with time frequency vector as input.

active neuron index for a typical pinger transient

active neuron index for interference transient

(a) AE transient

(b) Interference transient

Figure 16. Time Distribution of active neurons at the output of a trained SOM network 129-sample time window is used.

RESEARCH PLANS

Plans for M-URI year 5 include the continuation of the development of detectors and classifiers based on principal component, factor analysis, multiband filtering, and SOM neural networks. Interaction with Georgia Tech co-PIs conducting fatigue and fretting experiments (Sections 3.2 and 3.4) is planned to extend our techniques to spatiotemporal processing based on simultaneous measurements by multiple sensors for differentiating crack-generated AEs from other sources of AE and similar transients. In addition, work is underway to obtain additional data from maneuvering segments of the Honeywell helicopter flight test to determine the characteristics of the noise under more severe conditions.

M-URI PUBLICATIONS

M. Kaveh, "Mechanical diagnostics using acoustic emissions," Plenary lecture, Ninth IEEE Statistical Signal and Array Processing Workshop, Portland, OR, September 1998.

D. Zhang, G. Venkatesan, A. Tewfik and M. Kaveh, "Acoustic emission transient detection based on linear model residuals," *Proceedings of Ninth IEEE Statistical Signal and Array Processing Workshop*, Portland, OR, September 1998.

D. Zhang, G. Venkatesan, M. Kaveh and A. Tewfik, "Fault monitoring using acoustic emissions," *Proceedings of SPIE Conference on Sensory Phenomena and Measurement Instrumentation for Smart Structures and Materials*, March 1999.

G. T. Venkatesan, L. Tong, M. Kaveh and K. Buckley, "A deterministic blind identification technique for SIMO systems of unknown model order," *Proceedings of ICASSP99*, Phoenix AZ, April 1999.

H. Sun, M. Kaveh and A. Tewfik, "Self-organizing map neural network for transient signal classification in mechanical diagnostics," accepted for the IEEE Workshop on Nonlinear Signal Processing, June 1999.

MECHANICAL SYSTEM HEALTH MONITORING

-16-

1.1.5 INTERFACE CIRCUITS FOR PIEZOELECTRIC SENSORS

Co-investigator: Ramesh Harjani
Students: Kavita Nair and Jonghae Kim

DoD NEED

Real-time detection and characterization of material failure in vehicle components is desired as mechanical components nearing their design limit become fatigued and develop cracks. Development of cracks is accompanied by acoustic emission events. Detection of acoustic emission events is important not only in the prevention of catastrophic failure, but also in regular and routine maintenance.

PROJECT MISSION

The primary objective of this project is to develop real-time sensing devices and methods to accurately identify conditions leading to imminent failure of critical aircraft components. The two important technologies brought together for this purpose are microsensors and sensor conditioning electronics. The microsensor used is a thin-film acoustic emission (AE) sensor that detects the development of cracks and unusual wear in the body of aircraft and submarines. The signal conditioning electronics are used to identify and amplify the signal from the AE microsensor within an electrically and acoustically noisy environment.

A second goal of this project is to realize inexpensive and low power silicon chips that can be distributed over critical regions of the aircraft and submarine. To realize this goal, it becomes necessary to implement the complete system with a minimum number of external wires and components.

TECHNICAL PERSPECTIVE

At the onset of this project, only discrete and simple pre-amplifiers for acoustic emission (AE) sensors were available. Amplifiers could be attached to the AE sensor but required multiple wires for power, signal and grounds. Most of these designs targeted low-speed operation. Because discrete designs had to be combined, a large area was used. As the amplifiers were not tuned to the application, they were overdesigned and consumed high power. Lastly, sensor electronics and sensors were separate.

This is no longer the case as results from this project have advanced the state-of-the-art. Integrated interface circuitry with a two-wire signal and power transmission system has been completed. It is high speed (~ 2MHz signal operation) and occupies a small area. A new shielded-base amplifier with 10X reduction in power has been designed. Thus, there is now a great potential for complete integration of integrated sensors and electronics.

RESEARCH ACCOMPLISHMENTS

During the past year, the major accomplishment of this task has been the design and fabrication of a two-wire telemetry and signal conditioning circuit for piezoelectric sensors. The telemetry system uses an on-chip voltage regulator as part of the signal-vs.-supply filter. A new shielded-base bipolar operational amplifier design that exploits the properties of both MOS and bi-polar transistors was also introduced. The new design results in a 10X reduction on power for a 10 dB reduction in signal-to-noise ratio. Two designs have been implemented for a sensor capacitance of 100 pF. The first design has a bandwidth of 2 KHz to 1 MHz and the second design bandwidth is from 50 kHz to 1 MHz. Circuit design, simulation and measurement results are presented in the report "**Interface Circuitry for Piezoelectric Sensors,**" found in Appendix B.

RESEARCH PLANS

During M-URI year 5, plans include i.) assisting in accomplishing the goals for the wideband integrated AE microsensor task of Section 1.1.1. and ii.) advancing the state-of-the-art in sensor interface. Plans to improve the AE sensor include developing high-speed data converters to convert the AE signal to digital. The advantage of including an A/D converter on chip is the increased immunity to noise with a fewer number of external components, thereby enabling greater reliability.

M-URI PUBLICATIONS

K. Nair and R. Harjani, "A Telemetry and Interface Circuit for Piezoelectric Sensors," IEEE International Symposium on Circuits and Systems, May 30-June 2, 1999.

C. Zillmer K. Nair, R. Harjani, and D. Polla, "Data Acquisition and Conversion," Chapter in *Wiley Encyclopedia of Electical and Electronic Engineering,* ed. John Webster, March 1999.

1.2 DYNAMIC METROLOGY AS A BEARING WEAR DIAGNOSTIC

Co-investigators: Thomas Kurfess, Steven Liang, and Steven Danyluk (Georgia Tech)
Graduate Research Assistants: Chen Zhang, Yawei Li, Xavier Ribadeneira, Tracy Williams
M-URI Year 4 Funding Allocation: 6.7%

DoD NEED

A large portion of catastrophic failures in complex mechanical systems such as helicopters are the direct result of bearing failure. Such failures can yield damaging and cataclysmic results, and are increasing in probability as the average age of the helicopter fleet in the Navy continues to rise. Thus, real-time, on-line techniques to determine the current health and accurately predict future failures of bearings typically found on helicopters must be developed. Such techniques are critical in the maintenance of the helicopter fleet. The techniques are also applicable to a wide range of other systems that employ bearings.

PROJECT MISSION

To fully utilize the latest sensors available today in an intelligent fashion, this project targets the development and implementation of real-time and on-line methods for bearing wear and failure detection. The ultimate objective of the project is to develop a compact self-contained processing package that can be attached to an array of sensors used to monitor and predict bearing health during the operation of a rotary winged aircraft. To accomplish this, a number of sensors will be employed including contact potential difference probes (CPD), eddy current, accelerometer, and acoustic emission sensors. To successfully meet project objectives, these individual sensors must be calibrated and integrated into a single diagnostic and prognostic package. By using a multiple sensor approach, it is anticipated that a number of wear and failure modes will be detectable in real-time. Furthermore, the use of multiple sensors will improve the confidence interval on the estimation of a bearing's condition.

TECHNICAL PERSPECTIVE

Prior to this work, state-of-the-art techniques were capable of determining when a bearing had sustained significant damage. These diagnostic capabilities were thoroughly studied and incorporated into the present diagnostic routines used in this project as the foundation for the prognostic techniques. Yet it has been observed that the variation of a bearing's remaining life (the time to reach the final failure size) from the point where a defect can be detected may be substantially more than its L_{10} life, which is the life of 90% bearing population survival. Hence, there has been a lack of reliable prognostic methods to accurately predict the remaining life of a defective bearing. This lack of capability has lead to the common practice of shutting down machinery immediately when a damaged bearing is detected to avoid catastrophic consequences.

A significant amount of economic gains can be realized by the avoidance of such practices at inconvenient times and when there is still a significant amount of useful bearing life remaining. This research has successfully provided inroads into developing reliable prognostic techniques that are based on fundamental physical principles, as opposed to black box methods that do not incorporate the physics of damage growth and propagation. These techniques have been experimentally demonstrated to accurately predict remaining bearing life.

RESEARCH ACCOMPLISHMENTS

During the course of the project, a bearing test bed has been developed to perform thermal, load and speed calibrations, as well as sophisticated diagnostics using multiple sensors. During M-URI year 4, the test stand has been enhanced with a 10 hp drive system, an active lubrication system and new tooling permitting it to run tapered roller bearings, ball bearings and straight roller bearings. The research was

further enhanced by engineering support and guidance from the TIMKEN COMPANY, the TORRINGTON COMPANY, and EXPERTECH, INC. The test stand has been used to simulate a variety of operational systems, most recently the Pratt & Whitney F-119 engine. Successful diagnostic tests have also been conducted on a variety of actual systems including turbo-pumps and high speed spindles. Based on the diagnostic tools developed, a successful prognostics program has been initiated. This section concentrates on the results generated in the prognostic area as they inherently employ the results of the research in diagnostics. In particular, results are presented from an actual experiment to demonstrate the capabilities of the diagnostic and prognostic techniques developed in this research.

For this particular set of experiments, the new 10 hp Baldor AC motor was employed. Vibration signals were low-pass filtered at 10 kHz by a Krohn-Hite #3384 programmable filter for anti-aliasing prior to digitizing at 30kHz. The test bearing was a Timken LM50130 cup (outer race) and LM501349 cone (inner race). It is a tapered roller bearing with a bore diameter of 4.12 cm (1.625 in.) and an outer diameter of 7.34 cm (2.891 in.). The taper angle is 13.13 degrees from the bearing axial centerline. The pitch diameter is 5.72 cm (2.250 in.). Its rated radial load is 15,160 N for a 90 million cycle-life rating at 500 RPM.

To accelerate the failure propagation process, a defect was artificially located on the loading zone of the outer raceway by electrical discharge machining. It was a crack, oriented along the bearing axial direction to simulate a real-life fatigue crack with width of 0.28 mm and depth of 0.065 mm. Operating conditions for the experiment were 1,800 rpm shaft speed and 88,388 N radial load (about 6 times the rated radial load). The system temperature was regulated to 70-degrees C by a thermal controller on the oil circulation system. The system was lubricated by thin spindle oil with a viscosity of 57 SSU at 37.8 degrees C. A set of data of length 2^{16} points was acquired every 15 minutes corresponding to 0.027 million cycles for the prescribed set of experimental conditions. Testing was interrupted and the system disassembled at 0.378, 1.566, 3.51, 7.452 and 9.666 million cycles to permit physical inspection of the defect. Defect propagation did not occur prior to 9.666 million cycles. This is consistent with the diagnostic analysis based on measured vibration signals. No obvious change of signal characteristics was observed. The last defect inspection occurred at 9.666 million cycles, and testing continued until 13.986 million cycles were achieved. Excessive vibration was observed after 9.666 million cycles. After the testing stopped at 13.986 million cycles, the test bearing was disassembled and it was found that the defect on the outer race had propagated to an area size of 100 mm^2 in the running direction.

Since defect propagation was observed to happen after 9.666 million cycles, a detailed analysis was performed only for that period. Several research groups have showed that wear severity is proportional to the resulting vibration energy. This relationship is used to relate forecasted vibration levels to predictions of bearing damage propagation. The bearing life testing indicated that a vibration RMS in the range of 7500-9000 Hz is closely correlated to the defect propagation process shown in Figure 1. For this reason, vibration RMS in this range was used to test the proposed prediction method.

Figure 1 reveals that the change of RMS can be separated into three different stages. In the first stage, during the first 2.9 million cycles, RMS has no underlying trend of change. Therefore, the uncertainty of measurement due to noise can be calibrated by the standard deviation of RMS during the first 2.9 million cycles, which is 0.03. In the second stage, between 2.9 and 3.6 million cycles, RMS increases slowly to a level of 1.34. In the third stage, after 3.6 million cycles, RMS increases significantly.

A prediction algorithm was employed at running cycle numbers of 2.16, 2.7, 2.97, 3.105, 3.186, 3.24, 3.348, 3.5, and 3.51 million. The corresponding results are shown in Figure 2. It is shown that before 2.9 million cycles, the RMS mean prediction is almost constant, resulting in a small prediction uncertainty. This is due to the lack of an underlying trend in the RMS. After 2.9 million cycles, the algorithm begins to predict the change of RMS. Additionally, it is observed that the predicted variances are large in magnitude after 3.6 million cycles and RMS cannot be tracked by the proposed prediction method because of the rapid increase in RMS, yielding a large uncertainty level in the prediction.
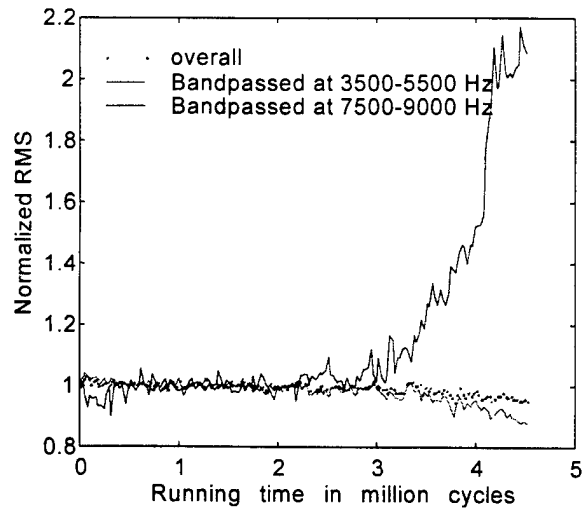
Figure 1. Normalized RMS vs. running cycle in the last assembly at different frequency band.
(Normalization is with respect to the value of the first point)
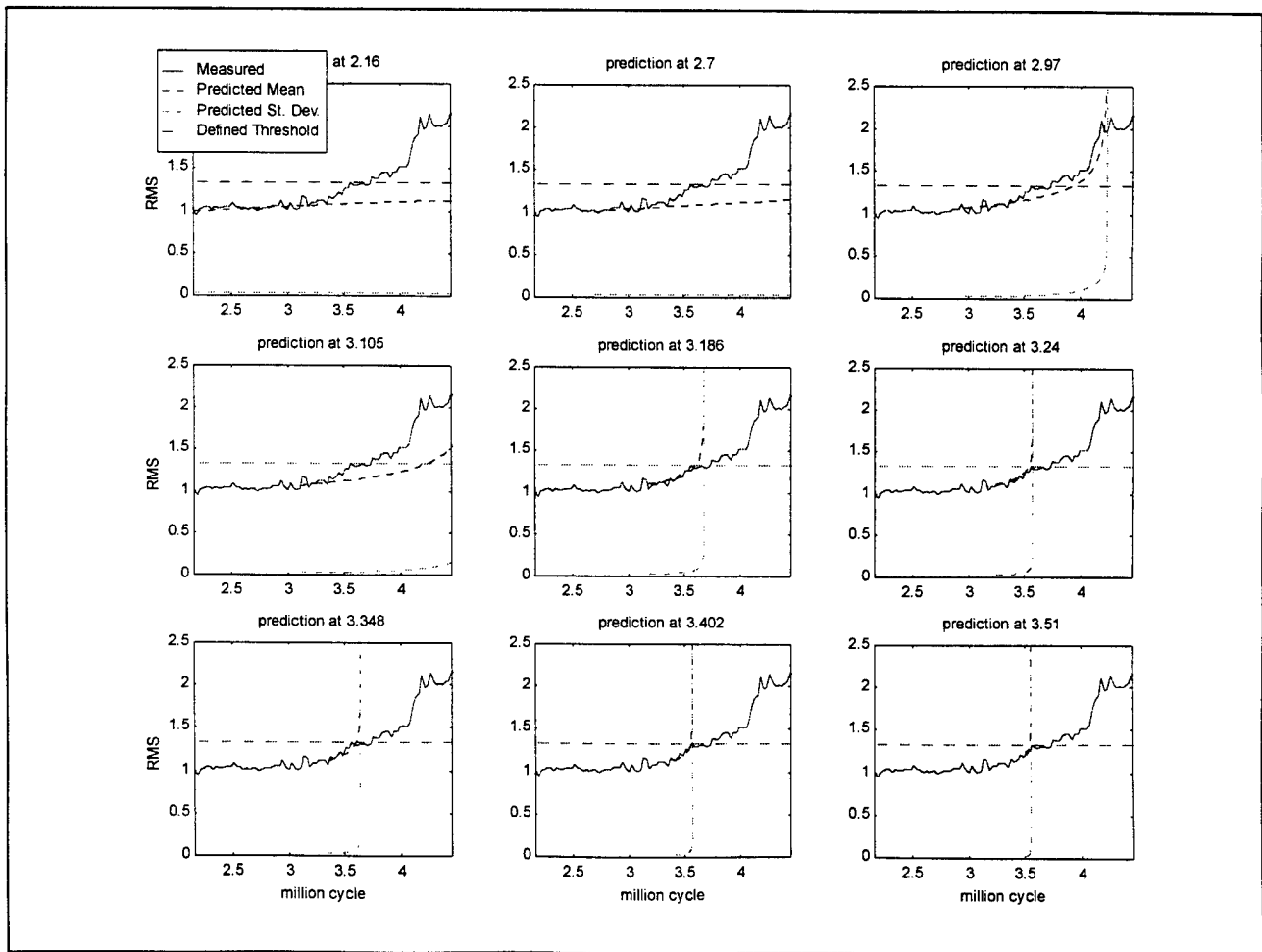
Figure 2. Predicted Mean RMS and standard deviation at different cycles.

Since the rapid increase in RMS above a critical value physically indicates an unstable propagation of defects that result in an imminent fatal failure, a bearing replacement is justified. For this reason, a RMS threshold of 1.34 is used as is denoted by the dashed line in Figure 2. The threshold provides an indicator as to when a defect has begun to propagate and, consequently, when the prognostic routines should be employed. Before this threshold is achieved, the application of the prognostic tools is not recommended, as the statistics used to construct the propagation model are not well developed. After the threshold has been reached, the prognostic tools should be used to closely monitor the bearing and plan for a scheduled maintenance of the system where the bearing can be replaced. Figure 3 plots the predicted time when the RMS reached the threshold at each prediction instance. It is shown that after 3.186 million cycles, 0.4 million cycles before the measured RMS reached the threshold, prediction errors are within ± 0.1 million cycles. (Note that 0.4-million cycle corresponds to 3.7 hours and the bearing was running at the radial load of 6 times its rated load.) These experimental results imply that the proposed approach offers a prediction that is early enough for maintenance actions before bearing life reaches critical damage levels.
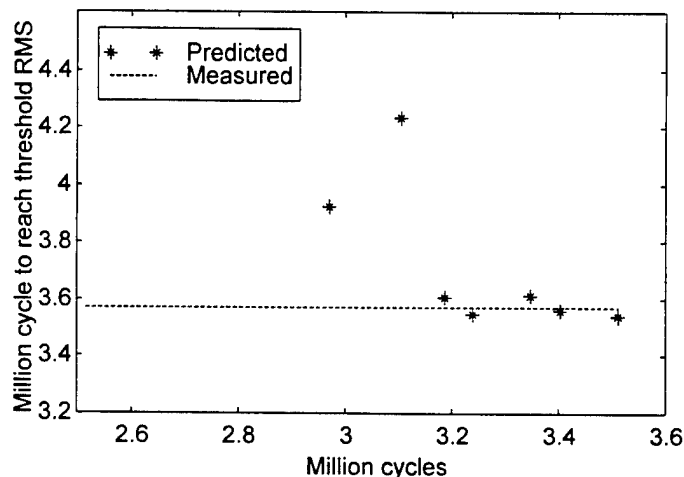

Figure 3. Predicted time to reach a threshold of RMS

Conclusions

The results of this year's research effort demonstrate a strong and proven capability in bearing diagnostics. Furthermore, the diagnostics have been used as the basis for successful work in the damage prediction or prognostics area. Initial results on both roller bearings as well as ball bearings indicate that the techniques developed in this research are useful for predicting both the remaining life of a bearing once it starts to degrade, as well as a confidence level in the prediction results. It should be noted that the results of this work are fairly consistent with many concerns of engineers interested in applying prognostic techniques.

The biggest concern is that once some finite life is estimated for the component, maintenance crews will have a tendency to replace the part. The question that arises is, "Would you like to be flying this helicopter today given the fact that we anticipate a critical bearing in the aircraft has one week of life remaining?" Clearly, such a question will make both air crews as well as maintenance personnel nervous. The approach used in this research will not begin to estimate remaining life if there are no problems in the bearing. That is to say, if no damage is detected, the approaches developed in this research will not, and cannot, generate expected life predictions. This is due to the fact that the statistical models of damage propagation require some damage to be propagated before the statistics, upon which the life model is built, can be developed. This is consistent with a variety of approaches that are employed in bearing life testing, and makes good physical sense.

RESEARCH PLANS

Future work in this area will further explore the non-linear response of signals to operating conditions, as well as their interaction with bearing damage level and type. Additionally, non-linear approximations and heuristic modeling approaches to address operating condition effects will be investigated as a practical addition to current diagnostic and prognostic methods. A new probe, the contact potential difference (CPD) probe, will be integrated into the system. Recent experiments with a CPD probe mounted in the outside race of a roller bearing have demonstrated its utility in identifying roller damage in real-time.

Furthermore, we are currently updating the data monitoring system to run via the world-wide-web. This will permit easy monitoring of the system from any select locations in the world as well as efficient and fast data transfer from a test site to an analysis site. The exciting application of the network capability is that it provides a quick, simple and inexpensive means by which data can be transferred throughout a larger system such as a helicopter, a ship or a plant.

M-URI PUBLICATIONS

Shiroishi, J., Li, Y., Liang, S., Kurfess, T., Danyluk, S., "Bearing Condition Diagnostics Via Multiple Sensors," *Mechanical Systems and Signal Processing*, Vol. 11, No. 5, pp. 693-705, September, 1997.

Shiroishi, J.W. , Li, Y., Liang, S., Danyluk, S., and Kurfess, T.R., "Vibration Signal Analysis for Bearing Race Damage Diagnostics," Keynote paper for the 7th *International Conference on Dynamic Problems in Mechanics*, Brazil, pp. 187-190, March 1997.

Billington, S.A., Li, Y., Kurfess, T.R., Liang, S.Y., Danyluk, S., "Roller Bearing Defect Detection with Multiple Sensors," *Emerging Technologies for Machinery Health Monitoring and Prognosis*, ASME TRIB-Vol. 7, R. Cowan, ed., pp. 31-36, Dallas, TX, November 1997.

Shiroishi, J., Li, Y., Liang, S., Kurfess, T., Danyluk, S., "Vibration Analysis for Bearing Outer Race Condition Diagnostics," *Journal of the Brazilian Society of Mechanical Sciences* (in press).

Li, Y., Billington, C., Zhang, C., Kurfess, T., Danyluk S., and Liang, S. Y., "Adaptive Prognostics for Rolling Element Bearing Condition," accepted by *Mechanical Systems and Signal Processing*, 1998.

Li, Y., Billington, C., Zhang, C., Kurfess, T., Danyluk S., and Liang, S. Y., "Dynamic Prediction of Defect Propagation on Rolling Element Bearing," accepted by *Tribology Transactions of Society of Tribologists & Lubrication Engineers (STLE)*, 1998, (in press).

Yang, Y., Kurfess, T. R., Liang, S. Y., and Danyluk, S., "Application of A Specialized Capacitance Probe in Bearing Diagnosis," accepted by *Wear*, 1998, (in press).

Li, Y., Billington, S. A. , Kurfess, T. R., Danyluk, S., Liang, S. Y. "Dynamic Prognostics of Rolling Element Bearing Condition," *Proceedings of 52nd Meeting of the Society for Machinery Failure Prevention Technology*, pp. 429-430, Virginia Beach, March 30-April 3, 1998.

Billington, S. A., Li, Y., Kurfess, T. R., Danyluk, S., "Operating Condition Effects on Rolling Element Bearing," *Proceedings of 52nd Meeting of the Society for Machinery Failure Prevention Technology*, pp. 313-322, Virginia Beach, March 30-April 3, 1998.

Li, Y., Kurfess, T. R., Danyluk, S., and Liang, S. Y., "Bearing Prognostics Based on Adaptation of Stochastic Defect Growth Model, accepted by *Proceedings of 53rd Meeting of the Society for Machinery Failure Prevention Technology*, April 19-22, 1999, (in press).

Yang, Y., Kurfess, T. R., Liang, S. Y., and Danyluk, S., "Application of A Specialized Capacitance Probe in Bearing Diagnosis," accepted by *Proceedings of the 12th International Conference on Wear of Materials*, Atlanta, April 25-29, 1999, (in press).

1.3 DETECTION OF THE PRECURSOR TO MECHANICAL SEAL FAILURE IN TURBOMACHINERY

Co-investigators: Richard F. Salant and Jacek Jarzynski (Georgia Tech)
Graduate Research Assistant: William Anderson
M-URI Year 4 Funding Allocation: 7.2%

DoD NEED

The U.S. Navy uses a large number of mechanical seals in such turbomachines as centrifugal pumps, compressors, turbines, turbopumps, propeller shaft assemblies, and gas turbine engines. Mechanical seal failure is one of the principal causes of breakdown of these machines. The use of a monitor to detect a precursor to seal failure will allow preventive action to be taken to avoid failure. Such a monitor will eliminate the need for scheduled preventive maintenance, thereby reducing costs, and will minimize the possibilities of catastrophic failure and the disruption of naval operations due to seal failure.

PROJECT MISSION

Mechanical seals generally fail as the result of the collapse of the lubricating film between the two seal faces. The goal of the present project is to develop a real-time monitoring system that will detect the collapse of the lubricating film before mechanical and thermal damage to the seal is sustained.

TECHNICAL PERSPECTIVE

Prior to this project, the only sensor for monitoring mechanical seals that had been investigated is the acoustic emission (AE) sensor. Several efforts to use this sensor had yielded mixed results [1-6]. While significant results could be obtained under controlled laboratory conditions, the method was not successfully implemented in the field. The major problem is the difficulty in distinguishing mechanical seal AE emissions from those produced by other sources. This is compounded by changes in AE characteristics from seal to seal, and with changing operating conditions, making it extremely difficult to develop a universal AE system for seal monitoring.

RESEARCH ACCOMPLISHMENTS

In the first three years of this project, a monitoring system has been built, analyzed, and successfully tested on a seal in a laboratory environment, under steady-state and transient conditions. The monitoring system utilizes actively generated ultrasonic waves to determine if the two seal faces make contact and, if so, the degree of contact. A piezoelectric transducer is placed behind one of the seal faces and is used as a source, generating a train of ultrasonic wave packets that propagate toward the interface between the seal faces. A second piezoelectric transducer is placed behind the other seal face, and is used to detect the waves that are transmitted across the interface. On the basis of theoretical work and work by other investigators [7-9], it had been expected that the transmitted signal would be virtually zero when the film is intact and nonzero when the film has collapsed, with an amplitude indicative of the degree of contact between the seal faces.

The monitoring system has been installed on the double mechanical seal shown in Figure 1. This seal, originally designed for a turbopump, seals air and is electronically controlled so that the separation between the seal faces can be varied at will. In the first stage of testing, a large number of steady-state tests have been run, in which the spacing between the seal faces was varied. Typical results are shown in figure 2. The transmitted signal strength, at the driving frequency, is plotted against the leakage rate. The latter is a measure of the spacing between the seal faces. As the leakage rate is reduced from approximately 12.4 l/min to approximately 1.7 l/min (by reducing the spacing), the signal strength remains substantially constant at the noise level (0.25 V). The leakage rate of 1.7 l/min corresponds to

the seal faces making contact (there is leakage bypassing the seal). At this contacting condition, the signal strength takes on values ranging from the noise level to approximately nine times the noise level.

To interpret these results, two series of bench tests were performed. In the first series, the shaft with the rotating tungsten carbide face and the two floating carbon face assemblies were placed in a jig, with the same relative positions as in the seal tester. The film thicknesses between the tungsten carbide and carbon faces were set using Mylar spacers of known thickness. Ultrasonic waves were generated and detected as in the seal tester. These tests showed that for all non-zero film thicknesses, the transmitted signal is essentially zero; it is non-zero only when there is mechanical contact between the faces, in agreement with the results of our analytic model. In the second series of bench tests, the seal components were stacked vertically, and ultrasonic measurements were made with various weights placed on the assembly to vary the contact pressure between the faces. These tests showed that as the contact pressure is increased, the transmitted signal strength increases. This is due to an increase in the real area of contact, and is in agreement with the work of other investigators [1-3].

It is therefore clear, from Figure 2, that the strength of the transmitted signal indicates whether or not face contact occurs. If the signal strength is equal to the noise level, there is no contact. If the signal strength is greater than the noise level, there is contact, and the magnitude of the signal strength is a measure of the contact pressure between the faces. This is a very favorable characteristic for a seal monitor, because it allows assessment of the severity of the contact.

In the second stage of testing, ultrasonic measurements were made on the seal under transient conditions in real time. Two types of transients were investigated. In the first, the coning was decreased rapidly to induce face contact, and then increased to resume normal operation. Typical results are shown in Figure 3. It is seen that each instance of face contact results in a sudden increase in the detected signal strength. In the second type of transient, face contact was induced by suddenly reducing the sealed pressure. Typical results, contained in Figure 4, show that each time the faces make contact, there is again a sudden increase in detected signal strength. These results, together with those of the steady state tests, confirm the effectiveness of this monitoring system.

During year 4 of this M-URI project, initial work was done on developing a similar monitoring system for a seal used in an actual Navy application. Since most Navy applications require single seals, rather than the double seal arrangement of Figure 1, it was necessary to modify the general scheme described above. That scheme, in which ultrasonic waves transmitted across the sealing interface are detected, requires two transducers, one behind each of the seal faces. Therefore, with a single seal, a transducer must be placed behind both the non-rotating and rotating face. It would then be necessary to use either slip rings or telemetry to transfer signals between the rotating transducer and ground. To eliminate such a complication, a method using only a single transducer, placed behind the non-rotating seal face, has been developed. In this method, the waves reflected from the sealing interface (rather than the transmitted waves) are monitored. When the lubricating film is intact, the reflected wave amplitude will be a maximum. When there is contact between the seal faces, the amplitude will be reduced; the greater the degree of contact, the lower the amplitude. The apparatus of Figure 1 has been used for this work, but with only one of the transducers activated. That transducer is used as both a source and a
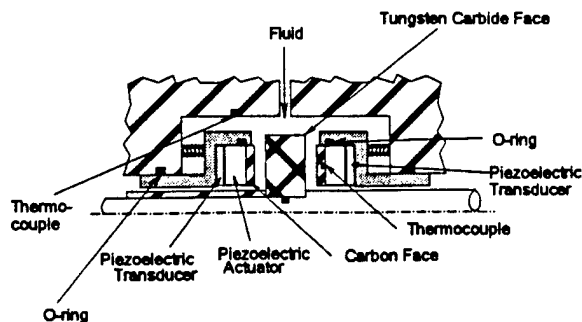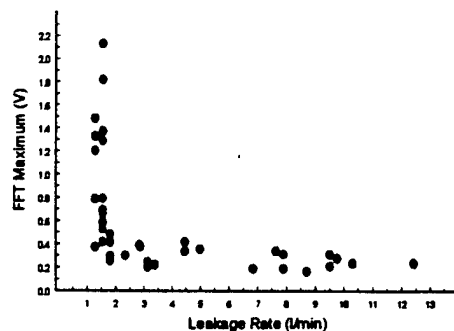

Figure 1   Apparatus

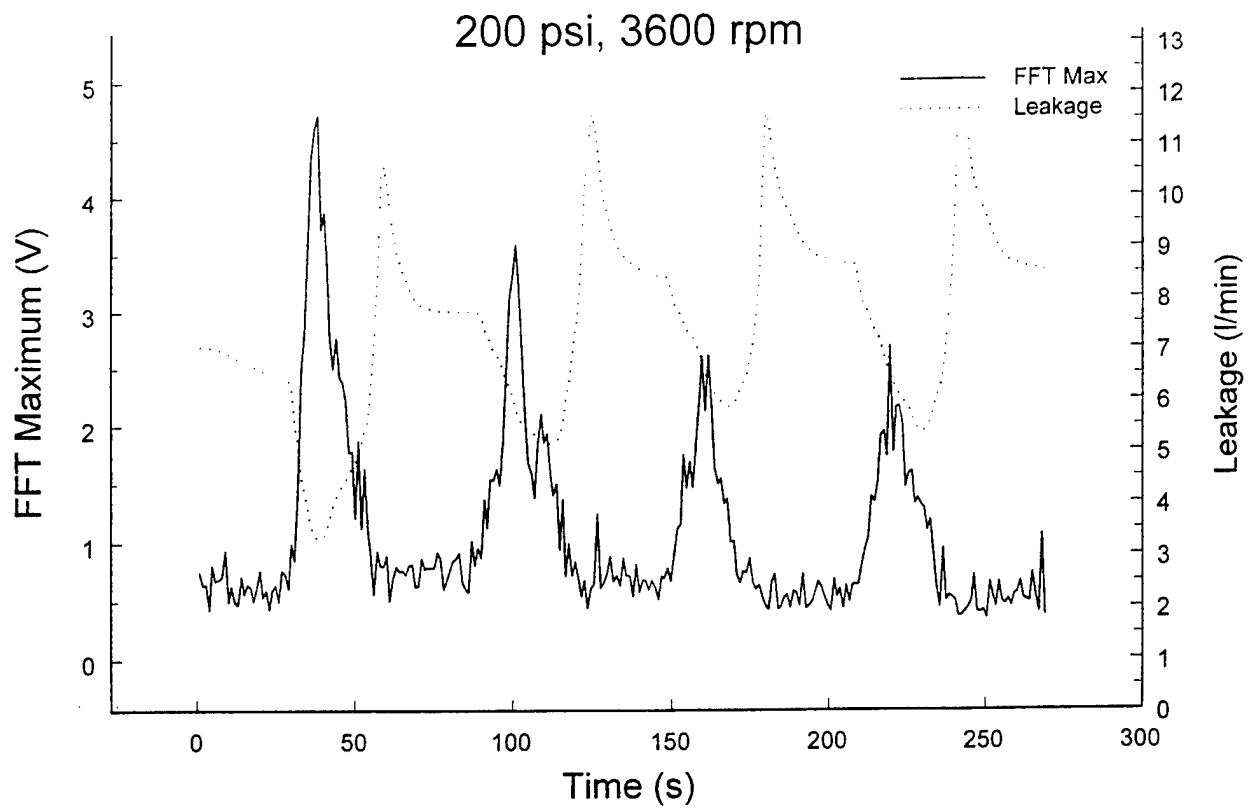Figure 2   Transmitted Signal Strength

MECHANICAL SYSTEM HEALTH MONITORING

200 psi, 3600 rpm

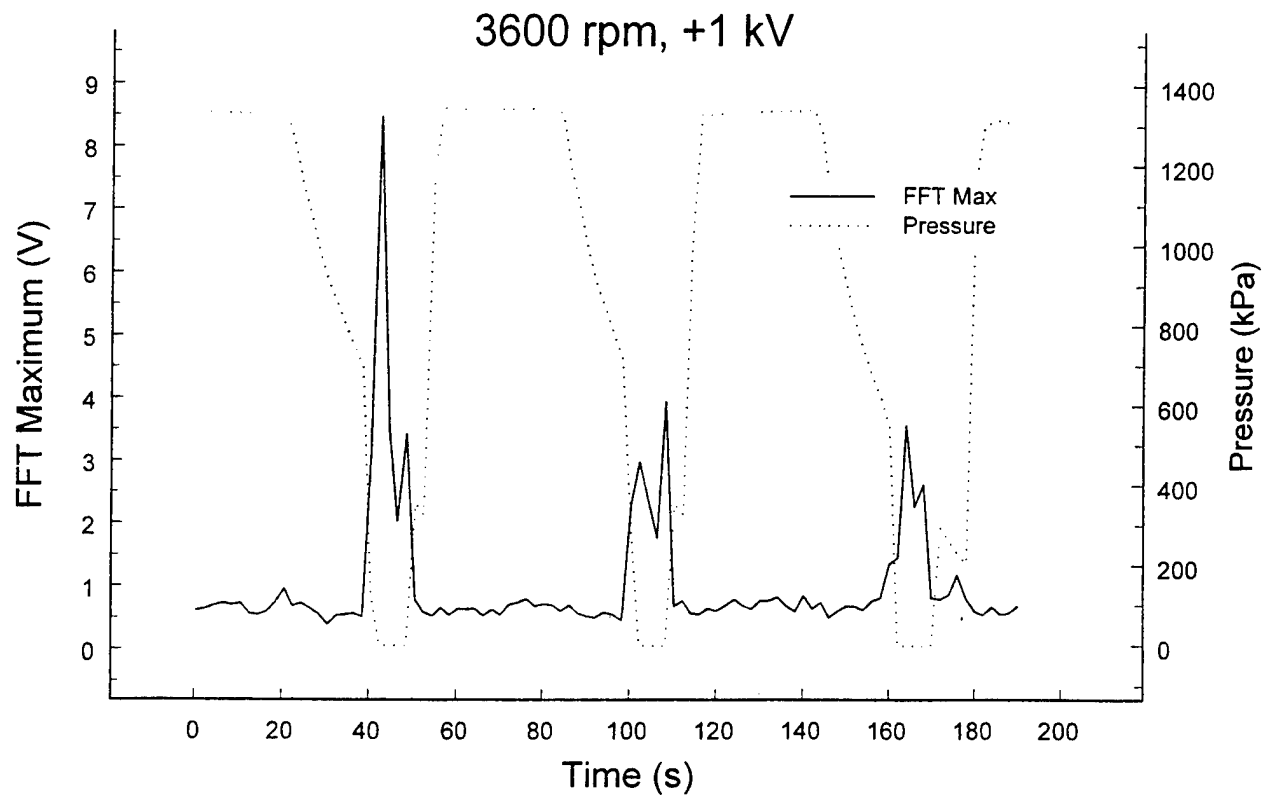**Figure 3.** Transient Coning (Transmission)

3600 rpm, +1 kV

Figure 4. Transient Pressure (Transmission)

receiver. It is driven to produce a continuous train of ultrasonic wave packets, each packet containing three or four waves (at 2 MHz) with 1 ms between consecutive packets. The transducer is gated, so that during times when the reflected wave packets are received, the received signal is transmitted to a processing system.

As in the case of the transmitted wave system, two series of bench tests were performed: one with calibrated film thicknesses using Mylar spacers, and one with face contact and calibrated contact pressures using weights. These tests showed that for finite film thicknesses, the reflected wave amplitude is substantially independent of film thickness, but when the film thickness is zero there is a substantial drop in amplitude. Furthermore, the higher the contact pressure (the greater the degree of contact), the lower the reflected wave amplitude.

Figure 5 shows some typical steady state tests, in which the film thickness (and leakage rate) was varied through electronic control. This is the complement of Figure 2. It is seen that at large film thicknesses (and leakage rates), the reflected signal is relatively large and independent of film thickness. However, once the film thickness (and leakage rate) is reduced to the point where face contact occurs, the signal amplitude decreases substantially, with the amount of decrease depending on the degree of contact.

The results of transient tests are shown in Figures 6 and 7. Figure 6 (the complement of Figure 3) contains the results of a test in which the coning was decreased to induce face contact, and then increased to resume normal operation. It is seen that each instance of face contact results in a significant increase in the detected signal strength. Figure 7 (the complement of Figure 4), shows the results of a test in which face contact was induced by suddenly reducing the sealed pressure. Each time the faces make contact, there is again a significant decrease in detected signal strength. These results, together with those of the steady state tests, confirm the effectiveness of this single transducer monitoring system. In its present form, it could be used on virtually any single gas seal.
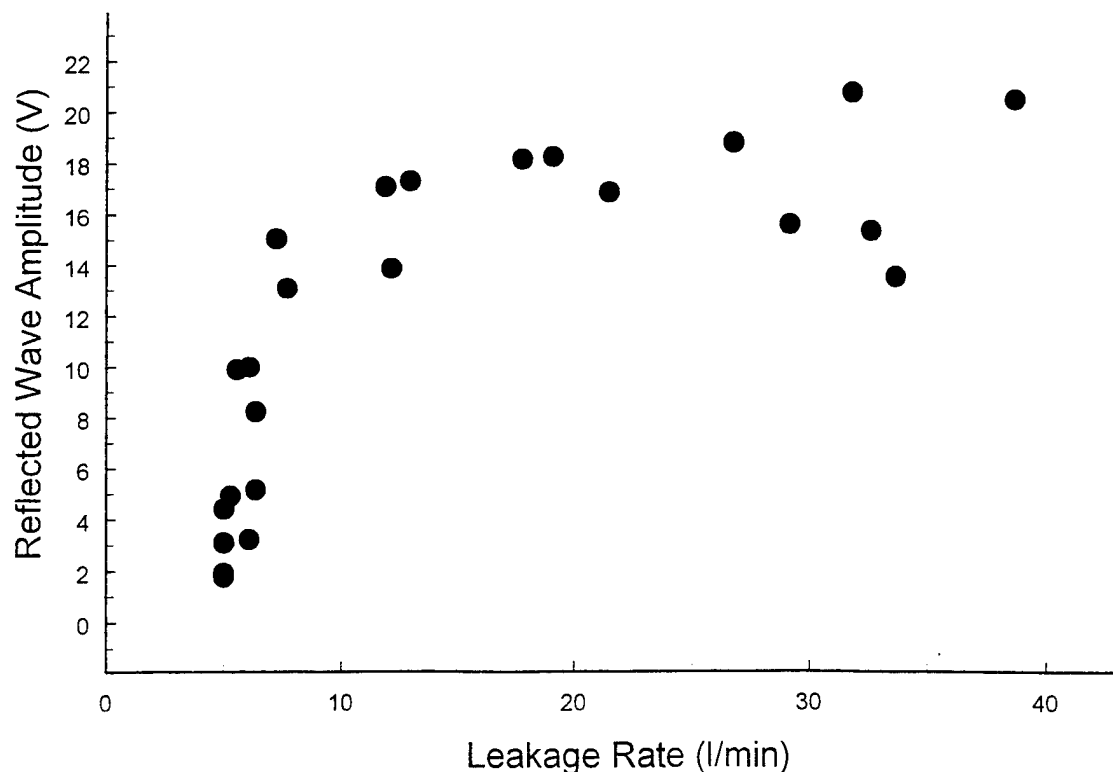
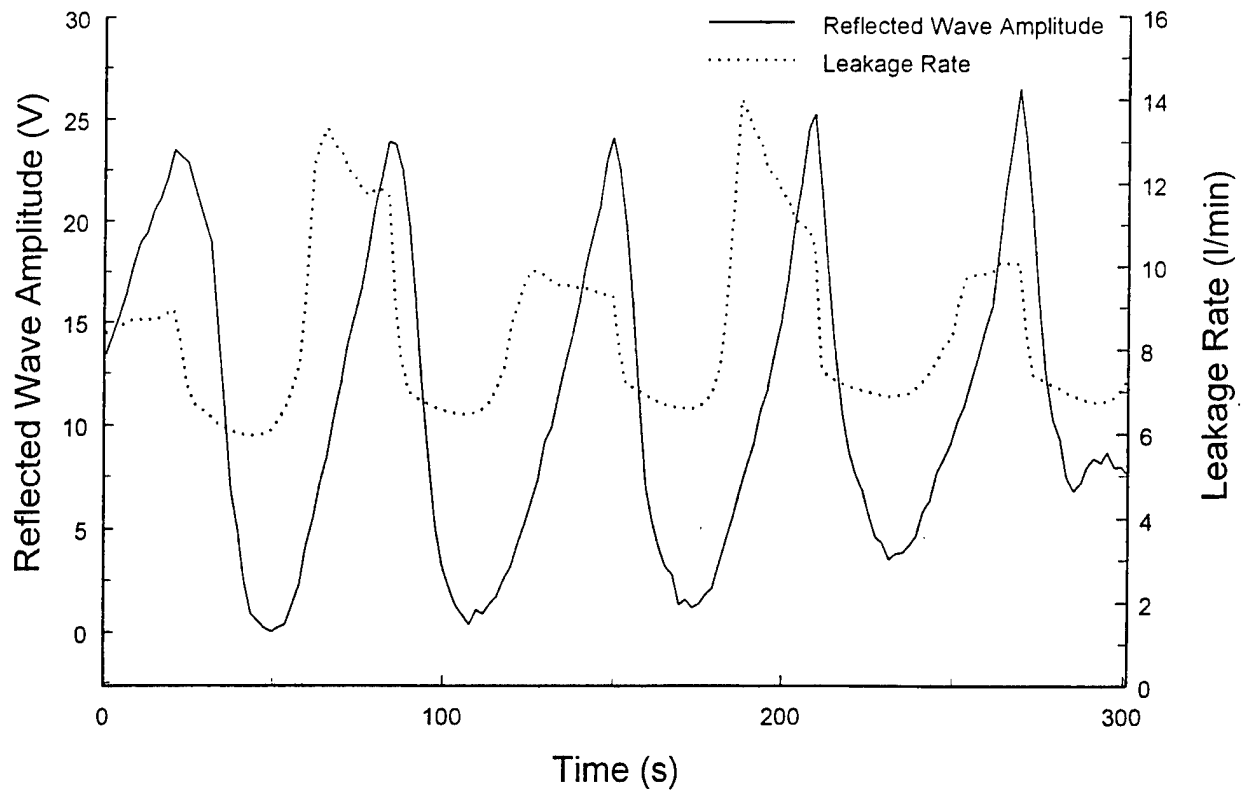**Figure 5** Reflected Signal Strength
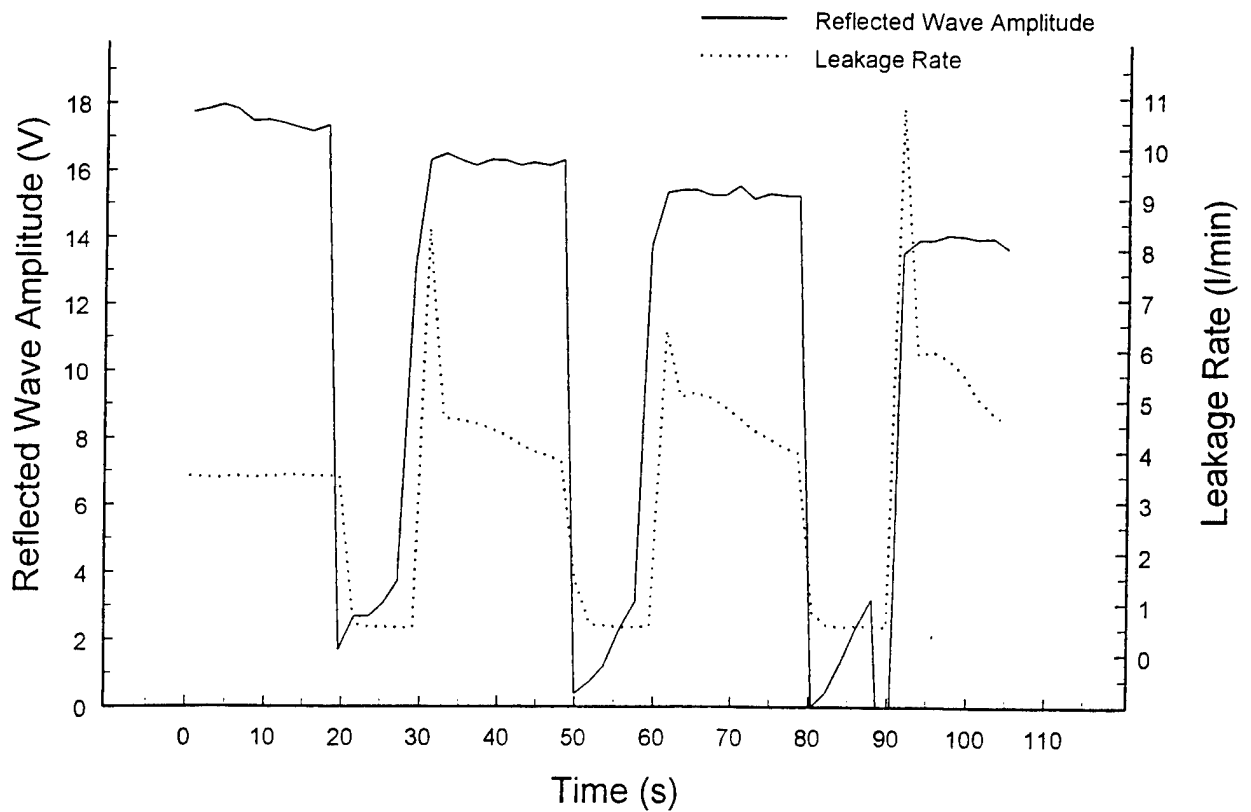
Figure 6. Transient Coning (Reflection)

Figure 7. Transient Pressure (Reflection)

While the above system is suitable for gas seals, it was decided to develop a similar monitoring system for a particular liquid seal used in naval applications: the John Crane type-1 seal, used for general shipboard service. A number of such seals have been acquired for testing. It should be noted that in the gas seal tests, described above, ultrasonic compressive waves were used. However, for the John Crane liquid seals, ultrasonic shear waves must be used instead, due to the higher acoustic impedance of liquid as compared to gas. Therefore, a number of bench tests on the John Crane seal (immersed in water) with shear wave transducers, instead of compressive wave transducers, have been performed. Figure 8 shows the results of a typical series of tests with calibrated film thicknesses using Mylar spacers. As in the analogous gas tests, for finite film thicknesses the reflected wave amplitude is substantially independent of film thickness, but when the film thickness is zero there is a substantial drop in amplitude. These bench tests are continuing in order to optimize the transducer geometry.

Following completion of the bench tests, steady state and transient tests will be performed to simulate the application. A seal tester, suitable for testing this seal, has been acquired from John Crane, Inc., and has been installed in the Integrated Diagnostics Laboratory at Georgia Tech. It is shown schematically in Figure 9. This is the same tester that was used for John Crane's NAVSEA qualification tests.

References

[1] Orcutt, F. K., 1969, "An Investigation of the Operation and Failure of Mechanical Face Seals," *BHRA 4th International Conference on Fluid Sealing*, p. 205-217.

[2] Kataoka, T., Yamashina, C. and Komatsu, M., 1987, "Development of an Incipient Failure Detection Technique for Mechanical Seals," Proceedings *of the Fourth International Pump Symposium*, Texas A & M University, pp. 121-129.

[3] Miettinen, J. and Siekkienen, V., 1995, "Acoustic Emission in Monitoring Sliding Contact Behavior," *Wear*, Vol. 181-183, pp. 897-900.

[4] Miettinen, J., Siekkienen, V. and Tornqvist, P-E, 1996, "A New Way to Use Mechanical Face Seal In Centrifugal Pump," *7th Nordic Symposium on Tribology*, Bergen, Norway.

[5] Williams, M. and Barnes, N. D., 1993, "The Use of Acoustic Emissions for Monitoring Mechanical Seals," 13th *BPMA Pump Technical Conference*.

[6] Holstein, A. P., 1996, "Diagnosis of Mechanical Seals in Large Pumps,"*Sealing Technology*, N. 33, pp. 9-12.

[7] Drinkwater, B. W., Dwyer-Joyce, R. S. and Cawley, P., 1995, "A Study of the Transmission of Ultrasound Across Real Rough Solid-Solid Interfaces," *Rev. Prog. Quantitative Non Destructive Evaluation*, Vol. 14, Plenum, New York.

[8] Drinkwater, B. W., Dwyer-Joyce, R. S. and Cawley, P., 1996a, "A Study of the Interaction Between Ultrasound and a Partially Contacting Solid-Solid Interface," *Proceedings, Royal Society of London A*, Vol. 452, pp. 2613-2628.

[9] Drinkwater, B. W., Dwyer-Joyce, R. S. and Cawley, P., 1996b, "The Interaction of Ultrasound with a Partially Contacting Solid-Solid Interface in the Low Frequency Regime," *Review of Progress in Quantitative Non Destructive Testing*, Vol. 15, Plenum, New York.
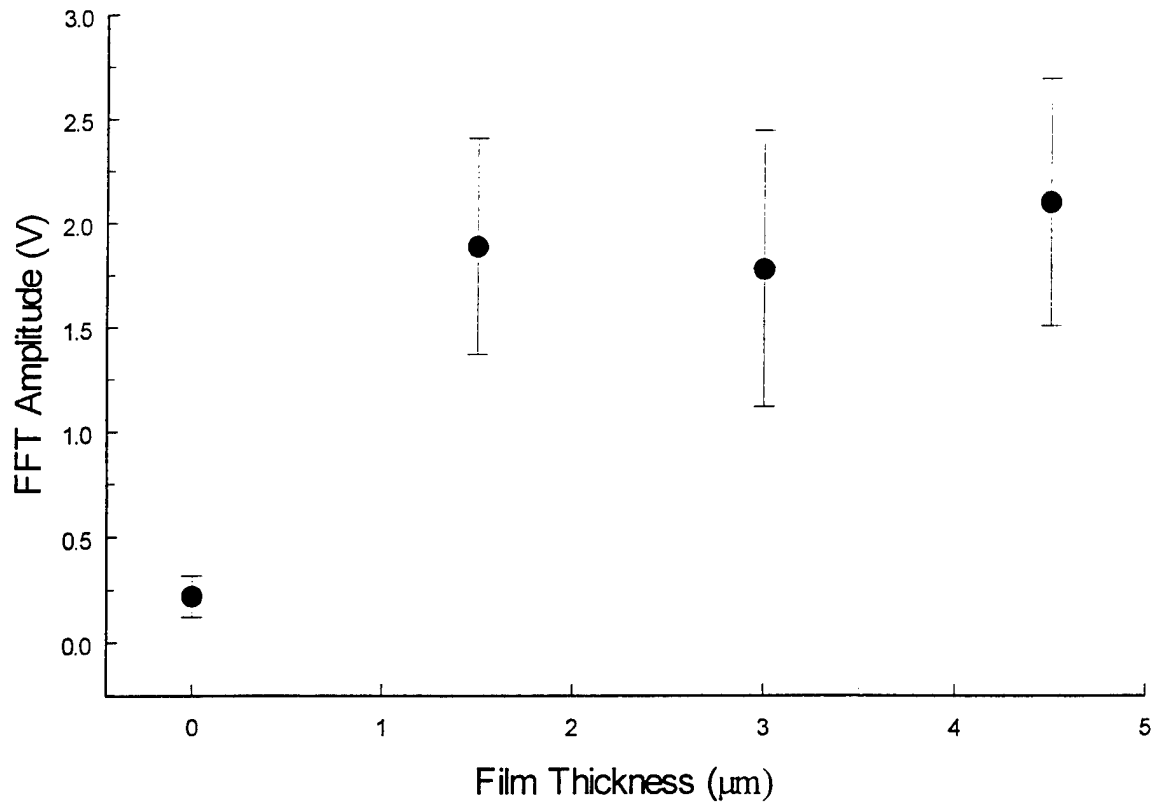
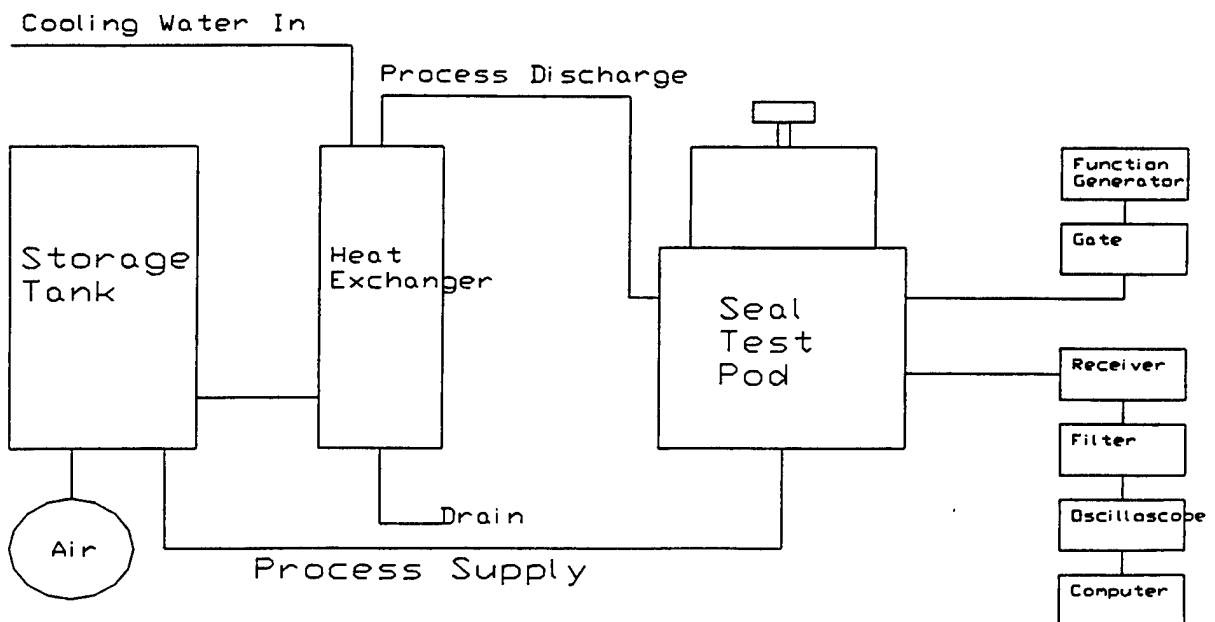**Figure 8.** Bench Test - Shear Waves

Figure 9. Seal Tester

RESEARCH PLANS

During M-URI year 5, the monitoring system will be tested on a John Crane type-1 seal in the seal tester described above. Both steady state and transient tests will be performed, to simulate Navy application conditions. Face contact will be induced by running at conditions outside the operating envelope, and by submitting the seal to extreme transients. Results will be compared with those obtained, on the same seal, by John Crane, Inc. in NAVSEA qualification tests.

M-URI PUBLICATIONS

Anderson, W. B., Salant, R. F. and Jarzynski, J., 1997, "Detection of Lubricating Film Breakdown in Mechanical Seals," ASME Public. TRIB-7, *Emerging Technologies for Machinery Health Monitoring and Prognosis*, R. Cowan, ed., ASME, 1997, pp. 25-29.

Anderson, W. B., 1997, "Detection of Lubricating Film Breakdown in Mechanical Seals," M. S. Thesis, Georgia Institute of Technology.

Anderson, W., Salant, R. F. and Jarzynski, J., 1999 "Ultrasonic Detection of Lubricating Film Collapse in Mechanical Seals," *Tribology Transactions*, accepted for publication and presentation at 1999 STLE Annual Meeting.

Anderson, W., Jarzynski, J, and Salant, R. F., 1999, "Condition Monitoring of Mechanical Seals: Detection of Film Collapse Using Reflected Ultrasonic Waves, *IMechE Journal of Mechanical Engineering Sciences*, submitted for publication.

Jarzynski, J., Salant, R. F., Anderson, W. B., "Condition Monitor for a Mechanical Seal," U.S. Provisional Patent Application, # 60/048,960, June 6, 1997.

Jarzynski, J., Salant, R. F., Anderson, W. B., "Improved Condition Monitor for a Mechanical Seal," U.S. Provisional Patent Application, serial no. to be issued, November 7, 1997.

1.4 REAL-TIME MONITORING AND CONTROLLING OF MECHANICAL FACE SEAL DYNAMIC BEHAVIOR

Co-investigator: Itzhak Green (Georgia Tech)
Graduate Research Assistants: Min Zou and Cody Casey
Visiting Professor: Joshua Dayan (Technion – Israel Institute of Technology)
M-URI Year 4 Funding Allocation: 6.7%

DoD NEED

Noncontacting mechanical face seals are extensively used in centrifugal pumps, compressors, powered vessels, and other high performance rotating machinery. Unpredictable mechanical face seal failure in critical applications may have severe implications. In addition maintenance cost attributed to mechanical seal failure is much higher than the cost of just the seal itself. The techniques of monitoring, detection, and control developed in this research can be applied to water seals in Naval chillers or other applications that critically need to be monitored to increase their reliability and reduce maintenance cost.

PROJECT MISSION

The objective of this research is to monitor and control the dynamic behavior of a noncontacting mechanical face seal having a flexibly mounted rotor in a seal test rig. In particular, the research focuses on detecting and controlling the contact between the rotor and stator that may cause severe face wear and imminent seal failure.

TECHNICAL PERSPECTIVE

At the start of this work, the exact cause of seal failure caused by higher harmonic oscillations has not been well understood. This research has revealed that the intermittent contact between the rotor and the stator caused by relative face misalignment is the cause of this harmful failure mode. Moreover, once such failure is detected corrective measure are implemented via active control to alter the system dynamics and eliminate the damaging behavior. It is emphasized that since contact is determined ad hoc (i.e., phenomenologically) the technology developed here can be applied equally to mechanical seals for compressible (gas/air) or incompressible (liquid) fluids.

RESEARCH ACCOMPLISHMENTS

Meaningful condition monitoring measures are taken by incorporating proximity probes and a universal controller board connected to a personal computer. The dynamic behavior of the noncontacting mechanical seal is monitored on-line. The monitoring system can display the orbit of the rotor angular misalignment in real-time where the shape of the orbit gives an indication of the seal dynamic behavior. Key dynamic parameters, such as seal clearance and relative angular misalignment between the rotor and the stator are chosen to be monitored. Contact between the rotor and stator is detected by a combination of relative angular misalignment and seal clearance. A dominant indication of contact is the presence of higher harmonics oscillations, which are multiples of the rotating shaft speed. The monitoring system can detect seal contact during operation using orbit plots and signal processing, and suppress it by incorporating an active control strategy. The control strategy is to eliminate contact between the rotor and the stator by adjusting the seal clearance. This is achieved by controlling a pneumatic air pressure in the rotor chamber, which governs the closing force. The fluid film stiffness and damping coefficients change with the clearance, which in turn causes changes in the rotordynamic response in both angular and axial modes.

The seal clearance and the instantaneous rotor response are determined from signals of three eddy-current proximity probes. Contact is determined phenomenologically from pattern recognition of probe signals and their power spectrum densities as well as angular misalignment orbit plots, all calculated and displayed in real-time. The contact elimination strategy is experimentally investigated for

various values of stator misalignment and initial rotor misalignment. Contrary to intuition, but compliant with a parametric study, the experimental results show that for the seal under consideration contact can be eliminated through clearance reduction.

Approach

An experimental test rig has been built to study the dynamic response of a flexibly mounted rotor (FMR) mechanical face seal. This rig is being used to study higher harmonic oscillations (HHO) because they have been detected under various operation conditions. The mechanical face seal was designed to operate in a noncontacting mode, but the detected HHO indicated the existence of contact between the rotor and stator. It is this contact that leads to face damage, which must be avoided. The seal system operates under the balance of the opening force and the closing force. The seal pressure drop provides the opening force across the sealing interface, while the sealed hydraulic pressure, the initial spring compression, and the air pressure in the rotor chamber provide the closing force. In previous experiments the air pressure was set manually by a pressure regulator and could not be automatically controlled. Currently an electro-pneumatic transducer automatically adjusts the pneumatic pressure in the rotor chamber, and thus the closing force. A monitoring system based on eddy-current proximity probes and a flow meter has been constructed to monitor the rotordynamic behavior and detect the existence of HHO. The flow meter can output a voltage that is proportional to the flow rate. A control algorithm on the closing force is incorporated such that once contact is detected it reduces relative misalignment between rotor and stator for maximum reduction of HHO.

Dynamic Simulation and Monitoring

The rotor dynamics has been investigated through both, simulation and real-time monitoring. Dynamic simulation has been performed to investigate the seal rotor angular response to the stator misalignment, the stator angle, the initial rotor misalignment, and clearance. Rotor angular response orbit has been introduced capable of characterizing the rotor dynamic response. A real-time monitoring system has been constructed in the test rig to monitor the instantaneous dynamic behavior of the seal rotor including its angular response, precession angle, and angular response orbit. Experimental results agree well with those of the dynamic simulation.

Clearance Control

Seal clearance control is an advancement in noncontacting mechanical face seal operation because seal clearance variation caused by process disturbances may cause either severe face contact or excessive leakage, each of which is regarded as seal failure. The objective of controlling the seal clearance at a desired value overcoming operation disturbances, including variations in shaft speed and sealed fluid pressure, has been accomplished. The clearance control concept is to adjust the closing force that acts upon the flexibly mounted rotor. The seal axial dynamic model has experimentally been determined for the design of a proportional-integral (PI) controller with anti-windup. The controller has been then applied to the test seal. Results have shown that the controlled seal maintains or follows set-point clearance changes with and without disturbances in sealed water pressure and shaft speed. The controlled seal has been shown to respond quickly (having a small time constant) with a small control effort.

Feasibility of Contact Elimination through Clearance Adjustment

The feasibility of eliminating contact in a noncontacting flexibly mounted rotor (FMR) mechanical face seal has been studied. The approach for contact elimination is based on a parametric study using FMR seal dynamics. Through clearance adjustment it is possible to reduce the maximum normalized relative misalignment between seal faces and, therefore, eliminate seal face contact. Contact has been determined phenomenologically from pattern recognition of probe signals and their power spectrum densities as well as angular misalignment orbit plots, all calculated and displayed in real-time. The contact elimination strategy

has experimentally been investigated for various values of stator misalignment and initial rotor misalignment. Contrary to intuition but compliant with the parametric study, the experimental results have shown that for the seal under consideration contact can be eliminated through clearance reduction.

Contact Elimination

The large relative misalignment between seal faces causes the intermittent seal face contact. Controlling seal clearance is the most versatile way of eliminating damaging face contact. A cascade controller that includes two PI feedback control loops has been used. The inner loop is a clearance control loop that maintains a desired clearance set-point. Eddy current proximity probes are used to directly measure the seal clearance. Clearance control is accomplished through adjusting the air pressure in the rotor chamber of the seal. The outer loop adjusts desired clearance when contact is detected, i.e., when the variances of the probe signals are different. Experiments have been conducted to test the cascade controller. Results have shown that, when coning angle is small (and contrary to intuition) reducing seal clearance can eliminate contact.

RESEARCH PLANS

The common concern in system diagnostics is whether the signals obtained originate at the monitored machine element (in this case the mechanical face seal) or some other machine component that has failed which yields signals that are contaminated with that mode of failure. We are in the process of manufacturing shafts with cracks across their section. The dynamics of the seal will be investigated both analytically and experimentally with the seal riding on these cracked shafts. The shafts will be manufactured with various crack lengths and the dynamic signals will be analyzed to provide insight on how the signals change with a simulated crack propagation.

M-URI PUBLICATIONS

Zou, M., and Green., I., "Real-time Condition Monitoring of Mechanical Face Seal" *Proceedings of the 24th Leeds-Lyon Symposium on Tribology*, London, Imperial College, (Sept. 4-6, 1997) 423-430.

Zou, M., and Green., I., "Clearance Control of a Mechanical Face Seal," *STLE Tribology Transactions*, Preprint No. 98-TC-2-B-1, (presented at the ASME-STLE Tribology Conference, Toronto, 1998)

Zou, M., Dayan, J., and Green., I., "Parametric Analysis for Contact Control of a Noncontacting Mechanical Face Seal," Accepted for presentation and publication at Vibration, Noise & Structural Dynamics, 1999.

Zou, M., Dayan, J., and Green., I., "Dynamic Simulation and Monitoring of a Noncontacting Flexibly Mounted Rotor Mechanical Face Seal," submitted October 1998 *to Journal of Mechanical Engineering Science* (IMechE).

Dayan, J., Zou, M., and Green., I., "Sensitivity Analysis for the Design and Operation of a Noncontacting Mechanical Face Seal," submitted October 1998 to *Journal of Mechanical Engineering Science* (IMechE).

Zou, M., Dayan, J., and Green., I., "Parametric Investigation for Passive and Active Control of a Noncontacting Mechanical Face Seal," submitted October 1998 to *STLE Transactions*, and for presentation at the STLE Annual Meeting in Las Vegas, May 1999.

Zou, M., Dayan, J., and Green., I., "Feasibility of Contact Elimination of a Mechanical Face Seal through Clearance Adjustment," accepted for publication is *ASME Transactions* and for presentation at the ASME TurboExpo 98' (ASME INTERNATIONAL GAS TURBINE INSTITUTE).

2.1 *LASER-BASED ULTRASONICS FOR INTEGRATED DIAGNOSTICS*
Co-investigators: Jan D. Achenbach and Alexei Kromine (Northwestern University)
M-URI Year 4 Funding Allocation: 3.6%

DoD NEED

Naval helicopter structures may suffer cracks or other defects at locations that are not accessible for in-service visual inspections. In this work, ultrasonic waves are used to detect such flaws without disassembly. One particularly attractive method of generating and detecting ultrasonic signals is by the use of laser-based techniques. Laser-based ultrasonic (LBU) methods provide a number of advantages over conventional ultrasonic techniques (non-contact, higher spatial resolution, curved surface applications, hard-to-access areas, ability to generate both narrowband and broadband ultrasound, scanning ease, ability to operate at high temperature and in a hostile environment). Fiber delivery is the most attractive feature of LBU for practical use. Fiber delivery allows access even to internal components, requiring only enough space for the passage of optical cables (i.e. a few millimeters in diameter).

PROJECT MISSION

The objectives of this study are:
- to design portable, reliable and completely fiberized non-contact ultrasonic devices for field applications.
- to develop an ultrasonic technique for the in-situ detection and characterization of flaws in components of complicated structures without disassembling or physically touching the component.

TECHNICAL PERSPECTIVE

When this project was initiated, there was no equipment available to generate and detect ultrasound in locations of limited access such as small diameter holes in components or notches with high curvatures. The laser-based ultrasonic system developed in this project, and the related techniques of signal generation and detection are providing suitable methods for crack detection in small holes and notches.

The experiments carried out during the first years of this project have demonstrated the advantages of laser generation of ultrasonic waves. Both narrowband and broadband generation were performed in laboratory conditions using a Q-switched Nd:YAG laser with both conventional optical elements (free-space generation) and a fiber delivery system. Non-contact detection of ultrasound using various types of interferometers was investigated. A fiberized Sagnac interferometer, which has significant advantages in terms of flexibility, small size, relative simplicity and low cost, was chosen as the prototype for the detection part. A piezoelectric transducer (PZT) was also employed in some experiments as the ultrasonic detector.

During M-URI year 3, a compact laser system for ultrasound generation and detection with a flexible fiber delivery using a Big Sky Laser and employing a Sagnac interferometer for detection was designed, manufactured and tested. The main efforts during M-URI year 4 were devoted to application of the new equipment and techniques for detection of small defects on curved surfaces.

RESEARCH ACCOMPLISHMENTS

A new approach for detecting surface-breaking and internal defects has been invented and applied. This approach is called the scanning laser source (SLS) technique. It does not monitor the interaction of a well-established ultrasonic wave with a defect, as in the case of traditional pitch-catch or pulse-echo methods, but rather monitors the changes in the generated ultrasonic signal as the laser source passes over the area of inspection. Changes in amplitude and frequency of the generated ultrasound are

NONDESTRUCTIVE EVALUATION

observed, which result from the changed conditions under which the ultrasound is generated when the source passes over a small crack. These changes are quite readily detectable using existing ultrasonic detectors. This proposed technique when compared to the conventional pitch-catch mode of operation is recognized for its ability to (i) enhance signal-to-noise performance, (ii) detect smaller defects, (iii) detect defects of various orientations with respect to the scanning direction, (iv) be used with either a laser interferometer or a conventional PZT, and (v) inspect surfaces of complex geometry.

The SLS approach has been experimentally verified by the testing of a flat aluminum specimen with a surface-breaking fatigue crack of 4 mm length and 50 μm width. When the source is far ahead of the crack, the amplitude of the generated ultrasonic direct signal is stable, and the signal is of sufficient amplitude above the noise floor to be unambiguously picked up by the laser detector. As the source approaches the crack, the amplitude of the detected signal significantly increases. This increase is more readily detectable with a laser interferometer than any weak echoes from the crack. We attribute this increase in signal amplitude to possible interference of the incident wave with the wave reflected by the crack, and possibly more importantly to the changes in the conditions of generation when the laser source is in the vicinity of the crack. As the source passes over the crack, the ultrasonic signal amplitude drops noticeably, again presumably due to changes in the conditions of generation. When the source is behind the defect, the amplitude remains low due to attenuation of the generated signal by the crack.

The spectral content of the generated ultrasonic signal has also been monitored as the SLS was scanned over a crack. It was found that the presence of the crack introduces a detectable frequency shift in SLS generated ultrasonic signals. In the absence of a crack or when the source is far ahead of the crack, the SLS signal consists of relatively low frequency components with center frequency about 3 MHz. As the SLS approaches the crack, the spectral components of the detected signal in a 4-6 MHz frequency range become significantly stronger. The high-frequency components disappear from the spectrum of the detected signal when the SLS is behind the crack, due to the fact that high frequency waves are mostly reflected away by the crack.

A 50 μm diameter fiber was used in order to detect extremely small flaws. Small EDM notches of 125 μm length and depth, and 50 μm width (non-detectable by conventional ultrasonic techniques) were detected using the SLS approach.

The SLS technique has been successfully applied to a turbine disk specimen (provided by ALLIED SIGNAL, INC.) containing small notches (0.75 mm length, 0.38 mm depth and only 0.05 mm in width). The turbine disk, made from titanium alloy Ti6Al4V, has a complicated surface geometry and allows only limited access to the inspection surface (see Figure 1a). Ultrasound generation was provided by a 200 μm fiber mounted in a cylindrical holder, which was rotated with an angular step of 1-degree to
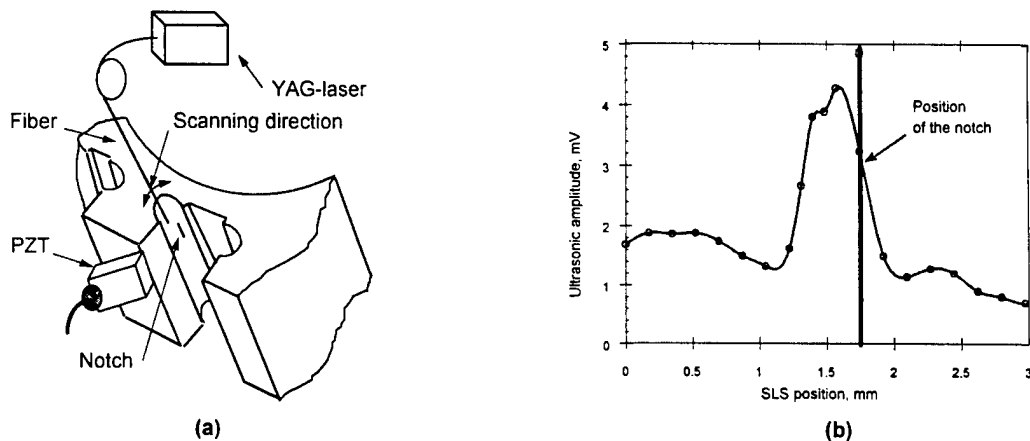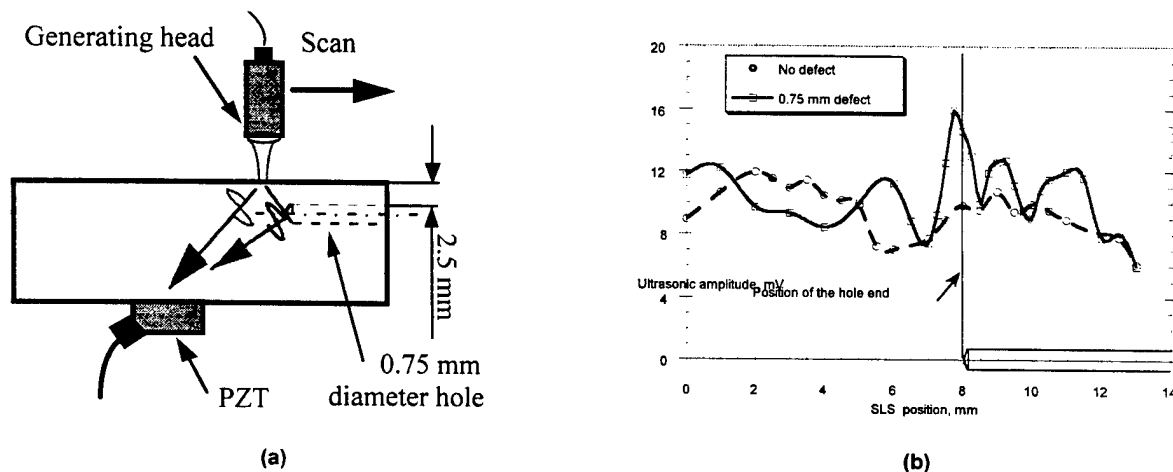

Figure 1. (a) Schematic illustration of the SLS approach applied to the detection of a flaw on the curved surface of a slot, and (b) a typical scan curve for the amplitude of the ultrasonic signal.

scan the laser point source over the investigated area. In a separate experiment, a fiber with a 45-degree angled tip was used to deliver a laser beam to the area of inspection inside the slot. The advantage of the latter is an ability to reach places through extremely small (less than 0.3 mm) holes or other spaces. The detection of ultrasound was carried out by a PZT attached to the easy-to-access surface of the specimen. It was found that cracks can be detected by monitoring the amplitude of the ultrasonic signal. The amplitude shows a typical variation when the SLS approaches the crack due to: (i) the interference of the incident ultrasonic wave with an ultrasonic wave reflected from the crack when the laser source is close to the crack and (ii) the change of conditions of generation when the laser source is moving over the crack. A typical view of the scan curve is shown in Figure 1b.

The SLS approach has also been applied to subsurface defects. Holes of 2 mm and 0.75 mm diameter and 13 mm depth were drilled at distances 2 - 5 mm from the flat surface of an aluminum specimen (see Figure 2a). The SLS of 6 mJ energy and 0.7 mm diameter, operating in the ablative regime, was moved over the area above the defect to generate ultrasonic bulk waves. It was found that the presence of a 0.75 mm diameter defect at a maximum depth of 2.5 mm produces a detectable variation in amplitude of the ultrasonic shear wave generated by the laser source, as compared to the case of no defect (see Figure 2b). The large peak of the ultrasonic amplitude when the SLS is right above the tip of the defect may correspond to an interference of the directly transmitted ultrasound with the ultrasound reflected from the defect tip.

The amplitude change significantly decreases with an increase of the defect depth because of beam spreading. It was found that a 2 mm diameter defect can be detected at a depth of 5 mm using this approach, but the increase of the ultrasonic amplitude does not exceed 25% of its value for the case of no defect. Defects smaller than 2 mm in diameter were found undetectable at 5 mm depth.

Figure 2. (a) Schematic illustration of the bulk waves approach to the detection of a subsurface defect, and (b) the scan curve of the ultrasonic amplitude of scattered bulk waves measured by the PZT for a defect at 2.5 mm depth.

RESEARCH PLANS

It is expected that a portable system, which combines laser generation and laser detection, will be finalized for field tests during M-URI year 5. Signal analysis by use of measurement models will also be investigated. Applications of laser-based ultrasonics for the detection of flaws in limited-access locations will be further developed.

M-URI PUBLICATIONS

L. S. Wang, J. S. Steckenrider and J. D. Achenbach. "A Fiber-Based Laser Ultrasonic System for Remote Inspection of Limited Access Components," in *Review of Progress in Quantitative Nondestructive Evaluation*. (D. O. Thompson and D. E. Chimenti, editors), Vol. 16A, pp.507-514, 1996.

P. Fomitchov, S. Krishnaswamy and J. D. Achenbach. "Sagnac Interferometer for Ultrasound Detection on Rough Surfaces," in *Proceedings of 8th Int. Symposium on Nondestructive Characterization of Materials*, Boulder, CO, June 15-20, 1997.

L. S. Wang, P. Fomitchov, A. Kromine, S. Krishnaswamy and J. D. Achenbach. "A Portable Laser-Based Ultrasonic System for the Inspection of Aging Aircraft Structures," in *Proceedings of the 1st DOD/FAA/NASA Joint Conference on Aging Aircraft*, Ogden, UT, July 8-10, 1997.

P. Fomitchov, A. Kromine, S. Krishnaswamy and J. D. Achenbach. "Characterization of Laser Ultrasonic Source using a Sagnac Interferometer," in *Proceedings of QNDE'97 Conference*, San Diego, CA, July 28 - August 1, 1997.

J. D. Achenbach, B. Moran and A. Zulfiqar, "Techniques and Instrumentation In Structural Diagnostics," in *Structural Health Monitoring: Current Status and Perspectives*, edited by F.-K.Chang, Technomic Publishing Co., Inc., pp. 179-190, 1997.

A. K. Kromine, P. A. Fomitchov, S. Krishnaswamy and J. D. Achenbach "Scanning Laser Source Technique and Its Applications to Turbine Disk Inspection," in *Proceedings of the 25th Annual Review of Progress in Quantitative Nondestructive Evaluation*, Snowbird, UT, July 19-24, 1998.

A. K. Kromine, P. A. Fomitchov, S. Krishnaswamy and J. D. Achenbach, "Laser Ultrasonic Detection of Surface-Breaking Defects: Scanning Laser Source Technique," *Materials Evaluation* (under review).

2.2 CRACK DETECTION IN ANNULAR STRUCTURES BY ULTRASONIC GUIDED WAVES

Co-investigators: Yves Berthelot, Jianmin Qu and Laurence Jacobs (Georgia Tech)
Graduate Research Assistants: Zongbao Li, Dan Cook, Christine Valle, C. Eisenhardt, Markus Kley
Post-doc: Guoli Liu
M-URI Year 4 Funding Allocation: 7.2%

DoD NEED

A recurring problem in many mechanical systems is the failure of annular components because of the formation and growth of radial cracks on their inner cylindrical walls. For example, there is a number of such critical components in the pitch shaft and the rotor hub of the CH-46 helicopter used by the US Navy. Traditional ultrasonic techniques (such as pulse-echo) are ineffective for inspection of these parts mainly because of problems associated with the curvature of the part, the complicated nature of the waveforms, and the lack of direct access to the part. This shortcoming is a critical missing link in determining the remaining life and structural integrity of a component.

PROJECT MISSION

The objective of the project is to develop an accurate, reliable, and robust ultrasonic nondestructive method to detect cracks at early stages before catastrophic failure occurs.

TECHNICAL PERSPECTIVE

At the time of undertaking this project in 1995, there was no reliable method to detect in situ cracks in thick annular components. Ultrasonic guided waves had been successfully used for crack detection in plates, or in the axial direction of thin cylinders, but not in the circumferential direction of short, thick cylinders such as collars.

The approach taken in this investigation is to a.) develop a quantitative understanding of the underlying principles of the propagation of guided circumferential waves in cylinders; b.) optimize the generation and detection of ultrasonic guided waves to maximize information about the integrity of a structure; and c.) concentrate the guided wave energy on a component interface or "hot spot" to determine information about the wavefield scattered by, or transmitted through, radial fatigue cracks during early stages of growth. In order to provide useful diagnostic/prognostic information for remaining life prediction, fatigue crack initiation is being studied to establish the correlation between fatigue crack growth and guided wave propagation. Results are being obtained through a combination of analytical, numerical, and experimental studies.

RESEARCH ACCOMPLISHMENTS

In the first three years of this project, a solution has been formulated for the transient excitation and propagation of circumferential ultrasound in a thick annulus. This solution provides valuable information on the modal content of the detected signals and the radial dependence of the ultrasonic field within the waveguide. The model can be used to select the best possible parameters (transducer wedge angle, frequency, source-receiver positions) to detect cracks on the inner surface of the waveguide. Experimental results confirm the trends predicted by the model. In addition, mode identification and crack detection have been greatly facilitated by the use of the time-windowed, frequency band-limited, amplitude of the wavelet transform of the received signal. The technique has been used successfully to detect hidden cracks (3 mm machine made notches that would not be detectable by the conventional ultrasonic technique) on a partially annular component of the pitch shaft of a CH-46 helicopter. Figure 1 shows the signals received on such a part by a 2.25MHz transducer in the send-receive mode, when the transducer was placed on a 30-degree wedge, at a distance of about 15 cm from the hidden crack.
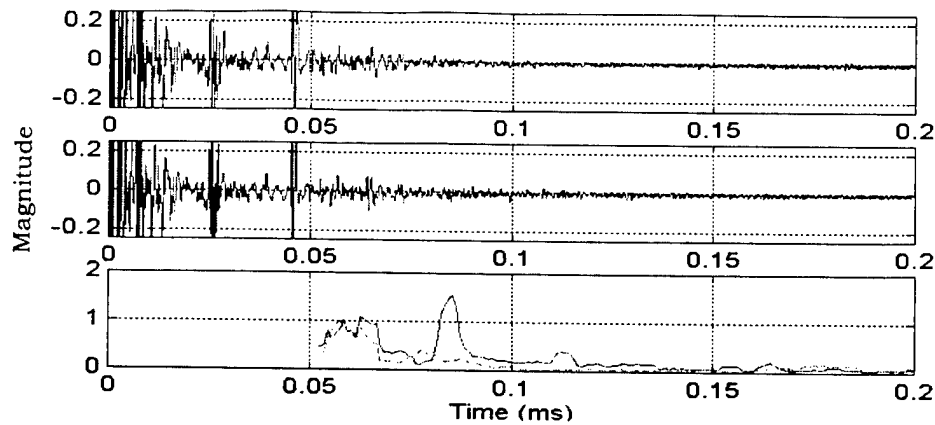
Figure 1 Detection of a hidden crack in the pitch shaft of the H-46 helicopter with 2.25 MHz transducer; (a) received time signal without crack; (b) received time signal with crack; (c) the time-windowed, band limited wavelet transform clearly locates the crack.
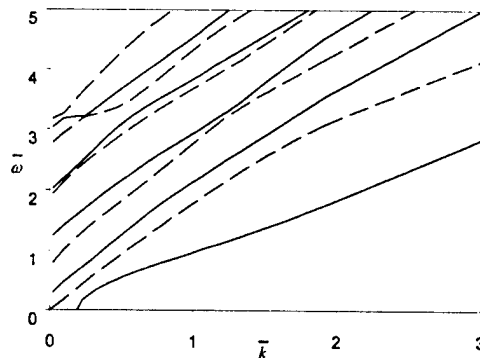
Wave propagation in a shaft/bearing assembly has also been investigated. The analytical/numerical model assumes that the interface is ideally lubricated. Under this assumption, it was found that waveforms are significantly affected by the presence of the shaft, a trend that was confirmed experimentally.

Experimental results have been compared with numerical predictions obtained with finite element modeling (FEM) using *Abaqus/Explicit* running on a desktop computer (PC). Calculations have been made for circumferential propagation of ultrasound in a thick cylinder with or without a crack on the inner surface. This work is at the forefront of the research on FEM modeling of ultrasound on simple computer platforms.

During year 4 of this project, the analytical problem of determining the propagation of ultrasound in a shaft/bearing assembly as shown in Fig. 2 was solved. Dispersion curves of the first 10 propagating modes are plotted in Fig. 3. To optimize the detection of radial cracks, it is desirable to generate wave modes that propagate along the shaft/bearing interface. It is shown in Fig. 4 that the second mode should provide the highest detection sensitivity.
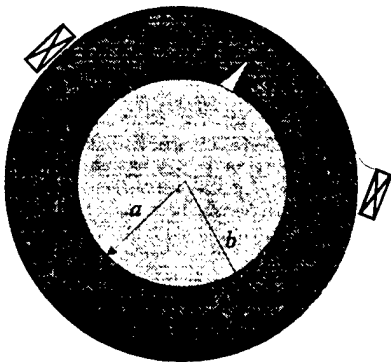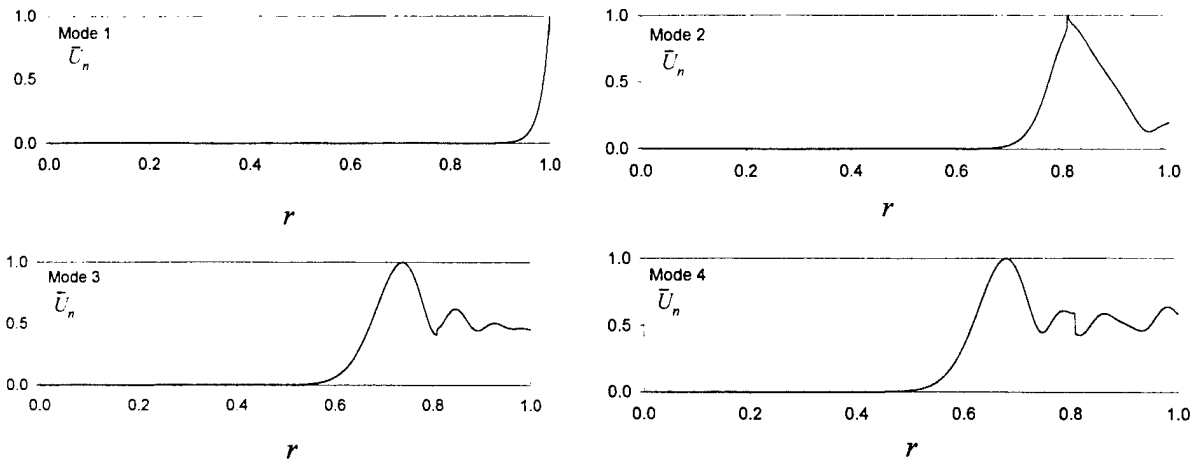

Figure 2 A shaft/bearing assembly with radial crack.

Figure 3 Dispersion curves of guided circumferential waves in a shaft/bearing assembly, where $\bar{\omega}$ and $\bar{k}$ are the non-dimensional frequency and wavenumber.

Figure 4. Displacement distribution in the radial direction. The horizontal axis is for the normalized (by the outer radius) distance, r, from the center, and the vertical axis is for the displacement amplitude, U_n, normalized by its maximum value. The shaft/bearing interface is at $r = 0.81$.

Numerically, the commercial finite-element code ABAQUS has been used to model transient wave propagation in cylindrical components, thus clearly demonstrating the effectiveness of using FEM methods to solve guided wave propagation problems where an analytical solution is not possible because of complicated component geometry. Visualization software has been used to demonstrate the robustness of the FEM models to understand guided wave propagation. The code has been used to study the influence of radial cracks on the scattered guided ultrasonic wavefield in cylindrical component. It has also been successfully used to determine the optimum inclination angle for transducer wedge assembly to generate guided waves along the inner surface of a cylindrical component where radial cracks tend to initiate.

Experimentally, two main experiments have been conducted. In the first one, laser ultrasonic techniques (i.e., laser generation and laser detection of ultrasound) were used to develop a quantitative understanding of the underlying principles of the propagation of guided circumferential waves in two-layered cylindrical components. The high fidelity, broad bandwidth, point source/receiver and non-contact nature of these optical techniques are critical elements to the success of this work. The experimental procedure consists of measuring a series of transient, circumferentially propagating waves in a cylindrical waveguide and then operating on these transient waveforms with signal processing techniques to develop the dispersion relationship for that waveguide. This procedure extracts the steady-state behavior from a series of transient measurements. As an example, the dispersion curve for the second mode is shown in Fig. 5 for the case of a single annulus. There is good agreement between the experimental and theoretical results, thus demonstrating the accuracy and effectiveness of using laser ultrasonic techniques to study the propagation of guided circumferential waves.
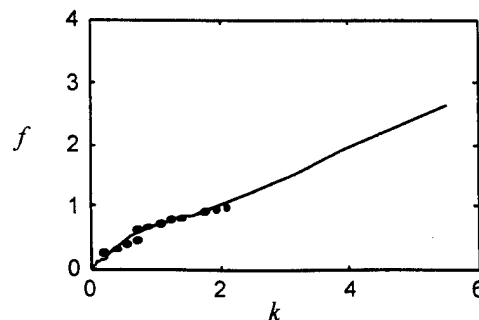

Figure 5 Comparison between experimental measurements and analytical predictions of the relationship between frequency (f) and wavenumber (k).

The second experiment was designed to detect crack initiation and growth during a fatigue test using ultrasonic guided waves (Rayleigh surface waves) with 5 MHz miniature transducers attached to a specimen with a "hot spot" as shown in Fig. 6. The transducers were placed in a send-receive mode and operated in the pulse mode with duration of the order of 1 microsecond. A portable data acquisition system was specifically instrumented for this application. The peak-to-peak amplitude of the received signal was monitored during the fatigue test, both at the minimum load of 4.45 kN (1,000 lbs), referred to as "closed crack", and 80% of full load or 35.6 kN (8,000 lbs) referred to as "open crack". Figure 7 shows the amplitude of the received signal as a function of the number of cycles. Clearly, crack growth can be detected at around N=100,000 cycles which, according to Table 1, is estimated to be when the crack size is of the order of 100 microns. This experiment shows that 5 MHz guided Rayleigh waves might be used to detect crack initiation near a hot spot, in the transmission mode, down to a crack size of about 100 microns without much signal processing.
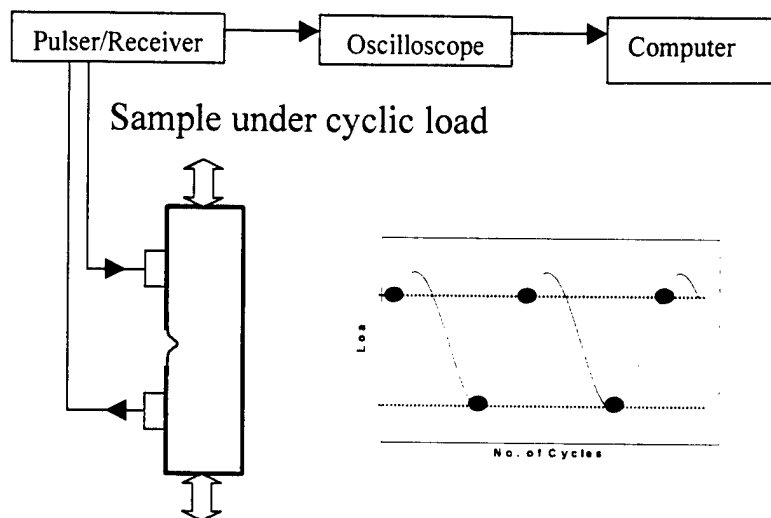
Figure 6 Schematic of the fatigue test experiment to detect crack initiation near a "hot spot" by using guided surface waves. Black circles indicate time of ultrasonic data acquisition.

Figure 7 Peak-to-peak received signal amplitude as a function of life cycle, N.
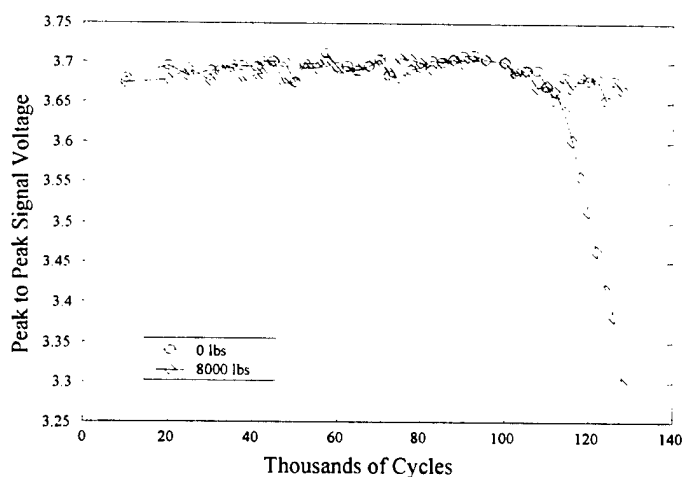
Table 1 Crack length vs. N

No. of Cycles	crack length a (mm)
109997	0.33
112001	0.38
114002	0.42
116004	0.45
118001	0.52
120003	0.57
122001	0.66
124003	0.75
126003	0.86
127999	0.95

RESEARCH PLANS

During M-URI year 5, two avenues of research will be pursued in parallel. First, the fundamental relationships between wave propagation and fatigue crack initiation and growth will be investigated. To this end, the experimental work will focus on the characterization of crack initiation and growth during fatigue tests using ultrasonic guided waves. Specifically, the experiments will be designed to relate ultrasonic signal amplitude to crack size and crack growth during the life cycle of the specimen. Experiments will be performed both in the transmission and the back scattering mode (low Rayleigh scattering). Signal processing techniques (e.g., coherence, or split spectrum) will be implemented to enhance the ability to detect small cracks. If the experiment is successful with surface waves and near surface defects, it could be extended to the case of Lamb waves and through thickness defects. Eventually, these results will be incorporated into the guided wave detection prototype to detect and monitor radial fatigue cracks in realistic components, such as a helicopter rotor hub. Furthermore, the investigators pursuing an understanding of structural fatigue (Section 3.1) can also use such measurement results in their algorithms for remaining life predictions.

Parallel to the experimental investigation of guided wave interaction with crack initiation and growth, numerical/experimental work will continue to be pursued, implementing the methodologies and techniques developed in previous years to design and optimize a prototype of the crack detection system using guided waves in annular components. Major tasks will include a.) identifying optimal transducer/receiver configurations (wedge shape, size, transducer direction, etc.), b.) determining minimum crack size detectability with a given system, c.) developing a systematic methodology for identifying crack size and location, d.) improving signal-to-noise ratio, and e.) studying the effects of crack face roughness and contact.

By combining a fundamental understanding of guided wave interaction with cracks and optimal detection configurations, this research results in a new, effective detection methodology for detecting fatigue cracks in realistic structure components.

M-URI PUBLICATIONS

Qu, J., Berthelot, Y., and Li, Z., "Dispersion of Guided Circumferential Waves in a Circular Annulus," *Review of Progress in Quantitative NDE, Review of Progress in Quantitative NDE,* Vol. 15A, p. 169-176, 1996.

Liu, G. and Qu, J., "Guided Circumferential Waves in a Circular Annulus," *J. Appl. Mech.,* Vol. 65, p.424-430, 1998.

Liu, G. and Qu, J., "Transient Wave Propagation in a Circular Annulus Subjected To Impulse Excitation on Its Outer Surface," *J. Acoust. Soc. Am.,* Vol. 103, p.1210-1220, 1998.

Moser, F., Valle, C., Jacobs, L.J., and Qu, J., "Application of Finite Element Methods to Study Transient Wave Propagation in Elastic Wave Guides," *Review of Progress in Quantitative NDE, Review of Progress in Quantitative NDE,* Vol. 16A, p.161-167, 1998.

Li Z. and Berthelot, Y. H., " An experimental investigation of crack detection in annular components by ultrasonic guided waves," *Review of Progress in Quantitative NDE, Review of Progress in Quantitative NDE,* Vol. 17, Plenum, p. 193-201, 1998.

Liu, G. and Qu, J., "Guided Transient Waves in a Circular Annulus," *Review of Progress in Quantitative NDE,* Vol. 16A, p.153-160, 1998.

Li Z. and Berthelot, Y. H., "Propagation of transient ultrasound in a thick annulus: modeling, experiments, and application to crack detection," *J. Acoust. Soc. Am.,* Vol. 104, No 3, Pt .2, p.1790, 1998.

Moser, F., Jacobs, L.J. and Qu, J, "Application of Finite Element Methods to Study Wave Propagation in Wave Guides," *NDT & E Int.*, Vol. 32, pp 225-234, 1999.

Valle, C., Qu, J., and Jacobs, L., "On The Dispersion And Displacement Distribution of Circumferential Waves In a Composite Circular Cylinder," *Review of Progress in Quantitative NDE, Review of Progress in Quantitative NDE,* Vol. 18A, pp.247-254, 1999.

Valle, C., Qu, J. and Jacobs, L.J., "Guided Circumferential Waves in Layered Cylinders," *International Journal of Engineering Science,* accepted for publication, 1998.

Kley, M., Valle, C., Jacobs, L.J., Qu, J. and Jarzynski, J. "Development of Dispersion Curves for Two-Layered Cylinders using Laser Ultrasonics," *Journal of the Acoustical Society of America,* accepted for publication, 1999.

Qu, Jianmin, Berthelot, Y.H. and Jacobs, L.J., "Crack Detection in Thick Annular Components using Ultrasonic Guided Waves," *Journal of Mechanical Engineering Sciences,* submitted, 1998.

Eisenhardt, C., Jacobs, L.J. and Qu, Jianmin "Application of Laser Ultrasonics to Develop Dispersion Curves for Elastic Plates," *Journal of Applied Mechanics,* submitted, 1999.

Valle, C., Qu, J. and Jacobs, L.J., "Guided Circumferential Waves in Layered Cylinders," presented at the *25th Annual Review of Progress in Quantitative Nondestructive Evaluation,* Snowbird, Utah, July 19-24, 1998, to appear Vol. 18, 1999.

Kley, M., Valle, C., Jacobs, L.J. and Qu, J., "Development of Dispersion Relationships for Layered Cylinders using Laser Ultrasonics," presented at the *25th Annual Review of Progress in Quantitative Nondestructive Evaluation,* Snowbird, Utah, July 19-24, 1998, Vol. 18A, pp. 263-268, 1999.

Li Z. and Berthelot, Y. H., "Modeling and experiments on the propagation of transient ultrasound in a thick annulus," presented at the *25th Annual Review of Progress in Quantitative Nondestructive Evaluation,* Snowbird, Utah, July 19-24, 1998, Vol. 18A, pp. 263-268, 1999.

Li Z. and Berthelot, Y. H., "Propagation of transient ultrasound in thick annular waveguides: modeling, experiments, and application to crack detection," submitted to *NDT & E Int* (January 1999).

NONDESTRUCTIVE EVALUATION

2.3 EDDY CURRENT MICRO SENSORS FOR INTGRATED DIAGNOSTICS

Co-investigator: S. Ramalingam (University of Minnesota)
Graduate Research Assistants: Jianhua Xue and Zheng Shi
M-URI Year 4 Funding Allocation: 6.4%

DoD NEED

Catastrophic failure of highly stressed, critical components of fixed and rotary wing flight systems occur due to flaw initiation and growth when a flaw within its components reaches a limiting size. The limiting flaw size depends on the stresses imposed on the component during service and the fracture toughness characteristics of the constructional materials used. On-board sensors can be useful to detect and monitor flaw initiation and growth in real-time. When such sensors are unavailable, components prone to failure will have to be disassembled and inspected off-line. Flaws, several mm in size (or more), are readily detected and repaired. However, a significant part of the critical component's life is in its flaw initiation phase where flaw dimensions are small, i.e., well below a mm in size. Detection of initiation of such flaws is a skill and time-intensive process requiring highly trained operators. Flaws of this dimension are also below the detectability limit of commercial eddy current (EC) inspection systems available in the beginning of the 90's.

Developing and implementing low cost EC sensors compatible with eddy current imaging and automation of the inspection process can substantially lower the cost and the man-power requirements for off-line inspection of critical components. Inspection reliability is also improved.

PROJECT MISSION

One major goal of this project is to develop and demonstrate eddy current (EC) micro sensors with substantially improved spatial resolution so that EC inspection can extended to the flaw initiation phase of a critical component's life. Spatial resolution for flaw detection sought is 100 μm and less (transverse size or dimension). A second goal is to make EC inspection objective so as to reduce the skill/training requirements for EC flaw detection, i.e., to eliminate subjective flaw identification methods now in wide use. Imaging methods have been sought so that EC inspection practice can be automated.

TECHNICAL PERSPECTIVE

When the ONR/M-URI program was initiated, eddy current (EC) flaw detection/inspection relied on subjective interpretation of impedance plot measurements made by highly skilled and well-trained measurement personnel. Reliable EC flaw detection was restricted to the flaw propagation phase of a critical component's life - detection in the flaw initiation phase of component life was rarely, if ever, achieved. The EC micro sensors developed in the present program have achieved sub mm spatial resolution - 100 μm resolution has been demonstrated with flux focusing Pencil Probes. Continuing work seeks 50 μm resolution. Measurement methods devised have led to flaw imaging so that the flaws are mapped, i.e., the flaw imaging methods developed have made EC inspection objective. Pencil Probes developed have also been shown to be compatible with EC inspection in 3-axis DNC systems, paving the way for robotic inspection. Path control algorithms, necessary for automated EC inspection, are derived from current generation CAD software. All of these make the need for highly trained manpower for off-line EC inspection less necessary.

RESEARCH ACCOMPLISHMENTS

As the flux available to detect changes in the AC magnetic field due to the presence of a flaw in a test object decreases with decrease in sensor dimensions, and since the excitation coil current used for EC inspection can directly add to the sensor signals (adversely affecting the signal-to-noise ratio), flux

focusing methods were developed both to shield and to enhance the flaw signals sensed by EC micro sensors.

Flux focusing concepts were verified in the first year of M-URI effort using manually wound macro sensors. Digital flaw imaging methods were developed with the same sensors so that subjective flaw detection based on impedance measurements can be replaced with 3-dimensional flaw imaging. A computer-driven, scanning stage for automated data acquisition was developed and commercially available, off-the-shelf software was used to display the EC signals acquired for objective flaw imaging. Model flaws, created with electrical discharge machining (EDM) and drilling (cylindrical holes, slots and keyhole defects) were used. The wound core (macro) sensors used were satisfactory for flux focusing and flaw imaging but the flaw resolution sought could not be obtained.

Photo lithography techniques were then used to construct much smaller single element and 4 x 4 array micro sensors for eddy current inspection. Single element EC micro-sensors, 1300 μm x 1300 μm in size, implemented in Silicon, showed that a flaw resolution of 100 μm is feasible (through-the-thickness 5 mm long model flaw created by wire EDM using a 0.004" diameter brass wire). Spatial resolution of 100 μm was achieved and 3-D flaw images were constructed by scanning the test sample using the computer-driven scanning stage. Following this, 320 μm x 320 μm single element and 4 x 4 array sensors were implemented in Kapton substrates to realize low cost, disposable sensors. Geometry of two of the micro-sensors developed for objective EC inspection are shown in Figures 1 (a) and 1 (b). Image of a model flaw (a key hole flaw extended with a narrow slot) in a steel test sample obtained with the 320 μm x 320 μm EC micro-sensor is shown in Figure 2 (a).

Following a 100 μm resolution flaw imaging demonstration with disposable Kapton EC micro sensors, the ONR M-URI Program Officer and Principal Investigator sought the development of a Pencil Probe (incorporating EC micro sensors) compatible with fully automated EC imaging to facilitate multi-axis CNC/robotic inspection using motion control drive signals derived from the CAD database of the component.

For automated EC inspection, a rugged "Pencil Probe" was developed using the 320 μm x 320 μm single element EC micro sensor. The same model keyhole flaw (2 mm drilled hole extended with an EDM slot, 5 mm in length, created with 0.004" diameter brass wire), made in a steel test object, was scanned (scanning time of ~ 15 minutes). It is this reconstructed model flaw image that is shown in Figure 2 (a). Resolution limit of 100 μm has been achieved with the "Pencil Probe".

Test samples with model flaws used so far contain a single, well-defined model crack. There is no guarantee that a highly stressed component will fail by the nucleation and growth of an isolated crack. A number of closely-spaced flaws may well be initiated at 'hot spots' within the highly stressed components with catastrophic failure resulting from the competition among a number of competing flaws. Crack branching may also occur. These likely failure considerations suggest that the EC inspection method should have high spatial resolution, and at the same time, an ability to detect closely spaced flaws.

Reconstructed image of a test sample containing a pair of closely spaced 250 μm wide slots with a flaw spacing of 250 μm is shown in Figure 2 (b). Pencil Probe with the 320 μm x 320 μm EC micro-sensor was used for flaw inspection and imaging. It is clear that EC micro-sensors can be used to identify one crack in a field of many cracks as well as branching cracks.

Sub-surface Flaw Detection

Model flaws created so far and imaged with the EC micro-sensors developed are surface-breaking flaws. Although the hot spots in many highly stressed components are close to an external surface, flaws leading to catastrophic failure need not always be surface-breaking cracks. For the EC sensor to be useful in a broad range of applications, it is necessary to demonstrate that the micro sensors developed have the capacity to detect flaws that are not necessarily surface-breaking. To do so, sub-surface model flaws in the form of 2 mm diameter blind holes of variable depth were drilled in a block of
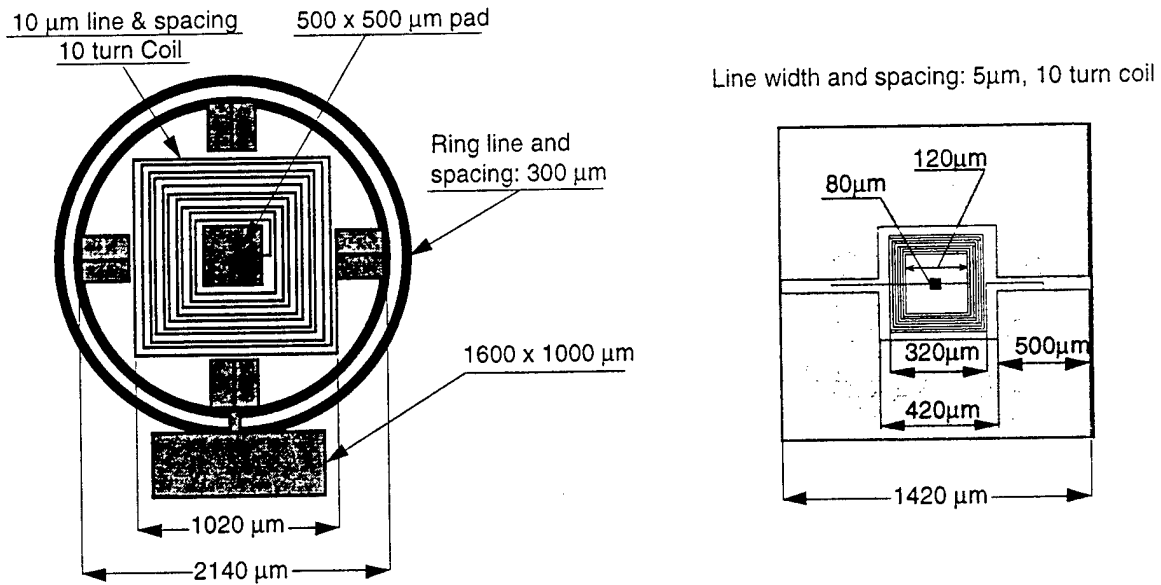
Figure 1. Geometry and dimensions of the 1020 μm x 1020 μm (left) and 320 μm x 320 μm (right) micro-sensors developed for eddy current flaw imaging.
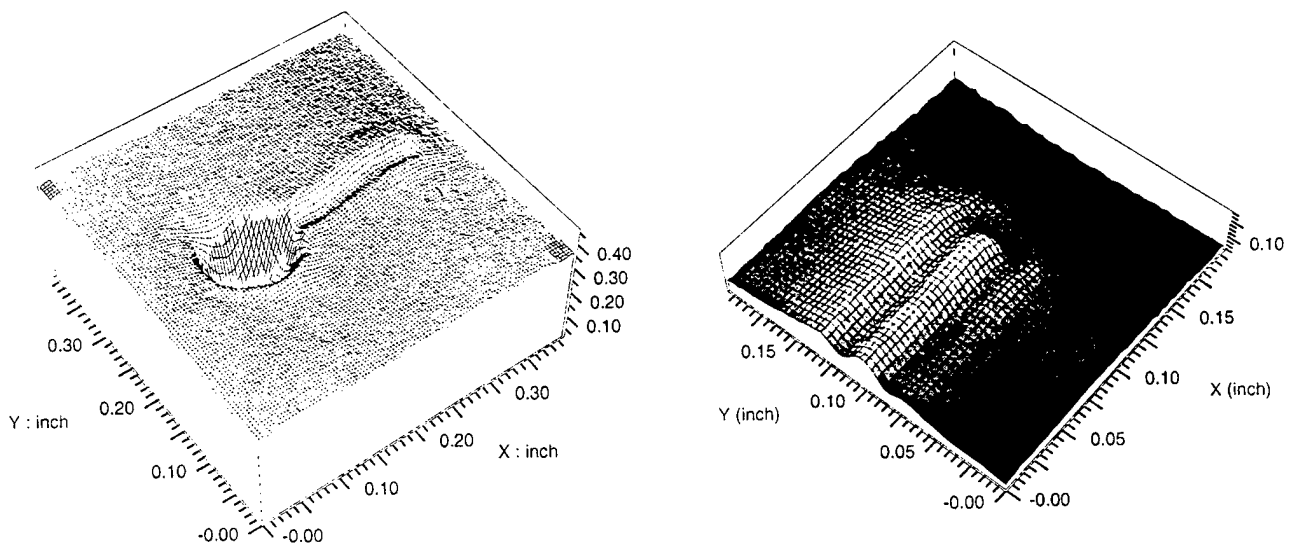
Figure 2. (a) Reconstructed eddy current image of a model keyhole flaw - 2 mm drilled hole extended with an EDM slot, 5 mm in length, created with 0.004" diameter brass wire. (b) Reconstructed image of a model flaw to detect closely spaced cracks - a pair of 100 μm wide slots with a spacing of 250 μm.

aluminum, 6.5 mm in thickness, as shown in Figure 3 (a). Eddy current inspection was made to detect the blind holes from the hole-free surface.

To detect sub-surface flaws lying well below the surface, eddy current 'skin depth' will have to be correspondingly large. Larger skin depths are obtained with lower EC excitation frequencies and higher test sample resistivity (skin depth δ is a function of frequency as well as the resistivity ρ of the material). Penetration depth of the excitation field also depends on the size of the flux-focusing pole piece.

Recognizing these, the 1020 μm x 1020 μm EC micro sensor was used to evaluate sub-surface flaw detection capabilities of the micro-sensors developed (excitation frequencies used are 20 kHz and 30 kHz). Line scan test data obtained, presented in the right part of Figure 3 (b), show that 1020 μm x 1020 μm EC micro sensors can detect subsurface flaws at a depth of about 60% of the pole piece (or sensor) dimension below the inspection surface. It has been shown that surface-breaking and non surface-breaking, sub-surface flaws can be detected with EC micro-sensors.

Untended Flaw Detection

To determine the off-line, untended inspection capability of EC micro sensors implemented as pencil probes using path control data automatically derived from CAD software (used to generate part geometry), model flaws in the form of drill holes were made in the two aluminum test samples shown in Figures 4 (a) and (b). The CL file (center line file) used to machine the step in a 3-axis Cincinnati-Milacron CNC milling machine (Pro-E software licensed from Parametric Technology Corporation) was used for eddy current inspection. The pencil probe with EC micro sensor replaced the milling tool for EC inspection.

The 'flawed' test sample surface was scanned in a moving bed-type Cincinnati-Milacron CNC milling machine (test sample, mounted on the machine table, was driven under DNC control; pencil probe was mounted in the stationary spindle) and the EC signal acquired was used to reconstruct the test part image with its model flaw.

Reconstructed image of the stepped block is shown in Figure 4 (c). Reconstructed image of the test sample with the cylindrical surface is shown in Figure 4 (d). In the case of the stepped block, z-axis motion was only necessary to go from higher elevation (left) to lower elevation at the step. Reconstructed images shown in Figure 4 (c) and 4 (d) demonstrate that automated EC inspection is feasible. To improve the signal-to-noise ratio (SNR), a digital signal processor equipped lock-in amplifier was used which allowed continuous EC measurement at table speeds of several ten mm/minute. Slow EC inspection speeds and large inspection times can be compensated for by using untended robotic systems.

For the cylindrical-surface sample, it is necessary to continuously vary the z position of the pencil probe as the sample surface is raster scanned. Since the CNC system used had only 3 controllable axes, probe normality condition had to be violated during EC flaw inspection. While the larger model flaws are unambiguously imaged, the SNR is significantly worse than that in the stepped-block test sample. This is seen by comparing Figures 4 (c) and 4 (d).

Results shown in Figure 4 (d) demonstrate that non-planar EC surface inspection for flaws will require inspection systems capable of meeting the probe normality requirement. This makes it necessary to have more than 3-axis for untended EC inspection, i.e., a robotic system with 4 or more controlled axes will be necessary (automated CL file derivation for 4-axis path control is feasible with most commercial CAD software). It is also desirable to minimize stand-off distance sensitivity during automated inspection which requires relatively large stand-off distances during EC inspection..

Flux Set Probes

Square loop magnetic cores offer a means of rendering stand-off distance variation less significant during automated EC inspection of parts with complex geometry. To achieve reduced sensitivity to stand-off distance, Fluxset probes may be made with an excitation and a concentric sensor coil, and a Metglass core within the concentric solenoidal coil assembly. In flux set probes, AC
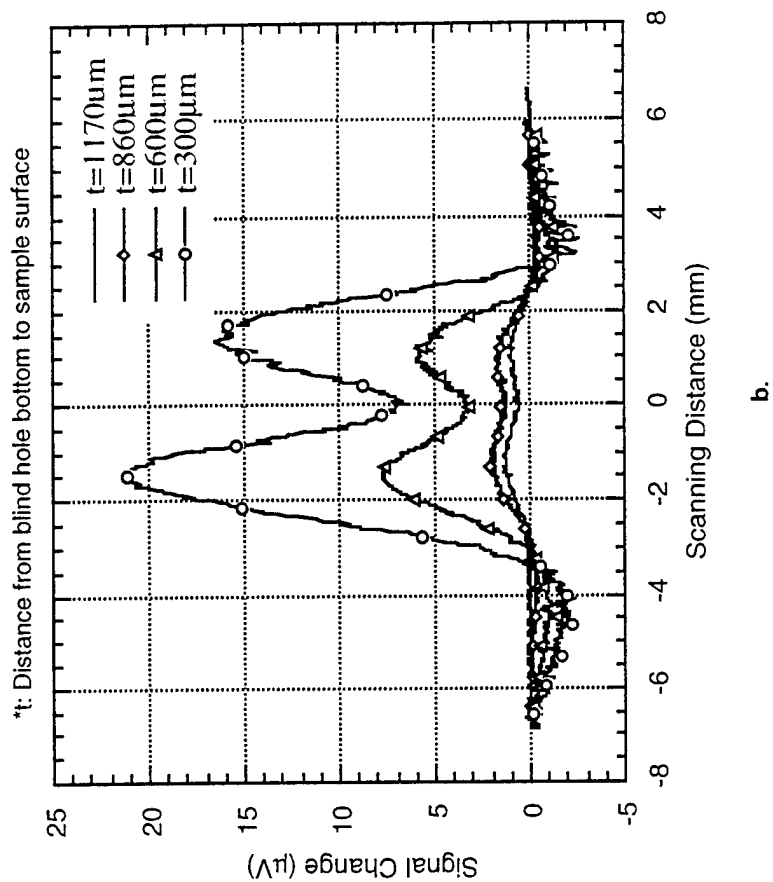
**Figure 3.** (a) Test sample with sub-surface model flaws - 2 mm diameter blind holes of variable depth drilled in a 6.5 mm thick block of Aluminum. (b) Line scan results - blind holes were detected with 1020 μm x 1020 μm EC micro sensors at 20 kHz or 30 kHz from the hole-free surface. Depth resolution is a function of test frequency and flux-focusing pole piece diameter.

Model flaws: 2.54mm and 2.28mm dia. holes

a.

Model flaws : 1mm, 1.3mm, 1.6mm and 2mm diameter holes

b.

c.

d.
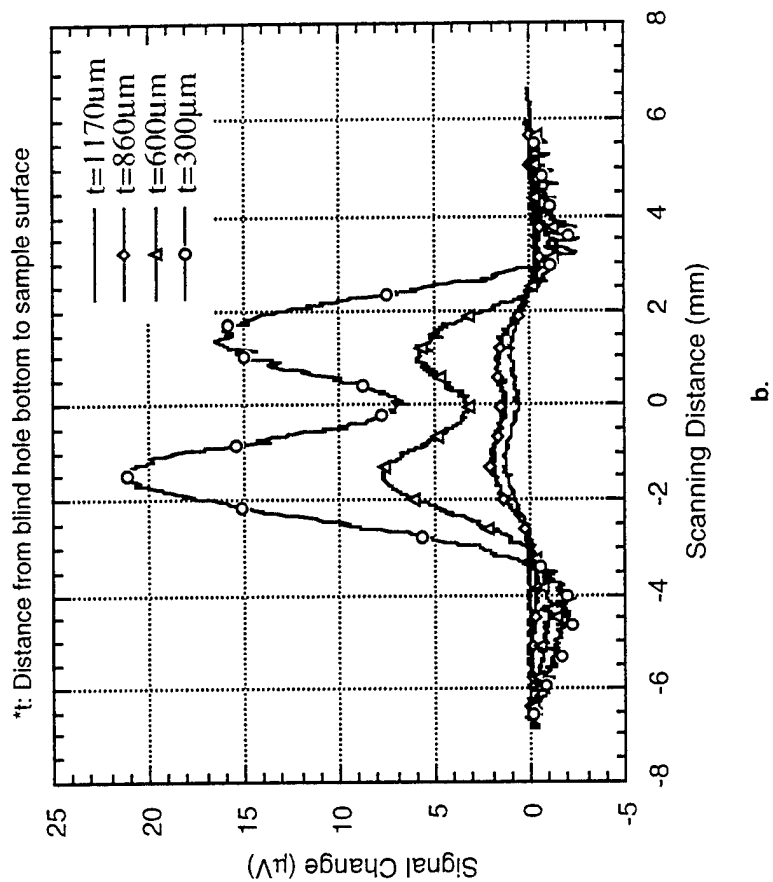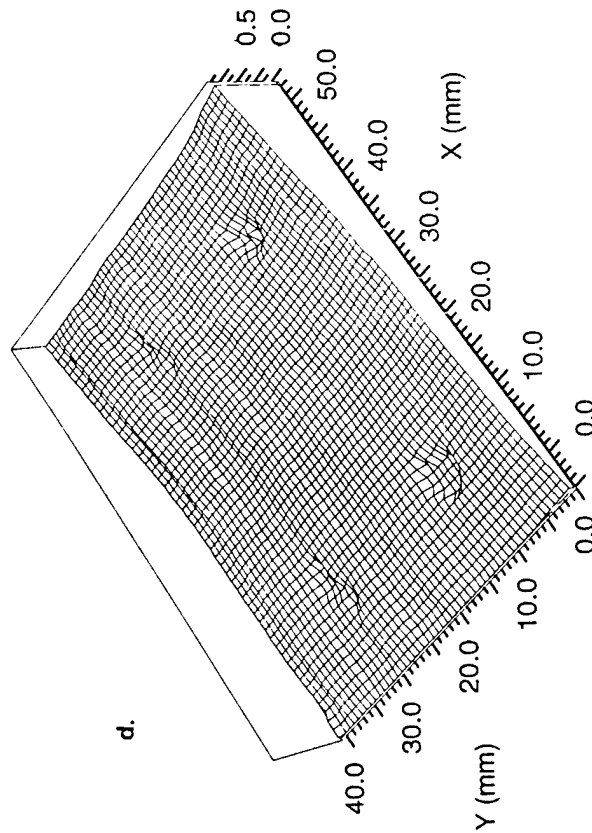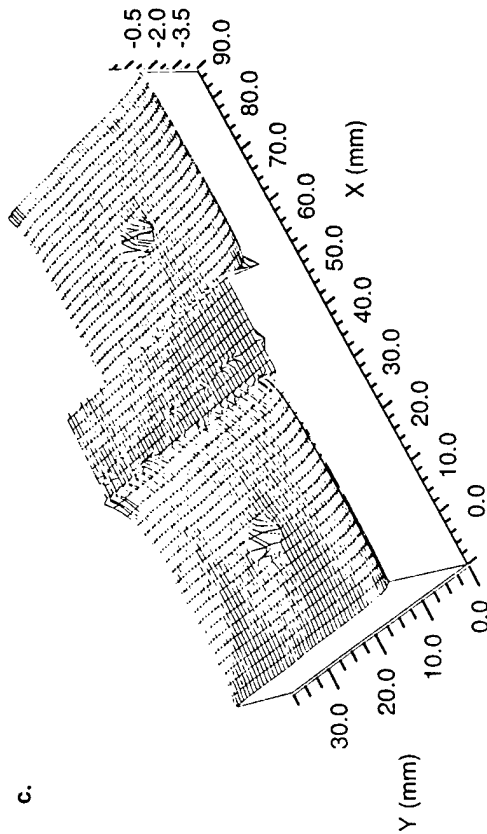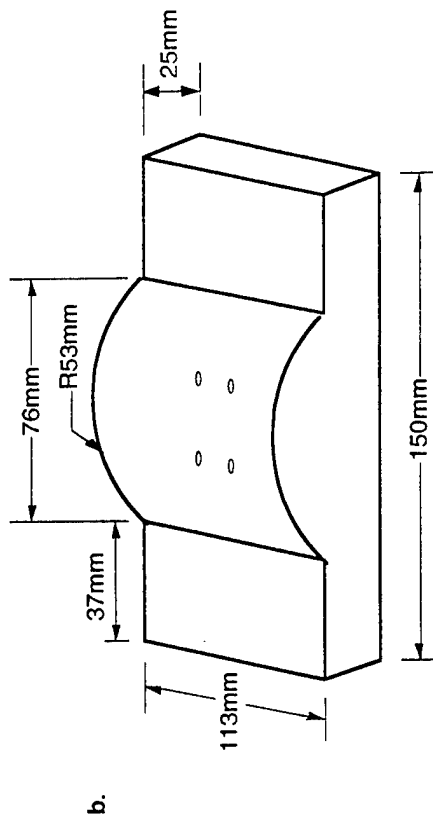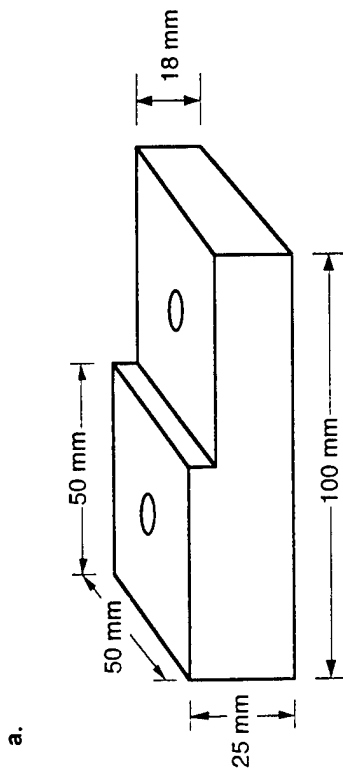
Figure 4. (a) Aluminum test sample - a stepped block with model flaws in the form of drilled holes - for automated EC inspection with the Pencil Probe. A 3-axis CNC mill was used with path control algorithm derived from ProE CAD software for automated EC inspection. (b) Test sample with a cylindrical surface and model flaws in the form of drilled holes for automated EC inspection with a Pencil Probe in a 3-axis CNC mill. (c) EC image of the stepped block containing model flaws. (d) Reconstructed EC image of the aluminum test sample with a cylindrical surface and model flaws

-50-

excitation of the primary (outer) coil leads to saturation of the square loop magnetic core. Field flipping in the core (AC-excited primary) is sensed by the inner solenoidal (sensor coil). In the presence of an external magnetic field, if the AC excitation current is maintained constant, the sensor coil voltage signal is time-shifted in saturation (forward saturation occurs sooner and reverse saturation is retarded). Measuring the time-shift with respect to the reference excitation current enables measurement of magnetic fields with high precision.

First set of prototype Fluxset probes have been constructed with commercially available Metglass cores and found to function as anticipated. Test samples with model flaws have been fabricated with drilled through-holes 3.25 mm and 4.76 mm in dia., and a 0.34 mm wide slot perpendicular to the hole axis (in aluminum, copper and stainless steel samples). The cylindrical flux set probe used, 2.5 mm in diameter x 8.00 mm in length, was able to unambiguously detect the model flaw.

Spatial resolution characteristics of the flux set probes have not yet been determined. Analysis involving numerical simulation which underpins the principles of the Fluxset sensing probe are underway. Flux set probe/sensor will be perfected in the M-URI year 5 effort to demonstrate automated EC inspection with less sensitivity to variations in stand-off distance.

Mesh Coil Sensors

Spatial resolution better than 100 μm displayed by the EC micro sensors and the pencil probes require fairly large inspection/scanning times. Data acquisition time for the keyhole flaw shown in Figure 2 (a) was 15 minutes! This may not be appropriate for geometrically complex, large components even in untended EC inspection systems.

Micro sensor arrays may be used to reduce scanning times. However, they will require signal multiplexing for data acquisition from each of the micro sensors raising measurement system complexity. A two stage EC inspection scheme where the first scan serves primarily for flaw detection and the second scan for detailed flaw imaging may be more appropriate.

Modified mesh coil sensors in which electrical drives replace mechanical rotation may be useful for two-stage flaw detection. A mesh coil sensor with a planar excitation coil, a planar sensing coil and a high permeability magnetic shield is shown in Figure 5 (a). Planar mesh coil sensors may be wound around a mandrel to build cylindrical sensors, as shown in Figure 5 (b), needed for inner as well as external surface flaw detection.

Mesh coil sensors of this form can also be miniaturized as shown in Fig. 6 (a). Partial-cylinder sensors may then be implemented for flaw detection (as for eddy current inspection of blade roots in turbine discs). A aluminum test sample with a model blade root, shown in Fig. 7, was made to demonstrate single-pass EC flaw search in turbine engine rotors. Slots with complex geometry will require a partial cylinder sensor with a small tip radius, 0.6 mm in the present case as seen in Fig. 6 (b), for the single-pass inspection of the flawed (model flaw) blade root.

Flaw signals obtained with the 16 mm planar mesh coil sensor, when it is used for the detection of a surface breaking flaw (aluminum test block with an EDM-cut model flaw on planar surface) is shown in Fig. 8. Comparable flaw detection performance is exhibited by the cylindrical mesh coil sensor when it is used to detect a 3 mm diameter model flaw drilled transverse to a semi-cylindrical surface generated to model an inner surface. Scanned signals are shown in Figure 9. Signal from the partial cylinder sensor - Figure 6 (b) - when it is used to detect the blade root model flaw (Figure 7) is shown in Figure 10.

In all instances, the mesh coil sensors used were powered with an off-the-shelf function generator (excitation coil drive). A DSP Lock-in Amplifier, Stanford Research System Model 830, was used to obtain the flaw signal from the mesh coil sensor. Measured flaw signals are typically of the order of microvolts.
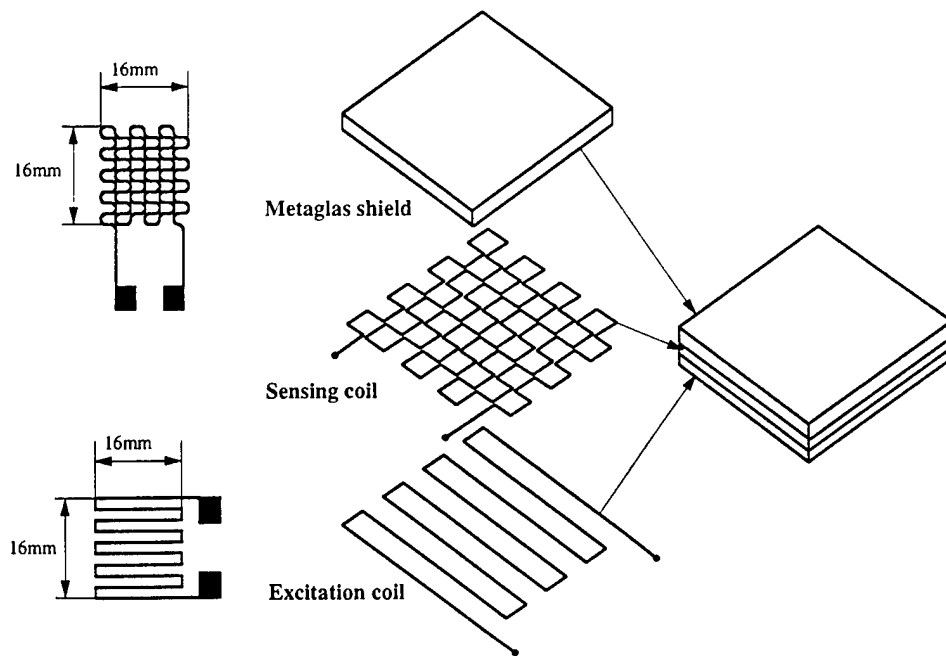
Figure 5. (a) Mesh coil sensor with a 16 mm square planar excitation coil, a planar sensing coil and a Met Glass magnetic shield.
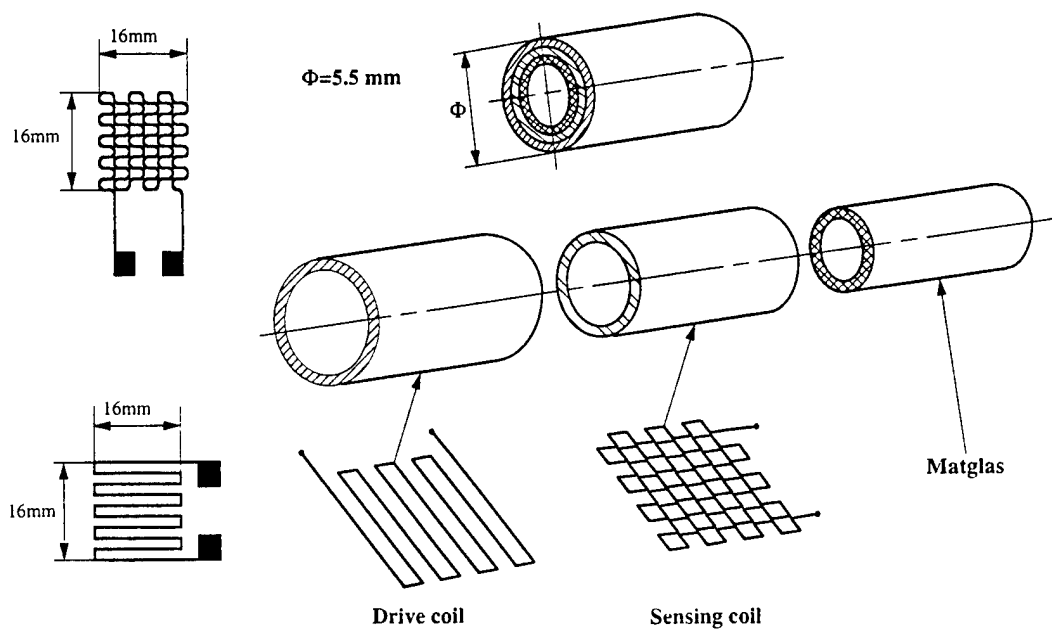
Figure 5. (b) Cylindrical mesh coil sensor, 5.5 mm in diameter, suitable for inner surface flaw detection, constructed by winding a 16 mm planar mesh coil sensor around a mandrel.
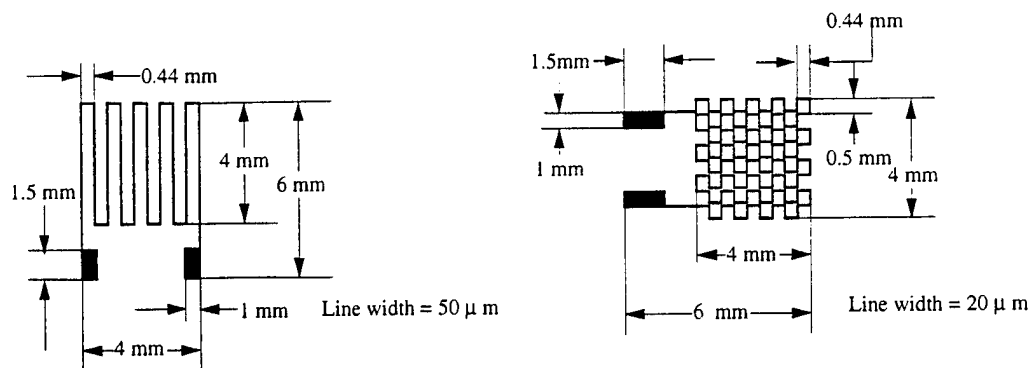
Figure 6. (a) Mesh coil sensor with a 4 mm square planar excitation coil, and a planar sensing coil.
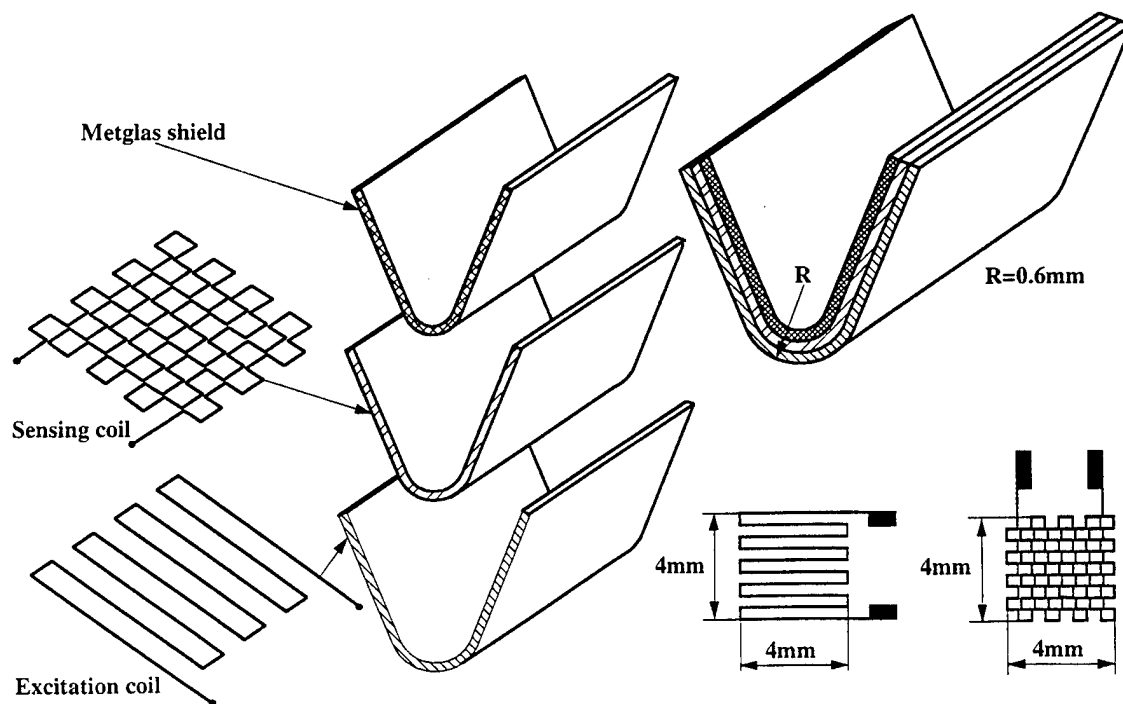
Figure 6. (b) A partially cylindrical mesh coil sensor, suitable for flaw detection in turbine blade roots, constructed by bending and mounting a miniature planar mesh coil sensor.

Material: Al
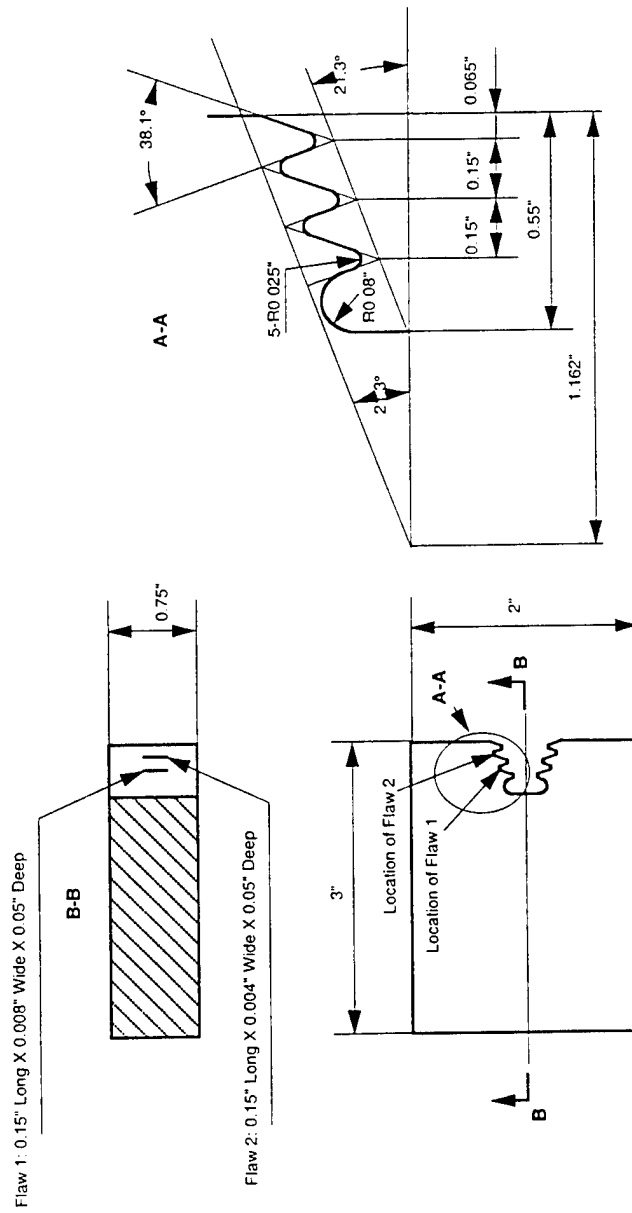
Figure 7. Geometry of a turbine blade root test sample containing model flaws representing cracks normal to the principal loading direction (centrifugal loading).
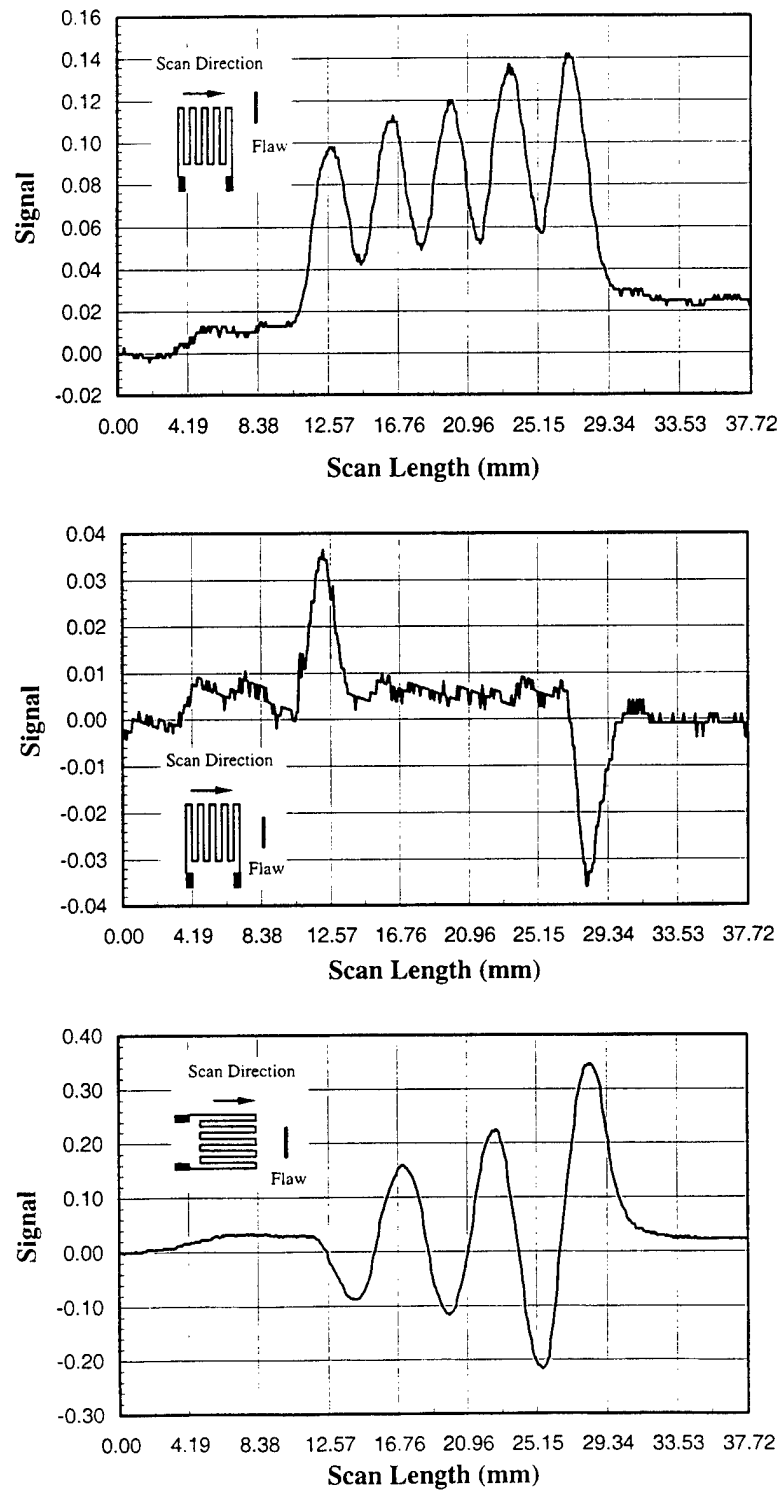
Figure 8. Eddy current signals obtained when a planar mesh coil sensor is used for flaw detection. Model flaw is a surface break on the flat external surface of an aluminum block made by EDM.
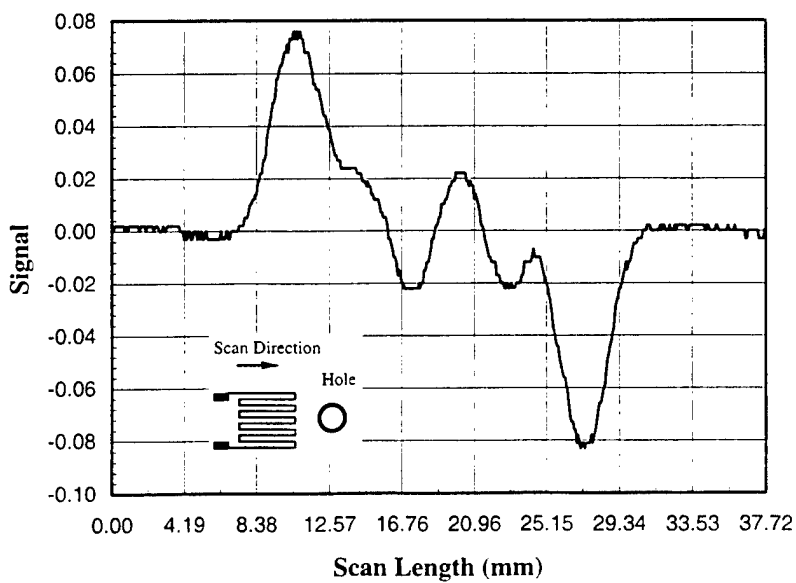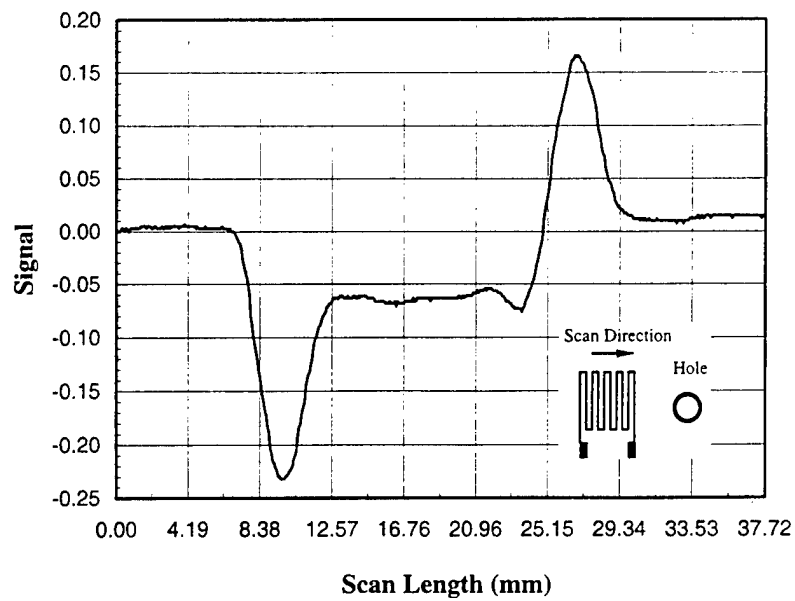
Figure 9. Eddy current signals obtained when the 5.5 mm diameter, cylindrical mesh coil sensor is used for flaw detection. Model flaw is a drilled hole, on the semi-cylindrical, concave 'internal' surface of an aluminum test block.
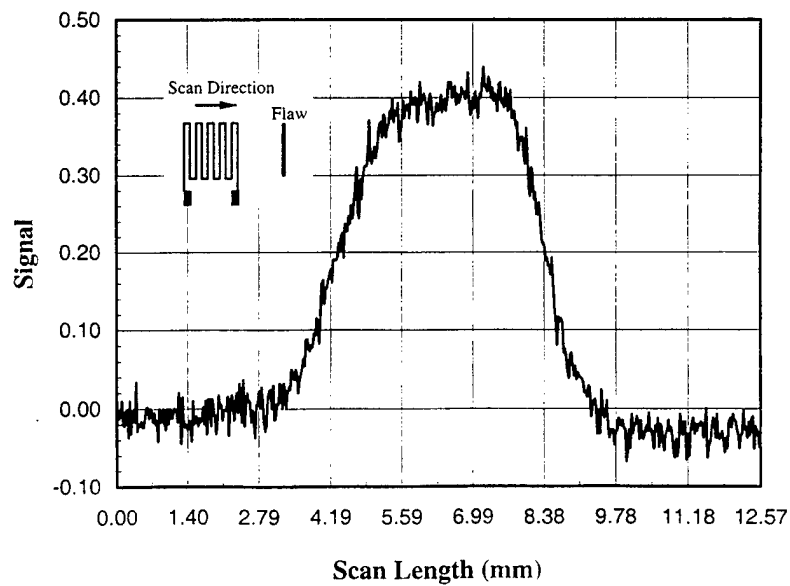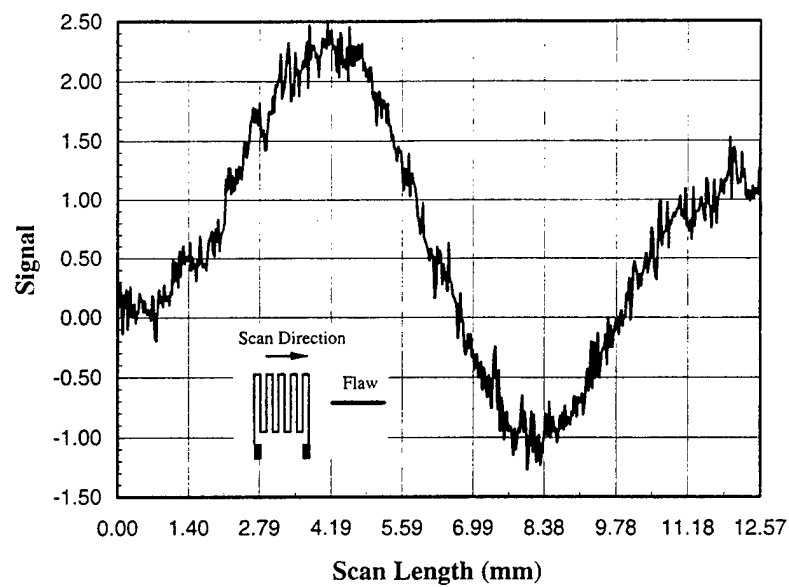
Figure 10. Eddy current signal from the partial cylinder sensor when it is used to detect blade root model flaw. Model flaw on the curved inner surface of blade root in an aluminum block shown in Fig. 7.

Modeling Mesh Coil Sensors

The mesh-coil sensor is modeled using Maxwell's Equations given by

$$\nabla \times H = J_s + J_e \qquad \nabla \times E = -\frac{\partial B}{\partial t} \qquad \nabla \cdot B = 0 \tag{1}$$

where   H = magnetic field intensity vector J_s = applied source current density vector
       J_e = induced eddy current density vector   E = electric field intensity vector
       B = magnetic flux density vector.

Constitutive equations for the test material, the material with the real or model flaw, are:

$$B = \mu_r \mu_o H \quad \text{and} \quad J_s + J_e = \sigma E \tag{2}$$

where μ_r = relative permeability μ_o = permeability of free space
      σ = electrical conductivity.

Maxwell's equations may be solved using the magnetic vector potential A and a scalar electric potential V.

$$B = \nabla \times A \qquad E = -\frac{\partial A}{\partial t} - \nabla V \qquad \nabla^2 V = 0 \tag{3}$$

Then, the induced eddy current density vector J_e can be expressed in terms of the magnetic vector potential A as :

$$J_e = -\sigma \frac{\partial A}{\partial t} \tag{4}$$

A commercial grade FEM Package, ANSYS, was used to solve the sensor modeling problem with the magnetic vector potential A as the primary unknown.

The problem geometry, shown in Figure 11, has 11.5 mm x 9 mm drive and sensing coils with wire thickness and width of 0.2 mm and 0.5 mm, respectively. The drive and sensor coils are made of copper (resistivity $\rho = 1.7 \times 10^{-8}$ Ωm) with the test sample made of 6 mm thick aluminum ($\rho = 2.8 \times 10^{-8}$ Ωm). Air elements were assumed to represent insulating layers between the aluminum block and the drive coil, and between the drive and sensor coils. Drive coil current assumed was 20 mA at 80 kHz. The entire modeling region is 50 mm x 50 mm x 50 mm in size containing a total of 14,850 8-node magnetic elements. All fields outside the modeling region were taken to be zero.

The calculated, total eddy current density distribution in the aluminum test block (test sample) in 3-dimensions (upper right) and in plan view (lower left) are shown in Figures 11 to 15. The test block of Figure 11 is the reference sample; blocks shown in Figures 12 and 13 contain surface-breaking flaws - cuts 4.5 mm long x 1 mm wide x 1.5 mm deep - along the Z direction in two different X positions; blocks shown in Figures 14 and 15 contain surface-breaking cuts along the X direction in two different Z positions. The y-component of the magnetic flux density, By, induced in the test blocks with and without surface breaking flaws, are shown in the lower right of Figures 11 to 15.

Presence of surface flaws lead to changes in eddy current distribution within the block and thus to changes in the y-component of the magnetic flux density By. A voltage signal, detected with the sensing coil, is due to the perturbations in By resulting from the presence of surface flaws or cuts.

The voltage signal generated in the sensor coil is determined by calculating the change in magnetic flux within each 3/4 turn sensing loop caused by the surface-breaking cuts, i.e., by comparing

the magnetic flux in test blocks with and without surface-breaking flaws. Magnetic flux passing through the sensing coil loop is calculated as follows:

$$B_y^i = B_{oy}^i [\cos(\omega t + \varphi_i) + j \sin(\omega t + \varphi_i)] = Re\,[B_y^i] + j\,Im\,[B_y^i]$$

$$\varphi_y^i = S_i\,B_y^i \qquad\qquad (5)$$

$$\varphi_m = \sum_{i=1}^{n} S_i\,B_y^i$$

where B_y^i = magnetic field density in the *ith* element of the sensing coil loop,

ω = $2\,\pi\,f$, where f is the drive current frequency,

φ_i = phase shift in the *ith* element with respect to the drive current,

S_i = area of the *ith* element of the sensing coil loop,

φ_y^i = magnetic flux along y direction in the *ith* element of the sensing coil loop,

φ_m = total magnetic flux passing through the sensing coil.

The real $Re\,[B_y^i]$ and imaginary $Im\,[B_y^i]$ parts of magnetic field density in the *ith* element of the sensing coil loop can be obtained directly from the FEM calculations. The voltage or the electromotive force, *Emf*, generated is given by:

$$Emf = \frac{d}{dt}\varphi_m = \sum_{i=1}^{n} S_i \frac{d}{dt} B_y^i = j\,\omega \sum_{i=1}^{n} S_i\,\{\,Re\,[B_y^i] + j\,Im\,[B_y^i]\,\}$$

$$\qquad\qquad (6)$$

$$Emf = Re\,[\,Emf\,] + j\,Im\,[\,Emf\,].$$

The sensing signal measured is:

$$\Delta\,Emf = \{\,Emf\,(\text{sample with flaw}) - Emf\,(\text{sample without flaw})\,\}. \qquad (7)$$

Calculated sensor output, in volts, for the assumed problem geometry and flaw geometries are shown in the table below:

	No flaw	Flaw 1	Flaw 2	Flaw 3	Flaw 4
Re [*Emf*] Volts	- 7.8303 E -07	- 6.7401 E -07	- 8.8382 E –07	- 6.9441 E -07	- 8.6762 E –07
Im [*Emf*] Volts	- 5.5238 E -06	- 6.1984 E -06	- 5.7616 E –06	- 6.3029 E -06	- 4.7411 E –06
IΔ *Emf* I Volts	0	6.8340 E -07	2.5828 E –07	7.8413 E -07	7.8723 E –07

Measured signals, in the absence of Metglass shields, are found to lie in the voltage range of 1.0×10^{-6} to 1.5×10^{-6} volts.

The fair agreement between the calculated and measured results suggest that a sound physical basis underpins mesh coil (Hoshi) sensors. The mesh coil sensor can be reduced to a pair of closely spaced lines for eddy current excitation and a single, 3/4 turn, meander coil for flaw sensing. This enables the design and use of inexpensive, flexible, disposable small area (as well as large area) flaw sensors for any EC inspection task. Verification of this notion and the evaluation of rotating field, mesh coil sensors are currently under way. Commercially available NOVAFLEX® (from Sheldal, Northfield, MN) films - polyimide sheets with two-sided copper plating - will be used. It is anticipated that disposable, mesh coil sensors for rapid (single pass) inspection of turbine engine rotor discs can result from the 5th year effort (field evaluation at Cherry Point, NC).

NONDESTRUCTIVE EVALUATION
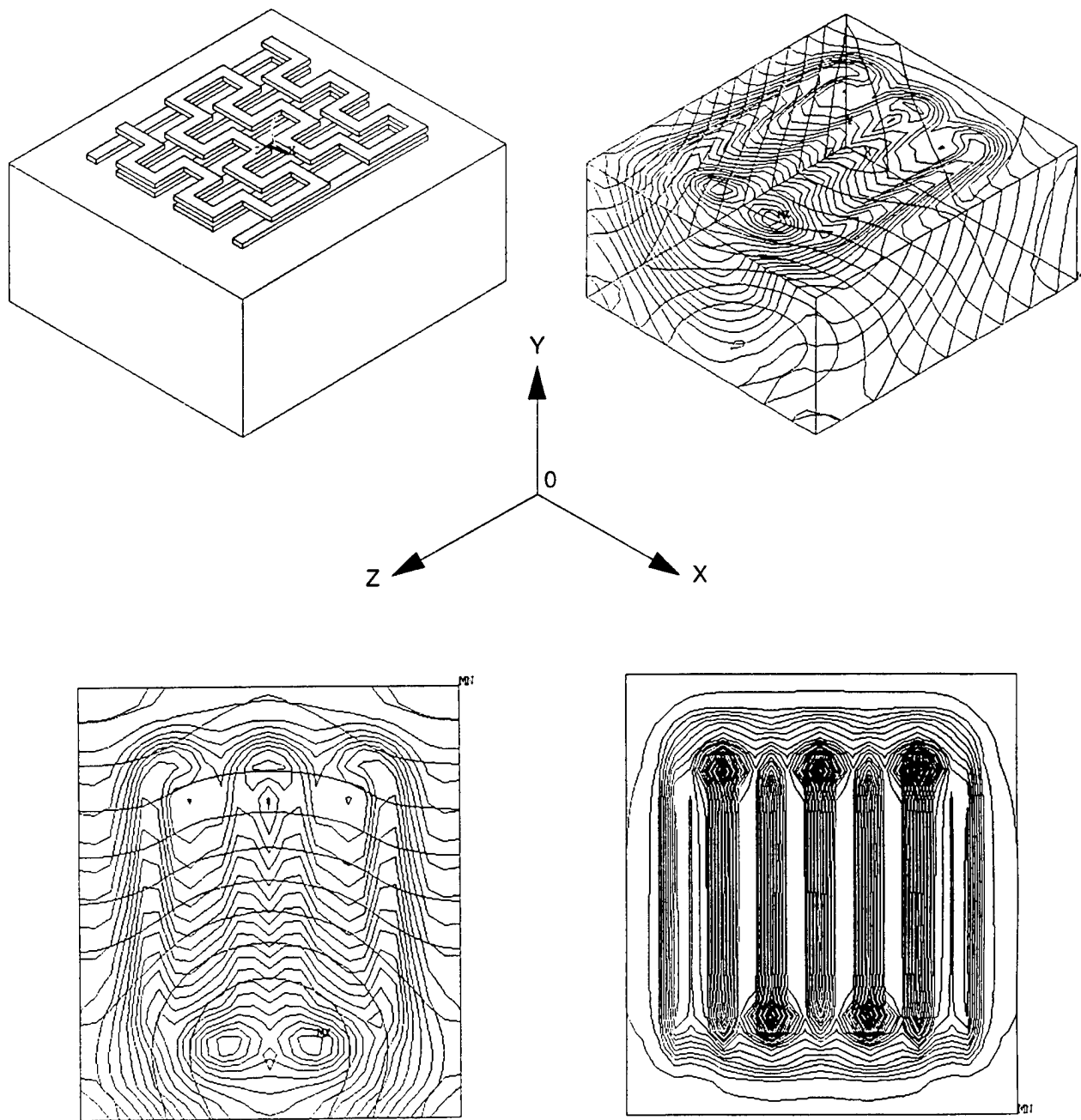
Figure 11. Flaw-free aluminum test block with superposed meander excitation and sensing coils (upper left), calculated total eddy current density (upper right), calculated total eddy current density : plan view normal to y-axis (lower left) and the calculated values of the y-component of magnetic flux density B_y in the test block (lower right)
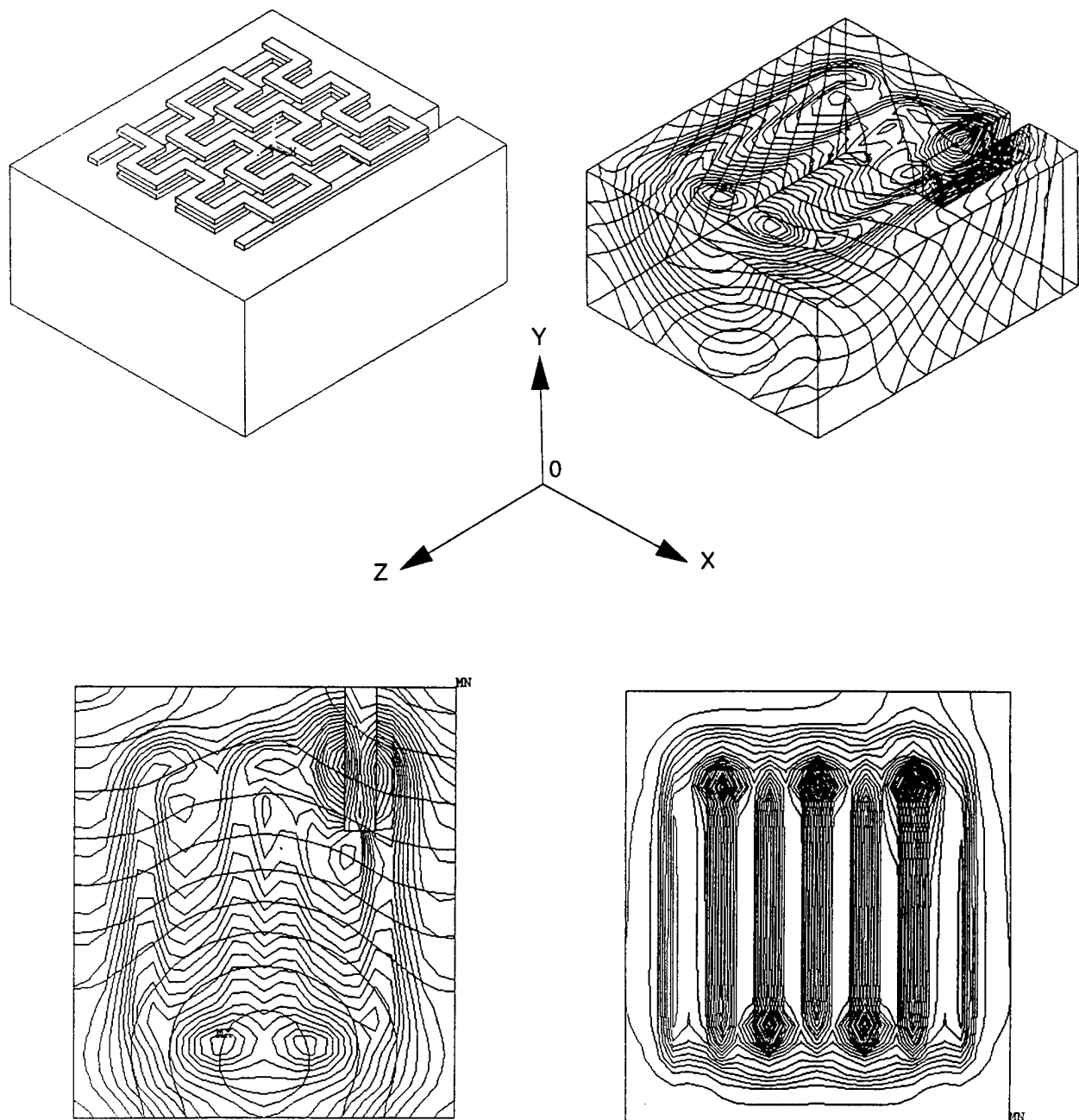
Figure 12. Flawed aluminum test block with superposed meander excitation and sensing coils (upper left), calculated total eddy current density (upper right), calculated total eddy current density : plan view normal to y-axis (lower left) and the calculated values of the y-component of magnetic flux density B_y in the test block (lower right). Flaw parallel to z-axis.
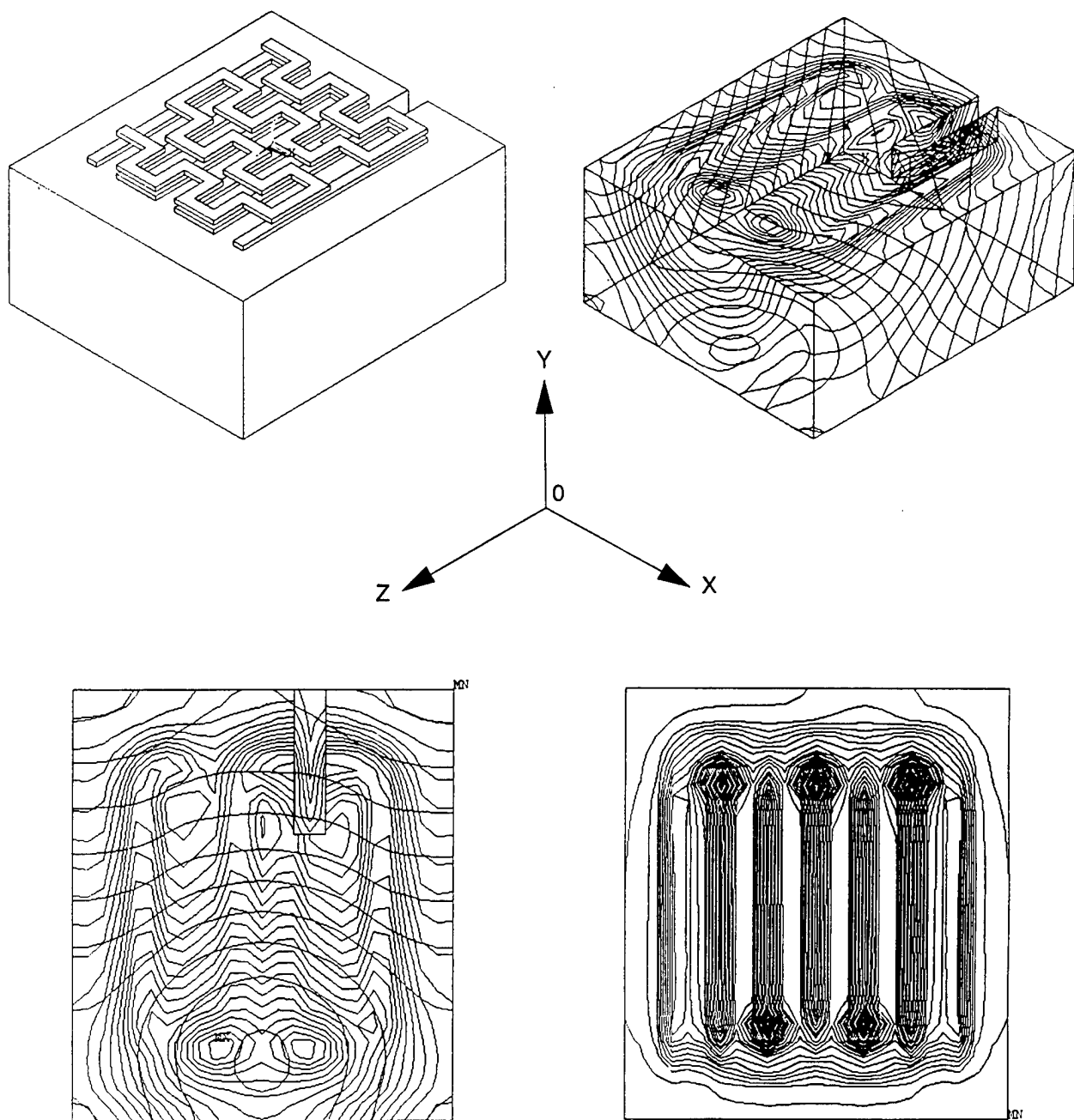
Figure 13. Flawed aluminum test block with superposed meander excitation and sensing coils (upper left), calculated total eddy current density (upper right), calculated total eddy current density : plan view normal to y-axis (lower left) and the calculated values of the y-component of magnetic flux density B_y in the test block (lower right. Flaw parallel to z-axis displaced with respect to the flaw of Figure 12.

Figure 14. Flawed aluminum test block with superposed meander excitation and sensing coils (upper left), calculated total eddy current density (upper right), calculated total eddy current density : plan view normal to y-axis (lower left) and the calculated values of the y-component of magnetic flux density B_y in the test block (lower right). Flaw parallel to x-axis.

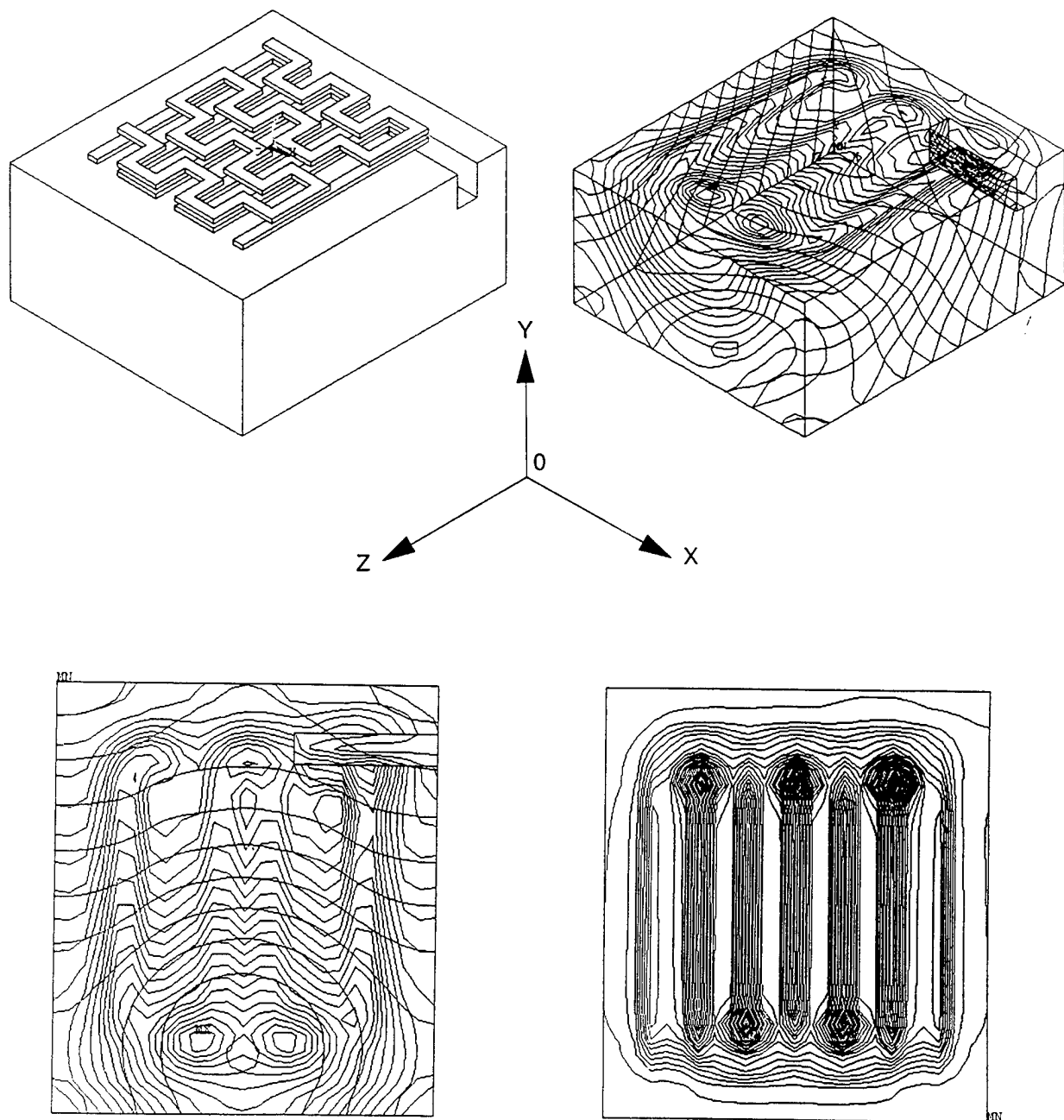**Figure 15.** Flawed aluminum test block with superposed meander excitation and sensing coils (upper left), calculated total eddy current density (upper right), calculated total eddy current density : plan view normal to y-axis (lower left) and the calculated values of the y-component of magne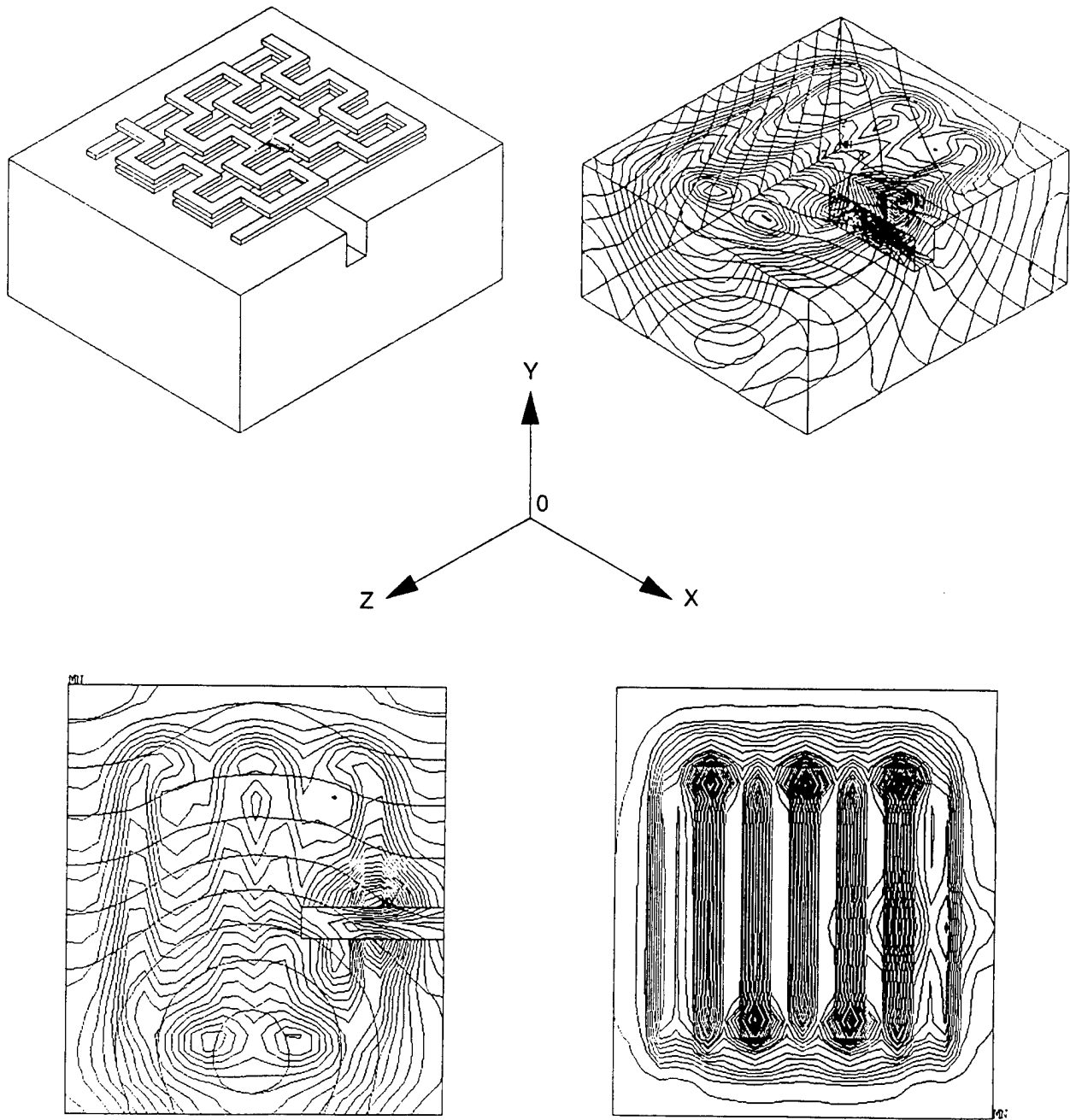tic flux density B_y in the test block (lower right). Flaw parallel to x-axis displaced with respect to the flaw of Figure 14.

Flaw Growth Monitoring In Real-Time With Mesh Coil Sensors

The 16 mm square mesh coil sensors, as implemented in the 4th year of this M-URI program, may also be suitable for real-time flaw growth monitoring during fatigue tests. A set of four 16 mm square mesh coil sensors have been made available to the Georgia Tech co-PIs investigating material fatigue properties (Section 3.2). It is anticipated that if the suitability of mesh coil sensors for fatigue crack growth monitoring can be confirmed, newer mesh coil sensors can be made with better spatial resolution to track flaw growth under load with greater precision.

Summary

[1] Eddy current micro sensors have been developed and shown to have spatial resolution sufficient to detect 100 μm flaws. Continuing work is in progress to further lower the spatial resolution to 50 μm. High spatial resolution is achieved with flux focusing pole pieces for EC excitation and a single, multi-turn (10 turn) sensor coil implemented on Silicon with 5 μm technology. It has been shown that less expensive, disposable micro sensors can be made by implementing the same 5 μm technology on copper-coated Kapton substrates. Smallest single-element sensor implemented is 300 μm x 300 mm in size. Sensors of the same size can also be implemented as 4 x 4 micro sensor arrays to reduce the total inspection time (raster scan).

[2] Micro sensors developed can also be implemented as "Pencil Probes" without loss of flux focusing functionality necessary for high resolution flaw sensing. High resolution flaw sensing is a time-intensive inspection task. Inspection costs can be reduced by implementing digitally-driven, untended inspection systems equipped with "Pencil Probes". Multi axis, path control algorithms for digital drive can be derived from the same commercial CAD software used for part design. Simple part geometries can be accommodated with 3-axis drive systems but complex part geometries will require 4 to 6 axis direct numerical control systems (DNC) since probe normality conditions will have to be met during EC inspection. Inspection data can be acquired on-the-fly. Use of readily available Lock-In Amplifiers can facilitate high speed data acquisition.

[3] Micro sensors, implemented as Pencil Probes, have sufficient resolution to detect a single flaw in a field of closely spaced flaws. They also can detect sub-surface flaws. Detection depth is limited by 'skin depth' of the AC field used for flaw sensing and the dimensions of the flux focusing pole piece used.

[4] Imaging techniques have been developed to make EC flaw inspection objective. Reliance on qualitative interpretation of measured data (subjective judgment of impedance plot data) by highly trained operators is no longer necessary. EC inspection is automatable and can be implemented in untended systems with no loss in flaw detection reliability.

[5] Despite sophisticated signal processing, untended eddy current inspection with micro sensor - equipped Pencil Probes will still require fairly large times for flaw imaging. Separating flaw detection from flaw imaging can reduce the total EC inspection time and man power needs. A mesh coil (Hoshi) sensor may be used initially for flaw detection. This can localize the detect which can then be imaged with micro sensors.

To facilitate this planar mesh coil sensors have been designed and demonstrated for flaw detection applications. Flexible, disposable sensors (16 mm sq. and 4 mm sq.) have been made and their flaw detection capability verified. Flexible mesh coil sensors can be wound to make cylindrical sensors suitable for great many internal surface inspection applications. Performance of large diameter (5.5 mm) and small diameter cylindrical sensors (the latter as partial cylindrical sensor) have been verified.

[6] In addition to their utility for rapid flaw inspection, mesh coil sensors can also be configured for rapid, single-pass, EC inspection of narrow slots as in turbine rotors (blade root, Christmas tree slots). Mesh coil sensors may be enhanced with electrical drives using two excitation coils at 90° to each other. This can eliminate the orientation-dependence of the mesh coil sensor signal. Work is in progress to evaluate feasibility and utility of electrically rotated mesh coil sensors.

NONDESTRUCTIVE EVALUATION

[7] Numerical simulation has been used to verify the functionality of the of the mesh coil sensor. Calculated results suggest that the mesh coil sensors may also be suitable for real-time flaw growth monitoring under well-controlled test conditions. To evaluate feasibility of real-time flaw growth monitoring during fatigue, mesh coil sensors have been made available to Geogia Tech co-PIs *David McDowell* and *Richard Neu* of Section 3.2.

[8] Stand-off distance variation during untended inspection with EC micro sensors can introduce geometric artifacts in flaw images. This problem can be offset by reducing the stand-off distance sensitivity of EC sensors. Flux set probes, with their inherently much greater magnetic field measurement sensitivity, offer an opportunity to reduce stand-off sensitivity of EC probes. Feasibility of flux set sensors have been verified. Their flaw detection capability has also be demonstrated. A significant part of the fifth year effort will be devoted to the implementation of flux set sensor to reduce stand off distance variation sensitivity during EC inspections.

RESEARCH PLANS

The fifth year effort will focus on the following tasks:
- Evaluate the feasibility of accurate flaw localization with mesh coil sensors. Planar, cylindrical and electrically-driven, rotating field sensors will be evaluated.
- Flaw localization will be followed with flaw imaging using the already developed EC micro sensors - both in automated EC inspection mode.
- Field demonstration (at Cherry Point, NC) of mesh coil sensors for rapid, single pass EC inspection of turbine blade slots in turbine engine rotor discs.
- Evaluate the feasibility of real-time flaw growth monitoring during fatigue in collaboration with co-investigators at Georgia Tech.
- Determine the resolution limit of mesh coil sensors for flaw growth monitoring using numerical simulation. Develop second generation mesh coil sensors with the resolution limit suitable for real-time flaw growth monitoring.
- Implement flux set probes to reduce the stand-off distance sensitivity of EC sensors during automated, offline flaw inspection.
- Field demonstration of automated EC inspection with pencil probes equipped with EC micro sensors. This is best accomplished with the multi-axis coordinate measuring machines and/or robotic systems available at Cherry Point, NC with the path control algorithms derivied from CAD software in use there. Field demonstration of flaw localization with mesh coil sensors. Field demonstration of flux set probes with reduced sensitivity to variations in stand-off distance.

M-URI PUBLICATIONS

L. Zheng, J. Xue and S. Ramalingam, "Eddy-Current Micro-Sensors For Flaw Imaging: Numerical Simulation And Experimental Evaluation," ASME/STLE Joint Conference, San Francisco, CA, October 1996,

J. Xue, S. Ramalingam and Z. Shi, "Modeling Eddy Current Imaging with Thin Film Micro-Sensors," ASME International Mechanical Engineering Congress, November 1997, Dallas, TX.

J. Xue, S. Ramalingam and Z. Shi, "Eddy Current Flaw Imaging using Micro-Sensor Arrays," ASME International Mechanical Engineering Congress, November 1997, Dallas, TX

J. Xue, "Nondestructive Inspection with electromagnetic induction approach and eddy current micro-sensors," M. S. Thesis, Department of Mechanical Engineering, University of Minnesota, Oct. 1998.

J. Xue, Z. Shi and S. Ramalingam, "Eddy Current Micro-Sensors for Flaw Imaging and Identification," Reviewed and accepted for publication in Sensors and Actuators, Dec., 1998 (in print).

3.1 ACOUSTIC EMISSION MODELING FOR INTEGRATED DIAGNOSTICS

Co-investigator: Isaac M. Daniel (Northwestern University)
Graduate Research Assistants: J.-J. Luo and J. Choi
M-URI Year 4 Funding Allocation: 3.6%

DoD NEED

This project addresses the need to monitor in real time the condition of key components of naval systems, to detect and characterize critical flaws, monitor damage growth and provide input to life prediction modeling.

PROJECT MISSION

The objective of this project is to investigate and develop/adapt acoustic emission methods for the detection and characterization of fatigue damage growth in metallic components. This research applies to components whose failure results from initiation and propagation of a major crack at a known location of stress concentration.

TECHNICAL PERSPECTIVE

Since the inception of this M-URI project in 1995, results obtained represent breakthroughs in the application of acoustic emission methods for damage detection and characterization. Specifically, the introduction of loading phase as a relevant parameter, the development of an anthropomorphic (user friendly) interface for probing data and the introduction of covariance processing and categorization of data, are novel and significant advancements of the technology.

RESEARCH ACCOMPLISHMENTS

The primary accomplishments of this task since its inception are techniques for acoustic emission (AE) data acquisition, simultaneous measurement of physical damage and innovative approaches for processing, analysis and correlation of acquired data with physical damage [1-3].

Techniques were developed or adapted for monitoring AE output during cyclic loading of notched metallic specimens. Two materials were investigated, 2024-T3 aluminum and 4340 steel. Three types of specimens were used, edge notch and center notch tensile specimens and a compact tension specimen. The AE output was monitored with a pair of resonant transducers equally spaced from the specimen notch. Crack propagation was monitored independently and concurrently with AE output.

The latest specimens were 4340 steel bars of 2 x 0.5 in. cross section and 14 in. in length with a 0.8 in. long central through crack machined by EDM (Fig. 1). After machining the specimens were heat treated to a hardness of 38-40 RC. Acoustic emission was recorded by two 15 kHz resonant transducers placed on either side of the crack at a distance of 1.5 in. Crack propagation gages were mounted on the face of the specimen near the crack tips.
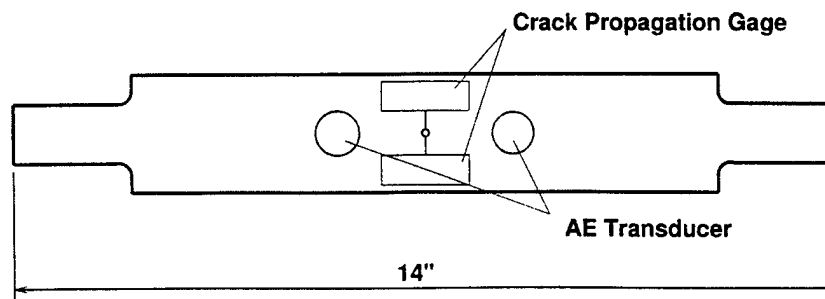

Figure 1. Specimen geometry and AE transducer location for fatigue loading.

The MISTRAS Acoustic Emission (AE) data acquisition system (PHYSICAL ACOUSTICS) was used to acquire the data. AE Waveforms were acquired at 1 MHz sampling rate during fatigue tests. The AE threshold was set at 47 dB, which is above the background noise of the test environment. The load level signal from the servo hydraulic machine (INSTRON) was fed to and recorded by the MISTRAS system. Traditional AE parameters as well as AE waveforms were recorded for later analysis. A typical fatigue test generated between 50-100 thousand waveforms, and required more than 1 GB of hard drive space. Tests were conducted at 2 Hz frequency under tension-tension loading with an R-ratio of 0.1.

It was found that crack growth plotted versus normalized fatigue cycles was independent of loading amplitude, i.e., fatigue lifetime [3]. The crack growth rate (da/dn) follows a power law relationship with the stress intensity range ΔK, i.e., it follows Paris law as shown in Fig. 2.
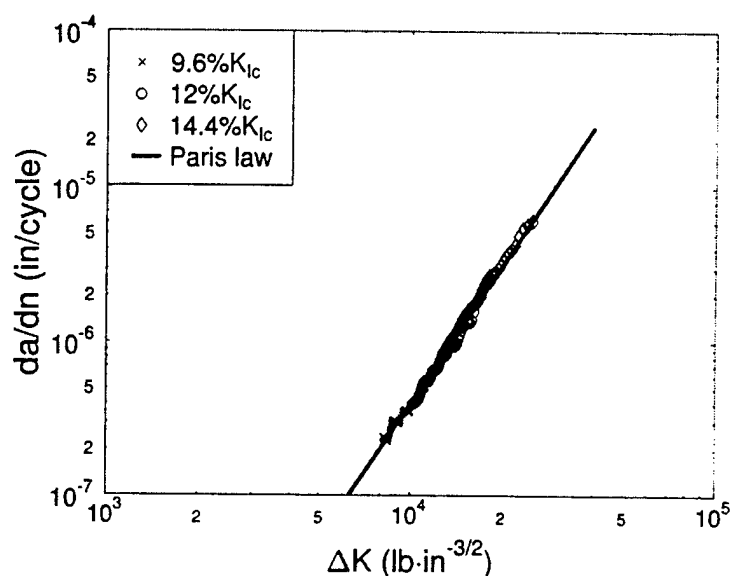
Figure 2. Crack growth rate versus range of stress intensity factors for fatigue testing of 4340 steel.

The phase of the loading cycle was identified as an important parameter in further filtering and analysis of AE data [1,2]. The AE output was separated into three groups or regions according to the phase of the loading cycle in which it occurs (Fig. 3). The origin of the AE signals of the various groups was also investigated by comparing amplitude distributions of the differential time of arrival at the symmetrically located transducers and of the signal duration. AE signals in group A, corresponding to the end of the unloading cycle are primarily associated with noise. AE activity in group B, occurring during the loading part of the cycles, corresponds to crack opening and crack propagation. AE signals in group C, occurring near the end of the fatigue lifetime near the peak of the loading cycle, correspond to rapid crack propagation in the final stage.

One puzzling observation was that, whereas crack growth was smooth, AE activity, especially near the middle of the fatigue lifetime included jumps as seen in Fig. 3. Examination of signal waveforms showed that waveforms corresponding to jumps in AE activity are distinctly different from those corresponding to a normal AE rate (Fig. 4). These signals have relatively high amplitudes and cannot be filtered out by raising the threshold. Since these jumps obviously cannot be correlated with crack growth, a major effort was directed and focused on a better algorithm for processing and categorizing AE signals.

In addition to analysis based on AE parameters, actual waveform data were used to provide a more comprehensive approach to signal processing. The sheer size of waveform data, however, poses big obstacles to this approach. In a typical AE experiment the data size collected is between 0.5 and 3 gigabytes. Most existing waveform analysis algorithms would take from a few hours to several months to process the data.

FAILURE CHARACTERIZATION AND PREDICTION

Figure 4. Acoustic Emission Waveforms

Figure 3. AE count distribution and cumulative counts versus fatigue cycles of compact tension 4340 steel specimen under fatigue loading.

A scientific visualization software package (DtaReader and DtaProbe) was written. This software allows the user to explore gigabytes of AE waveform data from an intuitive user interface of cumulative hit count graph. The user can click on any part of the graph with a mouse, then the following information is displayed (Fig. 5).

    a. An arrow pointing to the data point in question.

    b. The waveform data. It can be scaled (enlarged) by using the slide bar on the side in case the amplitude is too low to appear on the current scale.

    c. Fourier transform data. FFT (Fast Fourier Transform) is calculated on the fly and displayed for frequency component analysis.

    d. Parametric data. All conventional parametric data are displayed both numerically as well as graphically.
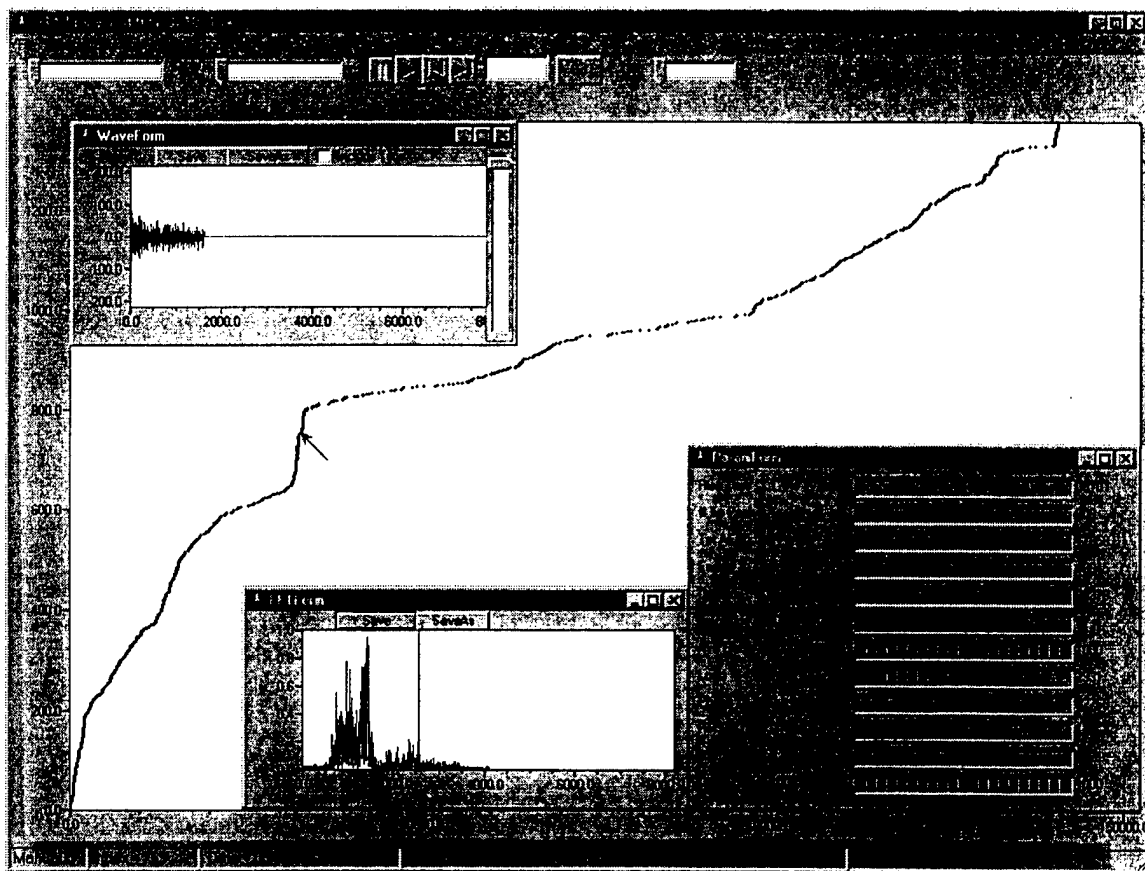
Figure 5. DtaProbe user Interface

DtaProbe is interactive software for the user to probe into the large waveform data intuitively and effectively. DtaProbe works on a set of data files that another pre-processing software package, named DtaReader, created. The creation of DtaReader and DtaProbe by itself was a major achievement because they provide a tool with which all researchers can visualize and analyze the waveform data interactively and intuitively. The software was written in C++ for the Windows environment. Any Windows 95, 98 or NT4 environment can run this software.

A second major development in the data processing task was the study of covariance of the waveform signals, i.e., correlation of waveforms among themselves. Each data set, or waveform, is compared with itself and all other data sets by sliding it over the other until a good matching point is found. The degree of match is called covariance value and is normalized so that a perfect match

corresponds to a covariance value of 1.0. The covariance value is represented graphically on a gray scale, with black corresponding to 1.0 and white to 0 covariance.

Covariance of a number of signals or data sets can be represented graphically in the form of a covariance matrix, where the data sets (or signals or waveforms) are arranged along two axes. For example, if ten signals representing only three different types of waveforms A, B and C are obtained in the sequence ABCBACCABB their covariance matrix can be represented as in Fig. 6a. Black squares represent maximum covariance value (1.0) and white squares zero (or low) covariance value. Given such a matrix, the challenge is to find and sort out the different types of waveforms that are represented in this matrix. An algorithm was developed to perform this task. This algorithm rearranges the matrix in such a way that most similar signals (resulting in the darkest black squares) will be placed next to each other. The result of rearranging is shown in Fig. 6b. It becomes clear that three different types of signals were present in the matrix. This rearranging (sorting) of the matrix is important because certain types of waveforms should be correlatable with specific physical events during the material or structure lifetime.

Fig. 7 shows gray scale covariance matrices of AE data from an actual fatigue test. The first matrix corresponds to a chronologically acquired sequence of data sets (waveforms). The second matrix was obtained after rearrangement by the "sorting algorithm."

(a)   (b)
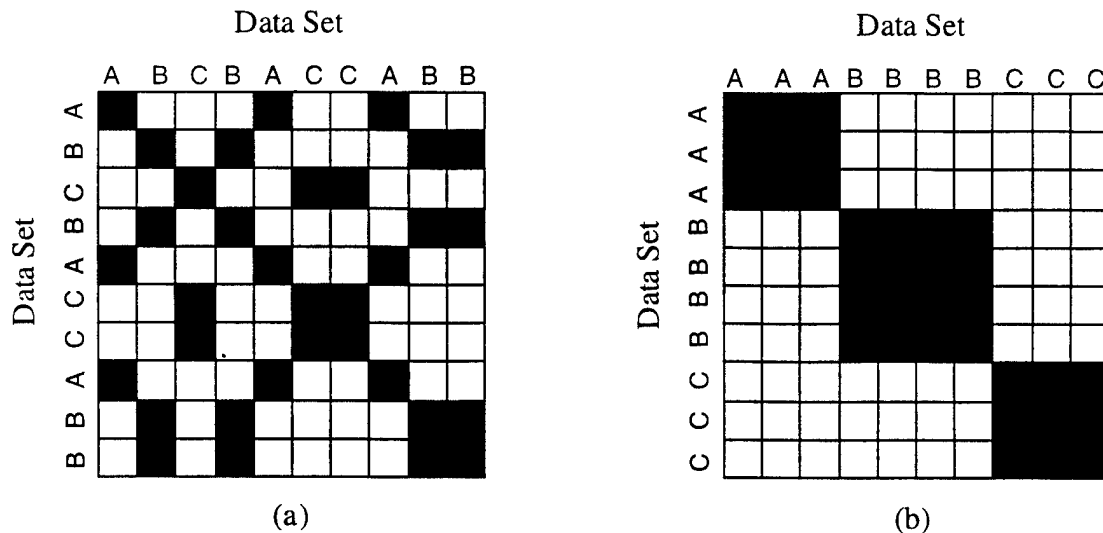
Figure 6. Covariance matrix of ten data sets representing three types of signals A, B, and C.
(a) as acquired sequence   **(b)** rearranged sequence.

Original matrix   After rearrangement
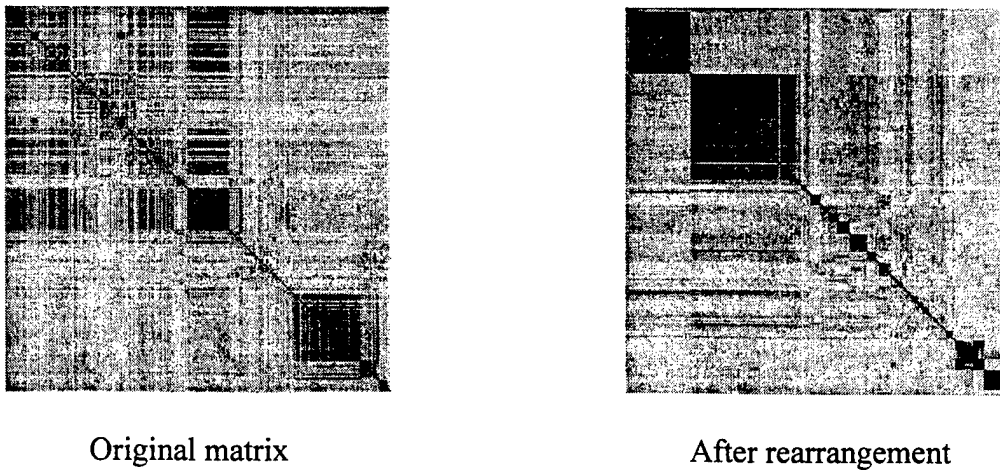
Figure 7. Covariance matrices of AE data from a fatigue test before and after sorting.

RESEARCH PLANS

The following work is planned for the coming year:

1. Optimization of the waveform sorting algorithm.

   The methods developed will be further refined to categorize or sort, waveform data sets, by choosing an adequate and representative sample with a minimum of storage requirements and processing time.

2. Matching of AE events with data set groups obtained by the "sorting algorithm."

   All acquired AE events will be separated into groups corresponding to the waveform groups obtained by the "sorting algorithm." Each group of AE events will be plotted versus fatigue cycles.

3. Correlation of sorted AE events with physical damage.

   The plots above will be compared with actual damage development, e.g., crack length, to select the most relevant group or groups.

4. Expansion of covariance processing to account for signal amplitude.

   It is obvious that signals can be similar but of different amplitude. Since physical events affect both the AE waveform features and its amplitude, the latter will have to be incorporated into an expanded data processing algorithm.

M-URI PUBLICATIONS (REFERENCES)

[1] I. M. Daniel, J.-J. Luo, C. G. Sifniotopoulos and H.-J. Chun, "Acoustic Emission Monitoring of Fatigue Damage in Metals," *Review of Progress in Quantitative Nondestructive Evaluation,* Vol. 16, ed. by D. O. Thompson and D. E. Chimenti, Plenum Press, New York, 1997, pp. 451-458.

[2] I. M. Daniel, J.-J. Luo, C. G. Sifniotopoulos and H.-J. Chun, "Acoustic Emission Monitoring of Fatigue Damage in Metals," *Nondestr. Test Eval.,* 1997, pp. 1-15.

[3] I. M. Daniel, C. G. Sifniotopoulos and J.-J. Luo, "Analysis of Acoustic Emission Output from Propagating Crack," *Review of QNDE,* Vol. 17, ed. by D. O. Thompson and D. E. Chimenti, Plenum Press, New York, 1998, pp. 1331-1338.

3.2 STRUCTURAL FATIGUE INVESTIGATION

Co-investigators: David McDowell (lead), W. Steven Johnson, Richard Neu, Jianmin Qu, Ashok Saxena
Graduate Research Assistants: A. Bell, V. Bennett, L. Cretegny, B. Gardner, R. Hamm, O. Jim,
       J. A. Pape, C. Rosen, D. R. Swalla-Michaud
Undergraduate research students: M. Kamel, T. Edwards, D. Van Dellan
Collaborator: Rosario A. Gerhardt (Professor, Materials Science & Engineering, Georgia Tech)
M-URI Year 4 Funding Allocation: 15.0%

DoD NEED

When this M-URI effort began, the state-of-the-art methodology for remaining useful life estimation was based on the manual inspection of stress-concentrators (hot spots) in aircraft structures. Results from this project extend this methodology, so as to develop the elements that will be relevant to near-real time estimation of the remaining life of general, complex structural components used by defense services (e.g., a CH46 helicopter rotor hub).

PROJECT MISSION

An integrated system for diagnosing the "health" of a structural component subjected to high cycle fatigue (HCF) will consist of sets of embedded or emplaced sensors at various locations, extracting information related to a.) the generation of material defects, b.) the presence of crack-like discontinuities and their progression, and c.) changes of system dynamics that may relate to this progression. Since the idea is to monitor the gradual changes of component performance and various local related indices *before* catastrophic failure to enable the operator to respond with a maintenance hold, it is essential to couple the diagnostics with prognostic capability; this facilitates a prediction of how much time remains within the window of viable servicing or repair.

In the HCF regime, the dominant fraction of total fatigue life may be spent at crack lengths on the order of $20\mu m$ to $500\mu m$. The detection of longer cracks near the end of component life is critical since component failure may lead to failure of the overall structure. This necessitates (i) the identification of finite-element algorithms for identifying component "hot spots" where failure is likely to occur; (ii) development of appropriate crack growth laws for cracks of different length scales, ranging from on the order of grain size to on the order of component dimensions, including consideration of contacting components (fretting fatigue) and environmental effects; and (iii) development of algorithms for identifying the progression of component degradation based on multiple sensor inputs at different time and length scales, providing feedback to support cause for maintenance shutdown. This investigation is dedicated to performing research to address the aforementioned needs, so as to develop a logic structure for detecting fatigue cracks and estimating the remaining useful life of complex in-service components with condition-based maintenance algorithms.

TECHNICAL PERSPECTIVE

This M-URI project focuses on "filling the critical gaps" identified at its inception in 1995 that are needed in fulfilling the mission of near real-time remaining life estimation of in-service structural components. These key technical elements include:

- a finite-element post processor for visualization and rapid identification of "hot spots" in components.
- supporting microstructure and structure-scale fatigue experiments and robust modeling concepts for small cracks in high cycle fatigue that are on the order of sub-grain size and above in length, including stress state dependence and multiple regimes of behavior.
- novel finite element calculations of small cracks in microstructures.
- fretting fatigue experiments and first generation critical plane models for fretting fatigue.
- integration of acoustic emission and wave propagation methods for small fretting fatigue and small crack propagation from notches, with experimental effort to support sensor classification of fatigue damage stage or level.

FAILURE CHARACTERIZATION AND PREDICTION

RESEARCH ACCOMPLISHMENTS

A number of significant advances have been made in the development of prognostic tools to serve condition-based maintenance (CBM) requirements within the overall Department of Defense M-URI program in Integrated Diagnostics. Listings of CBM technology innovations and basic scientific advances generated by the investigators of the Structural Fatigue task at Georgia Tech follow.

Technology Innovations

- Developed a finite-element based methodology for rapid identification of hot spot locations in components and verified for H-46 rotor hub by comparing to field data for failure locations.

- Interfaced with GT acoustic emission team to instrument laboratory specimens in smooth specimen and fretting fatigue to demonstrate capabilities of sensor arrays to monitor stages of fatigue damage evolution in smooth specimen fatigue and fretting fatigue.

- Performed critical assessment of near real time algorithms/methodologies for remaining life estimation, and proposed most potentially fruitful algorithms.

- Developed robust multi-stage fatigue model for propagation of small cracks spanning the LCF and HCF regimes for remaining life estimates.

Basic Scientific Advances

- Clarified mechanics challenges and essential developments for next generation fatigue crack growth models for small cracks.

- Experimentally evaluated and modified existing micromechanical models for growth of microstructurally small cracks (based on dislocation pile-up at obstacles) for helicopter alloys and Ti-6Al-4V, and identified strong microstructure barrier features.

- Conducted novel fretting fatigue experiments and suggested improvements for models of fretting fatigue.

- Used nanoindentation, Atomic Force Microscopy (AFM) and Impedance Spectroscopy (IS) as tools to explore surface roughening during fatigue cycling, changes in local hardness near the crack tip for long cracks during fatigue, and understanding fatigue mechanisms.

- Conducted novel computational cyclic crystal plasticity calculations for distribution of driving force parameters for formation and growth of subgrain-scale fatigue cracks in a polycrystal under HCF, as well as first-ever calculations for mixed mode behavior of microstructurally small cracks in surface grains in polycrystals.

- Developed algorithms for evaluating driving forces for long cracks with complex, 3-D crack fronts.

A comprehensive discussion of the accomplishments and work underway by the investigators of this Structural Fatigue Investigation M-URI project is presented in Appendix C as a report entitled **"Prognostic Tools for Condition-Based Maintenance."** The mission of developing the elements that will be relevant to near-real time estimation of the remaining life of general, complex structural components is discussed in the context of being decomposed into treatment of a relatively small number of critical locations or "hot spots" necessitating dedicated microsensors. These hot spots are defined as locations within components that are assigned high probability as failure sites based on preliminary elastic stress analysis that employs realistic loading conditions. A robust model for small fatigue crack propagation is described which is applicable to dedicated hot spot microsensor algorithms. Research is also described in numerous supporting areas (e.g., fretting fatigue) for understanding the formation and propagation of microstructurally small, mechanically small, and long fatigue cracks. The structure of a remaining life estimation scheme for hot spot locations is also outlined, focusing on near-real time prognostics.

Environmental effects generally contribute to accelerated evolution of fatigue processes in components. Environmental penetration is highly sensitive to local component design details, surface exposure, surface conditions and applied loading history. Although not explicitly discussed in the work of Appendix C, these effects may be incorporated in the remaining life estimation schemes in terms of their influence on bounds of remaining life estimates.

RESEARCH PLANS

A number of demonstration projects are underway. These projects, as summarized below, involve collaboration between various groups in the M-URI program to bring together advances in sensor and prognostic technology.

Multiple hot-spots

A collaboration with Georgia Tech co-PIs Laurence Jacobs and Jacek Jarzynski of Section 3.4.

This demonstration project will highlight the integration of the sensor and remaining life technologies in M-URI year 5. The goal of the demonstration tests is to show that sensors and prognostics can capture damage that may be occurring at multiple sites. The demonstration specimen contains two types of potential hot spots: notches and two-body contacts. Hot spots are sites where fatigue cracks are likely to nucleate in a component. The catastrophic fatigue crack may nucleate at either a notch or fretting location. The location where the catastrophic crack initiates will depend on the severity of the notch. Therefore, three different notch geometries, each with a different stress concentration factor will be considered. In addition, preliminary tests will be conducted to verify the differences in sensor signals between those coming solely from fatigue at notches and those solely from fretting fatigue. The preliminary tests will also provide information on the effect that notch size has on remaining life and on how the notch size influences the sensor signal. The material for this task will be PH 13-8 Mo stainless steel.

Fatigue crack detection using array of microsensors

A collaboration with University of Minnesota co-PIs of Section 1.1.

This demonstration project involves attaching an array of microsensors developed and fabricated by the University of Minnesota to Georgia Tech notched fatigue specimens. The material for this project is 4340 steel. Ten tests are planned.

Fatigue crack detection using surface waves

A collaboration with Georgia Tech co-PI Yves Berthelot of Section 2.2.

This demonstration project involves using surface waves to capture the size and growth of a fatigue crack initiated at a 0.5 mm diameter surface flaw. The material for this project is 4340 steel. Six tests are planned.

Other collaborative opportunities

Collaborations have led to some new ideas for using sensors to detect fatigue damage, especially focusing on smaller damage volumes. For example, it seems promising that surface and near surface (within 1 mm below the surface) flaws at Georgia Tech specimen notch roots can be detected using eddy current microsensors developed by *S. Ramalingam* at the University of Minnesota (Section 2.3). These eddy current microsensors may be ideal for detecting flaws as small as 10 μm in size near hot spots, which is considerably smaller than the current state-of-the-art technology.

M-URI PUBLICATIONS

Gardner, Brian, MS Thesis, "An Integrated Visualization Technique for 3-D Components," GWW School of Mechanical Engineering, 1996.

McDowell, D.L. and Bennett, V.P., "A Microcrack Growth Law for Multiaxial Fatigue," *Fat. Fract. Engng. Mater. Struct.*, Vol. 19, No. 7, 1996, pp. 821-837.

McDowell, D.L., "Multiaxial Fatigue Strength," *ASM Handbook on Fatigue and Fracture*, Vol. 19 ASM International, 1996, pp. 263-273.

Saxena, A. and Muhlstein, C., "Fatigue Crack Growth Testing and Applications," Fatigue and Fracture, *ASM Handbook*, Vol. 19, ASM International, Metals Park, Ohio, 1996, pp 168-184.

McDowell, D.L., "Basic Issues in the Mechanics of High Cycle Metal Fatigue," *International Journal of Fracture*, Vol. 80, 1996, pp. 103-145.

McDowell, D.L., "A Model for Multiaxial Small Fatigue Crack Growth," submitted for publication in *Proc. of Engineering Against Fatigue*, 17-21 March, 1997, revised April 1997.

Patel, A.M., "Growth of Small Fatigue Cracks in PH 13-8 Mo Stainless Steel," M.S. Thesis, Georgia Institute of Technology, May 1997.

McDowell, D.L. and Bennett, V., "Micromechanical Aspects of Small Multiaxial Fatigue Cracks," *Proc. 5th Int. Conf. On Biaxial/Multiaxial Fatigue & Fracture*, Cracow, Poland, 8-12 Sept., 1997, pp. 325-348.

McDowell, D.L., "Multiaxial Small Fatigue Crack Growth in Metals," *Int. J. Fatigue*, Vol. 19, No. 1, 1997, pp. S127-S135.

McDowell, D.L., "An Engineering Model for Propagation of Small Cracks in Fatigue," *Engineering Fracture Mechanics*, Vol. 56, No. 3, 1997, pp. 357-377.

McDowell, D.L., Neu, R.W., Qu, J., and Saxena, A., "Prognostic Tools for Small Cracks in Structures," *Emerging Technologies for Machinery Health Monitoring and Prognosis*, TRIB-Vol. 7, R. Cowan, Ed., ASME, 1997, pp. 1-12.

Pape, J.A., "Design and Implementation of an Apparatus to Investigate the Fretting Fatigue of PH 13-8 Mo Stainless Steel," M.S. Thesis, Georgia Institute of Technology, December 1997.

McDowell, D.L., Clayton, J.D. and Bennett, V.P., "Integrated Diagnostic/Prognositic Tools for Small Cracks in Structures," submitted to *J. Mech Eng Sciences*, August 1998.

Yang, F., Saxena, A. and Riester, L., "Use of Nanoindentation Technique for Studying Microstructure Crack Interactions in Fatigue of 4340 Steel," *Metallurgical and Materials Transactions A*, Vol. 29A, 1998, pp 3029-3036.

Hamm, R. W. and Johnson, W. S., "Survey of the State-of-the-Art in Small Crack Research," *Journal of Testing and Evaluation*, Vol. 26, No. 3, March 1998, pp. 168-175.

Hamm, R. W. and Johnson, W. S., "A Unification of Small and Large Crack Growth Laws," submitted April 1998 to the Journal Fatigue and Fracture of Engineering Materials and Structures, accepted.

Yang, Fan and Saxena, A., "Mechanisms of Fatigue Crack Initiation in Annealed and Tempered 4340 Steel," Submitted to a *Special Issue of Journal of Mechanical Engineering Science*, September 1998.

Pape, J.A. and Neu, R.W., "Influence of Contact Configuration in Fretting Fatigue Testing," 12th Int. Conf. on Wear of Materials, Atlanta, GA, April 25-29, 1999, accepted for publication in *Wear*, October 1998.

McDowell, D.L., "Damage Mechanics in Metal Fatigue," submitted for publication in a special volume of *International Journal of Damage Mechanics*, December 1998.

Hamm, R., "A Multi-Regime Model Comparison for Constant Amplitude Small Crack Behavior in Ti-6Al-4V," M.S. Thesis, School of Materials Science and Engineering, Winter 1998.

Bennett, V. and McDowell, D.L. ,"Polycrystal Orientation Effects on Microslip and Mixed Mode Behavior of Microstructurally Small Cracks," in review for publication in ASTM STP 1359, Eds. K.J. Miller and D.L. McDowell, submitted May 1998; revised December 1998; to appear in 1999.

Neu, R.W., Pape, J.A., and Swalla-Michaud, D.R., "Methodologies for Linking Nucleation and Propagation Approaches for Predicting Life under Fretting Fatigue," *Fretting Fatigue: Current Technology and Practices*, ASTM STP 1367, D.W. Hoeppner, V. Chandrasekaran, and C.B. Elliott, Eds., American Society for Testing and Materials, 1999, accepted for publication, March 1999.

Hamm, R. W., Jin, O., and Johnson, W. S., "Small Crack Growth Behavior in Ti-6Al-4V and the Microstructural Influence," submitted April 1999 to the *Journal Fatigue and Fracture of Engineering Materials and Structures*.

Patel, A.M., Neu, R.W., and Pape, J.A., "Growth of Small Fatigue Cracks in PH 13-8 Mo Stainless Steel," *Metallurgical and Materials Transactions A*, Vol. 30A, May 1999.

Swalla-Michaud, D.R., "Fretting Fatigue Damage Prediction using Multi-axial Fatigue Criteria," M.S. Thesis, Georgia Institute of Technology, May 1999.

Yang, Fan, Saxena, A. and Cretegny, L. " Use of Atomic Force Microscopy for Studying Fatigue Crack Initiation," to appear in the *Proceedings of the Seventh International Conference on Fatigue*", Beijing, China, June 8-12, 1999.

3.3 FAILURE PREDICTION METHODOLOGY/FATIGUE RELIABILITY

Co-investigator: Brian Moran (Northwestern University)
Graduate Research Assistant: Ali Zulfiqar
M-URI Year 4 Funding Allocation: 3.6%

DoD NEED

There is a need for the development of computational tools for the simulation of complex aspects of structural reliability as an integral part of engineering life cycle design and, in particular, the design of fatigue critical components in ships, helicopters and rotating machinery.

PROJECT MISSION

To develop robust and accurate computational tools for structural reliability and for the modeling of crack growth in complex three-dimensional components.

TECHNICAL PERSPECTIVE

At the start of this M-URI project in 1995, techniques for evaluation of stress intensity factors along curved cracks in 3D components were inadequate due to cumbersome mesh design requirements. We have remedied this situation by developing domain integral techniques for mixed-mode stress intensity factor evaluation, which work for arbitrary, unstructured meshes. The interaction energy integral formulation of the domain integrals takes account of crack curvature (necessary for accuracy) and is applicable to arbitrarily shaped cracks in 3D. A special integration procedure permits the use of the method for arbitrary meshing, and thus allows for the use of powerful automatic mesh generators in crack growth simulations.

Fatigue reliability calculations based on the first order reliability method are often inaccurate when the curvature of the failure surface is large in the vicinity of the failure surface. We have developed a method, termed the Limit State Surface Element Method, which discretizes the failure surface and eliminates the problems associated with large curvature.

RESEARCH ACCOMPLISHMENTS

Accomplishments have been made in the three areas of (i.) stress intensity factor computation for general curvilinear cracks in complex components, (ii) computer simulation of fatigue life, and (iii) development of the Limit State Surface Element Method for fatigue reliability.

Stress Intensity Factors for General Out-of-Plane Cracks

A differential geometry based formulation for the determination of stress intensity factors along arbitrary out of plane crack in complex components was completed. This methodology uses interaction energy integrals to extract mixed mode stress intensity factors. For 2-D problems and straight edge cracks, implementation of this method is simple. However extra curvature terms arise for curvilinear cracks. And if we ignore these curvature terms then significant errors are obtained in the region of high curvature. To test the accuracy of this method, it was applied to the case of an elliptical crack embedded in a homogenous and isotropic solid. In Fig. 1, numerical results for mode I are compared with the analytical solution. Excellent agreement is obtained (the error is less than 1%). The results are compared with those from the domain representation of the J-integral. It is noted that the interaction energy integral method improves the results for a curvilinear crack front. A similar trend was noticed for a straight edge crack.

The main difficulty in calculating the interaction energy integrals lies in the evaluation of the gradient of the auxiliary fields. We have used differential geometry concepts to develop techniques for calculating gradients and higher gradients for general out of plane cracks. To get accurate results, a smooth representation of the crack front is required and the radius of curvature should be continuous along the crack front. For this purpose, parametric cubic splines are used to define the crack front. A
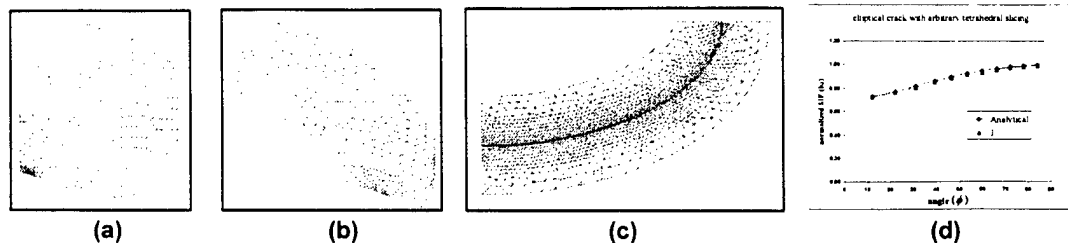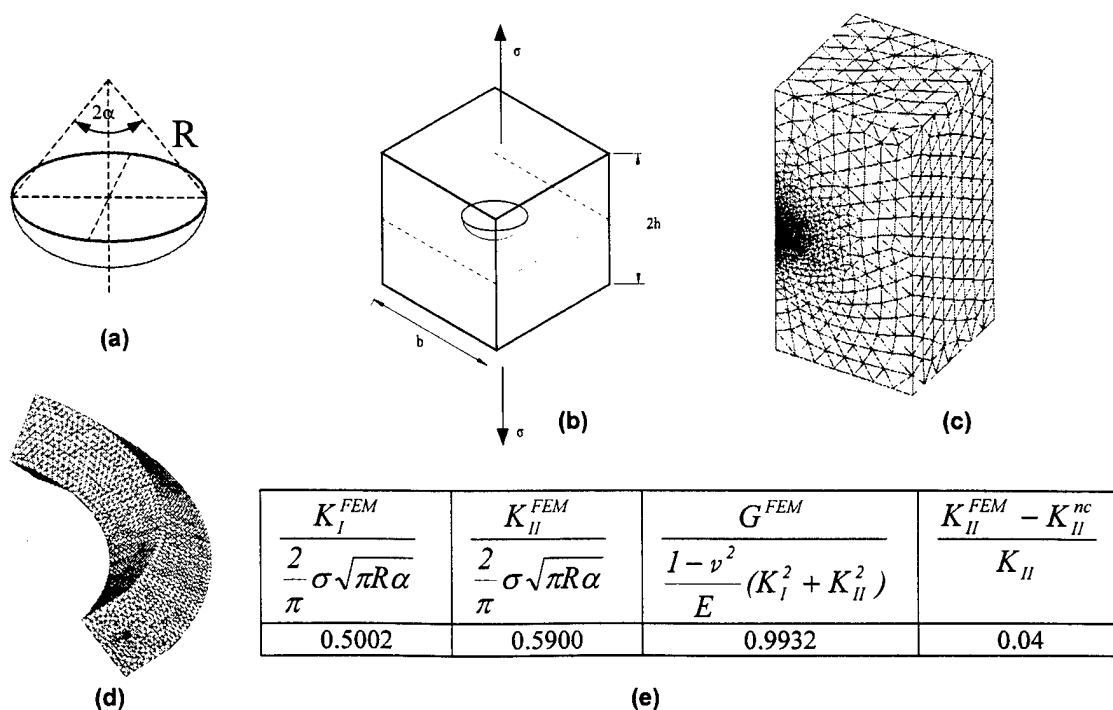
Figure 1. Elliptical Crack **(a)** FE mesh for the body, **(b)** side view of the mesh near the crack tip, **(c)** top view of the FE mesh, and **(d)** comparison of FE and analytical results.

cubic spline has a continuous radius of curvature and it is advantageous since it is the lowest degree curve that allows a point of inflection and has the ability to twist through space. A Newton-Raphson method is also implemented in the code to calculate some of the parameters used in establishing the location of points in the domain with regard to the crack front and normal plane to the crack front.

To test the accuracy and applicability of this method for an out of plane crack, a spherical cap shaped crack subjected to remote tension was modeled as shown in Fig. 2. To our knowledge an analytical solution is not available for the spherical cap shaped problem. However, this problem is actually an axisymmetric version of an arc crack problem in 2-D. Analytical results for an arc crack problem are available in the literature. Mixed mode stress intensity factors for the spherical cap shaped crack were calculated using the domain form of the interaction energy integral method as shown in Fig. 2e. The energy release rate was also calculated for the spherical cap shaped crack. Energy release rate depends upon the combined effect of mixed mode stress intensity factors and it cannot be used to separate them. The combined effect of stress intensity factors from the interaction energy integral method was calculated. The results from both methods are approximately the same. This is an indication that the results obtained from the interaction energy method are accurate.

| $\dfrac{K_I^{FEM}}{\dfrac{2}{\pi}\sigma\sqrt{\pi R\alpha}}$	$\dfrac{K_{II}^{FEM}}{\dfrac{2}{\pi}\sigma\sqrt{\pi R\alpha}}$	$\dfrac{G^{FEM}}{\dfrac{1-v^2}{E}(K_I^2+K_{II}^2)}$	$\dfrac{K_{II}^{FEM}-K_{II}^{nc}}{K_{II}}$
0.5002	0.5900	0.9932	0.04

(e)

Figure 2. **(a)** Cap shaped crack, **(b)** Geometry of the body, **(c)** FE mesh for one-fourth of the body, **(d)** FE mesh around the crack tip, and **(e)** Table showing normalized stress intensity factors.

FAILURE CHARACTERIZATION AND PREDICTION

The benefits of this method are (a) mixed mode stress intensity factor calculation, (b) unstructured meshing, so it can be coupled with any general purpose mesh generator and solver, (c) can be used for both simple and complex components and (d) applicable to all kinds of cracks e.g., in-plane, out of plane and general 3-D curvilinear cracks.

Fatigue Crack Propagation

During fatigue crack propagation in a 3-D component, the crack generally becomes an arbitrary shaped crack due to boundary effects and complex loading. Existing methods approximate the arbitrary crack with an elliptical crack and grow it in such a way that it remains self similar. These existing methods do not take into account boundary effects and consequently the fatigue life calculation may not be accurate. During the past year, we have developed a method that can be used for complex 3-D components with complex loading. This method is easy to use and can be coupled with any general finite element software.

To simulate the real life problem, a sinusoidal crack in a fatigue specimen is modeled. The specimen measures 11mm thick, 10 mm wide and 75 mm long with a reduced gage section of 11 mm thick and 5 mm wide with a radius of 25.4 mm at the gage section as shown in the Fig. 3a. A sinusoidal crack is modeled in the center of the specimen with an inscribing radius of 500 μm as shown in Fig. 3c. Taking advantage of the symmetry, only one eighth of the specimen is modeled as shown in Fig. 3b. The specimen is made of die cast aluminum A356 alloy and it is fatigue cycled at 10 Hz with a maximum stress of 124.8 MPa, which is 60% of the nominal ultimate tensile strength. The specimen is loaded in Mode I and constrained to grow in-plane using Paris Law $da/dn = CK^m$, with $C=4.5 \times 10^{-10}$ and $m=2.17$. The specimen is made of tetrahedral elements and finite element mesh around the crack tip is shown in the Fig. 3d. Simulations of crack growth are underway and will be reported (Zulfiqar and Moran, 1999c).
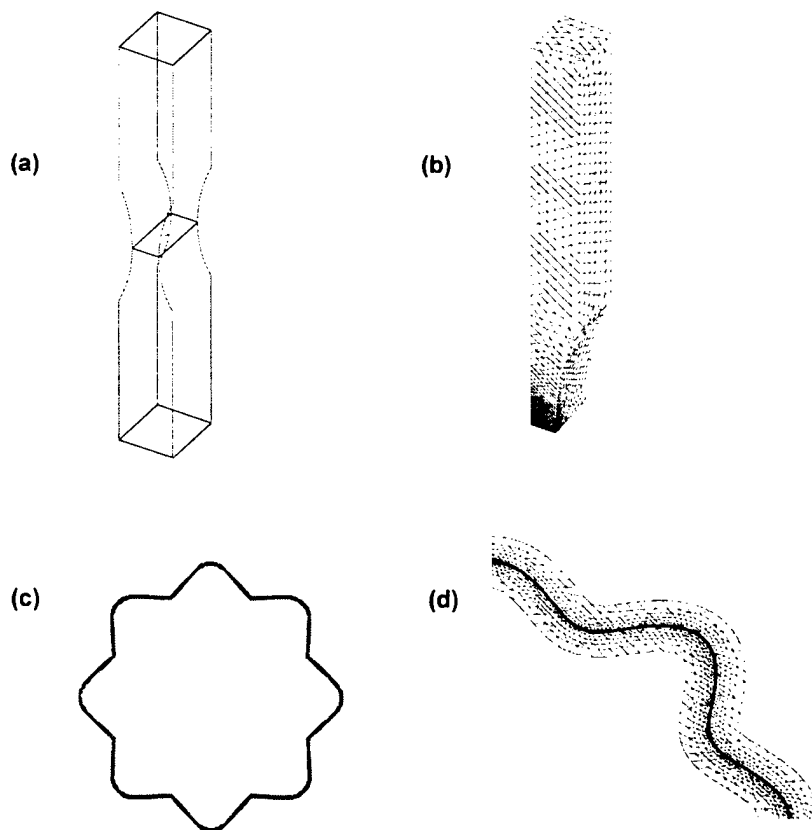
Figure 3. Sinusoidal Crack (a) Fatigue specimen, (b) FE mesh for the body, (c) Top view of the crack front and (d) FE mesh around crack tip.

FAILURE CHARACTERIZATION AND PREDICTION

Methodology for Fatigue Reliability

A new method, termed the Limit State Surface Element (LSSE) method, for problems in structural reliability has been developed. The first order reliability method (FORM) is a popular method for problems in fatigue reliability because the number of realizations or trials of the problem being simulated is vastly reduced over traditional Monte Carlo methods for example. This is especially true for cases where each trial involves computationally intensive simulations in three dimensions such as fatigue crack growth in complex components. A limitation of the method, however, is that it is inaccurate when the curvature of the limit state surface is large and this is often the case in fatigue reliability problems. In contrast, the LSSE method developed in this project, which is based on the discretization of the limit state surface into a number of elements in the vicinity of the most probable failure point, allows for a better representation of the limit state surface in regions of high curvature (Moran and Xu, 1999) leading to more accurate risk assessments (or reliability).

RESEARCH PLANS

The limit state surface element method will be further developed as a robust computational tool for fatigue reliability. The finite element techniques for stress intensity factor determination and fatigue crack growth modeling provide a foundation for computational simulation of crack growth in life-cycle engineering design. These two methods can be combined to develop a framework for probabilistic structural integrity of helicopter and ship components.

M-URI PUBLICATIONS

Achenbach, J., Moran, B., and Zulfiqar, A., 1997, "Techniques and instrumentation for structural diagnostics," in *Proceedings of the International Workshop on Structural Health Monitoring*, Edited by Fu-Kuo Chang, pp.179-190.

Moran, B. and Xu, Y., 1999, "Limit State Surface Element Method for Reliability Analysis," submitted for publication.

Moran, B. and Zulfiqar, A., and Sukumar, N., 1996, "On the Direct Integration Method for Fatigue Reliability Calculations," Technical Report to the Center for Integrated Diagnostics, Georgia Tech, July 1996.

Zulfiqar, A. and Moran, B., 1999a, "Domain Integral Method for Mixed-Mode Stress Intensity Factors for Arbitrary Cracks in 3D," manuscript in preparation.

Zulfiqar, A. and Moran, B., 1999b, "Domain Integral Method for Unstructured Meshes," manuscript in preparation.

Zulfiqar, A. and Moran, B., 1999c, "Finite Element Modeling of Fatigue Crack Propagation in 3D" manuscript in preparation.

3.4 STUDY OF ACOUSTIC EMISSION AND TRANSMISSION FROM INCIPIENT FATIGUE FAILURE

Co-investigators: Laurence Jacobs, Jacek Jarzynski and Scott Bair (Georgia Tech)
Graduate Research Assistants: Zhiqiang Shi, Stephan Hurlebaus and Brad Beadle
M-URI Year 4 Funding Allocation: 5.8%

DoD NEED

(a) Catastrophic failure of an in-service, structural component can be prevented if small cracks can be identified and arrested before they propagate into large cracks. As a result, it is necessary to develop a technique that can accurately detect and characterize any small cracks that may exist in complex, in-service components; such ability is a critical step towards developing a methodology for quantitatively predicting remaining service life.

(b) Successful implementation of the detection technique described in (a) requires the development of ultrasonic sensors (for acoustic emission and transmission) which are capable of improved discrimination against environmental noise and reverberation.

PROJECT MISSION

The goals of this research are to:

(a) develop quantitative, waveform based acoustic emission (AE) techniques that can locate and characterize small cracks in complex engineering components.

(b) develop two new ultrasonic receiving transducer designs: (1) an array of piezoactive ceramic (PZT) elements, and (2) an optical fiber sensor designed to measure tangential (in-plane) surface strains.

TECHNICAL PERSPECTIVE

When this M-URI project was initiated in 1995, there were no studies that monitored acoustic emission (AE) waveforms from a small fatigue crack. Fatigue studies up to this point in time were based on counting the number of acoustic emission signals. There was also no work on AE signals from fretting fatigue; no optical sensors to detect in-plane motion; and no work on arrays to improve signal strength in a noisy environment.

Achievements made during the first three years of this M-URI effort follow:

- Obtained an accurate, reliable and comprehensive set of acoustic emission waveforms due to a) distributed damage in a torsion specimen; b) short cracks originating at a notch; and c) fretting fatigue.

- Developed a repeatable experimental procedure that uses point receivers to accurately monitor and digitize AE signals that occur during fatigue tests.

- Developed an optical technique to construct transfer functions to remove unwanted geometry effects and deconvolve transducer response.

- Applied quantitative, mechanics based techniques such as point source models, ray based wave propagation models and transducer response models to interpret and characterize measured acoustic emission waveforms.

- Developed and successfully tested an optical fiber sensor for acoustic emission and transmission measurements that is designed to measure in-plane surface strains. This sensor provides discrimination against environmental noise, which produces mainly out-of-plane surface vibrations.

- Developed PZT sensors for acoustic emission (AE) and transmission measurements in metal samples undergoing fatigue tests. These sensors are less expensive than commercial sensors and, because of their small size (2x6 mm), they are a better approximation to a point sensor and can be configured as arrays.

RESEARCH ACCOMPLISHMENTS

Acoustic emission tests have been conducted on "hot spot" demonstration fatigue specimens (Section 3.2) using both lab-developed PZT sensors and broadband digital wave sensors. Comparable results were obtained. Three stages of AE activity were identified: (1) severe quasi-noise AE activity in the initial stage of fatigue, 20-35% of the fatigue life; (2) plateaus of AE growth during the middle stage of fatigue, 40-80% of the fatigue life, with waveforms (barely) discernable above the noise levels; and (3) severe AE activity in the final stage of fatigue, 10-20%, with distinctive AE signals that originate from the notch crack (sub-mm range). Figure 1 is a plot of AE activity versus number of fatigue cycles. Figure 2 is a plot of typical AE waveforms that occur during the final stage (10-20%) of fatigue.

Major project achievements that occurred in M-URI year 4 include:

- Developing a system for rejection of noise from authentic AE (this is a post processing procedure) using time of arrival and a cross-correlation function; a time window was calculated for the "hot spot" signal to eliminate a signal originated from out-of-the-region of interest.
- Performing signal analysis of AE waveform (Post Processing). Applied window and filter to enhance the waveform frequency spectrum and identification procedure.
- Adopting detailed testing procedures to ensure accurate and repeatable AE testing. Procedures include: reciprocity check of sensor bonding during the fatigue test; and sensor location to maximize the ability to pickup AE's from the component "hot spot" while reducing noise source triggering.
- Performing sensor calibration of compact PZT sensor, commercial broadband sensor and sensor supplied by the University of Minnesota (Section 1.1). Calibration procedure includes sensitivity and frequency response function.
- Providing acoustic emission waveforms to the Signal Processing group at the University of Minnesota (Section 1.1.4) for analysis.

In addition, a comprehensive study continues in developing a quantitative understanding of the AE signals that emanate from fatigue cracks. Two critical components of this study are: i.) the development of a transfer function that quantifies and removes geometric effects from a measured AE waveform; and ii.) an experimental program that monitors and identifies AE signals that occur during the fatigue of cylindrical stainless steel specimens under torsion. Typical waveforms are collected during torsional fatigue and correlated with fracture mechanisms from different stages of testing. Three stages of (torsional) fatigue are identified by AE waveform characterization and confirmed by microscopic replica observation. Distinct fracture and deformation phenomena are quantitatively linked with their associated acoustic emission signatures. This linkage is only possible with the theoretical source models. Previously developed transfer functions for specimen geometry and receiver response have been combined with this new theoretical source model. Specific acoustic emission waveform characteristics have been quantitatively correlated with the exact fracture and deformation features that caused the waveform.

RESEARCH PLANS

During M-URI year 5, the following research activity will be pursued:

- Specific acoustic emission waveform characteristics will be quantitatively correlated with the exact fracture and deformation features that caused the waveform; this is the next step in developing a prognostic technique. Specific waveform features of interest include (but are not limited to) energy content, rise time, and frequency distribution. These acoustic emission waveforms will be sent to the Signal Processing M-URI group at the University of Minnesota for analysis using recently developed pattern recognition algorithms.
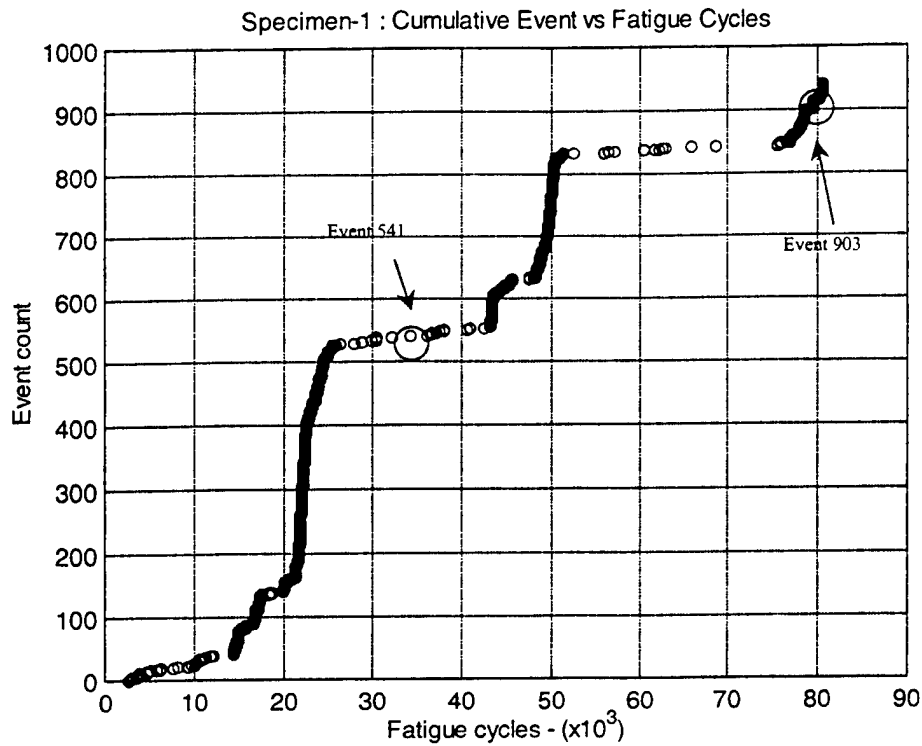
Figure 1. AE activity (Counts) versus Fatigue Cycles (in Thousands of Cycles)
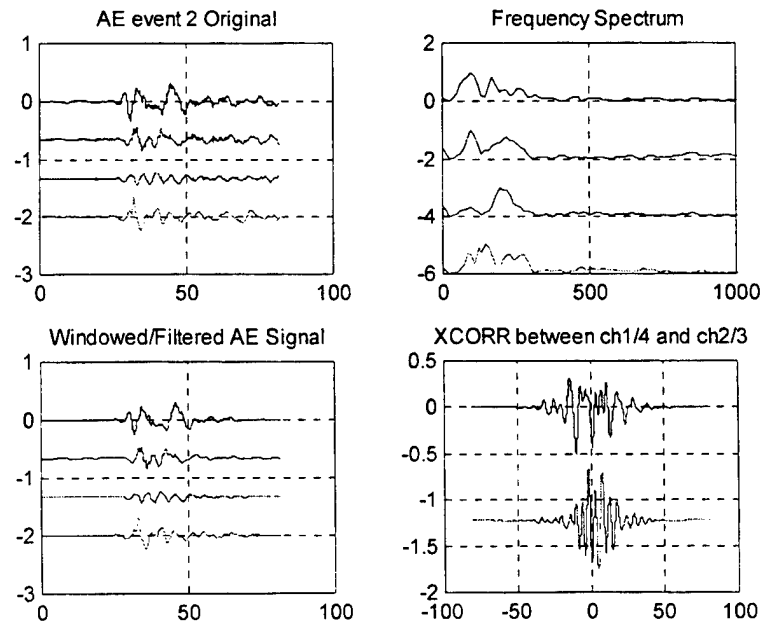
Figure 2. Typical AE Waveforms from Final Stage of Fatigue. Clockwise from top left: Time domain signals measured by four different sensors (amplitude versus time in microseconds); Frequency spectrum of the same signals (amplitude versus frequency in kHz); Cross correlation function of channels 1 and 4 and 2 and 3; and Windowed and filtered time signals to show effect of post processing (amplitude versus time in microseconds).

FAILURE CHARACTERIZATION AND PREDICTION

- A three-dimensional, finite element model of the actual "hot spot" fatigue specimens will continue to be developed. This model will assist in removing geometric wave propagation effects, determining optimum location of sensors, and deconvolve transducer response.

- In-situ acoustic emission measurements will continue to be made for the Structural Fatigue Investigation M-URI project (Section 3.2) and quantitatively link distinct fracture and deformation phenomena with their associated acoustic emission signatures. This work includes determining a probability of detection of function for growth of short cracks (sub-mm and below) and fretting fatigue.

- Fracture phenomena will be examined in more complex structural components as a more realistic test of the robustness of the proposed technique.

- Real-time analysis methods will continue to be developed, including noise discrimination/rejection as a function of source location, and enhanced triggering to enable rejection of noise and extraneous signals.

- Wavelet and neural network techniques will be investigated to enhance signal identification.

- Point, robust, piezoelectric receivers will continue to be manufactured to enable point detection of acoustic emission waveforms, thus facilitating better comparison between experimental and analytical models.

- Development of the new optical fiber sensor will be completed, including development of an analytical model for sensor response and development of a portable configuration that can be used for field tests.

- A four-element PZT array will be tested on a "hot-spot" fatigue sample (Section 3.2). It is hoped that the increase in gain from the array will be used to capture the weak AE waveforms in the middle stage of fatigue (40-80% of the fatigue life).

M-URI PUBLICATIONS

Hurlebaus, S., Jacobs, L.J. and Jarzynski, J., "Laser Techniques to Characterize the Effect of Geometry on Acoustic Emission Signals," *Nondestructive Testing and Evaluation*, Vol. 4, pp. 21-37, 1998.

Shi, Zhiqiang, Jarzynski, J., Bair, S., Hurlebaus, S. and Jacobs, L.J., "Characterization of Acoustic Emission Signals from Fatigue Fracture," *Journal of Mechanical Engineering Sciences,* submitted 1998.

Hurlebaus, S., Jacobs, L.J. and Jarzynski, J., "Optical Techniques to Develop Transfer Functions to Remove Geometric Features in Acoustic Emission Signals," presented at the 23rd *Annual Review of Progress in Quantitative Nondestructive Evaluation*, Brunswick, Maine, July 29-August 3, 1996, Vol. 16A, pp. 421-426, 1997.

Shi, Z., Koutsak, M., Bair, S., Jarzynski, J. and Jacobs, L.J., "Characterization of Acoustic Emission Signals from Fracture Events," presented at the 24th *Annual Review of Progress in Quantitative Nondestructive Evaluation*, San Diego, California, July 28-August 1, 1997, Vol. 17A, pp. 565-570, 1998.

Shi, Z., Bair, S., Jarzynski, J. and Jacobs, L.J., "Study of Acoustic Emission from Incipient Fatigue Failure," presented at the 25th *Annual Review of Progress in Quantitative Nondestructive Evaluation*, Snowbird, Utah, July 19-24, 1998, to appear Vol. 18, 1999.

PRINCIPAL INVESTIGATOR (1)

Ward O. Winer	Georgia Tech	Mechanical Engineering

CO-INVESTIGATORS (25)

Jan D. Achenbach	Northwestern	Quality Engineering
Scott Bair	Georgia Tech	Mechanical Engineering
Yves Berthelot	Georgia Tech	Mechanical Engineering
Richard S. Cowan	Georgia Tech	Mechanical Engineering
Isaac Daniel	Northwestern	Mechanical & Civil Engineering
Steven Danyluk	Georgia Tech	Mechanical Engineering
Lorraine F. Francis	U. of Minnesota	Chemical & Materials Engineering
Itzhak Green	Georgia Tech	Mechanical Engineering
Ramesh Harjani	U. of Minnesota	Electrical Engineering
Laurence Jacobs	Georgia Tech	Civil & Environmental Engineering
Jacek Jarzynski	Georgia Tech	Mechanical Engineering
W. Steven Johnson	Georgia Tech	Materials Science & Engineering
Mostafa Kaveh	U. of Minnesota	Electrical Engineering
Thomas Kurfess	Georgia Tech	Mechanical Engineering
Steven Liang	Georgia Tech	Mechanical Engineering
David L. McDowell	Georgia Tech	Mechanical Engineering
Brian Moran	Northwestern	Civil Engineering
Richard Neu	Georgia Tech	Mechanical Engineering
Dennis Polla	U. of Minnesota	Electrical Engineering
Jianmin Qu	Georgia Tech	Mechanical Engineering
S. Ramalingam	U. of Minnesota	Mechanical Engineering
William P. Robbins	U. of Minnesota	Electrical Engineering
Richard Salant	Georgia Tech	Mechanical Engineering
Ashok Saxena	Georgia Tech	Materials Science & Engineering
Ahmed Tewfik	U. of Minnesota	Electrical Engineering

SUPPORT FACULTY (6)

	Collaborating with:	
Kevin Buckley	Kaveh/Tewfik	U. of Minnesota
William Gerberich	Polla	U. of Minnesota
Rosario A. Gerhardt	Saxena	Georgia Tech
Susan Mantell	Polla	U. of Minnesota
Waymond Scott	Winer	Georgia Tech
George Vachtsevanos	Winer	Georgia Tech

POST-DOCTORAL RESEARCHERS (2)

	Sponsor:	
C. R. Cho	Francis	U. of Minnesota
Yun Woo Nam	Polla	U. of Minnesota

VISITING RESEARCHERS (3)

	Sponsor:	
Dr. Joshua Dayan (2/98-2/99)	Green	Georgia Tech
Alexei Kromine	Achenbach	Northwestern
Dr. Yonglin Xu	Moran	Northwestern

UNDERGRADUATE STUDENTS (6)

	Advisor:	
Dan Cook (6/98-8/98)	Berthelot	Georgia Tech
Tim Edwards (10/97-8/98)	McDowell	Georgia Tech
Mohammed Kamel	McDowell	Georgia Tech
Sam Toas	Neu	Georgia Tech
D. Van Dellan	McDowell	Georgia Tech
Jon Wallace (1/98-9/98)	Neu	Georgia Tech

GRADUATE STUDENTS (40)

	Advisor:	
William Anderson	Salant/Jarzynski	Georgia Tech
P. Andersson	Kaveh/Tewfik	U. of Minnesota
Brad Beadle	Jarzynski	Georgia Tech
Anthony Bell (9/98-12/98)	McDowell	Georgia Tech
Valerie Bennett	McDowell	Georgia Tech
Cody Casey	Green	Georgia Tech
J. Choi	Daniel	Northwestern
J. D. Clayton (3/98-6/98)	McDowell	Georgia Tech
Dan Cook	Berthelot	Georgia Tech
Laurent Cretegny	Saxena	Georgia Tech
David Drinkwater-Lunn	Francis	U. of Minnesota
Christoph Eisenhardt	Jacobs	Georgia Tech
Brian Gardner	Qu	Georgia Tech
Stephan Hurlebaus	Jacobs	Georgia Tech
O. Jim	Johnson	Georgia Tech
Jonghae Kim	Harjani	U. of Minnesota
Markus Kley (6/98-8/98)	Jacobs	Georgia Tech
X. Li	Polla	U. of Minnesota
Yawei Li (3/95-8/98)	Liang	Georgia Tech
Zongbao Li (3/95-8/98)	Berthelot	Georgia Tech
J. -J. Luo	Daniel	Northwestern
Kavita Nair	Harjani	U. of Minnesota
John Pape	Neu	Georgia Tech
Joseph Plummer	Robbins	U. of Minnesota
Xavier Ribadinera	Kurfess	Georgia Tech
Charles Rosen	McDowell	Georgia Tech
Zheng Shi	Ramalingam	U. of Minnesota
Zhiqiang Shi	Jarzynski/Jacobs	Georgia Tech
Haoying Sun	Kaveh/Tewfik	U. of Minnesota
Dana R. Swalla-Michaud	Neu	Georgia Tech
Christine Valle	Jacobs/Qu	Georgia Tech
Gopal Venkatesan	Kaveh/Buckley	U. of Minnesota
Tracy Williams	Kurfess	Georgia Tech
Jianhua Xue (3/95-12/98)	Ramalingam	U. of Minnesota
J. Ye	Polla	U. of Minnesota
Chen Zhang	Liang	Georgia Tech
Danlu Zhang	Kaveh/Tewfik	U. of Minnesota
Long Zhang	Polla	U. of Minnesota
Min Zou (3/95-12/98)	Green	Georgia Tech
Ali Zulfiqar	Moran	Northwestern

Interface Circuitry for Piezoelectric Sensors

Kavita Nair, Jongae Kim, and Ramesh Harjani
University of Minnesota
Minneapolis, MN 55455

Supplement to Section 1.1.5
"Interface Circuits for Piezoelectric Sensors"

Interface Circuitry for Piezoelectric Sensors

ONR M-URI Center for Integrated Diagnostics

Kavita Nair, Jonghae Kim and Ramesh Harjani
University of Minnesota, Institute of Technology
Minneapolis, MN 55455

1   Introduction

Sensors and sensor interfaces allow us to interact with real world signals. Increasingly, sensors are now being integrated using micromachined techniques with integrated circuit components [4]. In this project we describe a CMOS interface circuit for a piezoelectric acoustic emission sensor and the necessary telemetry circuits to provide the signal externally. This sensor is intended to be used to detect acoustic emission that are precursors to catastrophic failures in military equipment [2, 3]. The primary objective is to develop real-time sensing devices and methods to accurately identify conditions leading to the imminent failure of critical aircraft components. The two important technologies brought together for this purpose are microsensors and sensor conditioning electronics. The microsensor used is a thin film acoustic emission (AE) sensor which detects the development of cracks and unusual wear in the body of aircrafts and submarines. The signal conditioning electronics is used to identify and amplify the signal from the acoustic emission microsensor within an electrically and acoustically noisy environment. The other goal of this project is to realize inexpensive and low power silicon chips which can be distributed over critical regions of the aircraft or submarine. To realize this goal it becomes necessary to implement the complete system with a minimum number of external wires and components. We use a two-wire system for both power delivery and telemetry. A block diagram for the complete system is shown in Figure 1.

The microsensor used is a piezoelectric thin film because of its high reliability, superior performance and small area. A piezoelectric sensor acoustically coupled to an aircraft component is shown in Figure 2. The magnitude of the output signal from the microsensor is proportional to the magnitude of the outgoing ultrasonic waves from any acoustic emission event. The design and fabrication of thin film piezoelectric microsensors is not discussed in this report. However, a microphotograph of the integrated acoustic emission sensor to be used with our circuit is shown in Figure 3.

The signal bandwidth of the acoustic emission signals vary from about 50 KHz to about 1 MHz. Mixed in with the desired acoustic emission signal is vibration and fretting noise due to the mechanical parts. However, this noise is limited to about 50 KHz and can be filtered out. We exploit this frequency differentiation to perform telemetry, and supply power to the signal conditioning circuits along the same two wires. Power is supplied to the remote sensor and signal conditioning circuitry via two wires. The amplified sensor signal is carried back along the same two wires that are used to supply the power to the sensor interface. To accomplish this two-way power and data transmission an on-chip filter and power supply are required. The complete systems
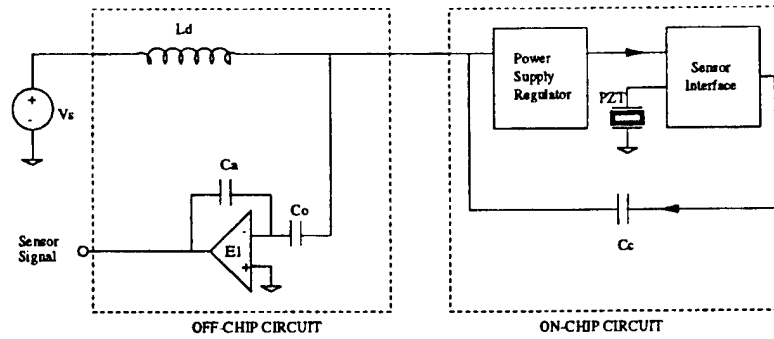
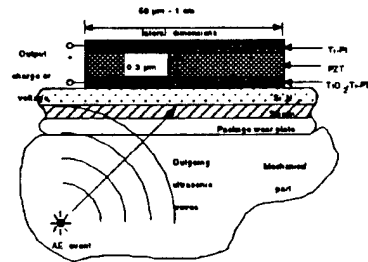Figure 1: Block diagram for the complete system

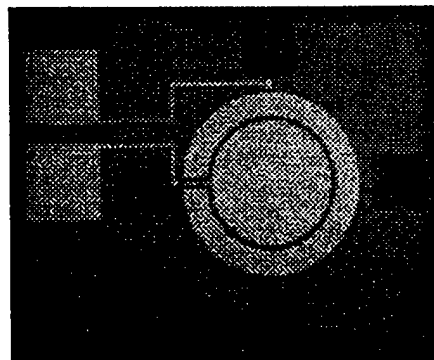Figure 2: Acoustic emission event

Figure 3: Integrated AE sensor

consists of a small discrete external interface and an integrated circuit that consists of an on-chip power supply, a charge amplifier, buffer, voltage amplifier and an integrated piezoelectric sensor.

Signals from the integrated piezoelectric acoustic emission sensor are first amplified via a charge amplifier. Further amplification is accomplished using a voltage amplifier. We use a charge amplifier to interface to the sensor for a number of reasons. First, the charge amplifier is not affected by parasitic capacitances associated with the sensor or at the input of the amplifier. Second, the output voltage of our piezoelectric sensor is very small. This is because of the high dielectric constant of PZT [1], which is the piezoelectric material used. However, we use PZT as our sensor material because of its extremely high piezoelectric constant. A voltage amplifier was designed for some additional gain and a buffer circuit was added between the charge amplifier and the voltage amplifier for impedance matching.

The rest of the report is organized as follows. The design of the telemetry and signal conditioning circuits are discussed in Section 2. Simulation and measurement results confirming the operation of these designs is discussed in Section 3. And finally, we provide some conclusions in Section 4.

2 Circuit Design

In this section we describe the circuit designs for the telemetry and signal conditioning circuitry. In particular we provide detailed designs for the power regulator and telemetry circuitry and the charge and voltage amplifiers. First we discuss the power regulator and telemetry circuits.

2.1 Power regulator and telemetry

The operation of the power regulator and telemetry circuitry is best understood with the help of the simplified circuit shown in Figure 4. Here V_s is the external power supply. L_d and R_d form the external discrete inductor. R_d is the parasitic series resistance of the inductor. R_x is a damping resistor to critically dampen the second order resonant system that is formed. E_1 is an external high-gain low noise amplifier. The amplified sensor signal is capacitively coupled via C_c to the single signal-power line. With the help of the capacitor C_o the external amplifier E_1 provides an AC virtual ground at the common signal-power wire. An AC signal is directly coupled and amplified to generate the external sensor signal. The inductor L_d provides an AC open for the AC sensor signals and provides a DC short to the power being supplied to the chip. The damping resistor R_x is used to avoid oscillations. If the parasitic series resistance is assumed to be small and the damping resistor is assumed to be large then it can be shown that the signal transfer function from RHS of C_c to the output is given by equation 1.

$$\frac{Vo_{ext}}{Vo_{int}} = \frac{s^2 L_d \frac{C_o C_c}{C_a}}{1 + s^2 (C_o + C_c) L_d} \tag{1}$$

$$fo = \frac{1}{2\pi\sqrt{L_d(C_o + C_c)}} \tag{2}$$

If we assume that $C_c \ll C_o$, then for frequencies greater than fo shown in equation 2, the transfer function is given by C_c/C_a, which is just a fixed gain.

The in band noise transfer function of the external amplifier is given by equation 3 in out signal band. For typical component the noise of the external amplifier is amplified, thereby mandating an extremely low noise amplifier. It is possible to meet the design specification of approximately 60dB SNR with an appropriate choice of amplifier.
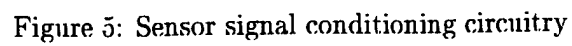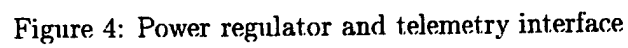
$$Hn(s) = \frac{C_o}{C_a L_d s} \tag{3}$$

An AC variation in the power consumption cannot be distinguished from the signal. Therefore, it is necessary to maintain as constant a power consumption for the signal conditioning circuitry as possible. To this end as shown later, all the designs for the amplifiers use constant current topologies, i.e., class A.

2.2 Signal conditioning circuitry

Next, we consider the circuits used to amplify the sensor signals [5, 6]. A simplified circuit diagram for the signal conditioning circuit is shown in Figure 5. The inverting terminal of the operational amplifier is at virtual ground and therefore any charge that is generated across the sensor flows into the feedback capacitor C_f. The voltage gain of the circuit is given by the ratio of C_s, where C_s is the sensor capacitance, over C_f. Hence to obtain high gain, C_f must be made much smaller than C_s. This basic topology has a number of limitations including low frequency flicker noise of the amplifier, operational amplifier offset and long term drift. Traditionally, correlated double sampling and chopper stabilization are used to remove low frequency noise and offset. However, our signal band does not include the frequencies from DC to 50KHz. Additionally we do not have a clock signal available to us which is necessary for both correlated double sampling and chopper stabilization. Hence a resistor, R_f, connected across the feedback capacitor is used as a low frequency feedback path to reduce the effect of low frequency noise and offset. The transfer function of the charge amplifier circuit is now given by equation 4.

$$\frac{V_o}{V_{in}} = -\frac{R_f C_s s}{1 + R_f C_f s} \tag{4}$$

In our design the gain of the charge amplifier is selected to be 20dB for a number of reasons, therefore we include a voltage amplifier for additional gain. The voltage amplifier circuit has a gain of 10 which is obtained by using resistor ratios. The same amplifier is also used as a buffer between

Figure 4: Power regulator and telemetry interface

Figure 5: Sensor signal conditioning circuitry

the charge and the voltage amplifier for impedance matching. In the next paragraph we introduce a novel shielded-base BiCMOS operational amplifier for the charge amplifier stage.

2.3 Shielded-base opamp design

The simple transistor level circuit diagram for the shielded-base opamp is shown in Figure 6. The transconductance for bipolar transistors is proportional to the current while the transconductance for MOS devices is proportional to the square root of current. Therefore, as is shown below, the power savings from using a bipolar input differential pair can be substantial. However, in our charge amplifier application it is necessary to maintain zero input current. Therefore, we use MOS devices (M1 and M2) to shield the base of the bipolar transistors (B1 and B2). The bipolar transistors provide the transconductance while the MOS transistors, used as source followers, provide infinite input impedance. The complete charge amplifier circuit with bias and common mode feedback circuitry is shown in Figure 7.

Next, we compare our design with traditional designs in terms of power and noise. Let us first consider power. We compare our design with a traditional MOS only input pair. For MOS transistors operated in strong inversion the minimum power requirements is given by equation 5.

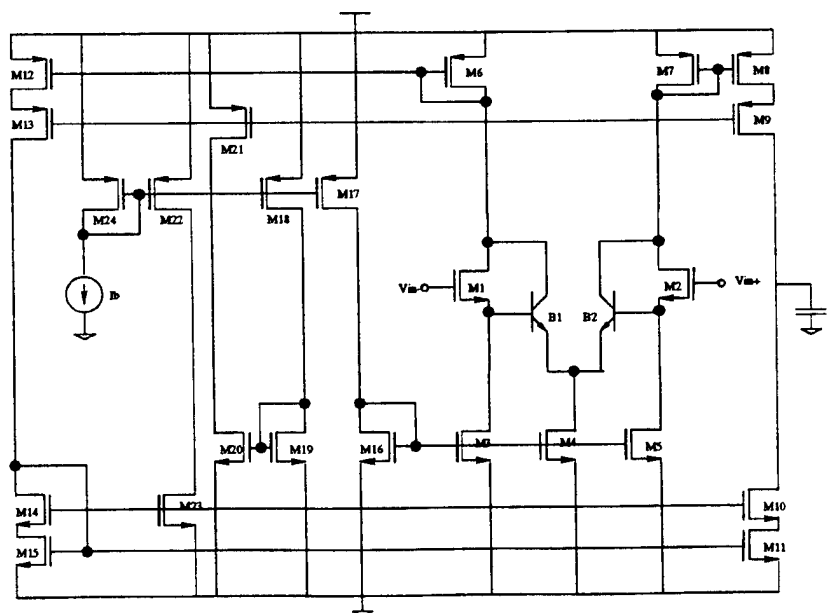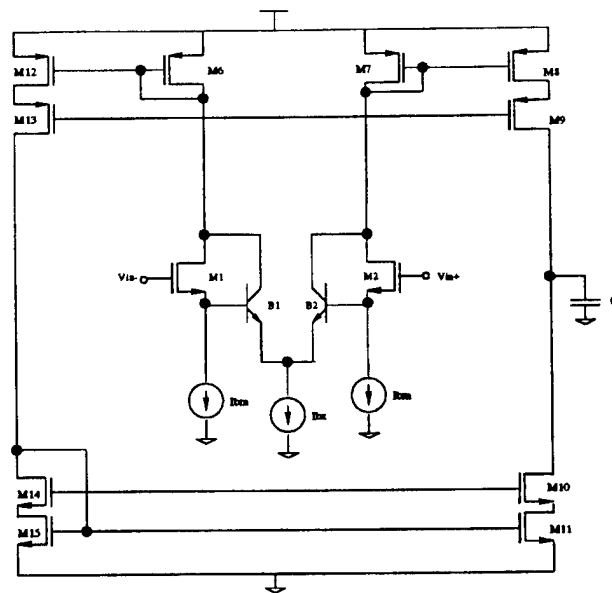$$P = V I = \frac{V (2 \pi \, BW \, C)^2}{2 \, kn \, \frac{W}{L}} \tag{5}$$

where, BW is the bandwidth, C is the sensor capacitance, kn is the transconductance factor and W/L is the aspect ratio of the transistor. On the other hand, the minimum power requirement for bipolar transistors is given by equation 6.

$$P = V I = V \, 2 \pi \, BW \, U_T \, C \tag{6}$$

Here, U_T is the thermal voltage which is equal to 26mV at room temperature. From equations 5 and 6 it is clear that in MOS transistors the power is proportional to the square of the bandwidth and the sensor capacitance, whereas in bipolar transistors, the power is linearly proportional to both bandwidth and sensor capacitance. This difference in power consumption vs. sensor capacitance between bipolar and MOS implementations for a signal frequency of 1MHz is shown in Figure 8. From Figure 8 we see that MOS transistors behave similar to bipolar transistors in weak inversion but consume significantly more power in strong inversion for the same performance.

Next, let us consider the design tradeoffs in connection with device noise. The power spectral density for the wide band gate referred noise voltage for MOS transistors is given by equation 7, where K is the Boltzmann's constant and T is the temperature.

$$V_{nT}^2 = \frac{8 \, K \, T \, gm}{3 \, gm \, C} = \frac{8 \, K \, T}{3 \, C} \tag{7}$$

Figure 6: Shielded-base charge amplifier circuit

Figure 7: Complete charge amplifier circuit

Likewise, for bipolar transistors the input referred power spectral density is given by equation 8.

$$V_{nT}^2 = \frac{2\,q\,U_T}{C} = \frac{2\,K\,T}{C} \tag{8}$$

For both MOS and bipolar implementations, the input referred noise is independent of frequency and inversely proportional to the sensor capacitance. Further, it can be shown that for the same signal bandwidth and sensor capacitance the ratio of the power spectral density of a MOS only design in comparison with our MOS-bipolar design is given by equation 9

$$\frac{Vn_{MOS}^2}{Vn_{MOS-bipolar}^2} = \frac{1}{\frac{3}{4} + \frac{gm_{bipolar}}{gm_{MOS}}} \tag{9}$$

It is clear from equation 9 that the transconductance of the MOS devices (M1 and M2) should not be made significantly smaller than the transconductances of the bipolar transistors (B1 and B2). We select a transconductance ratio of 10, i.e., the MOS transconductances are 10X smaller which results in a 10dB loss in SNR. However, the current ratios are 1 is to 4, i.e., MOS power is one fourth the bipolar power. This still results in a 10X savings in power. We are able to exploit the particulars of our design requirements for this new design. For our design, the sensor capacitance is 100pF due to other processing constraints and the bandwidth is 1MHz. Our SNR requirement of 60dB results in a minimum capacitor size of about 4.45pF. Clearly, this is much larger than is required from a noise perspective. We are therefore, able to tradeoff slightly increased noise for lower power with our new circuit.

The total power dissipation for the new opamp is about 900uW. A feedback capacitor of 10pF is used in the charge amplifier and this gives a gain of 20dB. The feedback resistor used is a 6Meg well resistor. There are a couple of problems with well resistors. Well resistors normally can vary by almost 30%. Secondly, the well-substrate junction has to be strongly reverse biased for it to operate as a resistor. However, both these factors are not critical in our application.

2.4 Amplifiers for the sensor condition circuit

As mentioned in the power regulator subsection, an AC variation in the power consumption cannot be distinguished from the signal. Therefore, it is necessary to maintain as constant a power consumption for the signal conditioning circuitry as possible. Hence, all the designs for the amplifiers use constant current topologies, i.e., class A. The operational amplifier used is the same in all three circuits namely, regulator, buffer and voltage amoplifier. The amplifier design is a simple two stage Miller compensated OTA design with a compensation capacitor of 5pF and total power compensation of about 100uW. The transistor level circuit for the operational amplifier is shown in Figure 9.

The complete voltage regulator circuit is shown in Figure 10. This transistor level circuit includes the operational amplifier, the single MOS transistor which separates the unregulated input signal
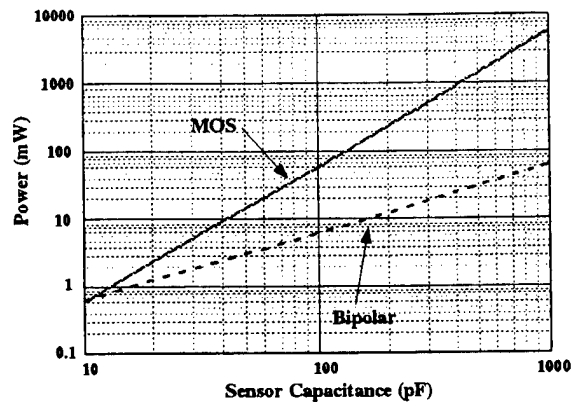
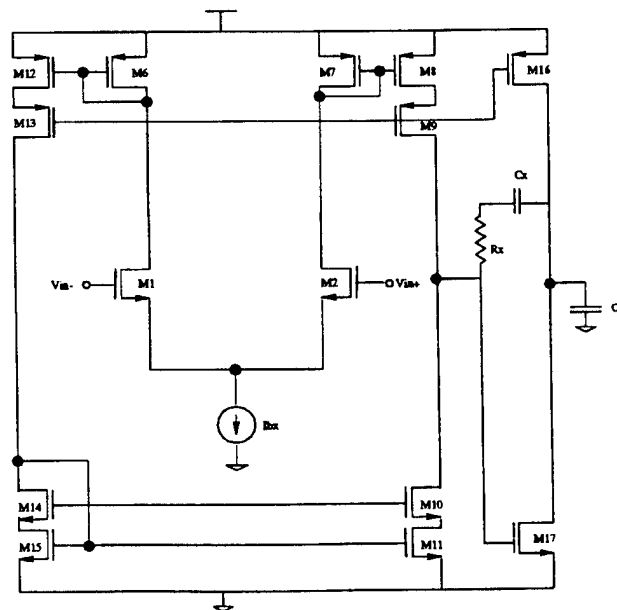Figure 8: Power comparison for MOS and bipolar diff pairs

Figure 9: Opamp for regulator, buffer and voltage amplifier

form the regulated output signal and resistors $R1$ and $R2$.

2.5   Voltage reference and current sources

A bandgap voltage reference is used to provide the reference voltage for the regulator. The voltage reference used is a bandgap voltage reference. The opertion of a bandgap reference is based on subtracting the voltage of a forward-biased diode having a negative temperature coefficient from a voltage proportional to absolute temperature(PTAT). The PTAT voltage is rtealized by amplifying the voltage difference of two forward biased base-emitter junctions.A bandgap reference voltage system is shown symbolically in Figure 11. From Figure 11 the equation for Vref can be written as shown in equation 10.

$$V_{ref} = V_{BE2} + K \, \delta \, V_{BE} \qquad (10)$$

The transistor level circuit diagram of the bandgap reference used is shown in Figure 12. The leftmost part of the circuit is the startup circuitry. A current mirror loop maintains a constant current through bipolar transistors $B1$ and $B2$. Resistor Rx converts this voltage into current which flows through transistors $M12$ and $M13$ and gives a reference voltage. Resistor Ry and bipolar transistor $B3$ provide the necessary gain. Extending this circuit, current mirrors are used to provide internal bias currents to the regulator, charge amplifier, buffer and voltage amplifier.

2.6   Control switches

Control switches are used to switch between the internal and external bias currents for the charge amplifier, regulator, buffer and voltage amplifier. The internal bias currents are supplied from the current sources in the voltage reference circuit. The external current is supplied through resistors. The control switch is made up of two T-gates and an invertor as shown in Figure 13. An external control pin cobtrols the switching between the two options.

3   Results

In this section we present some results to confirm our design and analysis. For this design the bandwidth is 1MHz and the sensor capacitance is 100pF. The external amplifier used for simulation is a high gain, low noise amplifier used in the simple inverting amplifier configuration with an input capacitor of 30uF (we use a polarized tantalum capacitor for this design) and a feedback capacitor of 25pF (similar to the decoupling capacitor). A feedback resistance of about 6Meg is connected across the feedback capacitor to compensate for opamp offsets.
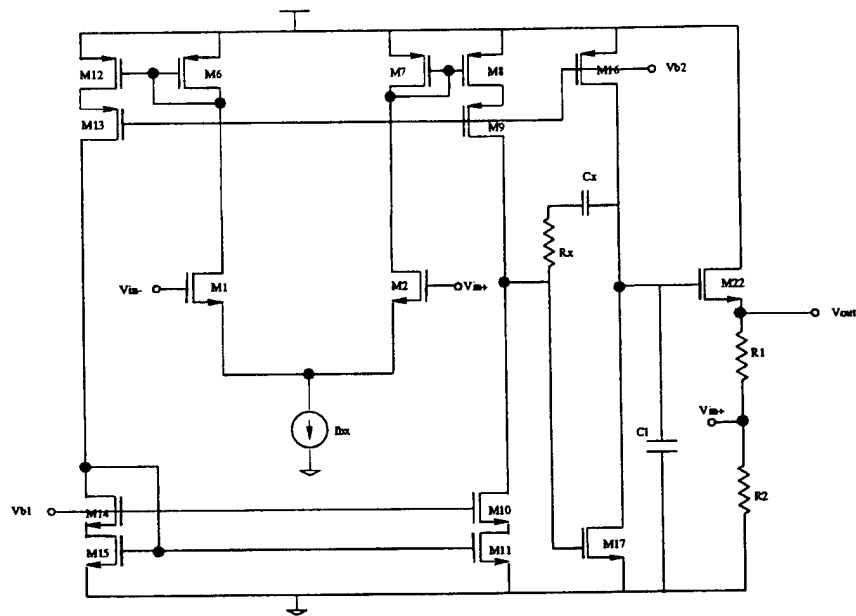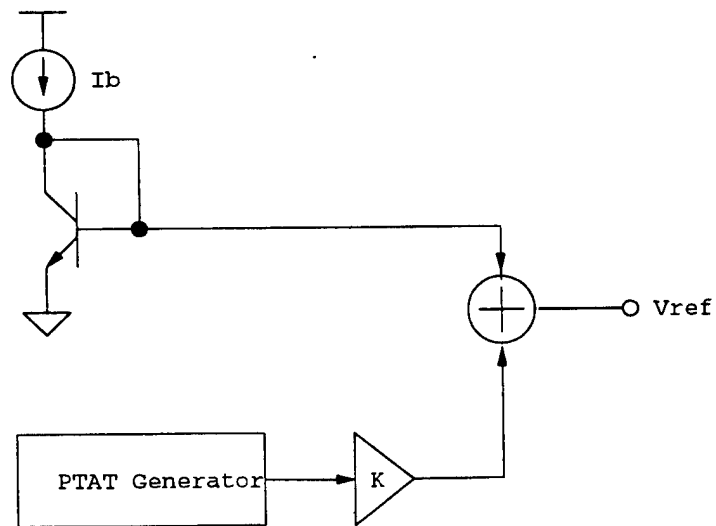
Figure 10: Voltage regulator circuit

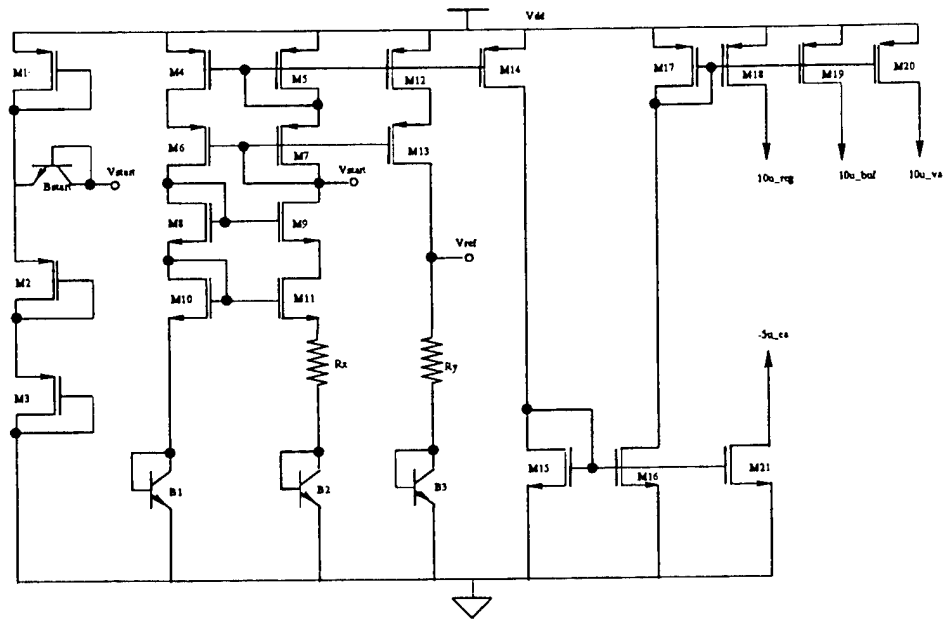Figure 11: Simplified circuit of a bandgap reference circuit
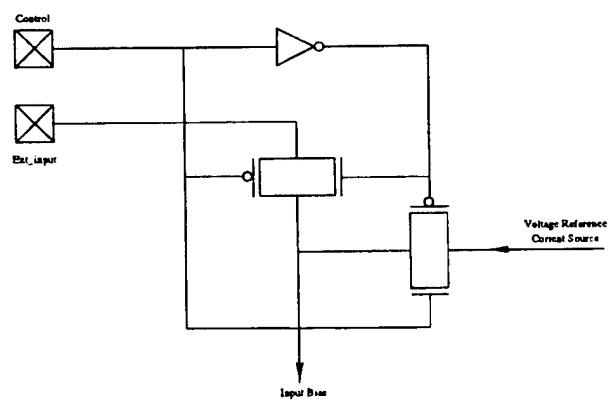
Figure 12: Voltage reference and current sources

Figure 13: Control switch

3.1 Simulation results

The first simulation result (Figure 14) shows the AC response of the system. This graph shows two plots namely, the output of the amplifier before the decoupling capacitor and the external amplifier output both in decibels. A gain of 40dB is seen because of the two gain stages, namely the charge amplifier and the voltage amplifier each providing a gain of 10. We also note the near unity gain transfer function between the output of the voltage amplifier and the external output for inband signals.

The second simulation result (Figure 15) shows the transient response of the system. The plot on top shows the voltage regulator output. As expected, the voltage is steady at 5V, with less than a 1mV ripple. The plot in the middle shows the transient output of the sensed and amplified signal from the output of the voltage amplifier. As seen this has a peak-to-peak voltage of about 1V. The last plot is the final output from the external amplifier. As expected, this signal has a peak-to-peak voltage of 1V and a phase shift of 180 degrees from the amplified sensor signal. This change in phase it due to the inverting nature of the external amplifier.

3.2 Measurement results

The first measurement result (Figure 16)shows a snapshot of the results from the regulator as seen on a Tektronic TDS 540 digitizing oscilloscope. The input is around 8V and the regulated output is at 5.24V. The noise on the regulated output is small and within limits.

The next result (Figure 17) shows the measured AC response of the charge amplifier circuit. The voltage gain is 10 for a sensor capacitance of 100pF and a feedback capacitance of 10pF. Some more measurement results from the charge amplifier circuit are shown next. The charge amplifier input and output signals are shown in (Figure 18). This figure shown the input signal magnitude of 200mV and the output signal magnitude of 2V. This means that the charge amplifier has a gain of 10V as expected. Figure 19 shows the FFT response of the charge amplifier output signal. Figure 20 shows the meaured input and output signal amplitudes for the charge amplifier. As expected the input/output curve is linear for some time and there plateaus off beyond a certain voltage.

Figure 21 shows the measured input and output signal amplitudes for the buffer circuit. As expected, the input and output signal amplitudes are the same(100mV). Finally, Figure 22 shows the voltage amplifier input and output signal amplitudes. The expected gain is 10 doe a resistor ratio of 10 : 1 but the measured output signal only shows a gain if 7. This is due to the n-well resistor variation.

The following measurement result (Figure 23) shows the variation of the measured n-well resistor value from its expected value. This figure shows the ideal and measured voltage for a midpoint between two equal resistors. The supply voltage is varied from 3V to 7V.

Finally, the layout for the complete system is shown in Figure 24. As can be seen from the
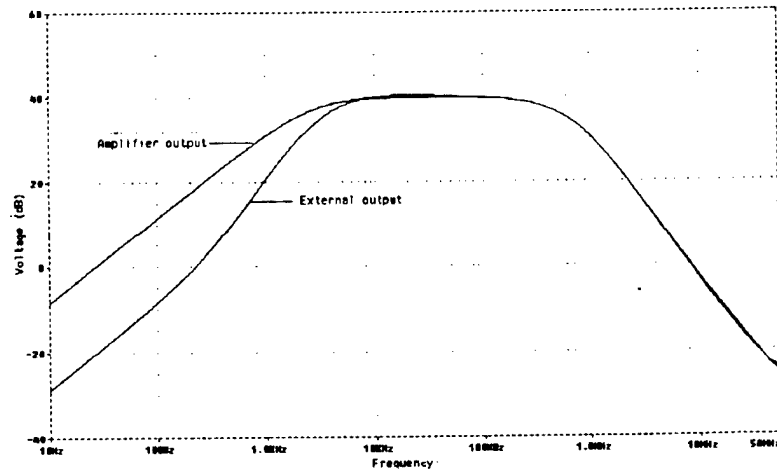
Figure 14: AC response of the system
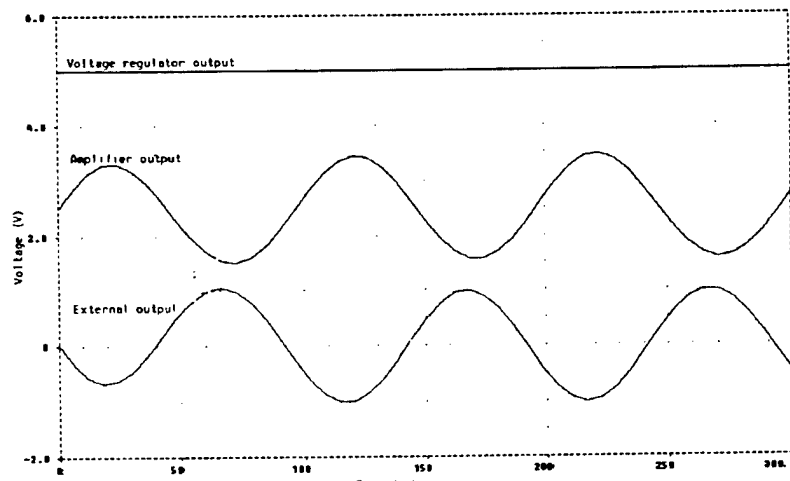
Figure 15: External transient output for a 10mV sensor signal
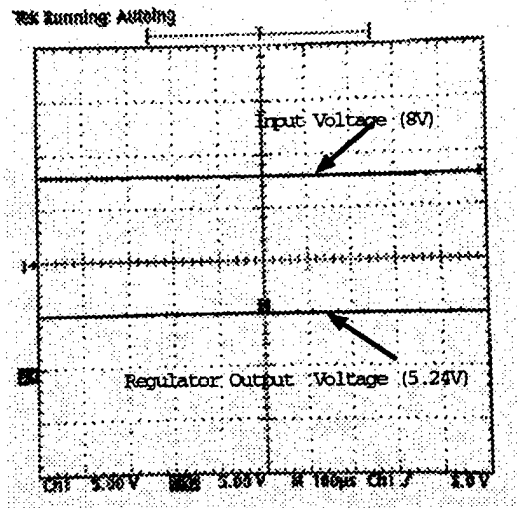
Figure 16: Snapshot showing input and output signals of the regulator
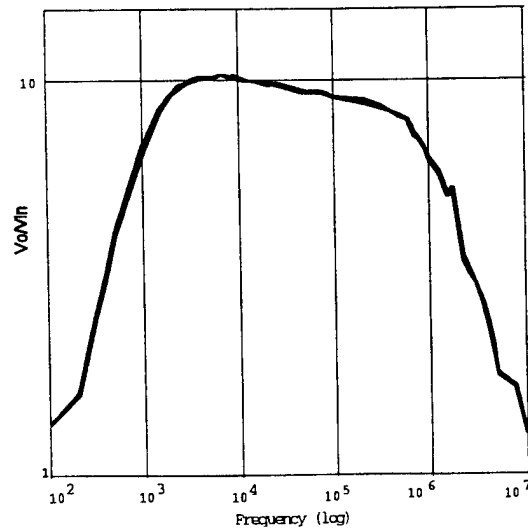
Figure 17: Measured AC response of the charge amplifier
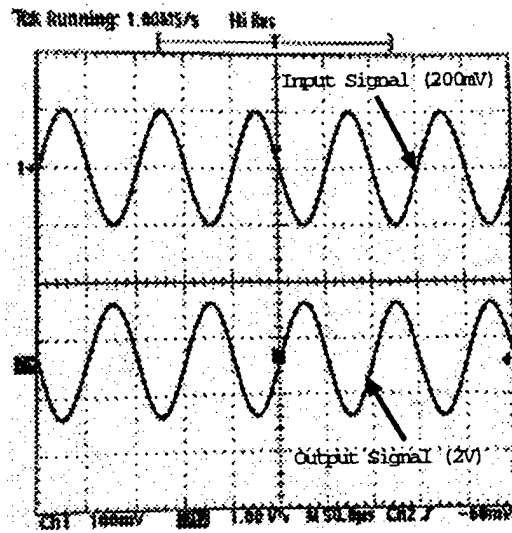
Figure 18: Snapshot showing charge amplifier input and output signals
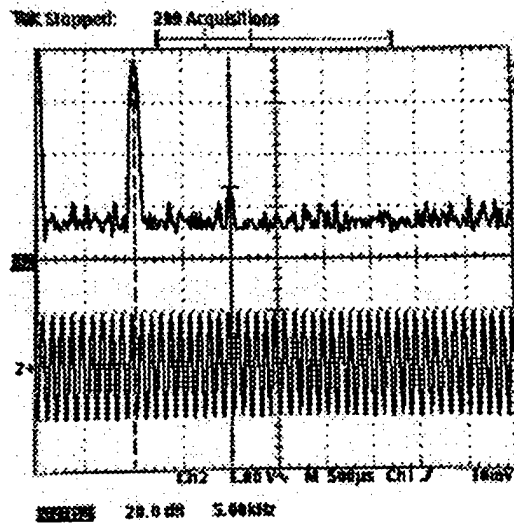
Figure 19: Snapshot showing FFT of the chare amplifier output
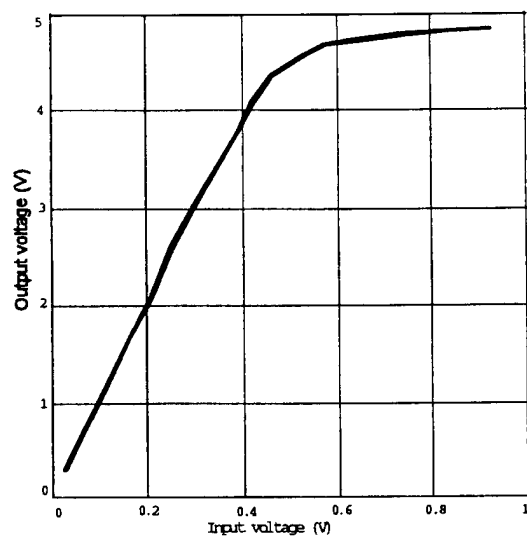
Figure 20: Measured input/output signal amplitudes for the charge amplifier
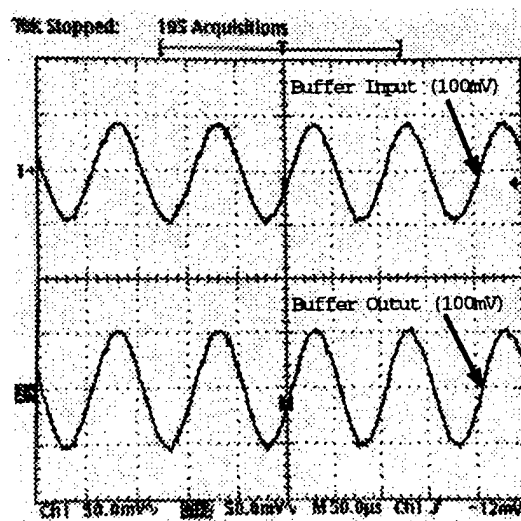
Figure 21: Snapshot showing buffer input and output signals

B-19
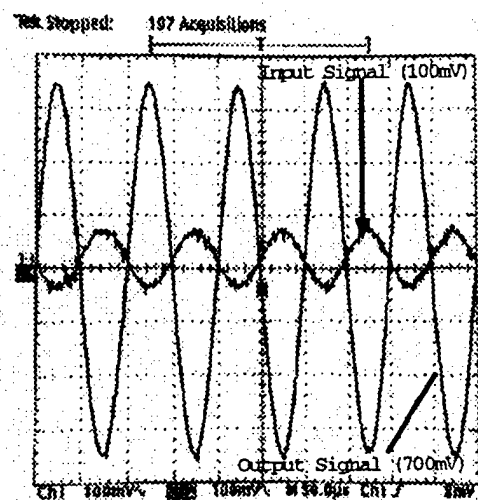
Figure 22: Snapshot showing voltage amplifier input and output signals
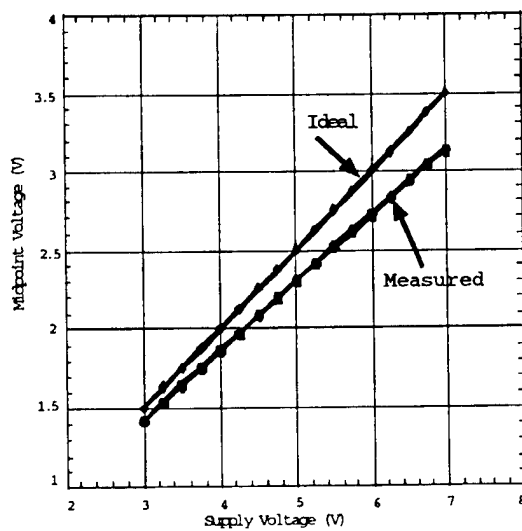
Figure 23: N-well resistor caliration
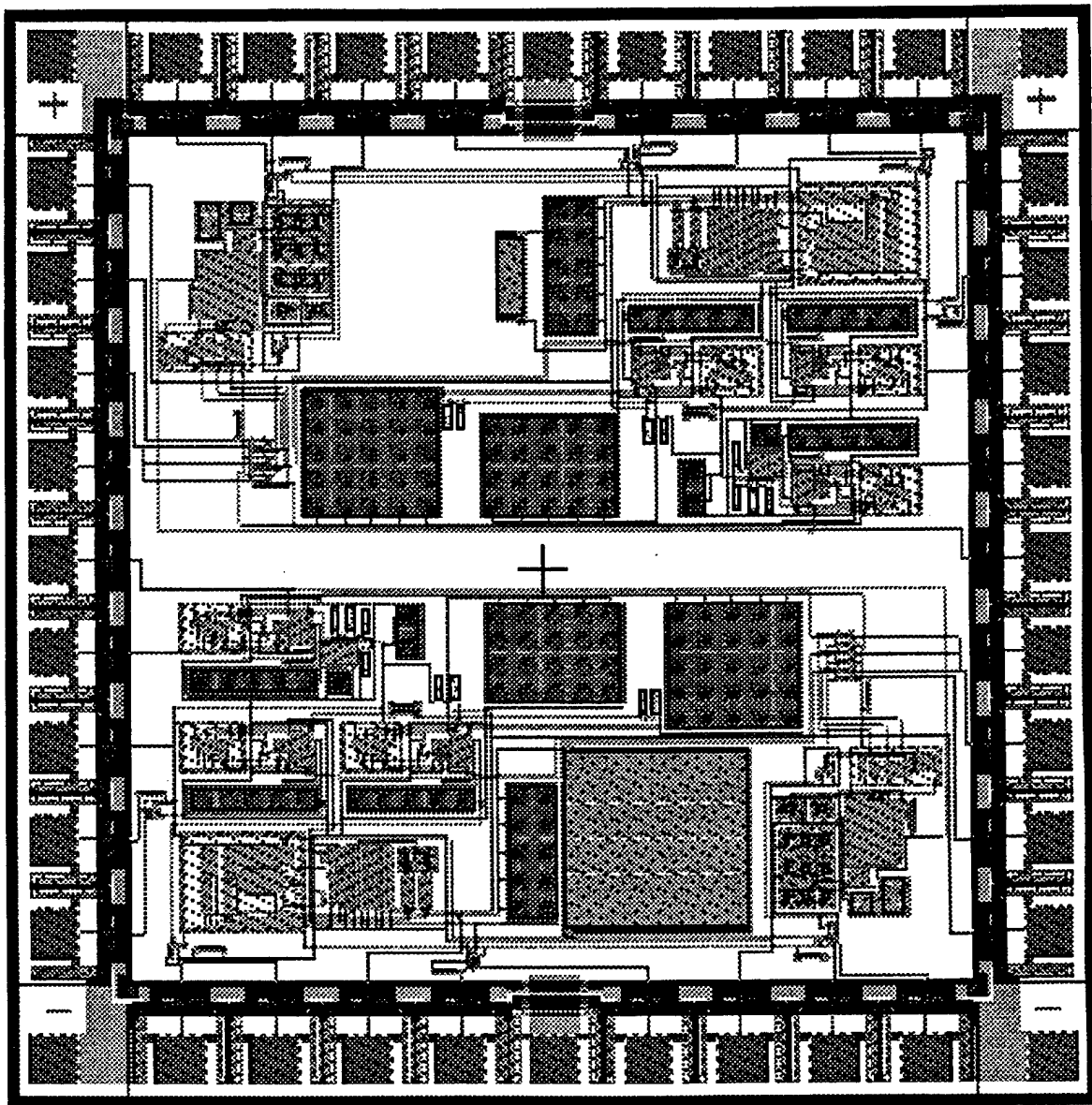
Figure 24: Layout for telemetry and signal conditioning circuitry

layout, most of the area in the chip is occupied by the well resistors and the capacitance. The complete design was fabricated by MOSIS in the AMI 1.2u CMOS process with bipolar option.

4 Conclusions

In this project report we present the design, implementation and fabrication results for a two-wire telemetry and signal conditioning circuit for piezoelectric sensors. The telemetry system uses a on-chip voltage regulator as part of the signal-vs-supply filter. We also introduced a new shielded-base bipolar opamp design that exploits the properties of both MOS and bipolar transistors. The new design results in 10X reduction in power for a 10dB reduction in signal-to-noise ratio. All simulation and measurement results are presented which closely match each other. Two chips were fabricated by MOSIS in the AMI 1.2u process with bipolar option.

References

[1] H. S. Kim, J. H. Kim , S. Zurn and D. L. Polla, "Electrical and Mechanical Properties of PZT(54/46) Thin Films for Silicon Micromachined Devices", *IEEE International Symposium on Application Ferroelectrics*, Piscataway, N.J. 1996.

[2] D. F. Bahr and W. W. Gerberich, "Relationships Between Acoustic Emission Signals and Physical Phenomema During Indentation", *Journal of Materials Research*, Vol. 13, No. 4, pp 1065-74, April 1998.

[3] G. T. Venkatesan, D. West, K. M. Buckley, A. H. Tewfik, M. Kaveh, "Automatic Fault Monitoring using Acoustic Emission" , Proc. ICASSP, 1997.

[4] K. Najafi, K. D. Wise and N. Najafi, "Integrated Sensors", *Semiconductor Sensors*, Edited by S. M. Sze, 1994.

[5] Donald C. Thelen, Jr. and Dahlon D. Chu, "A Low Noise Readout Detector Circuit for Nanoampere Sensor Applications", *IEEE Journal of Solid-State Circuits*, Vol. 32, No. 3, March 1997.

[6] P. Wouters, M. De Cooman and R. Puers, "A Multi-Purpose CMOS Sensor Interface for Low-Power Applications", *IEEE Journal of Solid-State Circuits*, Vol. 29, No. 3, August 1994.

Prognostic Tools for Condition-Based Maintenance

D. L. McDowell, R. W. Neu, J. Qu, A. Saxena and W. S. Johnson
Georgia Institute of Technology
Atlanta, GA 30332

Supplement to Section 3.2
"Structural Fatigue Investigation"

PROGNOSTIC TOOLS FOR CONDITION BASED MAINTENANCE

**Years 1-4 Progress Report of Task Group B-4 on Structural Fatigue
ONR M-URI on Integrated Diagnostics**

D.L. McDowell, R.W. Neu and J. Qu
GWW School of Mechanical Engineering

A. Saxena and W.S. Johnson
School of Materials Science and Engineering

MultiUniversity Center for Integrated Diagnostics
Georgia Institute of Technology
Atlanta, Georgia 30332-0405

EXECUTIVE SUMMARY

An integrated system for diagnosis of the "health" of a structural component subjected to high cycle fatigue (HCF) consists of sets of embedded or emplaced sensors at various locations, extracting information related to generation of material defects, presence of crack-like discontinuities and their progression, and changes of system dynamics which may relate to this progression. Conceptually, signals from these sensors are fed into a processing environment that can ascertain deleterious conditions related to the onset of loss of function or propagation of cracks to critical dimensions. Since the idea is to monitor the gradual changes of component performance and various local related indices <u>before</u> catastrophic failure to enable the operator to respond with a maintenance hold, it is essential to couple the diagnostics with prognostic capability; this facilitates a prediction of how much time remains within the window of viable servicing or repair. In the HCF regime, the dominant fraction of total fatigue life may be spent at crack lengths on the order of 20 to 500 μm. The detection of longer cracks near the end of component life is critical since component failure may lead to failure of the overall structure. This necessitates the identification of (i) finite-element algorithms for identifying component "hot spots" where failure is likely to occur, (ii) development of appropriate crack growth laws for cracks of different length scales, ranging from on the order of grain size to on the order of component dimensions, including consideration of contacting components (fretting fatigue) and environmental effects, and (iii) development of algorithms for identifying the progression of component degradation based on multiple sensor inputs at different time and length scales, providing feedback to support cause for maintenance shutdown. This report discusses accomplishments and work underway in the Structural Fatigue Task B.4 within the ONR MURI on Integrated Diagnostics at Georgia Tech.

SUMMARY OF ADVANCES IN PROGNOSTICS
Structural Fatigue Task B-4 at Georgia Tech

Innovations in CBM Technology

♦ Developed a finite-element based methodology for rapid identification of hot spot locations in components and verified for H-46 rotor hub by comparing to field data for failure locations

Brian Gardner, MS Thesis, "An Integrated Visualization Technique for 3-D Components," GWW School of Mechanical Engineering, 1996.

♦ Interfaced with GT acoustic emission team to instrument laboratory specimens in smooth specimen and fretting fatigue to demonstrate capabilities of sensor arrays to monitor stages of fatigue damage evolution in smooth specimen fatigue and fretting fatigue

---

♦ Performed critical assessment of near real time algorithms/methodologies for remaining life estimation, and proposed most potentially fruitful algorithms

McDowell, D.L, Winer, W.O. and Cowan, R.S., "Developing an Integrated Diagnostic System," ASME IMECE Symp. On Quantitative Nondestructive Evaluation in Integrated Diagnostics, Dallas, TX, November 17, 1997.

McDowell, D.L., Clayton, J.D. and Bennett, V.P., "Integrated Diagnostic/Prognositic Tools for Small Cracks in Structures," submitted to J. Mech Eng Sciences, August 1998.

McDowell, D.L., Neu, R.W., Qu, J., and Saxena, A., "Prognostic Tools for Small Cracks in Structures," Emerging Technologies for Machinery Health Monitoring and Prognosis, TRIB-Vol. 7, R. Cowan, Ed., ASME, 1997, pp. 1-12.

♦ Developed robust multi-stage fatigue model for propagation of small cracks spanning the LCF and HCF regimes for remaining life estimates

McDowell, D.L. and Bennett, V.P., "A Microcrack Growth Law for Multiaxial Fatigue," Fat. Fract. Engng. Mater. Struct., Vol. 19, No. 7, 1996, pp. 821-837.

McDowell, D.L., "Mechanics of Small Fatigue Crack Growth in Metals," 1st Int. Conf. on Fatigue Damage in Structural Materials, Hyannis, MA, Sept. 22-27, 1996.

McDowell, D.L., "Multiaxial Small Fatigue Crack Growth in Metals," Int. J. Fatigue, Vol. 19, No. 1, 1997, pp. S127-S135.

McDowell, D.L., "An Engineering Model for Propagation of Small Cracks in Fatigue," Engineering Fracture Mechanics, Vol. 56, No. 3, 1997, pp. 357-377.

McDowell, D.L., "A Model for Multiaxial Small Fatigue Crack Growth," submitted to Proc. of Engineering Against Fatigue, 17-21 March, 1997, revised April 1997.

Basic Scientific Advances of Task B.4 that Support Prognostics

♦ Clarified mechanics challenges and essential developments for next generation fatigue crack growth models for small cracks

McDowell, D.L., "Multiaxial Fatigue Strength," ASM Handbook, Vol. 19 on Fatigue and Fracture, ASM International, 1996, pp. 263-273.

McDowell, D.L., "Basic Issues in the Mechanics of High Cycle Metal Fatigue," International Journal of Fracture, Vol. 80, 1996, pp. 103-145.

McDowell, D.L., "Damage Mechanics in Metal Fatigue," submitted for publication in a special volume of International Journal of Damage Mechanics, December 1998.

♦ Experimentally evaluated and modified existing micromechanical models for growth of microstructurally small cracks (based on dislocation pile-up at obstacles) for helicopter alloys and Ti-6Al-4V, and identified strong microstructure barrier features

Patel, A.M., "Growth of Small Fatigue Cracks in PH 13-8 Mo Stainless Steel," M.S. Thesis, Georgia Institute of Technology, May 1997.

Hamm, R. W. and Johnson, W. S.: "Survey of the State-of-the-Art in Small Crack Research," Journal of Testing and Evaluation, Vol. 26, No. 3, March 1998, pp. 168-175.

Hamm, R., "A Multi-Regime Model Comparison for Constant Amplitude Small Crack Behavior in Ti-6Al-4V," M.S. Thesis, Dept. of Materials Science and Engineering, Winter 1998.

Hamm, R. W. and Johnson, W. S., "A Unification of Small and Large Crack Growth Laws," submitted to the Journal Fatigue and Fracture of Engineering Materials and Structures, (April 1998), accepted.

Hamm, R. W., Jin, O., and Johnson, W. S., "Small Crack Growth Behavior in Ti-6Al-4V and the Microstructural Influence," submitted to the Journal Fatigue and Fracture of Engineering Materials and Structures, (April 1999).

Patel, A.M., Neu, R.W., and Pape, J.A., "Growth of Small Fatigue Cracks in PH 13-8 Mo Stainless Steel," Metallurgical and Materials Transactions A, Vol. 30A, May 1999.

♦ Conducted novel fretting fatigue experiments and suggested improvements for models of fretting fatigue

Pape, J.A., "Design and Implementation of an Apparatus to Investigate the Fretting Fatigue of PH 13-8 Mo Stainless Steel," M.S. Thesis, Georgia Institute of Technology, December 1997.

Pape, J.A. and Neu, R.W., "Influence of Contact Configuration in Fretting Fatigue Testing," 12th Int. Conf. on Wear of Materials, Atlanta, GA, April 25-29, 1999, accepted for publication in *Wear*, October 1998.

Neu, R.W., Pape, J.A., and Swalla-Michaud. D.R., "Methodologies for Linking Nucleation and Propagation Approaches for Predicting Life under Fretting Fatigue," Fretting Fatigue: Current Technology and Practices, ASTM STP 1367, D.W. Hoeppner, V. Chandrasekaran, and C.B. Elliott, Eds., American Society for Testing and Materials, 1999, accepted for publication, March 1999.

Swalla-Michaud, D.R., "Fretting Fatigue Damage Prediction using Multi-axial Fatigue Criteria," M.S. Thesis, Georgia Institute of Technology, May 1999.

♦ Used nanoindentation, Atomic Force Microscopy (AFM) and Impedance Spectroscopy (IS) as tools to explore surface roughening during fatigue cycling, changes in local hardness near the crack tip for long cracks during fatigue, and understanding fatigue mechanisms.

F. Yang, A. Saxena and L. Riester, "Use of Nanoindentation Technique for Studying Microstructure/Crack Interactions in Fatigue of 4340 Steel," Metallurgical and Materials Transactions A, Vol. 29A, 1998, pp 3029-3036.

A. Saxena and C. Muhlstein, "Fatigue Crack Growth Testing and Applications," Fatigue and Fracture, ASM Handbook, Vol. 19, ASM International, Metals Park, Ohio, 1996, pp 168-184.

Fan Yang and A. Saxena, "Mechanisms of Fatigue Crack Initiation in Annealed and Tempered 4340 Steel," Submitted to a Special Issue of Journal of Mechanical Engineering Science", September 1998.

Fan Yang, A. Saxena and L. Cretegny, " Use of Atomic Force Microscopy for Studying Fatigue Crack Initiation," to appear in the Proceedings of the Seventh International Conference on Fatigue", Beijing, China, June 8-12, 1999.

♦ Conducted novel computational cyclic crystal plasticity calculations for distribution of driving force parameters for formation and growth of subgrain-scale fatigue cracks in a polycrystal under HCF, as well as first-ever calculations for mixed mode behavior of microstructurally small cracks in surface grains in polycrystals

McDowell, D.L. and Bennett, V., "Micromechanical Aspects of Small Multiaxial Fatigue Cracks," Proc. 5th Int. Conf. On Biaxial/Multiaxial Fatigue & Fracture, Cracow, Poland, 8-12 Sept., 1997, pp. 325-348.

Bennett, V. and McDowell, D.L. ,"Polycrystal Orientation Effects on Microslip and Mixed Mode Behavior of Microstructurally Small Cracks," in review for publication in ASTM STP 1359, Eds. K.J. Miller and D.L. McDowell, submitted May 1998; revised December 1998; to appear in 1999.

♦ Developed algorithms for evaluating driving forces for long cracks with complex, 3-D crack fronts

Gardner, B. and Qu, J.,"A numerical technique to calculate the stress intensity factors for cracks with multiple kinks," presented at the ASTM Mixed Mode Crack Behavior symposium, 1998, Atlanta, GA.

Students Involved

Graduate:

F. Yang, (3/95 – 6/96)
V. Bennett, Ph.D. (in-progress)
B. Gardner, MS in 1996; Ph.D. (in-progress)
O. Jin, Ph.D. (in-progress)
R. Hamm, M.S. (Winter 1998)
L. Cretegny, Ph.D. (in-progress)
A. Bell, M.S. (Summer-Fall 1998 on AASERT)
C. Rosen (started M.S. in January 1999 on AASERT)
A.M. Patel, M.S. (Spring 1997)
J.A. Pape, M.S. (Fall 1997)
D.R. Swalla-Michaud, M.S. (to defend in Spring 1999)
J.A. Pape, Ph.D. (in-progress)

Undergraduate:

M. Kamel, 1996-present
T. Edwards, Winter 1997-Summer 1998
A. Bell, Summer 1997-Spring 1998
D. Van Dellan, Fall 1998-present

Post Doctoral Researchers
Dr. Fan Yang (7/96 – 8/97)

Other Collaborators
Rosario A. Gerhardt, Professor, MSE, Georgia Tech
Brian Moran, Professor, Mechanical Engineering, Northwestern University

1. INTRODUCTION

One of the key issues in current procedures for maintenance of high speed machinery and transportation vehicles is the ability to accurately estimate the remaining life and to set safe inspection intervals for the critical structural parts of complex systems. With on-board diagnostics and high speed digital signal processing, an effective maintenance strategy relies on periodic assessment of the degradation of components during service and specification of conditions for shutdown and/or maintenance. The detection refresh rate (inspection interval), the nature and interpretation of the sensor signal (choice of inspection technique(s)) and the updated projection of remaining life must be specified as part of an overall strategy which provides the basis for making decisions such as continuation of operation, retirement, replacement at present or replacement at a future date (possibly during a scheduled maintenance outage). Such a strategy must address the risk due to the uncertainties in the predicted component life which are related to:

- detection difficulties for small cracks in actual components,
- unusual characteristics of propagation of small cracks and long 3-D cracks in fatigue, and
- complex service loading conditions

In many cases, the cracks may be essentially undetectable by optical methods, due either to small length or lack of accessibility. This is particularly true of metallic components subjected to high frequency, relatively low amplitude fatigue loading such as rotor and drive components of helicopters. Under such conditions, fatigue cracks may remain very small (e.g. 20 to 500 μm) for over 90% of the life, amenable to optical detection only near the very end of component life. Moreover, the three-dimensional shape of typical components often leads to fairly complex shaped crack fronts and crack face contact during fatigue. In components, the determination of whether or not a crack is on the verge of catastrophic propagation depends on the rate of change of the driving force for crack growth as a function of crack length (e.g. dK/da), which varies among possible crack initiation sites in components. Consequently, the operator may be faced with the relatively rapid in-flight onset of deleterious structural performance, including loss of control, landing capabilities, etc. Accordingly, it is prudent to assess the evolving state of damage at hot spots (stress concentrations) or sites of enhanced contact fatigue using micro sensors and/or acoustical methods with resolution necessary to track the development of fatigue cracks and to estimate when these cracks may become long enough to warrant maintenance decisions. In some cases, fretting fatigue, foreign object impact damage or surface defects introduced through component assembly or material processing serve as the initiation sites for fatigue cracks, leading to the need for a robust diagnostic capability which can detect such cracks over the entire component volume, outside the envelope of cataloged hot spots. These "rogue" cracks fall outside the regular categorization of pre-defined hot spots, and demand an enhanced degree of robustness for both detection and remaining life estimation. The detection of rogue flaws that are uncorrelated with hot-spot detection may give rise to the need for component inspection or adaptive, multi-sensor, multi-spectral signal analysis at multiple length scales combined with an artificially intelligent algorithm for estimation of the crack propagation rate and remaining life. However, it is important to recognize that the gist of the

problem lies in real-time characterization of the hot-spot behavior, since field observations corroborate computational results, as pointed out in the next section.

A schematic showing the overall philosophy of an integrated, multi-scale diagnostic/prognostic system for component fatigue response appears below:
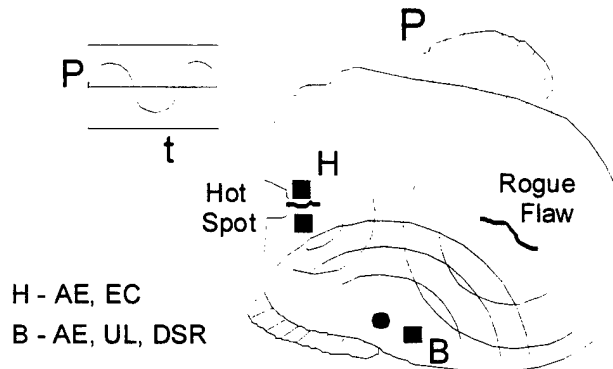
Integrated diagnostic/prognostic schematic for HCF of a component subjected to generalized cyclic loading, P, showing hot spot and associated focused micro sensors (H) and a rogue flaw with broad area scanning detection (B). Legend: Acoustic emission (AE), eddy current (EC), active ultrasound (UL), and changes of dynamical system/component response (DSR).

2. IDENTIFICATION OF "HOT SPOTS"

Stress and stress concentration are major causes of failure in mechanical systems. To develop an integrated diagnostic tool with predictive capabilities for remaining life, one must fully understand the failure mechanisms. How are fatigue cracks initiated? How fast do these fatigue cracks grow? What are the conditions for criticality or maintenance? Component failure? Conceivably, two aspects need to be considered, namely, the material resistance and the driving force. In this section, some considerations are given on how to carry out stress and fracture analysis in complex 3-D components to estimate crack driving forces. The objective was to develop techniques for calculation of stress distribution in complex 3-D components.

Due to the complexity of the components, the finite element method was identified as the effective tool for the stress analysis. Several commercially available finite element packages were evaluated for this purpose. The main requirements for the finite element packages were ease of model creation for complex structures (pre-processor), and appropriate visualization techniques (post-processor) for evaluating the results. The Table below shows a comparison of the packages investigated.

Comparison of several major commercial FEM packages.

Package	Pre-Processor	Post-Processor
I-DEAS	Very Good	Good/limited to surface
Patran	Good	Good/limited to surface
Abaqus Post	N/A	Good/limited to surface

After extensive studies, it was concluded that the visualization capabilities of the post-processors for each of the packages investigated were rather limited. They all provide good presentation of results on the surface of the component, but none provides adequate representation of results inside a three-dimensional body.

Because of the many small features inside a real component, it is extremely to have a visualization technique that can provide stress distribution on any given cross-section of the components. To this end, a visualization program was developed for both effective visual representation of component response and ease-of-use. It can be tailored to desired applications. Major features of the visualization program include:

(1) It is compatible with most commercial FEM code (such as ABAQUS). This enables the visualization of field results from many FEM codes.

(2) It displays the field results on any cross-section plane (cutting planes) defined by the user.

(3) It automatically extracts the maximum (minimum) values and locations of the field quantities of interest on any cross-section defined by the user.

(4) The cross-sections can be animated to move and rotate through the entire body.

(5) It is flexible so that the user can tailor the visualizations to the desired application.

The visualization program was applied to the analysis of an H-46 rotorhub. A finite element model of the rotorhub was created and analyzed using I-DEAS. The loads from a ground-air-ground cycle were used in the analysis, as this cycle represents one of the worst-case scenarios. Several potential "hot spots" were located from the finite element results.

As shown in Fig. 1, locations of such hot spots coincide with the cracks observed on the actual components. Additionally, the stress fields on the planes corresponding to maximum principal stress were identified. One of such plane is shown in Fig. 2.
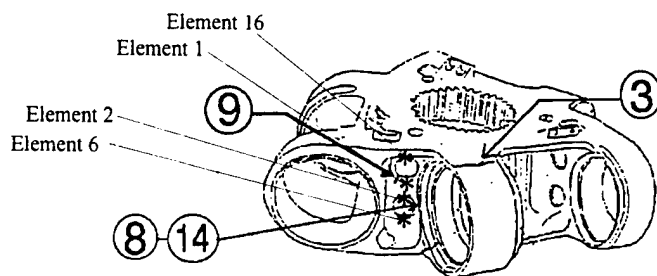
Fig. 1 Rotorhub showing predicted 'hot spots' and observed damage sites.
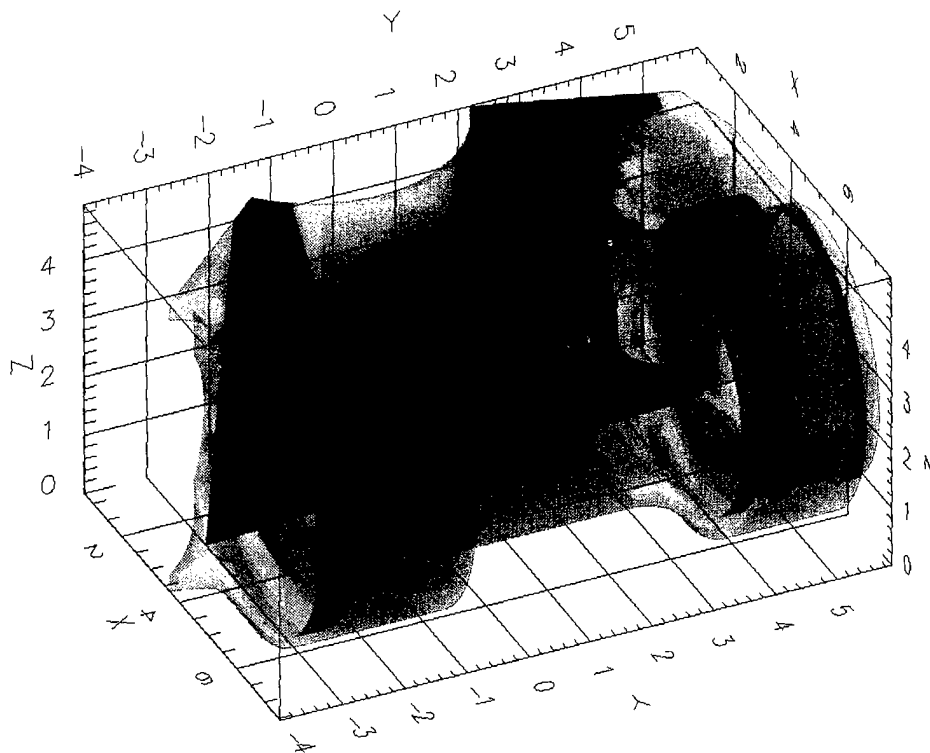
Fig. 2 Cross-section view of the maximum principal stress distribution.

3. TRACKING PROGRESSION OF DAMAGE

Once a set of hot spots in each component are identified, dedicated sensors may be applied to monitor the occurrence and progression of cracking during service. Under HCF conditions, the processes of crack nucleation and small crack propagation are of great importance at these hot spots.

The proximity of small HCF cracks to free or contacting surfaces and interaction with microstructural barriers vastly alter the crack tip stress and strain fields and the rate of crack propagation. Heterogeneity of cyclic plastic deformation under low amplitude loading conditions is also an important consideration, as are associated near-surface residual stress fields.

Small cracks in polycrystalline metals often display lower apparent threshold stress intensities and much higher propagation rates than long crack data when interpreted within the framework of either linear elastic fracture mechanics (LEFM) or elastic plastic fracture mechanics (EPFM) solutions for long cracks in homogeneous, isotropic materials. Small cracks in single crystals show little or no evidence of a threshold, particularly in predominantly mode II loading conditions. At locations where cracks occur in components, the stress state is often of multiaxial character due to changes of the mixity of applied loading (e.g. excitation of multiple dynamical modes), structural constraints (e.g. change of geometry) or local contact with adjacent structures (e.g.

joints). Hence, modeling concepts that address only uniaxial and/or Mode I loading conditions are not sufficiently general to meet diagnostic requirements.

Use of classical initiation approaches for HCF (S-N curves, Goodman diagrams) is not effective in supporting the estimation of remaining component life since they do not predict the rate of propagation of detected cracks. Moreover, use of LEFM solutions based on long cracks in homogeneous, isotropic materials does not match the fatigue crack growth rate observed for cracks on the order of a few grain sizes in dimension, in general. Ample evidence exists to confirm that for cracks with length at the scale of repeating microstructure, the propagation behavior is quite distinct from that of mechanically long cracks which exceed this scale by over an order of magnitude. Therefore, a major technical challenge in support of integrated, near real time diagnostics is to develop new models for microstructurally and physically small fatigue crack growth that can be deployed in a manner analogous to conventional fracture mechanics methods. In this section, we discuss some of the considerations for modeling the behavior of small crack development and growth at sites of stress concentration.

3.1 Nucleation

Cracks in critical locations in components subjected to nominally HCF conditions may form from pre-existing machining- or process-induced defects, precursory events such as fretting fatigue (relative microslip of contacting components), impact of foreign objects, or from periodic overload cycles which induce fracture of inclusions or interfaces and enhance cyclic slip. A large fraction of the HCF lifetime is typically spent in the formation and growth of small cracks. Hence, there is a potentially strong dependence upon surface conditions, pre-existing or service-induced defects, and microstructure. The nucleation or incubation period required to form sharp cracks either from intrinsic or extrinsic defects typically comprises a very significant fraction of total fatigue life, often in excess of 90%. In this case, total fatigue life is defined as the combination of formation of cracks and their subsequent propagation to dimensions where either rapid crack advance and catastrophic failure occurs, or to the point where component response is unacceptably degraded. From a design perspective, initiation models may be used to estimate the number of cycles to formation of cracks, while fracture mechanics approaches then apply to their propagation (cf. Socie, 1977). Various schemes have been proposed along these lines. In the context of an integrated diagnostic/prognostic system for components, however, it is the propagation of crack-like defects that is most relevant to component evaluation. It may be useful to monitor, for example, local acoustic emission events that correspond to the development of localized inelastic deformation or "pop-in" of cracks, but each microsensor is generally limited in its resolution of such microscale events. Above a certain limit of resolution, crack length can be reliably monitored, and its progression compared to that estimated by a life estimation scheme correlated to a specific material, for a specific range of crack length and for the stress intensity (driving force) appropriate to that hot spot location.

Standard fracture mechanics approaches for long cracks cannot be applied to very small cracks in a direct manner to address the relevant mechanisms. Crack propagation analyses have relied heavily upon a fracture mechanics-based description of crack tip stress fields that assume the material is homogeneous and isotropic. The notion of self-similar crack growth for these small cracks is known to be a leap of faith in many

respects. Furthermore, there are processes that may consume a significant fraction of total fatigue life that involve the formation of cracks from pre-existing defects such as foreign object damage (FOD) or precursor events such as periodic LCF or fretting that are well beyond the scope of conventional fracture mechanics and are also outside the domain of intended applications of the local stress approach to fatigue crack initiation. Novel experimental and analytical or computational mechanics approaches which focus on formation and growth of small cracks under HCF conditions are necessary to resolve these issues from a basic perspective. Development of improved concepts for fatigue crack driving and material resisting forces are necessary, including appropriate extensions of fracture mechanics as well as new approaches that recognize key physical aspects of the HCF problem, such as the influence of local cyclic plasticity, free surfaces and attendant gradients of dislocation density, and fretting fatigue in promoting the propagation/opening of small cracks, orientation and spatial distribution of microplasticity among grains in polycrystals, local mode mixity, interaction of small cracks with microstructure, crystallographic propagation across grain boundaries into misoriented grains, stochastic and probabilistic aspects of HCF crack propagation.

3.2 Crack Propagation Mechanics

Current models for HCF have been divided largely into two classes: (1) initiation approaches for endurance/fatigue limit concepts based on S-N curves or local stress-life approaches, and (2) application of LEFM for suitably long cracks in components. Much of fatigue design for rotating/reciprocating machinery is based on the former, while damage tolerance concepts for airframes which make use of periodic inspections are employed in the latter. Here, we focus first on the development of models for propagation of small cracks in fatigue. Then, we will point to some complexities associated with modeling the growth of longer cracks in three-dimensional components.

The growth of small cracks in polycrystalline metals is subject to several characteristic regimes (Miller, 1993; Tanaka, 1987). Microstructurally small cracks within the first surface grain are relatively less constrained than long cracks, resulting in increased crack tip opening and sliding displacements. As discussed by Miller (1993), microstructurally small cracks are subject to strong interactions with microstructural barriers. Microstructurally small crack growth is characterized by a series of periodic activation of slip in adjacent grains of different orientation, followed by dislocation blockage by grain boundaries and associated deceleration of da/dN (Hussain et al., 1993). Oscillatory da/dN behavior is commonly observed for microstructurally small cracks (Nisitan,i 1987; Tanaka and Akiniwa, 1989; Wang and Miller, 1992). Typically, the experimentally observed crack length for the minimum da/dN, d, is somewhat higher than the characteristic grain size, δ, assumed in slip transfer models. Other mechanisms which slow the growth of small cracks include development of plasticity- and roughness-induced closure, and both may contribute to the observed minimum da/dN. The relative balance of these mechanisms is highly dependent upon slip mechanisms and microstructure. If the applied stress is insufficient to nucleate cyclic slip in adjacent grains, small cracks will decelerate and arrest at this length scale (a $\approx$ d), giving rise to a fatigue limit. In general, d depends on the particular composition and arrangement of microstructure, and does not correspond simply to optical identification (Wang and Miller, 1992). If cracks propagate past the strongest barrier (minimum da/dN), they

continue to be subject to a diminishing influence of microstructure for several multiples of this length scale (a < kd, k $\approx$ 2 to 7) (Tanaka, 1987; Tanaka and Akiniwa, 1989; Hussain et al., 1993). Comprehensive reviews of the mechanics challenges in developing fatigue crack growth laws for small cracks are available in the literature (Leis et al., 1986; McDowell, 1996).

An international survey was conducted by ASTM Committee E08.06.04 and was executed by the investigators to determine the state of small-crack research and knowledge. The survey consisted of short answer questions regarding the nature of the research, the materials studied, applications of the investigators' research, smallest crack size monitored, techniques used to monitor crack growth, testing environment, surface conditioning/preparation, and models used to predict crack growth. In addition, survey participants were asked to say what critical questions they were addressing with their research and what some important unresolved questions are in the area of small-cracks. Some results from the survey that apply to the project are as follows:

- Titanium alloys make up 40.81% of all the materials studied by the survey participants. But, only 8.16% of all replies indicates that small-crack research is being done on Ti-6Al-4V.
- Only 15% of all replies indicated that load interaction effects were being investigated on small-cracks. The most common type of loading was constant amplitude loading with different stress ratios, totaling 82.5% of how loading was characterized by survey participants.
- 48.84% of replies stated the smallest crack size being monitored was smaller than equal to ten microns in length.
- 70% of all small crack specimens are being mechanically polished with only 3.33% incurring no polish. Of the specimens that are mechanically polished, 26.06% are being electropolished as well. Specimens for the current research are mechanically polished and electropolished.

Some of the unresolved issues, noted by survey participants, included: load interaction effects are for small cracks, modeling of these effects and how metallurgical features influence small-crack growth. These are some of the questions being addressed by the current research.

3.2.1 Extensions of Existing Small Fatigue Crack Growth Relations

The models considered in this study were specifically formulated for either mechanically small cracks or microstructurally small cracks or both. When a crack is considered small, local stress gradients due to geometry are negligible. However, as a crack extends beyond the small crack regime, stress gradients and constraint caused by geometry cannot be ignored. The stresses that a crack feels decays from the local stresses to the nominal applied stresses. A fracture mechanics treatment of these cracks must be able to integrate Microstructural Fracture Mechanics (MFM), Elastic-Plastic Fracture Mechanics (EPFM), and Linear-Elastic Fracture Mechanics (LEFM) seamlessly. The models presented in this study have not done so. Hence, an enhancement is proposed to unify MFM, EPFM and LEFM through a single growth law. The goal of the modeling is

not to explore the possible forms of the equation or values in the equation, but rather to show the merit of the concept.

The enhancement was inspired by the growth laws used in the Wang [1] and Nisitani [2] models, but modified to link small crack growth characteristics to long crack growth characteristics. The enhancement assumes a growth law of the form:

$$\frac{da}{dN} \propto \rho^{\lambda} \tag{1}$$

where ρ is the plastic zone and λ is the crack growth exponent. While a crack is small large stresses are required to propagate the crack. The large stresses may come from large far-field stresses or they may be due to a stress gradient caused by specimen geometry, such as notches. The proposed extension assumes the latter. At this point, the plastic zone may be the same order of magnitude as the crack. This can be considered an MFM or EPFM plastic zone size characteristic. As a crack grows beyond the first microstructural boundary into a long crack and out of the stress gradient, the stresses are generally low and the plastic zone size decays to a small fraction of the crack length, which are LEFM characteristics. The models used in this study with plastic zone formulations predict the plastic zone size stays on the same order as the crack length at all crack sizes. The proposed enhancement decays the plastic zone size from the same order of magnitude as the crack length to a small fraction of the crack length. The enhancement links the small crack MFM and EPFM behavior to the long crack LEFM behavior by the following:

$$\frac{\rho}{a} = \Theta\Psi + \Phi \tag{2}$$

where ρ is the plastic zone size, Θ is the MFM and/or EPFM behavior and Φ represents the LEFM behavior. Ψ is a decay function that is only dependent upon α and $2a/d$, where d represents the characteristic microstructural unit length and α is a multiple of $2a/d$. The advantages of using equation 2 are that it is general enough so as not to be model specific.

The role of λ in Equation (1) is to provide a link between exponents of the small crack and long crack formulations. Consider:

$$\frac{da}{dN} \propto \rho_{MFM/EPFM}^{m} \qquad \text{for small cracks} \tag{3}$$

$$\frac{da}{dN} \propto \rho_{LEFM}^{z} \quad \text{for long cracks in Paris regime} \tag{4}$$

where z equals 1/2 of the Paris exponent (n) since the LEFM plastic zone is $\rho_{LEFM}^{1/2} \propto \Delta K$.

Several models with plastic zone formulations use various values for the exponent, λ, in Equation (1). For example, the Wang model assumes a value of $\lambda = 1$ while the

Nisitani model prescribes a value $\lambda \gg 1$. The reason for the differences is due to the assumptions about which regime the small crack is in. To generalize λ for different values of m and to link the small crack and large crack exponents, the following conditions must be satisfied:

$$\lambda = m \text{ for } 2a/d < 1$$
$$\lambda = n/2 \text{ for } 2a/d \geq \alpha$$

Between $1 < 2a/d < \alpha$, λ changes from m to n/2. A linear interpolation function is assumed:

$$\lambda = \left(\frac{m - n/2}{1 - \alpha}\right)\frac{2a}{d} + \left(\frac{n/2 - m\alpha}{1 - \alpha}\right) \tag{5}$$

Combining everything together:

$$\lambda = \begin{cases} m & \text{for } 2a/d < 1 \\ \left(\frac{m - n/2}{1 - \alpha}\right)\frac{2a}{d} + \left(\frac{n/2 - m\alpha}{1 - \alpha}\right) & \text{for } 1 < 2a/d < \alpha \\ n/2 & \text{for } 2a/d \geq \alpha \end{cases} \tag{6}$$

Using Equations (1)-(2) and (6), a single formulation can be used to describe crack growth at any size, under any geometry with known boundary correction factors, under any constraint. The only drawback is that the formulation prescribes one fitting factor; α, which can roughly be connected to the length scales that define the various small crack regimes. The final formulation gives:

$$\frac{da}{dN} \propto \rho^{\lambda} = f(\rho_{MFM/EPFM}, \rho_{LEFM}, m, n, \alpha, a, d)$$

So as a crack grows from a small crack to a long crack, the unified growth law evolves smoothly:

$$\frac{da}{dN} \propto \rho_{MFM/EPFM}{}^{m} \quad =======> \quad \frac{da}{dN} \propto \rho_{LEFM}{}^{n/2}$$

The enhanced model was applied to all the small crack data used in the study. Plane strain conditions were assumed ($\beta = 6$). The results are shown in Figures 3 and 4 and are compared to the Wang model.
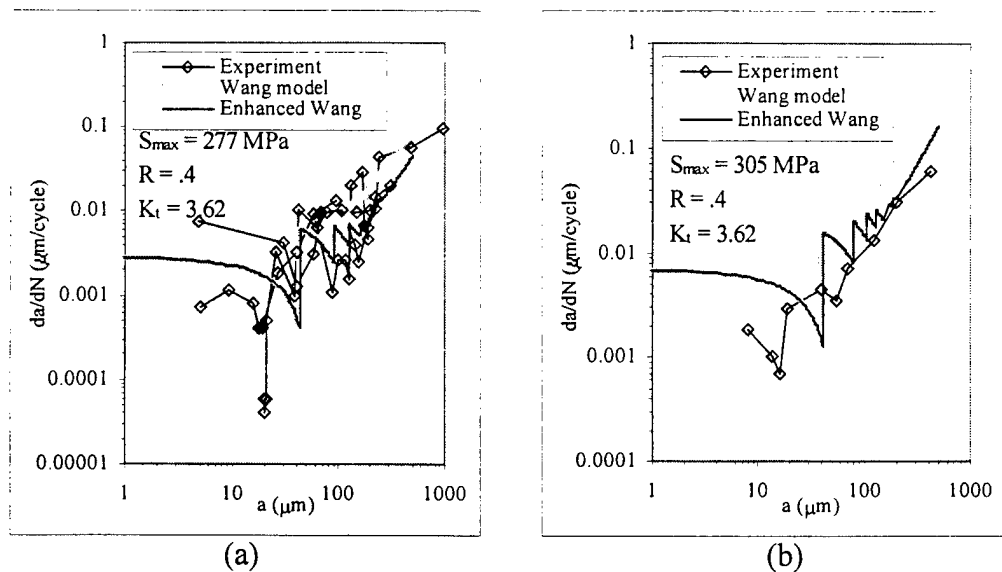
Figure 3: Enhanced Wang model crack growth predictions at R = 0.4.
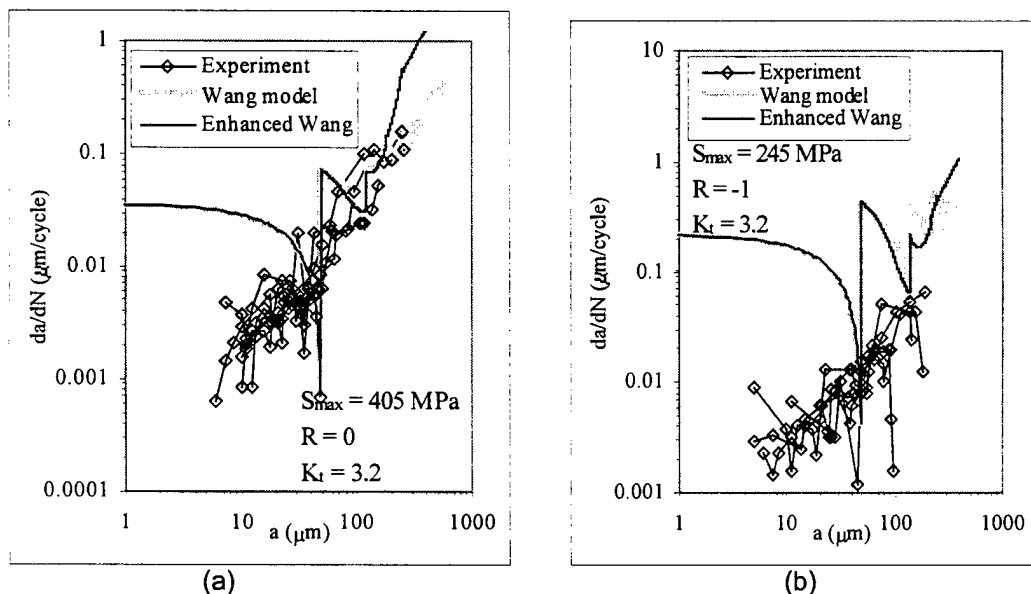
Figure 4: Enhanced Wang model crack growth predictions at (a) R = 0 and (b)R = -1.

The enhanced Wang model predicted lower crack growth rates than the Wang model at R = 0.4 while predicting higher rates at R = 0 and -1. One aspect of the predictions that is noteworthy is that the slope of the enhanced model was nearly the same as the Wang model and the data at all stress levels, validating the growth exponent formulation. The enhanced model showed reduced oscillatory behavior compared to the Wang model, downplaying the microstructural interaction as the crack length increases.

A material's microstructure plays a dominant role in many aspects of crack growth. One such influence is the role that microstructure has in determining a crack's path through the material. In addition, the type of microstructure can have a significant effect

on the material's crack growth rate characteristics.

Figure 5 shows a microstructure of Ti-6Al-4V that consists of lighter α grains with darker β grains. The microstructure exhibited textured bands of α-rich and β-rich material that ranged in width from approximately 20 to 100 μm with an average width of 41 μm and a standard deviation of 27 μm. The bands were oriented in the longitudinal direction, parallel with the material's loading axis. As such, the bands were perpendicular to the crack growth direction, so it was expected that they would have some effect on the small crack growth behavior of the material. The α grains had an average grain diameter in the crack growth direction of approximately 3-5 μm.
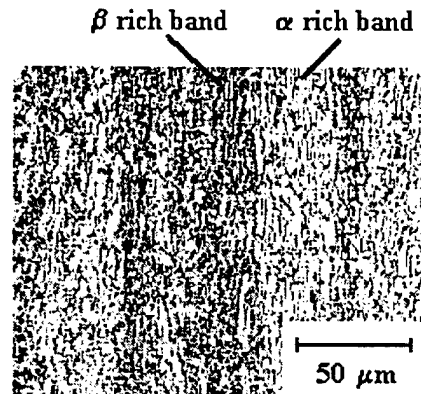
Figure 5: Bands of α– and β–rich material in the Ti-6Al-4V microstructure.

Bands of α grains clearly influences crack extension in Ti-6Al-4V. The dependence of crack growth rates on the bands of α grains is dependent upon the applied stress level. Specifically, a stronger dependence between growth rates and bands of α grains is noted as the maximum stress level increases. This microstructure promotes crack branching to absorb applied energy rather than impart resistance to an advancing crack. The size and orientation of α platelet colonies in $\alpha+\beta$ titanium alloys in relation to local stress fields were the chief parameters controlling the kinetics of fatigue crack propagation rather than the grains themselves.

Oscillations in the crack growth rates were found to occur with increasing crack length at all stress levels tested. This is shown in Figures 6a and 6b. In these Figures, a is equal to half the crack length as defined by Newman's stress intensity factor formulation for a SEN specimen. The oscillations seen in these figures have wavelengths between 50-100 μm. The wavelengths approximately correspond to the widths of the α-rich and β-rich bands exhibited by the microstructure. Hence, more evidence shows that the overriding characteristic microstructural length is defined by the microstructural band widths. As an example, consider the plot for a maximum stress at 305 MPa in Figure 6. In the plot, the crack growth rate reaches a minimum at a crack length of 20 μm.

As the cracks extend beyond approximately 300 μm, the growth rates collapse into a narrow scatterband, representing the overall large crack behavior. Figure 7 shows the comparison between small crack and large crack growth data in terms of the stress intensity factor range at a stress ratio of R = 0.4. There was little small crack effect. This can be partly explained in terms of crack tip shielding. At higher stress ratios, the level

of closure induced by roughness or plasticity does not play a significant roll in a crack's behavior, whether the crack is small or large. Hence, the average behavior of small and large cracks at higher stress ratios would be similar, as observed. The difference between the behavior of the two types of cracks is then seen in terms of scatter in the data.
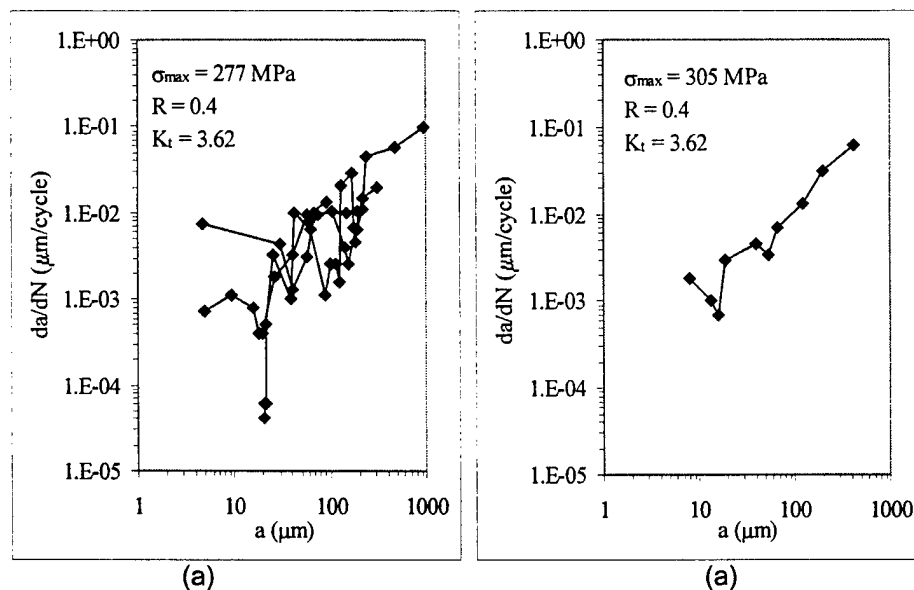
Figure 6: Crack growth rates versus crack length for small cracks at maximum stresses of (a) 277 MPa and (b) 305 MPa for R = 0.4 loading conditions.

The scatter in the small crack data at lower ΔK levels is due to the inability of ΔK to characterize the crack tip stresses and the fact that there may be error in the measured crack growth rates because of the small measured crack growth increments. In addition, microstructural influences on crack aspect ratio variations may have played a role in the scatter.
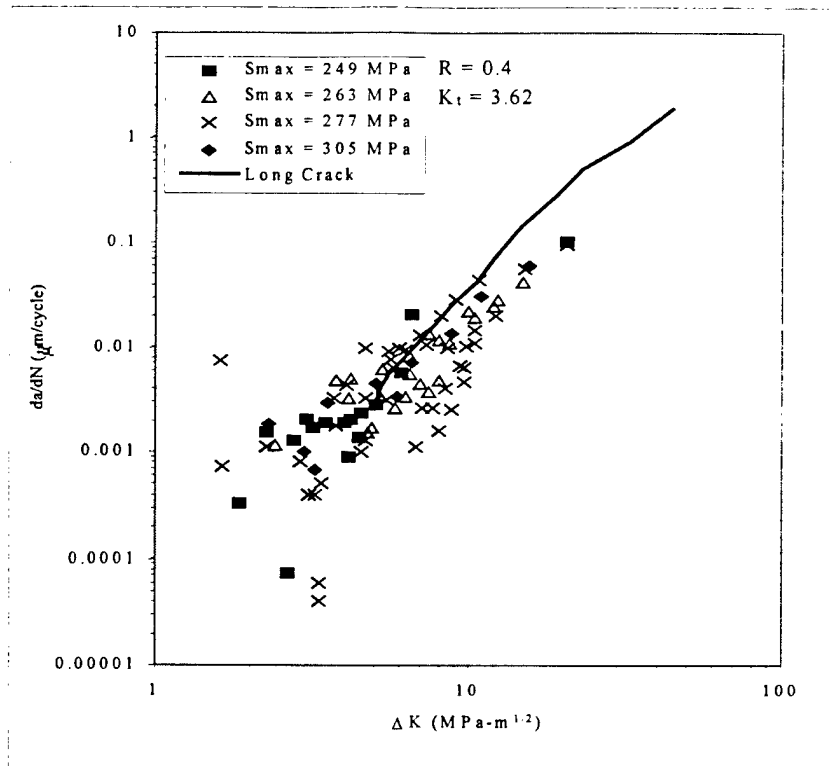
Figure 7: Comparison between large crack and small crack behavior for R = 0.4.

It is shown in Figure 7 that as the small cracks became longer, their growth rates do not exactly fall in-line with the long crack data. There is a possibility that the crack growth rate properties of the Ti-6Al-4V differ in the thickness direction (direction that the small cracks grew in) than in the width direction (direction that the long cracks grew in). This could be caused by microstructural influences in the two directions.

3.2.2 Robust Models for Small Crack Growth Behavior

In this section, we explain novel developments within the program of robust, approximate multistage model framework for the growth of microstructurally and physically small fatigue cracks which is inspired by observed cyclic crack tip displacement correlations with the FCP rate. Several phenomena should be recognized in development of a realistic small crack propagation model:

(i)   Arrest threshold for propagation of microstructurally small cracks (fatigue limit) and less microstructure-sensitive threshold for physically small cracks (LEFM threshold).

(ii) Adherence to the cyclic stress-strain and strain-life relations for loading above the fatigue limit.

(iii) Concurrence with the format of critical plane models for Stage I cracks in multiaxial fatigue which provide excellent correlation of the characteristic mixed mode propagation behavior of small cracks under various stress states.

The critical plane-based multiaxial small fatigue crack growth law developed by

McDowell and Berard (1992) with later refinements by McDowell and Bennett (1996) satisfies (ii)-(iii) above and serves as the starting point for addressing (I) above. We introduce a generalization of the small crack propagation approximation based on slip transfer (Hobson, 1985; Hobson et al., 1986; Miller, 1993; Hussain et al., 1993) within the context of the multiaxial critical plane approach set forth by McDowell and Bennett (1996), assuming completely reversed loading. We define Regimes I, II and III as the microstructurally small crack regime (MSC), transition from microstructure sensitivity to relative insensitivity, and the physically or mechanically small crack regime (PSC), respectively. The equations of the model appear in Table 1 for each of the three Regimes. The MSC regime model is observed to be a generalized form of the Hobson model (Hobson, 1985; Hobson et al., 1986; Miller, 1993) for deceleration of microstructurally small cracks, primarily associated with the primary barrier(s). In these equations, a is crack length with a_i as its initial value, d is the primary microstructure barrier spacing, kd is the transition crack length into the PSC regime, $\Delta\gamma_{max}$ and $\Delta\gamma_{max}^e$ are the maximum shear strain range and its elastic component, σ_n and τ_n are the normal and shear stresses, respectively, on the plane of maximum range of shear strain, ρ is a constraint factor for biaxial or triaxial stress states (μ is a proportionality constant), and ψ is the driving force parameter for fatigue crack propagation. The ψ parameter has previously been shown (McDowell and Berard, 1992) to provide accurate correlation of the full range of stress states. Constants C_e, C_p, m, M and parameters β_e and β_p have been thoroughly described, along with definitions of R_n, R_e, j_e, j_p, μ and ρ in earlier work (McDowell and Berard, 1992; McDowell and Bennett, 1996).

The form of D_{aN} in Table 1 is introduced to normalize the solution of the system of propagation relations to the strain life relations for uniaxial and torsional fatigue above the smooth specimen fatigue limit in each case, taken independently, assuming an initial crack length, $a_i < d$, and a final crack length, $a_f > kd$. Below a value of ψ slightly above the fatigue limit, ($\psi < \xi(\psi_{th})_I$, $\xi > 1$), D_{aN} is assumed to be fixed at the value corresponding to $\psi = \xi(\psi_{th})_I$. The crossover crack length between growth rates in Regimes I and II (i.e. minimum da/dN) occurs at $a^* < d$, in general.

Table 1. Equations of multiaxial small crack growth law.

$$\left(\frac{da}{dN}\right)_I = D_{aN}\psi A \psi^B\left(1 - \frac{a}{d}\right) \qquad (MSC, Regime\ I)$$

$$\left(\frac{da}{dN}\right)_{II} = D_{aN}\psi\left\langle\psi^r\left(\frac{a}{kd}\right) - D\right\rangle \qquad (Transition, Regime\ II)$$

$$\left(\frac{da}{dN}\right)_{III} = D_{aN}\psi\left\langle\psi^r\left(\frac{a}{kd}\right) - D\left(\frac{a}{kd}\right)^{1-Mr}\right\rangle \qquad (PSC, Regime\ III)$$

$$\frac{da}{dN} = \max\left(\left(\frac{da}{dN}\right)_I, \left(\frac{da}{dN}\right)_{II}\right) \qquad for\ a < kd$$

$$\frac{da}{dN} = \max\left(\left(\frac{da}{dN}\right)_{III}, \left(\frac{da}{dN}\right)_{FM}\right) \qquad for\ a \geq kd$$

with $\langle g\rangle = g$ if $g \geq 0$; $\langle g\rangle = 0$ otherwise. Here, $(da/dN)_{FM}$ is the long crack FCGR based on either EPFM (ΔJ_{eff}) or LEFM (ΔK_{eff}).

$$\psi = R_e C_e(\Psi_e)^M + (1 - R_e)C_p(\Psi_p)^m$$

$$\Psi_\alpha = (1 + \mu\rho)(\beta_\alpha R_n + 1)\left(\frac{\Delta\tau_n}{2}\frac{\Delta\gamma_{max}^\alpha}{2}\right), \qquad \alpha = e,p$$

$R_e = \Delta\gamma_{max}^e/\Delta\gamma_{max}$ ($0 < R_e \leq 1$), $R_n = (\Delta\sigma_n/2)/(\Delta\tau_n/2)$, $\rho = (\Delta\sigma_{kk}/2)/(2\Delta\tau_n/2) - R_n$

$$D_{aN} = 2\frac{d}{A\psi^B}\ln\left[\frac{d-a_i}{d-a^*}\right] + 2\frac{kd}{\psi^r}\ln\left[\frac{\psi^r - D}{\psi^r\left(\frac{a^*}{kd}\right) - D}\right] - 2\frac{kd}{\psi^r Mr}\ln\left[\frac{\left(\frac{a_f}{kd}\right)^{-Mr}(\psi^r - D)}{\psi^r - D\left(\frac{a_f}{kd}\right)^{-Mr}}\right]$$

for $\psi \geq \xi(\psi_{th})_1$; $D_{aN} = D_{aN}$ evaluated at $\xi(\psi_{th})_1$ for $\psi < \xi(\psi_{th})_1$, where $(\psi_{th})_1$ is the MSC threshold value of ψ (corresponding to the smooth specimen fatigue limit) and ξ is a constant, $\xi > 1$.

It is also noted that if a > d due to prior loading above the fatigue limit, then the nonpropagating crack threshold is decreased from the smooth specimen fatigue limit, in accordance with the Kitagawa diagram (Tanaka, 1987; Tanaka and Akiniwa, 1989; Miller, 1993). The mechanisms for the fatigue limit in Regime I and the mechanical threshold in Regime III differ. In Regime I, small cracks are arrested by microstructure blockage, while in Regime III they arrest if the mechanical state at the crack tip is insufficient to drive them. The former is considerably more sensitive to microstructure than the latter, and indeed is not subject to the same similitude and other LEFM requirements. General threshold conditions for nonpropagating cracks in each of the three regimes have been derived from these relations (McDowell, 1997), along with the specialized expressions for the completely reversed stress amplitude in the uniaxial case; here, σ_{FL} is the uniaxial fatigue limit. The Regime III threshold conforms to the LEFM threshold for mechanically small cracks. The model makes liberal use of standard constants based on fatigue tests above threshold, where a_i and a_f correspond to the initial and final crack length conditions which apply to these experiments. Most of the other parameters can be assessed from small crack observations (minima of FCGR and typical Kitagawa trajectories in Regime II) as well as the long crack threshold ΔK_{th}, as shown in Table 2.

Table 2. Identification of constants.

long crack LEFM threshold, ΔK_{th}
smooth specimen fatigue limit amplitude, σ_{FL}

r   *b/r is the slope of the transition regime in the uniaxial Kitagawa diagram, with typical values of r in the range of 0.2 to 0.5 for typical values of fatigue strength exponent b $\approx$ -0.1.*

d   *Discerned from minima of FCGR data for microstructurally small cracks (Wang & Miller 1992).*

k, D   *Established by intersection points on Kitagawa diagram for completely reversed uniaxial loading:*

$$k = \left(\frac{\Delta K_{th}}{\sigma_{FL}} \frac{1}{\sqrt{\pi d}} \right)^{\frac{2Mr}{Mr-1}} \quad , \quad D = \left(\frac{\Delta K_{th}}{\sigma_f'} \frac{1}{\sqrt{\pi k d}} \right)^{2Mr}$$

Constants A and B are selected to fit experimental data for crack growth rate in the

MSC Regime I. Figure 8 shows the Kitagawa diagram (logarithmic plot of stress amplitude versus crack length for threshold conditions) computed from the theory for completely reversed uniaxial loading, with branches corresponding to the threshold conditions in each Regime. The threshold curves for a < d and stresses below the fatigue limit σ_{FL} are computed using the MSC regime growth law with constant D_{aN} as specified in Table 1. This plot is very much characteristic of similar alloys as reported by Tanaka (1987) and Tanaka and Akiniwa (1989). Below these threshold stress amplitudes, cracks will arrest.
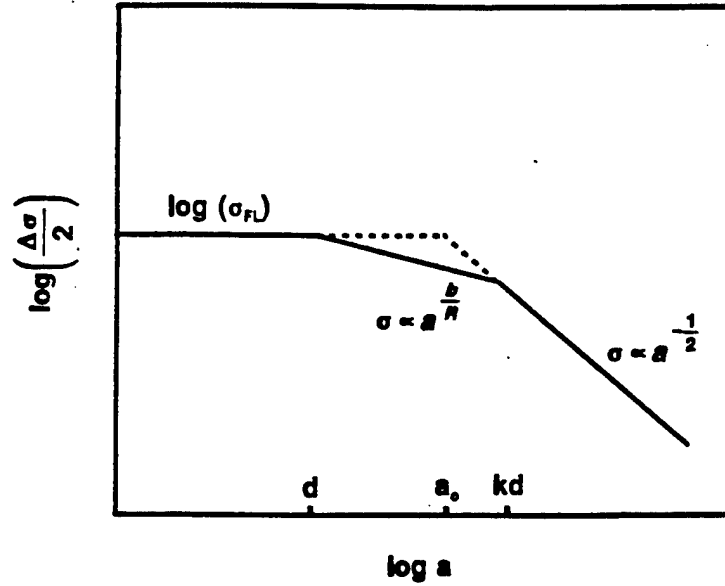
Figure 8 - Computed Kitagawa diagram for HCF thresholds, with multiple contours for cracks in MSC regime, corresponding to 10^8, 10^9 and 10^{10} cycles. Material: 1045 steel (McDowell, 1997).

In Figure 9 we plot the predicted FCGR under completely reversed uniaxial loading for cracks growing from 10μm initial length up to 1 mm in a manner that will be familiar to practitioners of LEFM and EPFM. An equivalent stress intensity factor range, ΔK_J, may be defined based on the ΔJ-integral (Dowling, 1977) according to

$$\Delta K_J = \sqrt{E \Delta J} = \sqrt{E(\Delta J_e + \Delta J_p)}$$

$$= \Delta \sigma \sqrt{\pi a} \sqrt{\frac{1}{\pi}\left(1.6 + \frac{4.25 E}{K'(1 + n')}\left(\frac{\Delta \sigma}{2K'}\right)^{\frac{1}{n'} - 1}\right)} \qquad (7)$$

As distinguished from $\Delta K = Y\Delta\sigma(\pi a)^{1/2}$, ΔK_J includes a contribution from plasticity

which may be very significant in the case of small cracks subjected to moderate to high remote stress amplitudes in the LCF regime. The calculated values of ΔK_J are based on only the fraction of the stress range (coefficient in Equation (1)) which is tensile, since closure effects are not explicitly considered. The characteristic dip in da/dN is evident in these calculations, as are a wide range of MSC Regime da/dN levels for different amplitudes; this dip is characteristic of experiments, and has also been predicted by plasticity-induced closure models which consider initially fully open small cracks growing from initial defects (Newman, 1994), analogous to short cracks growing from notches. The predicted da/dN versus ΔK_J trajectories generally approach the long crack R = 0 data (Hua and Socie, 1985) from the left, forming an asymptotic envelope. The minimum in da/dN is associated with the transition from Regime I to Regime II. Of course, for $\psi < (\psi_{th})_I$ the cracks would arrest at a = d, as shown for the lowest stress amplitude on the plot. The typical scatter for small crack behavior observed for moderate amplitudes to HCF can therefore be understood, at least some extent, to arise from deterministic amplitude dependence in addition to material microstructure variation, as pointed out in the plasticity-induced closure modeling of Newman (1994). The non-uniqueness of growth behavior in Figure 9 illustrates the apparent anomalies that can arise when interpreting small crack behavior in terms of standard long crack fracture mechanics, and the utility of the present framework.
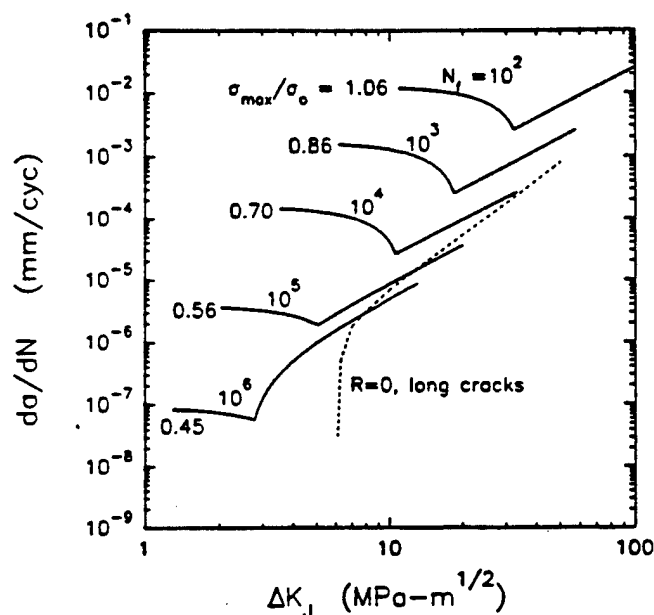
Figure 9 - Predicted da/dN versus ΔK_J for small cracks in 1045 steel for a range of completely reversed uniaxial stress amplitudes; $\sigma_o = 548$ MPa is the mean cyclic plastic flow stress (McDowell, 1997).

It is important to note that the framework presented here is more correlative than predictive in nature, but covers a broad range of crack lengths (including the MSC regime) and stress states that might be encountered in hot spot regions. This robustness, along with its its capacity for nonlinear amplitude and stress state sequence effects,

closed form integrability for constant amplitude loading (efficient for block loading integration), and compatibility with the format of crack growth required for consistency with the diagnostic inspection scheme based on distributed microsensors, renders such a framework particularly suitable for this particular class of applications. We have conducted axial-torsional fatigue experiments on AISI 304 SS, 1045 steel and preliminary tests on 13-8 PH Mo SS to evaluate sequence effect capabilities of model.

Once a crack propagates past the microstructurally small regime, it generally moves into Stage II propagation (mode I-dominated), but may still be under the influence of notch root gradients associated with the hot spot location. Hence, it is necessary to invoke the specific solution(s) obtained for each stress concentration to properly capture the change of fatigue crack driving force with crack extension. In some cases, the driving force falls off below threshold conditions to continue propagation, and crack arrest may occur. In other cases, the crack growth rate may accelerate, i.e. dK/da increases as the crack lengthens.

As the crack extends beyond the influence of the notch, the crack front often takes on a complex, tortuous path in response to the three-dimensional shape of the component. Complications arise for such mechanically long cracks due to phenomena such as premature crack face contact that reduces the driving force or wedging action that may enhance it, variation of crack driving force along the crack front and tunneling, complex changes of specimen compliance and associated dynamical response, etc. These are the principal technical challenges associated with the modeling the growth of long cracks in components. In most cases, the occurrence of long cracks represents a potential envelope condition for continued safe operation and therefore must be evaluated for impending criticality and associated component distress. It is the formation and early growth of such cracks that is of most practical interest to an integrated on-board diagnostic/prognostic system in terms of estimating service life well into the future.

References for Section 3.2

Dowling, N.E., 1977, "Crack Growth During Low-Cycle Fatigue of Smooth Axial Specimens," *Cyclic Stress-Strain and Plastic Deformation Aspects of Fatigue Crack Growth*, ASTM STP 63, pp. 97-121. Philadelphia: ASTM.

Hobson, P.D., 1985, "The Growth of Short Fatigue Cracks in a Medium Carbon Steel," PhD Thesis, University of Sheffield, Sheffield, UK.

Hobson, P.D., Brown, M.W. and de los Rios, E.R., 1986, "Two Phases of Short Crack Growth in a Medium Carbon Steel," in *The Behaviour of Short Fatigue Cracks*, K.J. Miller and E.R. de los Rios (eds), EGF Publ. 1, Inst. Mech. Engrs, London, pp. 441-459.

Hua, C.T. and Socie, D.F., 1985, "Fatigue Damage in 1045 Steel Under Variable Amplitude Biaxial Loading," *Fatigue Fract. Engng. Mater. Struct.*, Vol. 8, No. 2, pp. 101-114.

Hussain, K., de los Rios, E.R. and Navarro, A., 1993, "A Two-Stage Micromechanics Model for Short Fatigue Cracks," *Engng. Fract. Mech.*, Vol. 44, No. 3, pp. 425-436.

McDowell, D.L., 1996, "Basic Issues in the Mechanics of High Cycle Fatigue," *Int. J. Fracture*, Vol. 80, pp. 103-145.

McDowell, D.L. and Berard, J.-Y., 1992, "A ΔJ-based approach to biaxial fatigue," *Fatigue Fract. Engng. Mater. Struct.*, Vol. 15, No. 8, pp. 719-741.

McDowell, D.L. and Bennett, V.P., 1996, "A Microcrack Growth Law for Multiaxial

Fatigue," *Fatigue Fract. Engng. Mater. Struct.* Vol. 19, No. 7, pp. 821-837.

McDowell, D.L., 1997, "Multiaxial Small Fatigue Crack Growth in Metals," to appear in *Int. J. Fatigue*.

Miller, K.J., 1993, "The Two Thresholds of Fatigue Behaviour," *Fatigue Fract. Engng. Mater. Struct.,* Vol. 16, No. 9, pp. 931-939.

Newman, J.C., Jr., 1994, "A Review of Modelling Small-Crack Behavior and Fatigue-Life Predictions for Aluminum Alloys," *Fatigue Fract. Engng. Mater. Struct.,* Vol. 17, No. 4, pp. 429-439.

Nisitani, H., 1987, "Behavior of Small Cracks in Fatigue and Relating Phenomena," in *Current Research on Fatigue Cracks*, T. Tanaka, M. Jono and K. Komai (eds), Current Japanese Materials Research, Elsevier, Vol 1, pp. 1-26.

Nisitani, H., Kawagoishi, N. and Goto, M., "Growth Behavior of Small Fatigue Cracks and Relating Problems," Handbook of Fatigue Crack Propagation in Metallic Structures, Andrea Carpinteri, Ed., 1994, pp. 733-778.

Patel, A., 1997, "Growth of Small Fatigue Cracks in PH 13-8 Mo Stainless Steel ," M.S. Thesis, Georgia Instititute of Technology, Atlanta, GA.

Socie, D.F., 1993, "Critical Plane Approaches for Multiaxial Fatigue Damage Assessment," in *Advances in Multiaxial Fatigue*, ASTM STP 1191, D.L. McDowell and R. Ellis (eds), pp. 7-36. Philadelphia: ASTM.

Tanaka, K., 1987, "Short-Crack Fracture Mechanics in Fatigue Conditions," in *Current Research on Fatigue Cracks*, T. Tanaka, M. Jono and K. Komai (eds), Current Japanese Materials Research, Elsevier, Vol 1, pp. 93-117.

Tanaka, K. and Akiniwa, Y., 1989, "Propagation and Non-Propagation of Small Fatigue Cracks," in Advances in Fracture Research, Proc. ICF7, Houston, TX, March 20-24, Vol. 2, pp. 869-887.

Wang, C.H. and Miller, K.J., 1992, "The Effects of Mean and Alternating Shear Stresses on Short Fatigue Crack Growth Rates," *Fatigue Fract. Engng. Mater. Struct.,* Vol. 15, No. 12, pp. 1223-1236.

Wang, C.H., 1996, "Effect of Stress Ratio on Short Fatigue Crack Growth," *ASME J. Engng. Mater. Techn.,* Vol. 118, pp. 362-366.

3.3 Microstructural Studies of Crack Propagation

Figure 10 compares experimental measurements in our laboratory (Patel, 1997) for microstructurally small crack growth in PH 13-8 Mo stainless steel, a corrosion-resistant alloy for use in the next generation rotor hubs, with predictions using a sequential grain boundary blockage model (Wang, 1996). Most of this study focused on the small crack growth behavior to determine the limit of the applicability of conventional fracture mechanics which is often used in remaining life prediction methodologies. Constants for long crack growth models were also determined for this material. The experimental details are given in Patel et al. (1999). Much of the data needed for the remaining life prediction schemes is provided in the paper. In addition, two fatigue crack growth models (Newman, 1981; Wang, 1996) for predicting the growth of small cracks were evaluated. The details are given in Patel (1997).
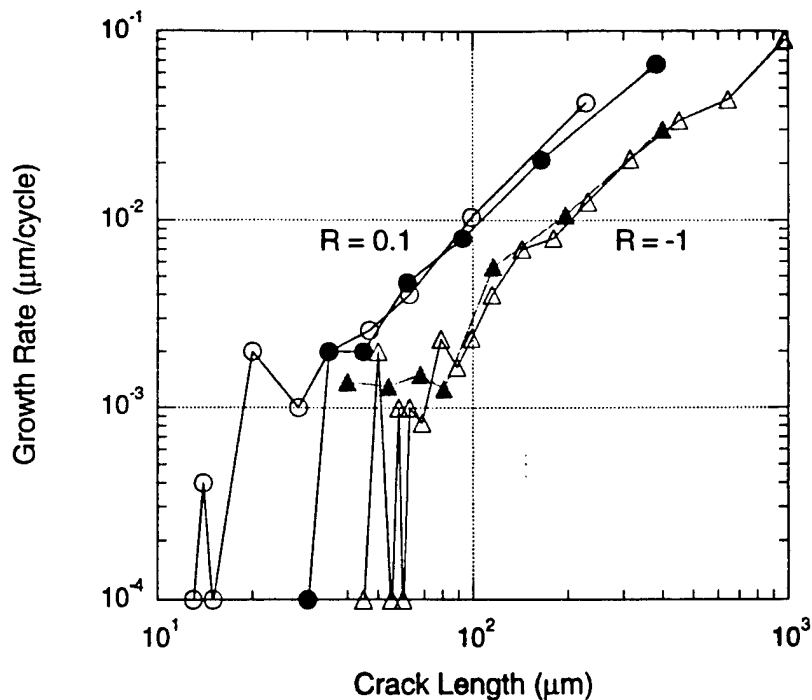
Figure 10 - Comparison of predicted and experimentally measured crack length versus cycles in 13-8 PH Mo stainless steel at room temperature (Patel, 1997).

3.3.1 Fatigue Crack Initiation and Growth Mechanisms in Helicoptor Rotor Materials

Fatigue crack initiation usually accounts for a significant fraction of the lives of engineering components such as helicopter rotors subjected to cyclic loading. Also, critical helicopter components are designed for damage tolerance because nondestructive techniques can reliably only detect cracks that are on the order of few millimeters. Therefore, a detailed understanding of both fatigue crack initiation and growth is essential for predicting remaining life, for improving the total fatigue life, and for reliably detecting cracks in order to take corrective actions to avoid catastrophic failures in critical components. Fatigue crack initiation usually occurs at locations where discontinuities are present or where plastic strain accumulates preferentially in the form of slip bands. For components free of significant internal defects, free surface is frequently the site for fatigue crack initiation. When the cyclic strain range reaches the levels required for plastic deformation, long-range dislocation motion takes place. Since some fraction of dislocations continuously emerge at the surface while the others pile-up against internal obstacles, slip bands on the surface evolve in the form of intrusions and extrusions, subsequently acting as stress concentrators and facilitating the nucleation of fatigue cracks. The growth of fatigue cracks, especially ones that are small in relation to the microstructural features, interact extensively with the microstructure which can alter their path away from the direction normal to the loading and can significantly influence their growth kinetics.

Several new and novel techniques, such as atomic force microscopy (AFM), nanoindentation hardness testing and impedance microscopy are being employed to

observe and quantify fatigue crack initiation and early damage development and crack growth in two helicopter rotor materials and a model material. The AFM technique has been used to study fatigue damage in one prior study [3.1] but the latter two are being used for the first time. For comparison and for assessment of the new techniques, established techniques such as scanning electron microscopy and optical microscopy are also employed.

Test Materials

The mechanisms of fatigue crack initiation and growth are being investigated as part of this project in three different materials including (a) American Iron and Steel Institute (AISI) 4340 steel in quenched and tempered as well as in annealed condition (b) 13-8 PH stainless steels and (c) C101 high purity grade copper. While the first two materials are of direct interest for helicopter rotor applications, copper is a model material and is very well suited for developing techniques such as atomic force microscopy (AFM) and impedance spectroscopy (IS) for studying fatigue mechanisms and then transferring the concepts and techniques to other microstructurally more complex materials such as 4340 and 13-8 PH steels.

The 4340 steel used in this research was acquired in the form of 50.8mm diameter bar. The compositions of the 4340 steel are listed in Table 2. To study the influence of various microstructures, two heat treatments were applied to the steel used in our research. The annealed steel consists of coarse pearlite domains and some proeutectoid ferrite, while the quenched and tempered steel consists of tempered martensite. Microstructural analyses along different orientations and at different locations of the bulk steel show that the microstructures are homogeneous for both heat treatment conditions. Table 3 provides the tensile properties of the steel under the two conditions. The fatigue crack growth behavior of the test material in the two conditions is reported in a recent paper [3.2].

13-8 PH is a martensitic precipitation-hardening stainless steel with low carbon content used in applications that require corrosion resistance, high strength, high fracture toughness and oxidation resistance to temperatures of up to 425 °C [3.3]. Table 4 shows the chemical composition of the alloy and the tensile properties are given in Table 3. The resistance to corrosion is mainly provided by a surface passivation layer of chrome-oxide, which is further reinforced by the presence of molybdenum which reduces the tendency for pitting in salt water environment [3.4]. The material was obtained in the form of solution treated bar 14.5 mm in diameter. It was subsequently aged in-house for 4 hours at 566°C in Argon environment. The resulting microstructure consists of essentially martensite lathes that also contain spherical intermetallic β-NiAl precipitates of less than 7nm size that are coherent with the matrix [3.5].

The chemical composition of the high purity grade C101 copper is given in Table 5. The material was heat-treated for 1 hour at 500°C to obtain uniformly shaped grains. The size of the grains ranged from 10 to 100 μm in size with an average value of approximately 40 μm. The mechanical properties of the copper are provided in Table 3.

Results and Discussion

In this section, some of the most significant results from this phase of the project over the past four years and the future work to be completed before the end of the project in

June of 2000 are briefly summarized. Also, the significance of the results in remaining fatigue life prediction and for the development of warning systems against catastrophic fatigue failures is briefly discussed.

Atomic Force Microscopy: The quantitative understanding of fatigue crack initiation has been limited by the lack of techniques to accurately observe and obtain quantitative measurements of slip band evolution during different stages of fatigue. Most of the small-crack measurement techniques used in previous studies [3.6-3.9] lack the necessary resolution to measure slip band characteristics. Typically, the height and spacing of the slip bands can reach several microns in single crystals [3.10], but their sizes are expected to be in the submicron range in polycrystals and are expected to decrease as the grain size decreases [3.1]. Scanning electron microscopy (SEM) has a typical resolution of ≥ 100 A. Transmission electron microscopy (TEM) of thin films has a lateral resolution of ≥ 2 A, but is not suited for a surface topographic image. Although TEM analysis of thin replica films shadowed with heavy metal can provide surface topography information, the experimental difficulties and uncertainties associated with the replication process severely constrain the applicability of TEM replica in the investigation of nanometer scale features. Most importantly, both SEM and TEM cannot provide quantitative information about the vertical depths of surface features, which are key to the measurement of slip bands.

By scanning a sharp stylus over a surface, AFM is capable of imaging solid samples with the lateral resolution of 2 Å and the vertical resolution of 0.1 Å [3.11,3.12]. The contrast of AFM image comes from the digital difference of vertical depths of the surface features. Consequently, the accurate depth and space of the surface features can be reliably obtained by using attached data analysis software. As long as the slip bands on a specimen surface are larger than the surface roughness, AFM can perform the quantitative measurement of the slip bands and the surface topography. In this research, AFM technique is explored for observing slip bands produced by cyclic plastic deformation on the surface of 4340 steel in quenched and tempered condition, on 13-8 PH stainless steel and on copper. We have come across one previous study on the use of AFM for observing slip bands produced by fatigue [3.1]. In this previous study, two different metals (a titanium alloy and a high strength low alloy steel) were fatigue tested under plastic strain ranges for ten thousand cycles, then the fatigue slip bands were measured. We have focused our research on the evolution of surface topological features at different stages of fatigue.

To first assess the potential of the AFM technique for characterizing surface features, a few specimens for which the microstructure is well established were subjected to AFM examination. Figure 11 shows the AFM image of a 35 x 35 µm scanning area on the annealed steel sample and a cross-section analysis of the image. Clear image and digital information are provided. As the scanning area decreases, the AFM resolution increases as shown in Figure 12 for a 3.5 x 3.5 µm pearlite colony on the same sample as in the previous image. The cross-section analysis of this image provides detailed information about the spacing and height of the cementite plates. For example, the first pair markers 1-1 show that the distance between the two adjacent cementite plates is approximately 550 nm, while the second pair markers 2-2 demonstrate that the corresponding cementite plate is approximately 300 nm high. The same test was performed on the martensite steel

samples and the corresponding microstructure dimensions were obtained. Therefore, the AFM is suitable for producing high quality images and accurate quantitative surface topographic information on the steel samples. The as-polished flat metallographic samples were also subjected to AFM examination to obtain the base-line surface roughness. From a 7 x 7 μm scanning area, the as-polished annealed steel sample showed a root mean square (RMS) surface roughness of 9.76 nm, while the quenched and tempered sample shows a RMS roughness of 11.41 nm. With the scanning area of 35 x 35 μm, the RMS roughness becomes 11.50 nm and 14.40 nm for the annealed and the quenched and tempered steels, respectively. These roughness values suggest that the polishing process produces similar roughness for the two steels.

Figure 13 shows the AFM image of a 35 x 35 μm scanning area on the untested LCF specimen and the cross-section analysis in both transverse and axial directions. The transverse sectioning trace shows the specimen curvature, while the longitudinal sectioning trace shows a straight base-line. The RMS roughness of this image is 55.15 nm which is significantly higher than that of the as-polished flat metallographic samples. The measured RMS roughness of the untested LCF specimens, with the scanning area of 7 x 7 μm, is about 11 and 8 nm for the annealed and the quenched and tempered steels, respectively. These roughness data agree well with the roughness of the flat metallographic samples showing insignificant influence of the specimen curvature. Therefore, 7 x 7 μm was chosen as the optimum scanning area on all the LCF specimens.

Figure 14 shows the AFM image and the surface profile of untested specimen LCFA1. Cementite platlets protrude from the ferrite base with heights ranging from 25 to 50 nm. In the specimen that was cycled for 1050 cycles at 1.5 % strain range, the slip bands show varying heights and widths, Figure 15. The surface profile of the image shows the height of one slip step as being approximately 100 nm, as indicated by the marker pair 1-1. The 2-2 marker pair shows the distance between adjacent slip steps to be approximately 218 nm. In the case of quenched and tempered conditions, because the martensite has a fine lathe microstructure, it is difficult to distinguish the plastic slip steps within the small martensite lathes.

Root mean square (RMS) surface roughness of the various LCF specimens tested from the annealed and quenched and tempered microstructures of 4340 steel were characterized and recorded. Figure 16 shows the RMS roughness as a function of the LCF cycles. The surface roughness clearly increases as fatigue cycles increase. Linear regressions of the two groups of the data shown in Figure 17 demonstrate that the trends of the roughness increase with fatigue cycles are similar for both annealed and the quenched and tempered steels. However, the annealed steel seems to have a larger scatter in the roughness data than the quenched and tempered steel. This may be due to the coarser microstructural features in the annealed steel consisting of pearlite and pro-eutectoid ferrite. The topographic changes due to plastic deformation are different in the two phases. Because the 7 x 7 μm scanning area is smaller than some pearlite domains, the measured surface roughness is strongly affected by the scan location leading to more scatter. On the other hand, the quenched and tempered steel has fine martensite lathes, leading to less scatter in the measured roughness among various scanning locations.

The correlation between surface roughness and the number of fatigue cycles has potential for predicting remaining fatigue crack initiation life in steels. However, tests at several intermediate lives and strain ranges are needed to establish such a correlation.

The results reported here are preliminary and must be followed by a more extensive test program.

The testing program and procedure for copper and 13-8 PH stainless steel are identical. Several specimens will be tested at the same strain amplitude and all but one test will be interrupted prior to failure allowing AFM surface topography characterization during different stages of the fatigue life. The tentative test matrix and the status of the tests completed are shown in Table 5. Copper will be tested first to identify the surface features of interest, and the investigation will then be extended to 13-8 PH stainless steel using a similar test matrix.

Figure 17 shows scanning electron microscope (SEM) images of slip bands at the surface of a copper specimen tested at $\Delta\varepsilon/2=.255\%$ until the appearance of a macroscopically visible crack. The uniform distribution of slip bands is characteristic of this strain amplitude at which considerable plastic deformation takes place. Figure 18 shows a 14x14 μm^2 AFM scan of this specimen, and a cross-section surface roughness scan along the line shown on the image. The average slip band height and spacing is .24 μm and 1.38 μm, respectively. The slip bands in the region with the line make a 45° angle with the loading axis and a 73° angle with the slip bands in the domain directly above. The root mean square roughness for this field of view is .16 μm. These values show that detailed measurements of the surface are possible using AFM. The analysis of surface features at several applied strain amplitude and different stages of fatigue will provide an extensive characterization of the evolution of surface damage during fatigue. The goal of this investigation is to determine parameters that uniquely characterize damage evolution during cyclic loading and to propose a physically based criterion for crack nucleation. The test matrix and the AFM analysis are due for completion by July of 1999.

Specimens of 13-8 PH stainless steel will be tested following the completion of the tests on copper specimens. SEM observations of an overaged stainless steel specimen tested 3320 cycles to failure at $\Delta\varepsilon/2= .5\%$ are shown in Figure 19. Surface slip was concentrated in a band 2.5 mm wide around the crack, and decreased with increasing distance from the crack. A set of optimally aged specimens is currently under preparation for testing (mechanical and electrochemical polish). This test matrix is expected to be completed by end of September 1999.

Nanoindentation Hardness Technique: The objectives for this aspect of the research is to better understand the interactions among the growing fatigue crack, the microstructure encountered by the crack, and the cyclic plasticity that develops in a small zone ahead of the fatigue crack. While previous studies have attempted to relate microstructure to fatigue crack growth resistance, the role of crack tip plasticity in determining the microstructure/crack interactions has not been investigated. In this study, fatigue crack growth tests were performed in the pearlite-ferrite and the tempered martensite microstructures. The microstructure/crack interaction was characterized using optical microscopy and scanning electron microscopy. Subsequently, nanoindentation hardness tests were performed to characterize the crack tip plasticity in various specimens. The results are used to shed more light on ways to improve the fatigue resistance of helicopter rotor parts.

Under cyclic plastic deformation, a metal may harden, soften, or remain stable, depending on the microstructure and test conditions such as the strain amplitude of the

fatigue cycle employed. Since hardness of a metal is directly correlated to its yield strength, the cyclic deformation zone may be delineated with precise hardness measurement around the crack tip. Nanoindentation hardness is a unique technique, which allows one to determine the mechanical properties down to the microstructural length scales. The definition and the calculation of the nanohardness are identical to the conventional Vickers hardness, but the former provides a much more accurate measure of hardness within smaller length scales.

Figures 20 and 21 show the plots of resulting hardness versus distance from the crack tip for the two heat treatment conditions. Figure 20 shows that the hardness close to the crack tip is higher than the far-field hardness, indicating that the annealed steel tends to cyclically harden. On the other hand, Figure 21 shows that the hardness decreases as one approaches the crack tip in the quenched and tempered steel, confirming a cyclic softening trend for this steel. In Figure 21, hardening is seen to occur even at distances in excess of 6000 μm. Thus, the monotonic plastic zone boundary is located at least that far away from the crack tip. The analytically estimated plastic zone size was 5757 μm which is in good agreement with the measured value. The analytically estimated fatigue plastic zone size is 870 μm which is also marked on Figure 20. This is also in good agreement with the onset of the plateau region of the hardness plot which is expected to coincide with the end of the fatigue plastic zone boundary. This result is extremely encouraging for nanoindentation hardness as a technique for studying microstucture/crack tip plasticity interactions. However, similar comparisons between the analytically estimated and measured fatigue and monotonic plastic zone sizes did not yield similar results for the quenched and tempered samples, Figure 21. In this instance, the measured zone sizes were considerably larger than the analytically calculated values. There are several possible reasons for this discrepancy, which have been discussed in reference [3.2].

This study of the mechanisms of fatigue crack growth in 4340 steels has led to the following conclusions. The microstructure plays an important role in determining the fatigue crack growth resistance of 4340 steel, especially in the low crack growth rate regime which is most important for helicopter rotors. The annealed steel, which has a coarser microstructure than the quenched and tempered steel, consistently has better fatigue crack growth resistance. The fatigue crack tends to grow within the ferrite base in the annealed steel, avoiding going through the cementite lamallae. In the quenched and tempered steel, the crack goes straight through the martensite lathes. The meandering of the cracks in the annealed steel to avoid going through cementite results in higher fatigue crack growth resistance. Nanoindentation technique has the potential for providing the data for understanding these microstructure/crack interactions. However, due to limited resources this technique is not being pursued any further within this project.

Impedance Spectroscopy: Impedance spectroscopy (IS) is a non-destructive method of material characterization, which has proven its effectiveness with various material systems. For instance, it has been used to determine corrosion rate and efficiency of corrosion inhibitors in metallic materials, to study the kinetics of electrochemical reaction (e.g. in batteries) and to investigate the bulk and surface properties of semi-conductor materials. The microstructural changes associated with fatigue damage in metals, such as multiplication and rearrangement of dislocations, increase in vacancy concentration and surface alterations (increase in roughness, microcrack formation), are likely to affect the

electrical properties of the material. IS has the potential to detect those changes and this study seeks to investigate the correlations between them. The implementation of such a method in industrial applications would have an enormous impact on economics and safety, (i) through prevention of premature retirement of expensive components from service, and (ii) through the ability to non-destructively determine the amount of fatigue damage in engineering components which would reduce the probability of service failures.

IS measurements are performed by applying an AC sinusoidal potential signal and monitoring the resulting current over a wide frequency range, typically 10^{-2} to 10^7 Hz. The impedance, Z^*, is a complex number representing the transfer function between the potential and the current. Depending on the evolution of the system being analyzed, some changes of the impedance spectra between measurements may appear minute. In that case, other formalisms may be used to emphasize those changes; they are the complex admittance, $Y^*=1/Z^*$, the electric modulus, M^*, and the complex permittivity, $\varepsilon^*=1/M^*$. M^* and Z^* are directly related to each other through geometrical parameters. For copper, the data is best represented through the admittance formalism. However, for 13-8 PH stainless steel, the complex impedance is best suitable. In the rest of the text, IS does not refer uniquely to impedance, but may involve any of the four basic formalisms (most generally, IS stands for Immittance Spectroscopy, which is a term denoting any of the four formalisms).

Fatigue tests have been performed on C101 high purity copper at a strain of $\Delta\varepsilon/2=.255\%$, and were interrupted at regular interval to perform IS measurements. One specimen was tested until the appearance of a macroscopically visible crack (specimen Cu-7), the other tests (Cu-9, Cu-10, Cu-11) were interrupted at certain fractions of the fatigue life.

Figure 22 shows the complex representations of the admittance spectra for specimen Cu-7 before cycling and after failure. Although both spectra taken at $N=N_f$ are smaller in magnitude than the spectrum measured before cycling, a significant difference exists between them. This type of discrepancy has been observed with other specimens as well, and it illustrates the challenge involved in the development of a method using IS to characterize the evolution of damage in fatigue. An identification of the parameters responsible for the discrepancies is necessary to accurately determine the influence of cyclic loading on the electrical response of a material. Furthermore, each test provides large amounts of data making the handling of the data and deciphering the most important parts of the data very challenging.

The spectra for specimen Cu-10, Figure 23, seems to follow the general trend of decreasing magnitude of the admittance as the number of cycle increases. This specimen also shows some variation of the spectra taken at $N=0$ and 100 cycles. IS spectra from specimen Cu-11 is shown in Figure 24. It shows the reduction in size of the half circle of the admittance with increasing number of cycles quite well. Systematic variations can be observed at certain fractions of life. Not all data obtained to date exhibit such well-behaved trends. Several improvements in data acquisition are being pursued to improve consistency in the data that is collected. IS has indeed potential for detecting structural changes experienced by materials during fatigue. To fully understand the relationship between the two, we need to identify the parameters that influence IS measurements. The future tests on copper and 13-8 PH stainless steel will address these issues.

References for Section 3.3.1

3.1 Harvey, S.E., Marsh, P.G. and Gerberich W.W., "Atomic Force Microscopy and Modeling of Fatigue Crack Initiation in Metals", Acta Metallurgica Materials, Vol.42, No. 10, 1994, pp 3493-3502

3.2 F.Yang, A.Saxena and L. Riester, "Use of Nanoindentation Technique for Studying Microstructure/Crack Interactions in Fatigue of 4340 Steel", Metallurgical and Materials Transactions A, Vol. 29A, 1998, pp 3029-3036.

3.3 Mil Handbook 5G, Nov.1, 1994, pp 2-147 – 2-156

3.4 Metals Handbook, ASM International, 1985

3.5 V.Seetharaman, M. Sundaraman, R.Krishnan, "Precipitation Hardening in a PH 13-8 Mo Stainless Steels" Materials Science and Engineering, Vol. 47. 1981, pp 1-11.

3.6 Swain, M.H., "Monitoring Small Crack Growth by Replication Method", Small-Crack Test Methods, ASTM STP 1149, American Society for Testing and Materials, 1992, pp 34-56.

3.7 Larsen, J.M., Jira, J.R. and Ravichandran, K.S., "Measurement of Small Cracks by Photomicroscopy: Experiments and Analysis", Small-Crack Test Methods, ASTM STP 1149, American Society for Testing and Materials, 1992, pp 57-80.

3.8 Sharpe, W.N., Jira, J.R. and Larsen, J.M. "Real-Time Measurement of Small Crack Opening Behavior Using an Interferometric Strain/Displacement Gage", ASTM STP 1149, American Society for Testing and Materials, 1992, pp 92-115.

3.9 Gangloff, R.P. Slavik, D.C., Piascik, R.S. and Vanstone, R.H. "Direct Current Electrical Potential Measurement of the Growth of Small Cracks", ASTM STP 1149, American Society of Testing and Materials, 1992, pp 116-168.

3.10 Fine, M.E.. and Chung, Y.W., "Fatigue Failure in Metals", ASM Handbook, Volume 19, Fatigue and Fracture, 1996, pp63-72.

3.11 Gould, S.A.C., Drake,B., Prater, C.B. et al., " The Atomic Force Microscope: A Tool for Science and Industry", Ultramicroscopy, Vol.33, 1990, pp 93-98.

3.12 "Metris-2000 Atomic Force Microscope", Operating Manual (Rev.E), Burleigh Instruments, Inc. Burleigh Park, Fishers, NY 14453-0755, 1997.

Table 2: Chemical composition of the 4340 steel bar (in weight %).

C	Cr	Mn	Mo	Ni	Si
.390	.82	.70	.26	1.70	.17

Table 3: Tensile Properties of the 4340 steel bar, 13-8 PH stainless steel and annealed C101 copper.

Material	σ_{uts} (MPa)	σ_{ys} (MPa)	RA (%)	Elongation (%)	Hardness
Annealed 4340	731	414	42.5		32 RC
Quenched + Tempered 4340	1124	1035	46.8		44 RC
13-8 PH Stainless Steel	1325	1286			42 RC
Annealed C101 Copper	210	33.3		60	10 RB

Table 4: Chemical composition of 13-8 PH stainless steel (in weight %).

Cr	Ni	Mo	Al	Si	C	Cu	Other Elements
12.41	8.28	2.2	1.02	.04	.033	.02	S, Mn, Co, Ti, Zr, P, Cb, W, V, N $\leq$ .01

Table 5: Chemical composition of C101 copper (in weight %).

Cu (% Min)	Ag	P	Te	Other Elements
99.99	—	.0003	.001	Se+Te+Bi+As+Sb+Sn+Mn=.004 Hg=Zn=Cd=.0001; S=.0018; Pb=Se=Bi=.001

Table 6: Test matrix for fatigue tests for both copper and PH 13-8 Mo stainless steel. All tests are to be performed at a strain rate of .005 s^{-1} to minimize the accumulation of heat that has been measured in stainless steel specimens at higher strain rates. (Tested = Test done; Planned = Test scheduled; None = No test scheduled)

Material	Expect total life	Actual total life	Fraction of life (N/N$_f$)				
			.1	.5	.75	.9	1
Copper	20,000	6,900	Tested	Tested	None	Planned	Tested
	100,000		None	None	Planned	Planned	Planned
13-8 PH stainless steel	20,000		Planned	Planned	None	Planned	Planned
	100,000		None	None	Planned	Planned	Planned
	200,000		None	None	Planned	Planned	Planned
	1,000,000		None	None	Planned	Planned	Planned
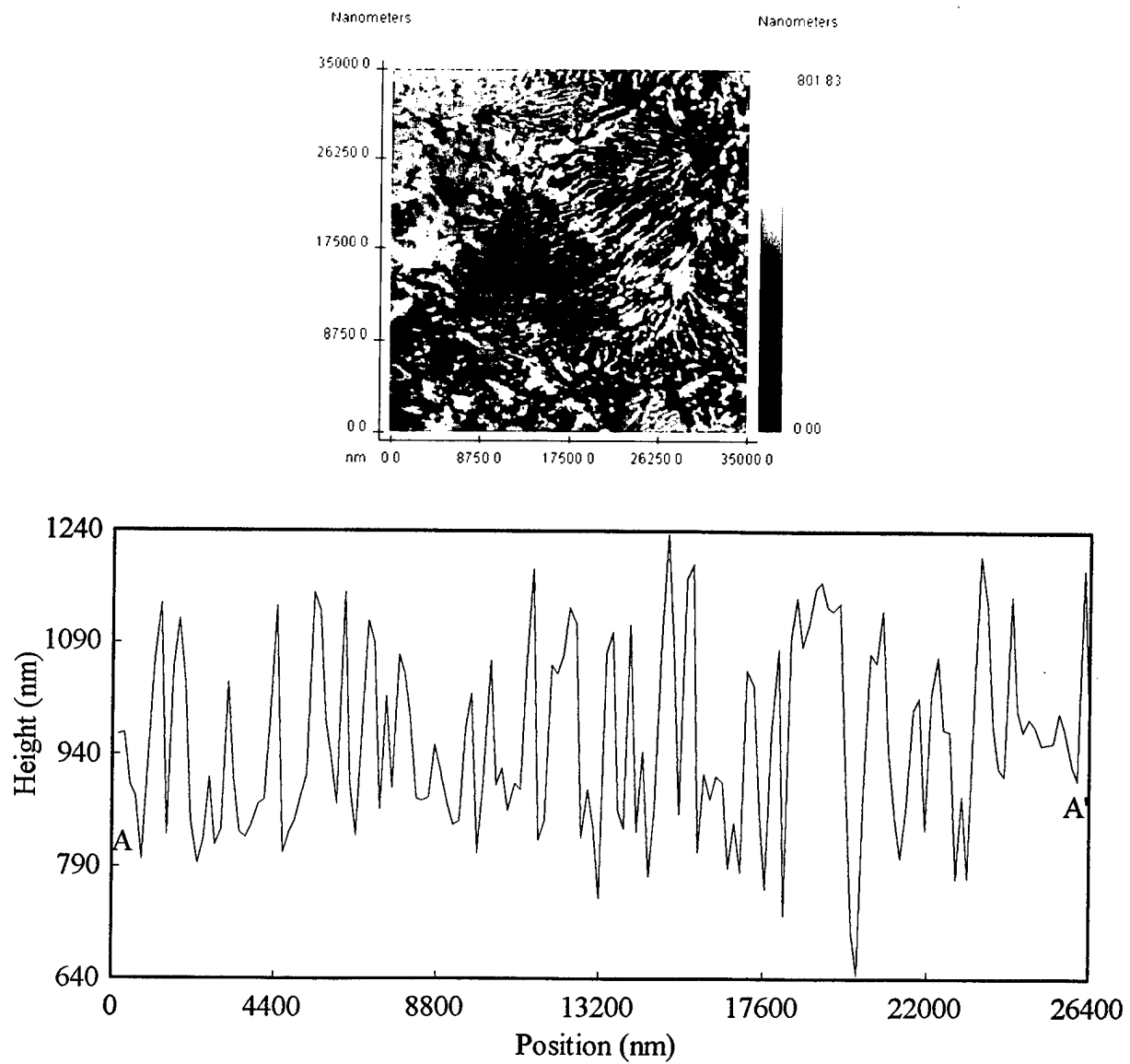
Figure 11 - AFM image of a 35x35 μm area of a flat polished and etched sample of annealed 4340 steel and a cross-sectional profile.
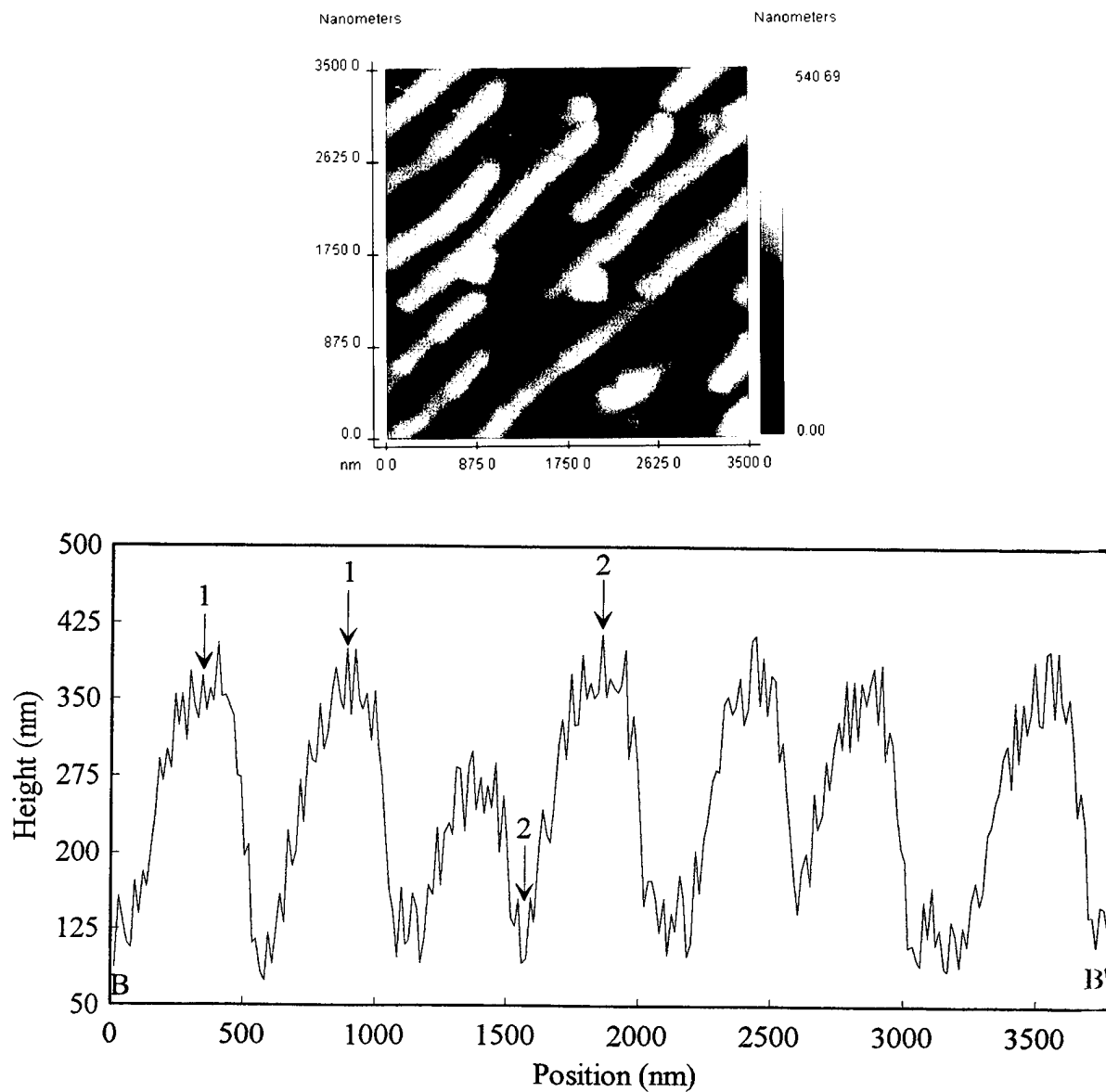
Figure 12 – A higher resolution AFM image and cross-sectional profile of a selected region from the previous figure.
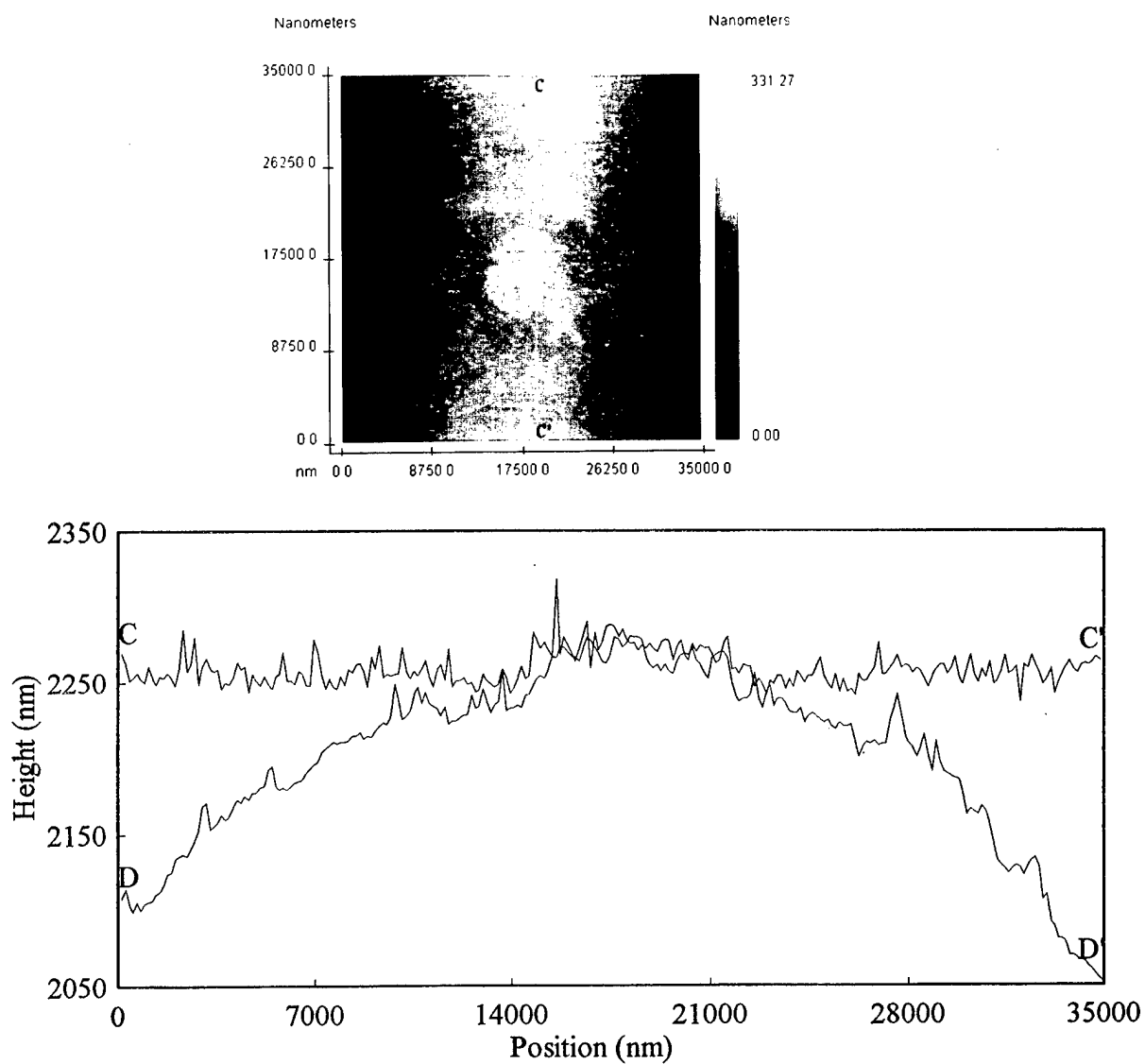
Figure 13 – AFM image of an untested cylindrical fatigue specimen and cross-section profiles along the axal direction and the transverse direction. The latter direction shows the curvature of the   specimen.
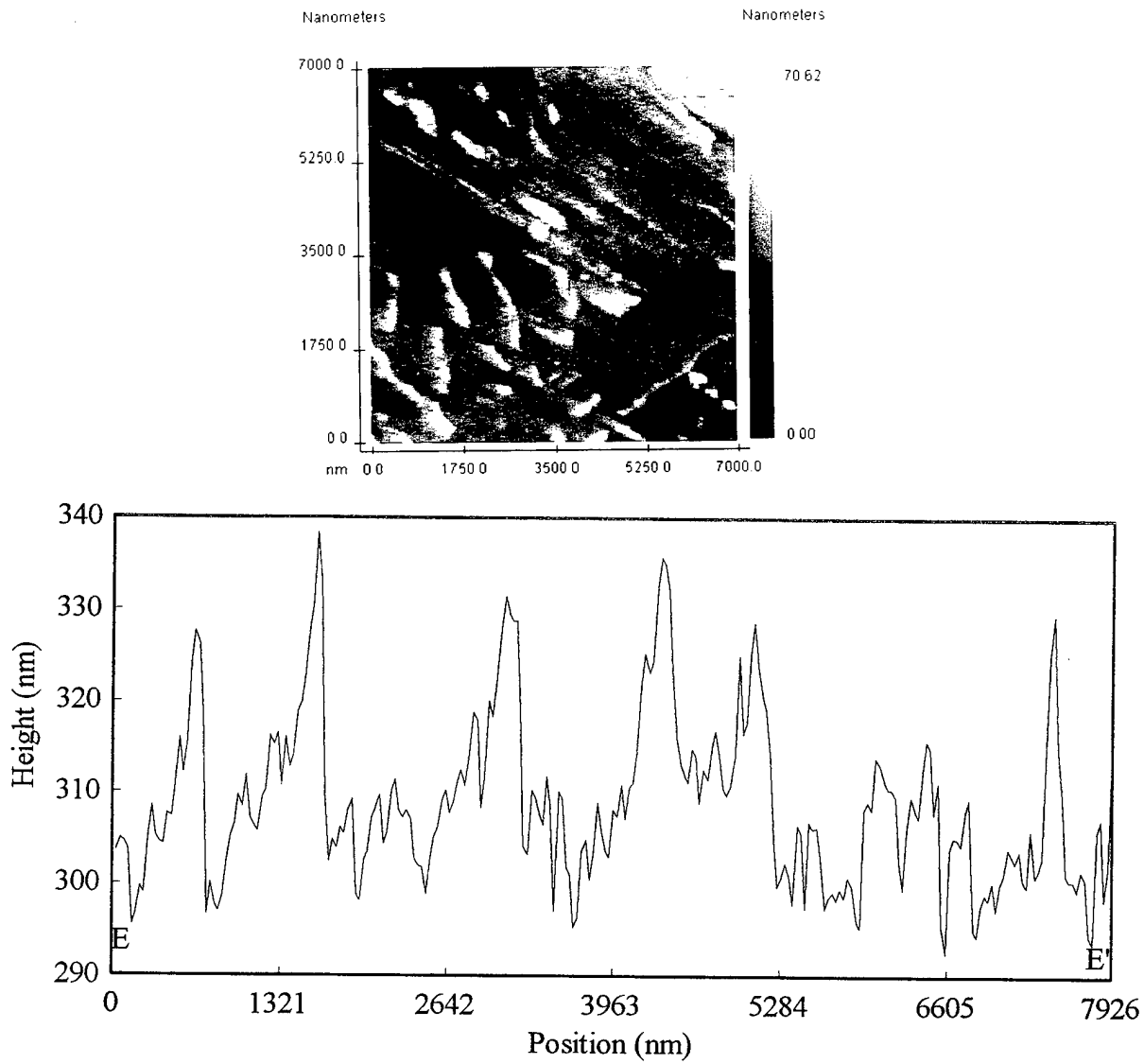
Figure 14 – AFM image of an annealed untested 4340 steel LCF specimen and a cross-sectional profile.
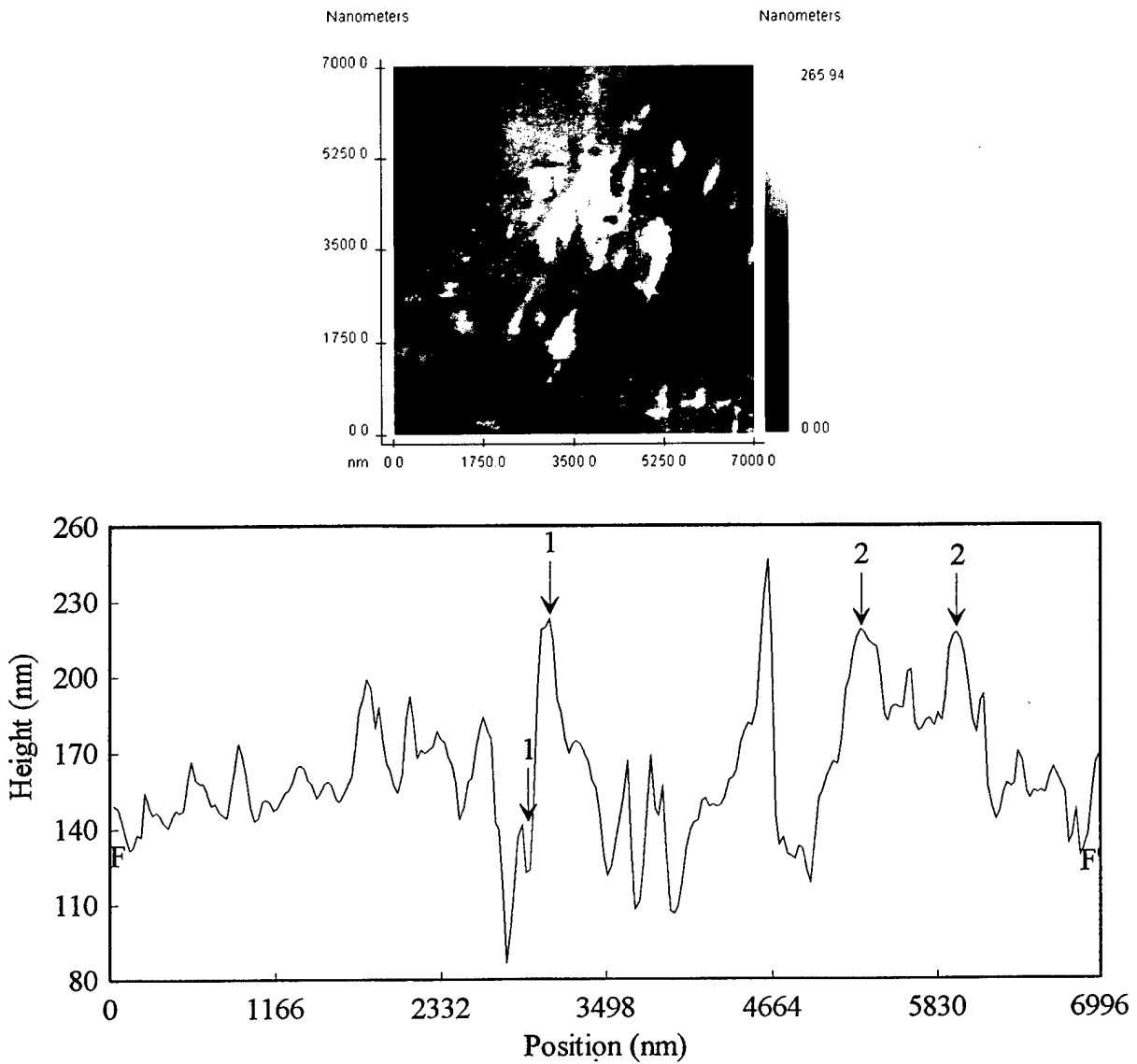
Figure 15 – AFM image and the surface profile of annealed 4340 steel LCF specimen fatigued for 1050 cycles at a strain range of 1.5 percent.
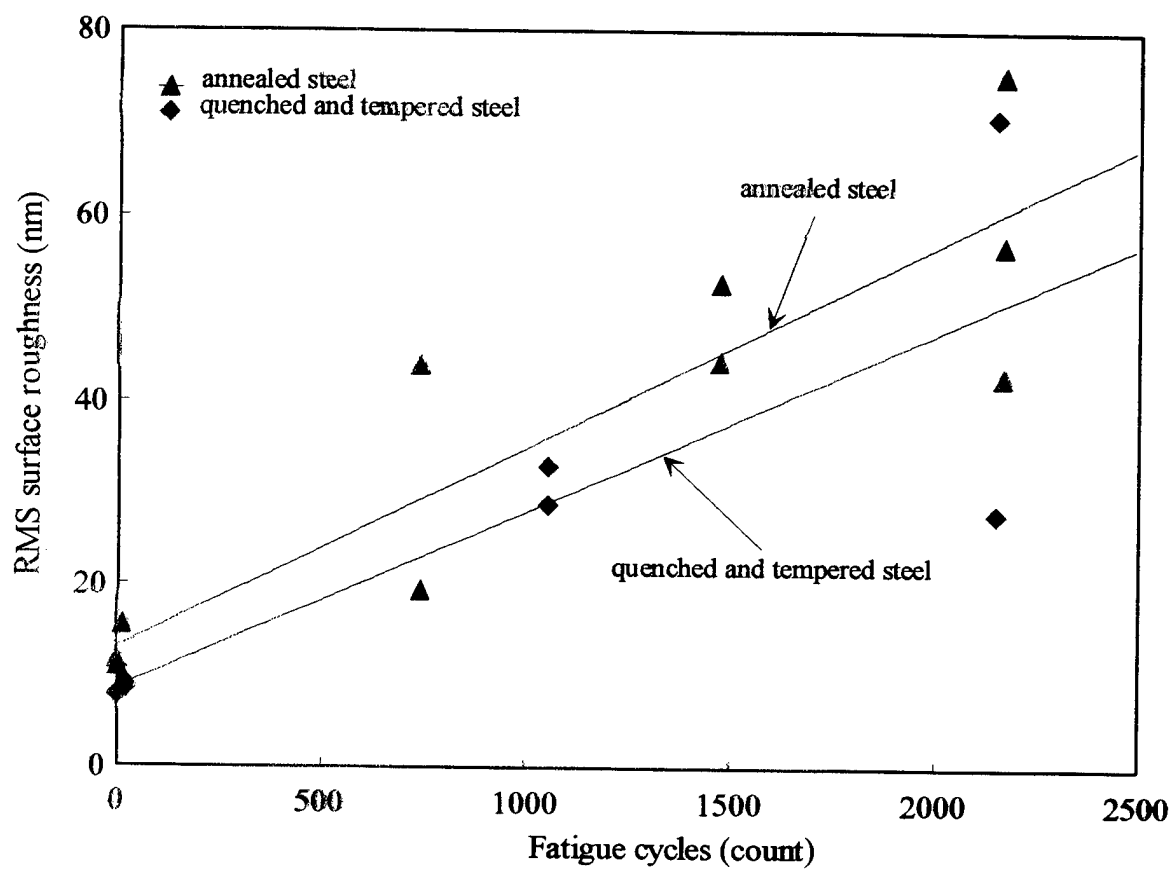
Figure 16 – RMS surface roughness versus fatigue cycles in annealed and quenched and tempered 4340 steel

(a)   Load Axis   (b)
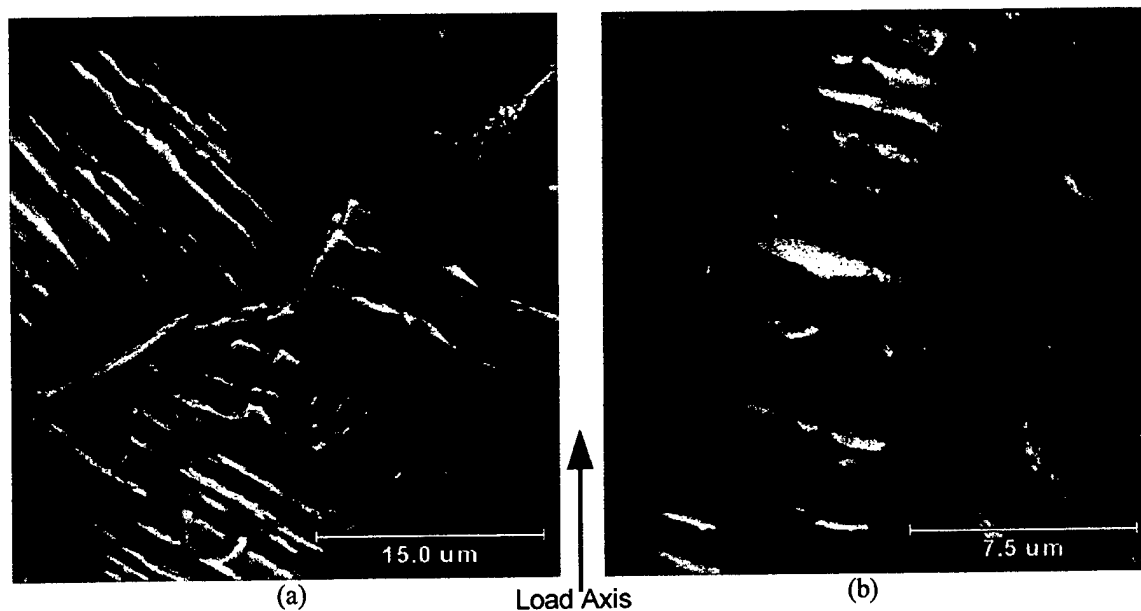
Figure 17 – scanning electron microscope (SEM) images of slip bands at the surface of a copper specimen tested at $\Delta\varepsilon/2=.255\%$ until the appearance of a macroscopically visible crack.
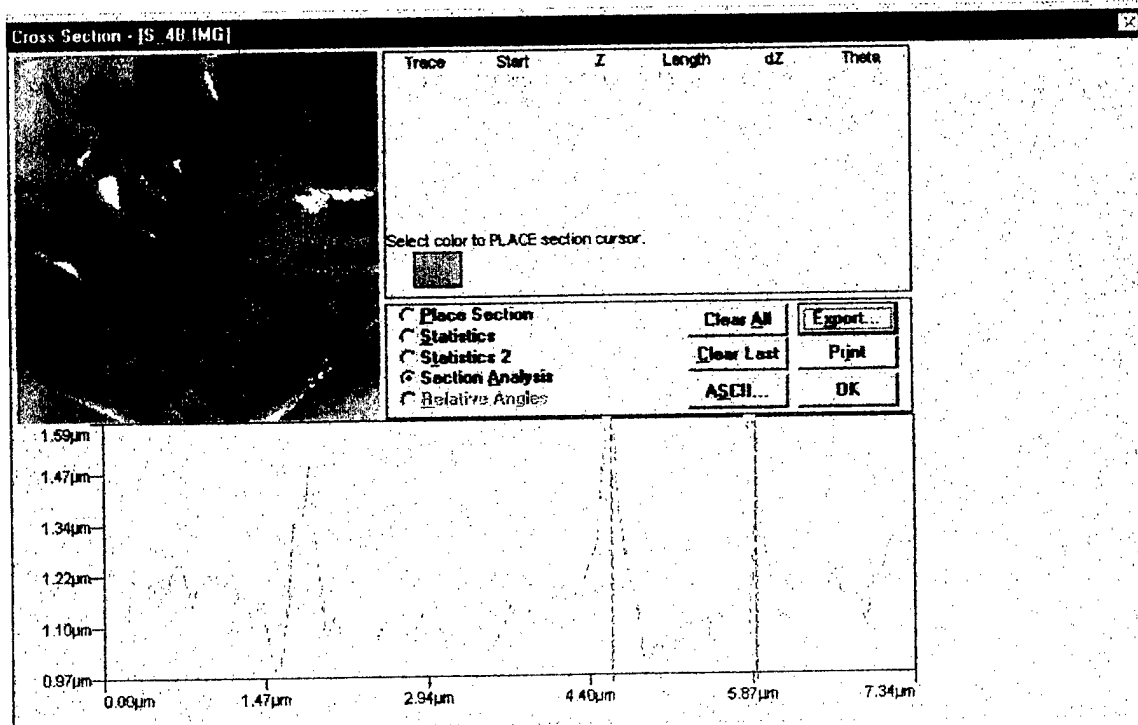
Figure 18 – 14x14 μm^2 AFM scan of the surface of a copper specimen tested at $\Delta\varepsilon/2=.255\%$ until the appearance of a macroscopically visible crack, and the cross-section surface roughness scan along the line shown on the image.

Load Axis

(a)   (b)
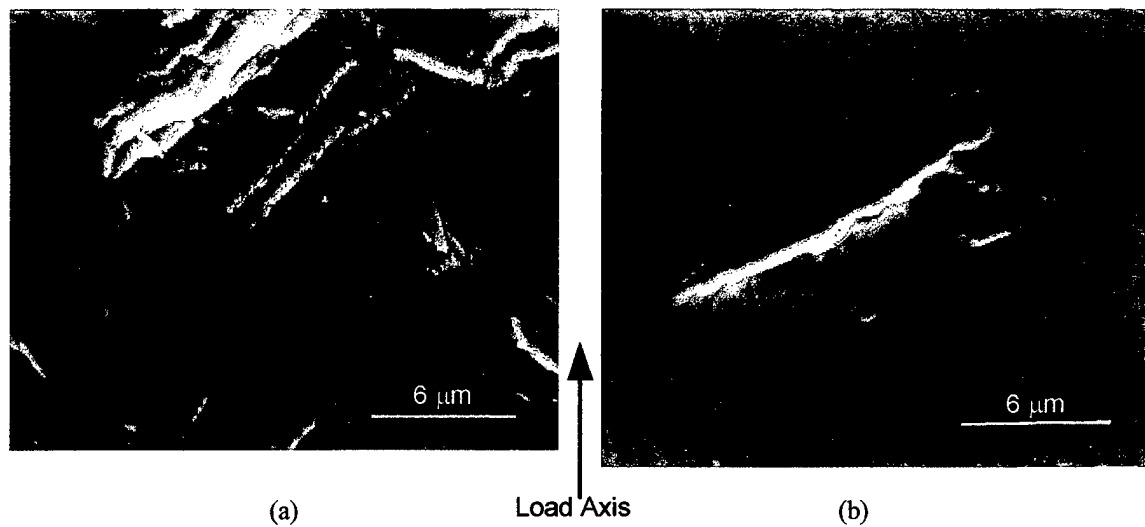
Figure 19 – SEM observations of an overaged 13-8 PH stainless steel specimen tested 3320 cycles to failure at $\Delta\varepsilon/2$= 0.5%. (a) was taken next to the crack and (b) 0.5 mm away from the crack, which shows significantly less slip. At 1.5 mm from the crack, no slip was observed.
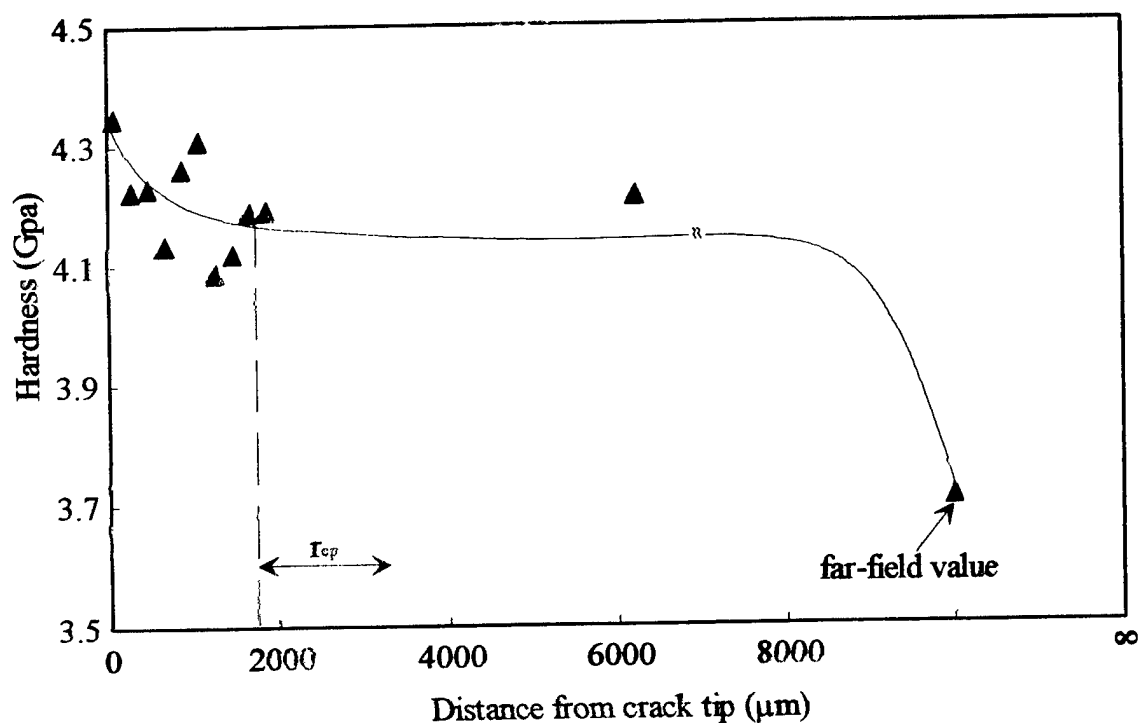
Figure 20 – Nanoindentation hardness versus distance from the crack tip of a fatigue crack growth 4340 steel specimen in annealed condition.
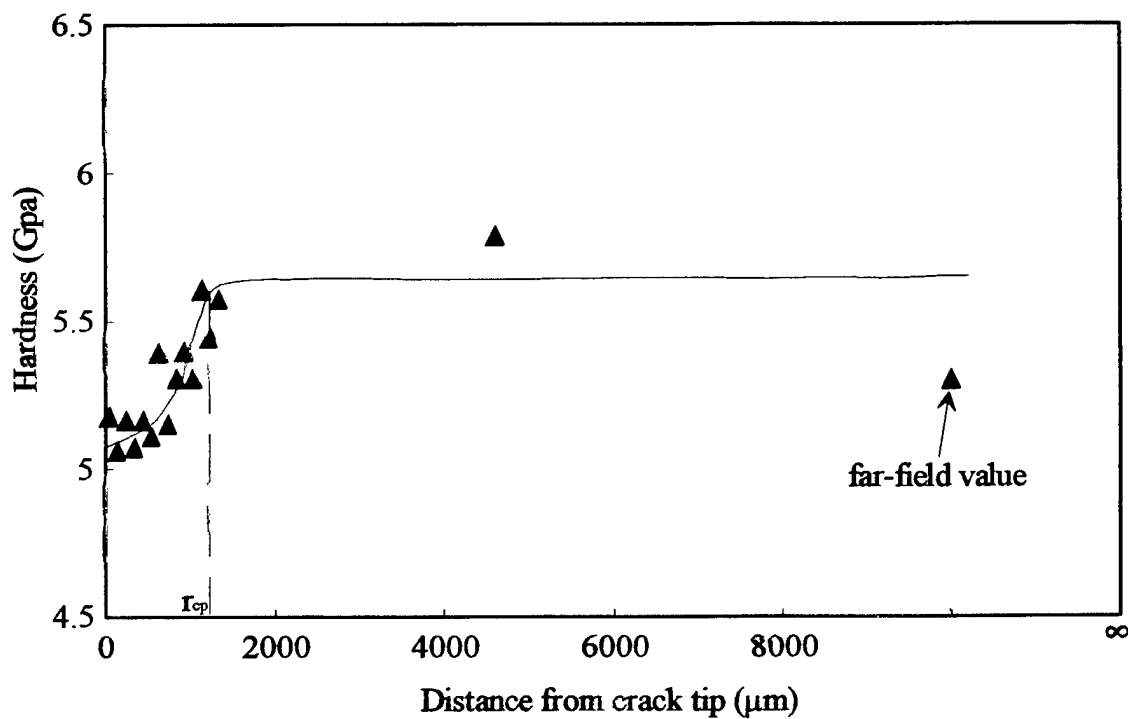
Figure 21 – Nanoindentation hardness as a function of distance from the crack tip from a fatigue crack growth specimen from quenched and tempered 4340 steel.
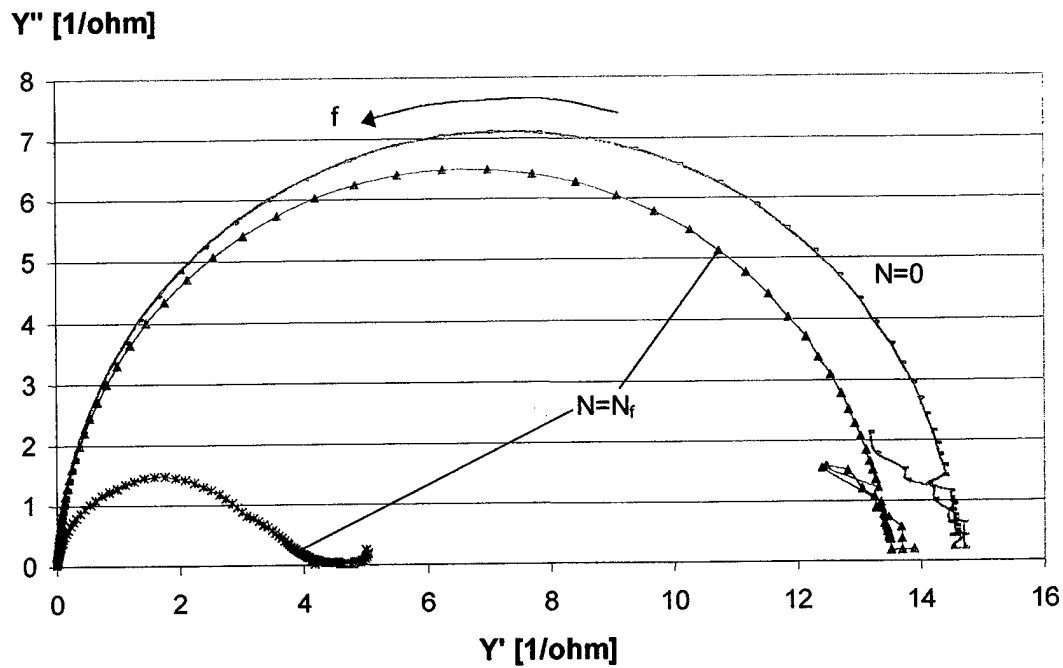
Figure 22 – Complex representations of the admittance spectra for specimen Cu-7 before cycling and after failure ($\Delta\varepsilon/2$=.255%, N_f= 6900 cycles).
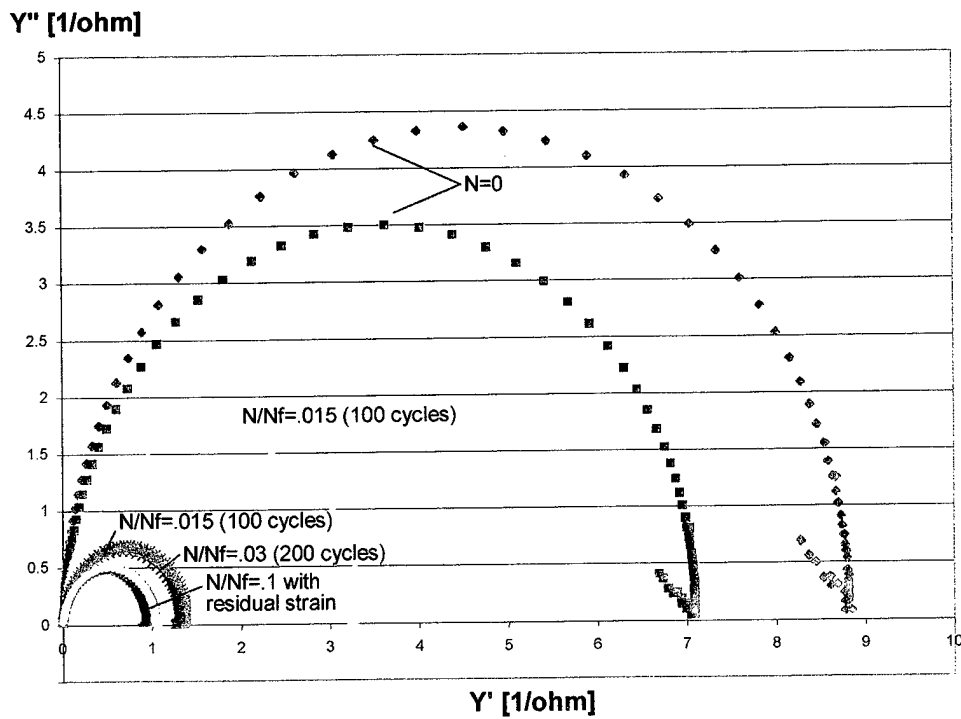
Figure 23 – Complex representations of the admittance spectra for specimen Cu-10 ($\Delta\varepsilon/2$=.255%, N_f= 6900 cycles).

Y" [1/ohm]
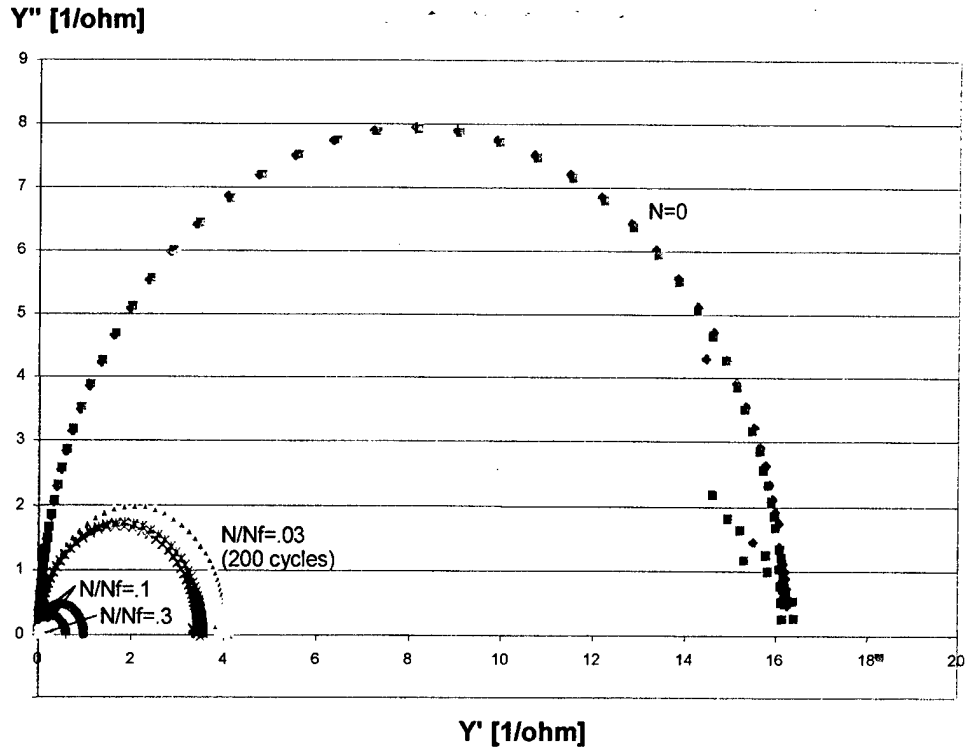
Figure 24 – Complex representations of the admittance spectra for specimen Cu-11 ($\Delta\varepsilon/2$=.255%, N_f= 6900 cycles).

3.3.2 Computational Micromechanics of Cyclically Loaded Polycrystalline Metals

To improve our understanding of the role of microstructure in small crack propagation, we have employed computational cyclic planar double slip crystal plasticity to develop a qualitative understanding of:

(i) the role of heterogeneity of grain orientation distribution on the cyclic microplasticity and other relevant candidate fatigue crack initiation parameters for polycrystals under nominally HCF loading conditions, and

(ii) crack tip opening and sliding displacements for microstructurally small surface cracks in polycrystals subjected to monotonic and cyclic loading as a function of crack length relative to grain size and applied stress state.

Understanding gained from these calculations is being used to develop an improved, "next generation" multi-stage small crack propagation law. There are two sources of mode mixity - on a *macro* level (combined loading situation), and on the *micro* level - which affect the propagation of small crystallographic cracks. This work explores mode mixity on the micro level by utilizing a computational model to simulate microstructural influences on driving forces for the formation and growth of small cracks. Two-dimensional computational cyclic crystal plasticity calculations have been conducted to study the distribution of cyclic slip and critical plane-type fatigue parameters in a material with nominal stress-strain characteristics of 4340 steel. Cases of applied cyclic tension-compression and cyclic shear have been analyzed at strain amplitudes below

macroscopic yielding. Emphasis is placed on stress state and amplitude dependence of the distribution of these parameters among grains. The role of anisotropic plasticity is isolated by assuming the elastic behavior of grains to obey homogeneous, isotropic linear elasticity. All grains are of equal dimension and are assigned a random orientation distribution. It is found that the distribution of the Fatemi-Socie critical plane fatigue parameter among grains is Weibull-distributed, and it is argued that it forms an improved linkage to cyclic crack tip displacement for microstructurally small cracks. We have also computed crack tip opening and sliding displacements as a function of maximum applied tensile strain (from well below to just above nominal yielding) for small cracks within surface grains surrounded by a nearly random orientation distribution of grains subject to both monotonic and cyclic remote loading conditions. Multiple realizations of the local microstructure are examined for each crack length for sub-grain size cracks, with results normalized to the ratio of crack length to grain size. Key results include a very strong role of the free surface on crack tip displacement, with opening displacement being much greater than the sliding for suitably small crystallographic cracks in the surface grains. There is also a strong effect of the orientation of the next grain ahead of the crack on local mode mixity of the crack tip displacements, which plays an increasingly influential role as the crack tip approaches the first grain boundary, with a lessened role for successive encounters with grain boundaries, analogous to previous idealized solutions based on pile-ups represented by continuously distributed dislocations, but different in detail. In effect, this work is the first-ever exploration of crack tip behavior in relative large scale polycrystal realizations.

Finite Element Models Based on Crystal Plasticity

A planar double slip idealization of cyclic crystal plasticity was implemented in ABAQUS [1] through the User MATerial subroutine, UMAT. Crystal plasticity models relate applied stress to the microscopic crystallographic slip response of the material. These models provide a phenomenological description of crystallographic slip and dislocation interactions at the grain level and offer insight into the nature of heterogeneous cyclic plasticity and driving forces for small crack growth due to intergranular misorientation. This micromechanical model is useful to (1) study the distribution of cyclic microslip amongst a set of grains in a polycrystal, (2) investigate the character of crack tip fields for small cracks in the presence of crystallographic anisotropy and heterogeneity, and (3) better understand the interaction of a crack with microstructural barriers. Naturally, the 2-D nature of planar double slip gives these calculations more qualitative value when assessing the influence of microstructure. Moreover, the effect of shear localization within slip bands is not explicitly treated with this model without the introduction of bands of preferred plastic flow or crystallographic systems with less resistance to flow. None-the-less, it offers a more direct treatment of crystallographic dislocation glide than most previous ad hoc models.

For an FCC crystal, there are 12 crystallographic slip systems in 3-D. For 2-D planar slip in a {110} plane, the deformation can be represented by a pair of effective slip systems [2]. These effective slip systems in 2-D (plane-strain assumption) maintain a fixed orientation with respect to each other and rotate with respect to the continuum. Figure 2a shows the geometry for the two effective slip systems. The bisector angle, θ, orients the slip system pair relative to the fixed specimen axis. The angle ϕ defines the

crystallographic close-packed planes in relation to the bisector angle, where $\phi = 35.1°$ for an FCC crystal.

The slip system level constitutive framework essentially follows that of Cailletaud et al. [3] and Jordan and Walker [4]. Pure nonlinear kinematic hardening was used to describe the cyclically stable response. To represent cyclically stable behavior, pure nonlinear kinematic hardening is employed according to the Armstrong-Frederick form. The backstress relates to long range interactions due, for example, to dislocation walls produced by cyclic loading and acts in the opposite direction of loading to resist deformation. Since the finest scale of resolution considered in the present model is the crystallographic slip system (CSS), it is assumed that all phenomena which are related to lengths scales below the grain level (e.g., atoms and lattice defects) are modeled at the CSS level using this phenomenological approach. The local resolved shear stress on each slip system is the driving force for the rate of dislocation shearing on each slip system. A backward Euler, fully implicit integration scheme was employed for the numerical integration. An incremental line search algorithm and a time step subincrementation scheme were both used to assist the rate of convergence [5]. The plane strain tension-compression hysteresis loops were assigned a behavior typical of uniaxial behavior of a 4340 steel for illustrative purposes, as shown in Fig. 25 for a 100 grain polycrystal. Elastic behavior in all calculations reported here is assumed to be isotropic and linear elastic. For certain metals such as Al and its alloys, the degree of elastic anisotropy is very mild, while for others it plays an important role.
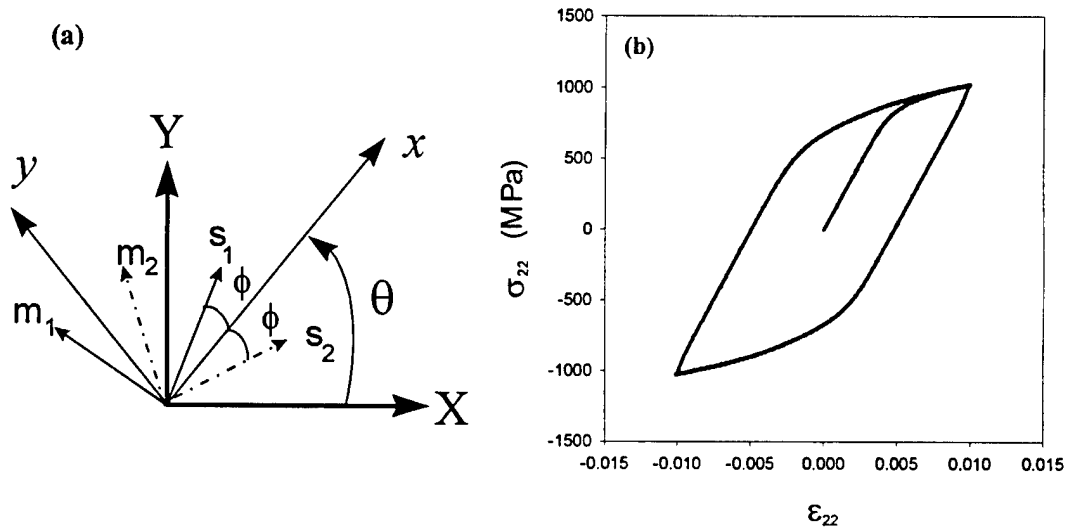

Fig. 25 - Simulation using planar double slip approximation: (a) assignment of bisector angle, and (b) cyclic stress-strain behavior of a 100 grain polycrystal subjected to cyclic tension-compression.

Polycrystal Distribution of Small Crack Formation and Growth Parameters

As discussed earlier, the extent and distribution of plasticity among grains is an important factor in fatigue crack formation and early Stage I growth. A direct measure of the cyclic microplasticity is the maximum cyclic plastic shear strain on a slip system normalized by the global cyclic plastic strain, defined here as the maximum cyclic plastic shear strain amplitude in individual grains normalized by the applied macroscopic cyclic plastic strain (N-CM parameter). Further, we consider similar distributions of two other prominent multiaxial fatigue correlation parameters, the Fatemi-Socie parameter (F-S)

$$\frac{\Delta \gamma_{max}^p}{2}\left(1 + k^{\cdot} \frac{\sigma_n^{max}}{\sigma_y}\right) = C_3$$

where C_3 is a constant for a given life, and the Mohr-Coulomb parameter (MC)

$$\frac{\Delta \tau_{max}^\alpha}{2} + k P_{hyd} = C_2$$

A series of 2-D (plane strain) finite element analyses were conducted to assess polycrystal distributions. The grains were modeled as 8-noded quadrilateral, biquadratic elements. A total of 576 grains were employed in the analyses. In each realization, grain orientations were randomly assigned to describe an initially isotropic effective medium. The strain amplitude levels for tension and shear ranged from well below to just above the total strain at the 0.2% offset plastic strain cyclic yield point (values are $\varepsilon_y = 0.006$ and $\gamma_y = 0.0063$, respectively) of the polycrystal. Strain was applied at an effective strain rate of 1.5×10^{-3} s^{-1}. Peak strain levels considered were fractions (0.3, 0.5, 0.7, 0.9, 1.0) of the cyclic total yield strain in order to investigate the cyclic microstrain distributions under predominately HCF conditions. A total of two completely reversed macroscopic strain cycles were applied to ensure a cyclically stable hysteresis loop in the simulation. The distribution of parameters among grains arising from microstructural inhomogeneity are assessed by the fitting of Probability Distribution Functions (PDFs). While details of each PDF is of little importance, the overall shape of these distributions may reveal useful information regarding the stress state and amplitude dependence of the driving forces for fatigue crack formation and microstructurally small crack propagation. They should not be confused with PDFs for fatigue strength per se, as it is only our intent to consider the distribution of various driving force parameters as a function of stress amplitude and stress state. For each strain level, the probability distribution among grains for normalized forms of the N-CM, F-S and MC parameters are shown in Fig. 26. With increasing strain, plots are skewed to the left. Error bars denote the range of the distribution obtained from several realizations of orientation distribution of grains; there is little variation among the simulations. Clearly, only a limited number of grains experience cyclic plastic strains that considerably exceed the macroscopic plastic strain; these grains are expected to control fatigue crack formation and early Stage I growth. For all strain levels considered here, the overall shapes of the distributions are very similar. In addition to such plots, we are also considering plots of distributions of the differences of these parameters among nearest neighbor grains and for different stress states.
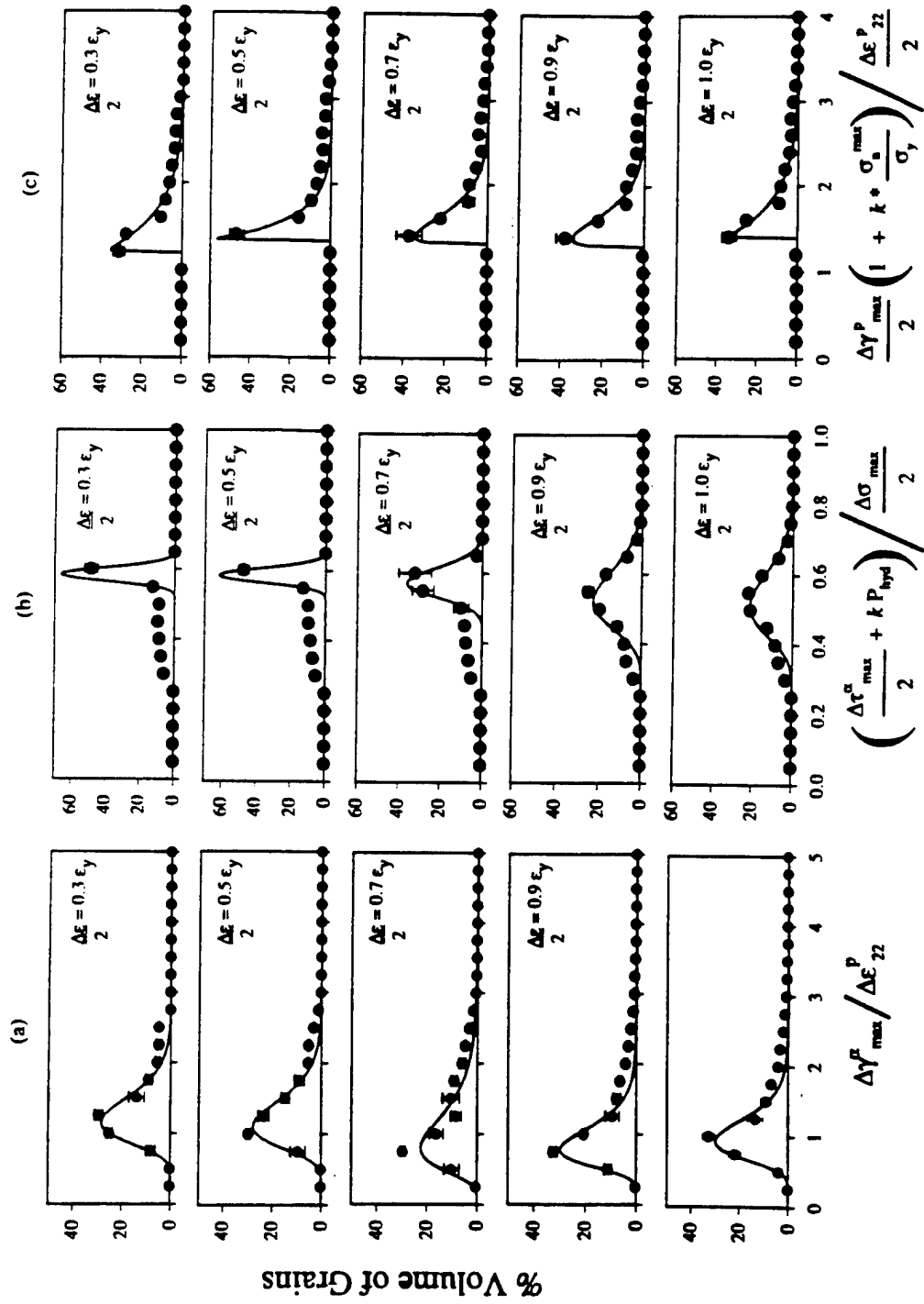
Fig. 26 - Distribution functions for the volume fraction of grains subjected to cyclic tension-compression loading for (a) the N-CM parameter, (b) the MC parameter and (c) the F-S parameter as a function of applied strain amplitude.

CTOD and CTSD Studies

For the propagation of small fatigue cracks in polycrystals, it is evident from both experimental observations and previous micromechanical calculations, based on slip band impingement, that grains, phases, and other high angle boundaries play a key role in at least temporarily retarding the advance of the crack front. The internal stress fields which arise from pile-ups of dislocations emitted from the fatigue crack at such boundaries and local constraint conditions on slip at the crack tip conspire to substantially reduce the fatigue crack growth rate prior to boundary impingement. According to the approach of Navarro and de los Rios [6], the stress concentration in the adjacent misoriented grain must reach the threshold level to initiate slip in that grain in order to nucleate new cracks and coalesce the cracks across the boundary. If the stress concentration in the next grain is insufficient, the crack will be arrested by the boundary interaction. They employ the Bilby-Cottrell-Swinden (BCS) model of continuously distributed dislocations for a freely slipping crack of length 2a embedded in a grain of diameter D and assume that the crack tip plastic zone extends to the boundary; dislocations are blocked at the grain boundary, giving rise to a backstress necessary to achieve equilibrium under a given applied stress. Propagation is assumed to follow in proportion to the CTSD. This model describes several key phenomena, including periodic retardation/acceleration behavior of microstructurally small cracks, an explicit relation for the fatigue limit, a prediction of the Kitagawa diagram for the threshold stress intensity factor for cracks beyond the first grain, and the transition to long crack behavior, which is assumed to occur when the size of the cyclic plastic zone just reaches the grain size (crack length on the order of 7-10 grains). This finding agrees with experiments [7] which show that the sensitivity to microstructure barriers is far more evident for small cracks growing over the first few grains in many cases. Similar observations are prevalent for other polycrystals. Long crack behavior corresponds to a condition where the plastic zone size is suitably small compared to crack length for SSY conditions to apply.

Calculations for the driving forces for growth of microstructurally small cracks in an heterogeneous polycrystal using computational crystal plasticity have been very limited. It behooves us to consider first the case of mixed mode crack tip displacements for surface cracks in a polycrystal subjected to monotonic loading to understand microstructure-level shielding and redistribution effects in the absence of slip band considerations in fatigue. In this section we report computational results for crack tip opening and sliding displacements as a function of applied average stress ranging from well below to slightly above nominal yielding for tensile loading of small crystallographic cracks in a surface grain which is surrounded by a range of nearest neighbor grain orientations, all grains being the same size. The grain ahead of the crack tip along the slip plane is assigned each of two orientations: either identical to that of the surface grain with the crack, or in a conjugate slip orientation with significant misorientation relative to the surface grain. The former assignment is to some extent analogous to a crack in a large surface grain and promotes shear localization or slip transfer to the next grain to the greatest extent, while the latter is expected to produce maximum blockage of the driving force (CTD) for growth. Results for the CTSD and CTOD are reported at 2μm and 25 μm behind the crack tip. For the smallest crack analyzed, a/d = 0.25, we report the CTSD and CTOD at a distance 18 μm behind the

crack tip. We might consider the values at 25μm to be CSD and COD, rather than crack tip values, but we do not make that distinction in the nomenclature here so as to facilitate presentation.

The crack is assumed to reside within a surface grain which is favorably oriented for single slip, with one of the two available slip systems aligned with the macroscopic maximum shear plane orientation. For the case of tensile loading, the surface crack is oriented at 45° to the tensile axis. The geometry used in the finite element analyses is a two-dimensional, plane strain specimen with a height of 0.9 mm and width of 1 mm. The grains are rectangular with the dimensions of 0.1 mm (= d) by 0.15 mm. The finite element program ABAQUS [1] is used to perform the analyses with the UMAT formulation for crystal plasticity described in a previous section. Two-dimensional, 8-noded quadrilateral, biquadratic (CPE8R) and 6-noded quadratic (CPE6) solid elements were used throughout the mesh. A typical mesh with a surface crack is shown in Fig. 27. Considerable mesh refinement is employed in the surface grain and nearest neighbors; the elements surrounding the crack tip are 0.5 μm in dimension to resolve the near tip CTSD and CTOD properly. The CTSD and CTOD are determined by resolving the relative displacements of two nodes along the initial crack surface into components along and normal to the original crack plane, respectively. Crack surfaces are assumed to be initially perfectly planar. Three a/d ratios (a = crack length) are analyzed in this study (0.25, 0.5, and 0.97). All cracks are stationary, i.e. introduced without prior effects of growth history. In the grain adjacent to the cracked surface grain and diagonally in the path of the crack plane, labeled as grain A, two different orientations of the slip systems are considered. These include an aligned orientation that promotes extended single slip on the plane of the crack and the conjugate slip case, where both systems are oriented equally with respect to the favored slip system in the surface grain. The remaining grains are constrained to have a minimum misorientation within 15 degrees of their nearest neighboring grain, but are otherwise randomly oriented. It should be recognized that while Grain A provides the most influence due to misorientation, the adjacent grains also contribute; their influence affects the solution differently from that of a crack interacting with a bicrystal grain boundary, as reported in Ref. [8]. The present study considers a range of peak applied strain levels as fractions (0.3, 0.5, 0.7, 0.9, 1.0) of the total strain at yield, $\varepsilon_y = 0.006$, corresponding to the cyclic stress-strain curve. Figure 27 also shows the contour plots of the plastic zones at the crack tip for a/d = 0.5, illustrating the role of the orientation of the next grain ahead of the crack tip in blocking slip and affecting the local mode mixity at the crack tip.

Reference elastic solutions were performed in each case using *precisely* the same mesh and boundary conditions, but suppressing the plasticity. Effects of the free surface are reflected in the elastic solutions as well. The elastic behavior in both sets of simulations is linear, isotropic and homogeneous; hence, there are no weak elastic singularities at junctions of grains. Of course, this is an approximation for crystals, but the intent here is to isolate the effects of plastic anisotropy.

Figure 28 shows plots of CTOD and CTSD from the calculations for monotonic loading, along with the elastic reference solutions. For both orientations of the adjacent grain considered in this work, the CTOD 2μm behind the crack tip is on the order of three to six times greater than the elastic solution as general yielding is reached. At 18 μm behind the crack tip, the opening displacements are two to three times greater than the

elastic solution. For both distances behind the crack tip, the CTOD in the single slip case significantly exceeds that for the conjugate slip orientation of Grain A for an applied strain less than $0.5\varepsilon_y$. The CTSD, on the other hand, lies below the elastic solution for an applied strain below half the macroscopic yield strain for both distances behind the crack tip. Above $0.5\varepsilon_y$, the CTSD for the single slip case increases significantly above the elastic solution, while it diminishes to small values as general yielding is approached for the conjugate slip orientation of Grain A. The largest difference between the elastic and the elastic-plastic solutions occurs for an aligned orientation of the adjacent Grain A. This might be representative of the case of a large, favorably oriented surface grain, for example, and suggests why the growth rates might be considerably higher than for cracks in smaller surface grains. Misorientation of the next grain ahead of the crack path does, however, cause the sliding displacements near the crack tip to be significantly less than for the favorable orientation of Grain A for single slip at the largest applied strain level of $0.9\varepsilon_y$.

These CTOD findings differ markedly from those calculated based on slip band impingement on a grain boundary ahead of the crack as in distributed dislocation [6-7, 9-10] or finite element solutions that use some type of constraint argument to represent slip bands [8]. Of course, Fig. 28 clearly shows that the CTOD dominates the CTSD even in the reference elastic solutions which do not depend in any way on the arrangement of grains or their orientation (due to elastic homogeneity), but does depend on the geometry and boundary conditions we impose. In particular, the CTOD near the tip departs significantly form the elastic solution well below $0.5\varepsilon_y$, and then continues to intensify relative to the elastic solution as general yielding is approached. The increase of the CTOD is at least that of the CTSD with an increase of applied strain for both realizations of the adjacent grain orientation. This illustrates why application of the elastic solution to the analysis of small cracks can produce anomalous results, even in the HCF regime. We also note that the ratio of CTOD/CTSD for both cases differs substantially at 2 μm and 18μm behind the crack tip, suggesting that surface measurements might not reflect crack tip mode mixity very well.

The CTOD solutions appear to be strongly influenced by the interaction of the crack tip with the free surface, and also by the full set of nearest neighbor grains surrounding the cracked grain. This is a feature that has not been provided by previous analyses. The capacity for multislip in the cracked surface grain is activated by stress redistribution associated with neighboring grains. Plots of von Mises stress contours and contours of equivalent plastic strain support this assertion.

Finally, Fig. 29 presents results of CTOD and CTSD calculations for three cycles of loading for both cases where the next grain is favorably oriented for slip or arranged in a "hard" orientation which tends to block slip from transferring from the surface grain. Interpenetration of crack surfaces is prevented by use of a contact algorithm in the finite element code (contacts assumed frictionless here), which is very time-consuming computationally. The cyclic crack tip opening and sliding displacements stabilize somewhat after several cycles. It is very interesting to note that a phase angle develops between the CTOD and CTSD as the degree of crack tip cyclic plasticity increases. There is a marked ratchetting behavior evident in the sliding – the mean sliding progressively increases with cycles; further, the amplitude of sliding decreases, while the opening amplitude increases at a decreasing rate with cycles.
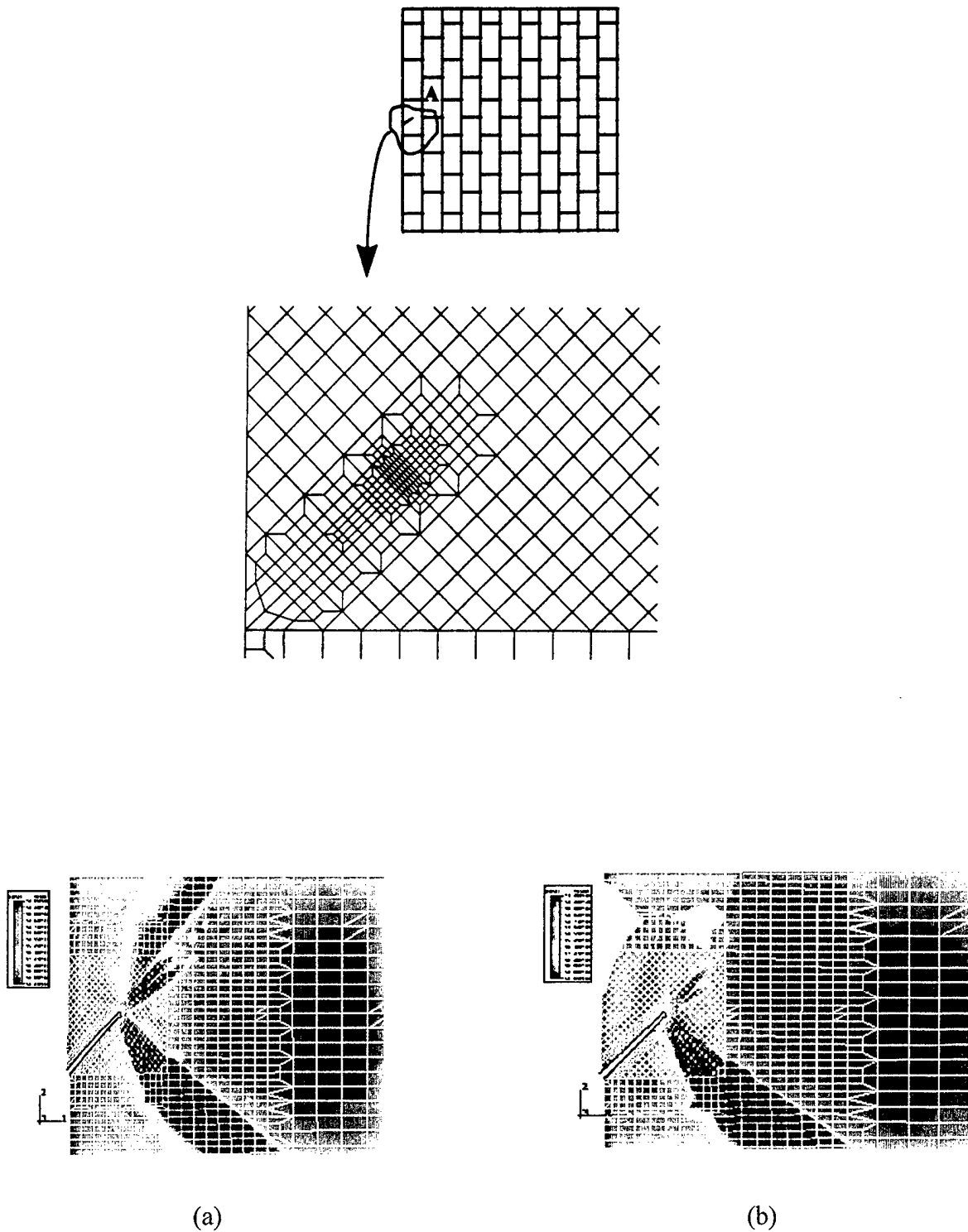
Fig. 27 - Typical FE mesh with the highly refined crack tip region within the surface grain (see inset), and contour plots of effective plastic strain for an applied tensile strain of $0.9e_y$ for (a) single slip and (b) conjugate slip orientation of the next grain for a/d = 0.5; the peak strain intensity (red) has a threshold of 1% plastic strain.
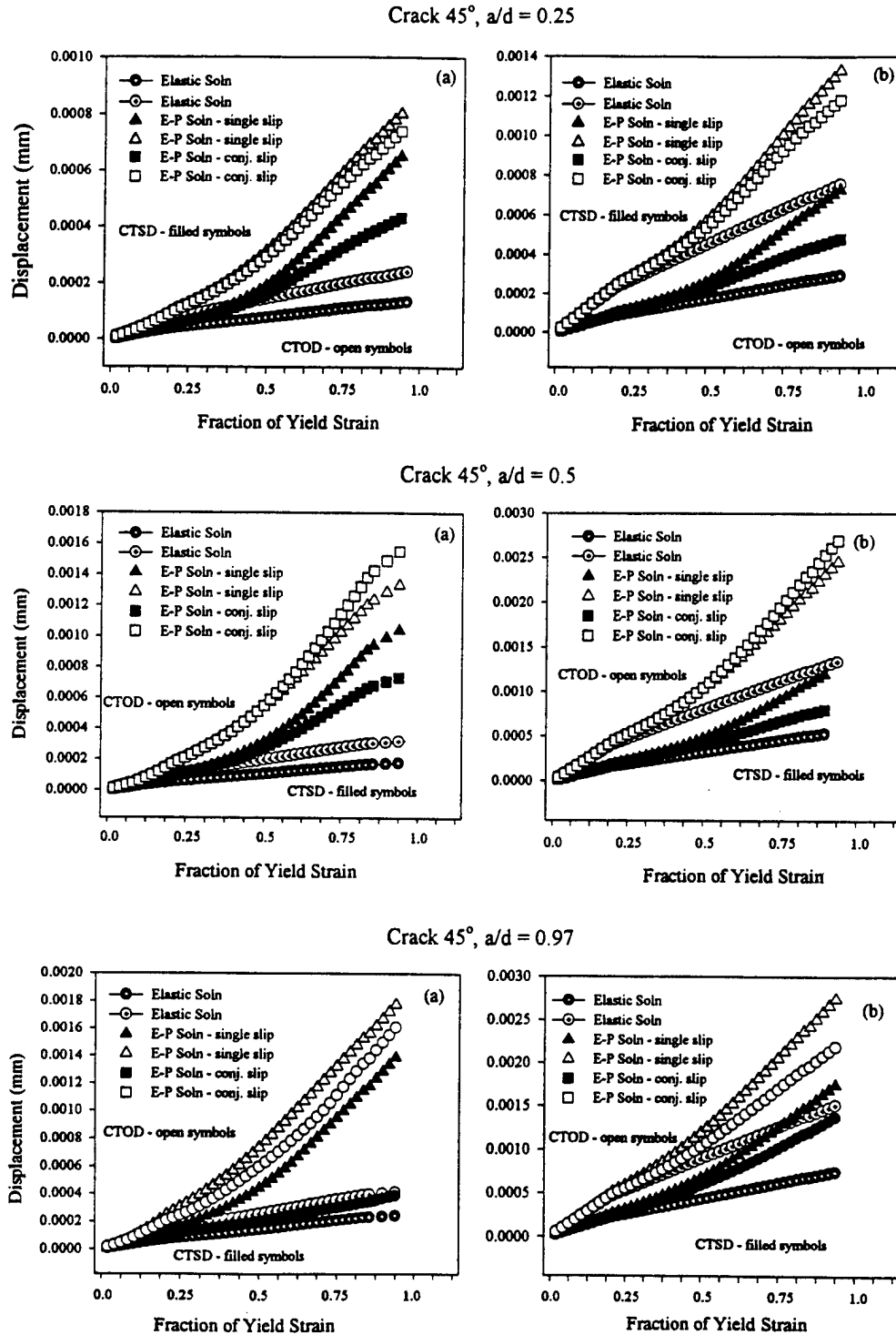
Fig. 28 - CTSD and CTOD for monotonic tensile loading as a function of applied polycrystal tensile strain for a surface crack inclined at 45 degrees to the loading axis (a/d = 0.25, 0.5 and 0.97) in a favorably oriented grain for single and conjugate slip orientations of the nearest neighbor grain, as evaluated (a) 2 μm and (b) 18 μm behind the crack tip.
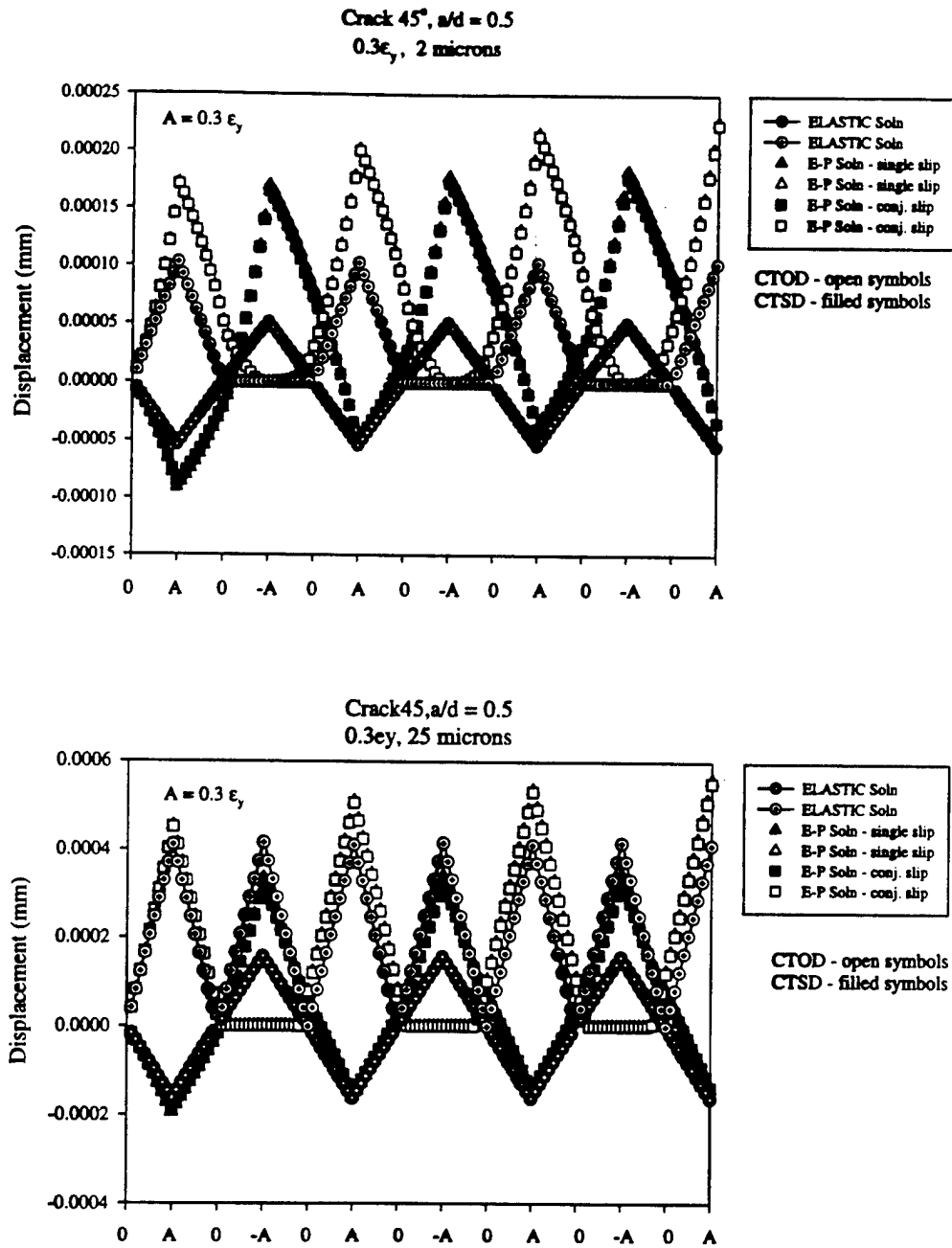
Fig. 29 - CTSD and CTOD as a function of applied cyclic polycrystal tensile strain for a surface crack inclined at 45 degrees to the loading axis (a/d = 0.5) in a favorably oriented grain for single and conjugate slip orientations of the nearest neighbor grain, as evaluated 2 μm behind the crack tip.

References for Section 3.3.2

[1] ABAQUS, Ver. 5.7, Hibbitt, Karlsson & Sorensen, Inc., Pawtucket, RI, 1998.

[2] Rashid, M. M., "Texture Evolution and Plastic Response of Two-Dimensional Polycrystals," *Journal of the Mechanics and Physics and Solids*, Vol. 40, No. 5, 1992, pp. 1009-1029.

[3] Cailletaud, G., Doquet, V., and Pineau, A., "Cyclic Multiaxial Behavior of an Austenitic Stainless Steel: Microstructural Observations and Micromechanical Modeling," in *Fatigue under Biaxial and Multiaxial Loading*, ESIS10, K. Kussmaul, S. McDiarmid, and D. Socie, Eds., Mechanical Engineering Publications, London, 1991, pp. 131,-149.

[4] Jordan, E. H. and Walker, K. P., "A Viscoplastic Model for Single Crystals," *ASME Journal of Engineering Materials and Technology*, Vol. 114, 1992, pp. 19-26.

[5] Cuitiño, A. M. and Ortiz, M., "Computational Modeling of Single Crystals," *Modelling and Simulation in Materials Science and Engineering*, Vol. 1, 1992, pp. 225-263.

[6] Navarro, A. and de los Rios, E.R., "A Model for Short Fatigue Crack Propagation With an Interpretation of the Short-Long Crack Transition," *Fatigue and Fracture of Engineering Materials and Structures,* Vol. 10, No. 2, 1987, pp. 169-186.

[7] Tanaka, K., "Short-Crack Fracture Mechanics in Fatigue Conditions," *Current Research on Fatigue Cracks*, eds. T. Tanaka, M. Jono and K. Komai, Current Japanese Materials Research, Elsevier, 1, 1987, pp. 93-117.

[8] Li, C., "On the Interaction among Stage I Short Crack, Slip Band and Grain Boundary: A FEM Analysis," *International Journal of Fracture*, Vol. 43, 1990, pp. 227-239.

[9] de los Rios, E. R., Mohamed, H. J., and Miller K. J., *Fatigue and Fracture of Engineering Materials and Structures,* Vol. 8, 1985, pp. 49-63.

[10] Tanaka, K., Akinawa, Y., Nakai, Y., and Wei, R. P., "Modeling of Small Fatigue Crack Growth Interacting with Grain Boundary," *Engineering Fracture Mechanics*, Vol. 24, 1986, pp. 803-819.

3.3.3 Computational Analysis of Long 3-D Fatigue Cracks

The work in years 3 and 4 focused on simulating crack growth paths in components with complex geometry and complex loading. The primary objective is the development of a robust algorithm to predict crack growth. The major requirements for the algorithm are:

(1) the ability to account for crack face frictional contact,

(2) treatment of non-planar cracks,

(3) automatic remeshing for fatigue crack growth, and

(4) the ability to incorporate user-defined crack growth laws.

After extensive survey, it was concluded that no commercial/academic code can meet all the above requirements, see Table 3.3.3.2.

Table 3.3.3.2 Comparison of the three most commonly used FEM codes.

Package	Friction contact	Non-Planar cracks	Automatic Remesh	User Defined Growth Law
ABAQUS	Yes	Yes	No	Yes
Franc2D	No	Yes	Yes (2-D)	No
I-DEAS	Yes	No	No	No

To meet our needs, a fatigue crack growth simulation algorithm was developed and coded into a C-program. Using ABAQUS as the background finite element solver, this program incorporated several features to meet the requirements outlined above for automatic remeshing and crack growth simulation. ABAQUS was selected as the finite element solver because of its capability to include complex boundary conditions, such as those seen in the analysis of fretting fatigue.

Major challenges in developing such a computational tool for simulating fatigue crack growth are:

(1) calculation of fracture mechanics parameters, particularly for 2D curved cracks and 3D non-planar cracks,

(2) the remeshing algorithm, and

(3) automatically repeating the crack tip analysis and remeshing.

Major accomplishments over the past two years include the completion of the 2D program. Input to this program is the component geometry, material, loads, and the initial crack geometry. In addition, crack growth law under fatigue loading needs to be specified by the user. The program will first perform a FEM analysis using ABAQUS to obtain the fracture mechanics parameters such as the SIF and energy release rate. Next, based on these fracture mechanics parameters in conjunction with the user defined fatigue crack growth law, the program will predict the crack growth increment and, consequently, the new crack front. Then, the program will proceed to remesh the new crack tip region and repeat the analysis again for the next crack growth increment. All these steps are fully automated. The user only needs to specify the number of steps in the simulation. The crack path trajectory will be predicted. The flowchart of this simulation algorithm is shown in Fig. 30.
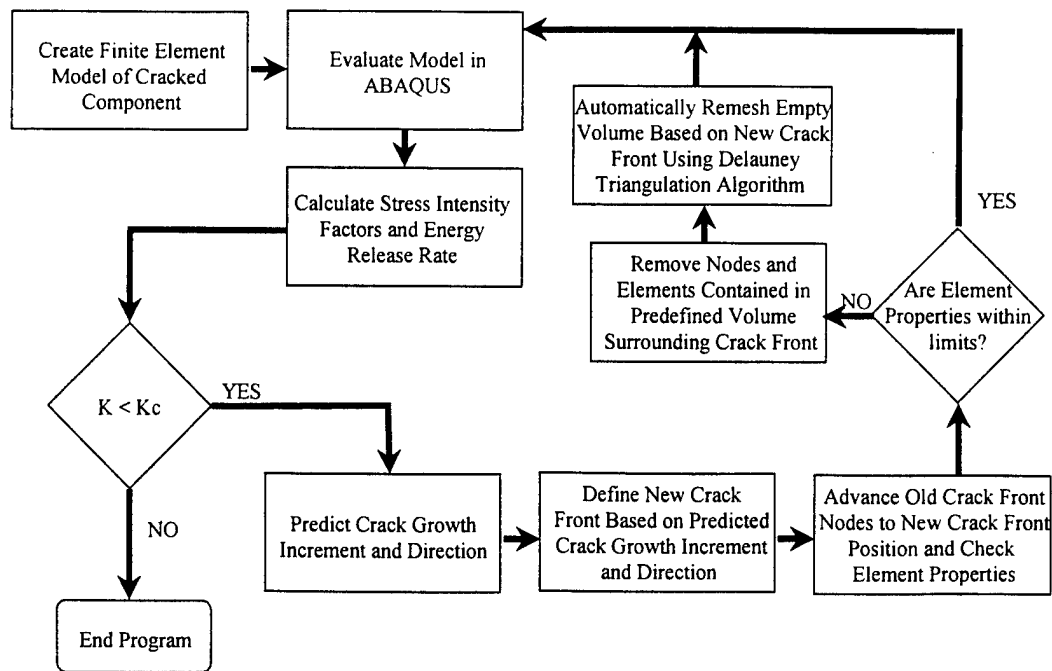
Fig. 30 Automatic crack growth simulation flowchart.

Two innovations used in developing the 2D simulation program are the application of interaction energy method for computing SIF for curved cracks and the Delauney trinangulation for automatic remeshing. A simple example of a straight crack under mixed mode loading is shown in Fig. 31. Under cyclic loading, the crack grew into a curved shape, see Fig. 32.
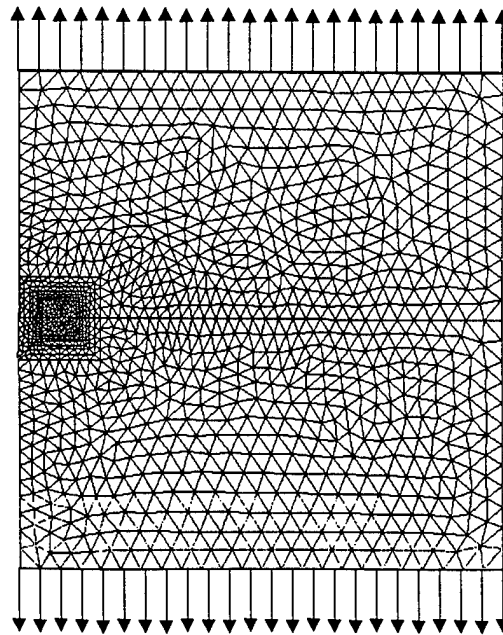
Fig. 31 A straight crack under mixed mode loading.
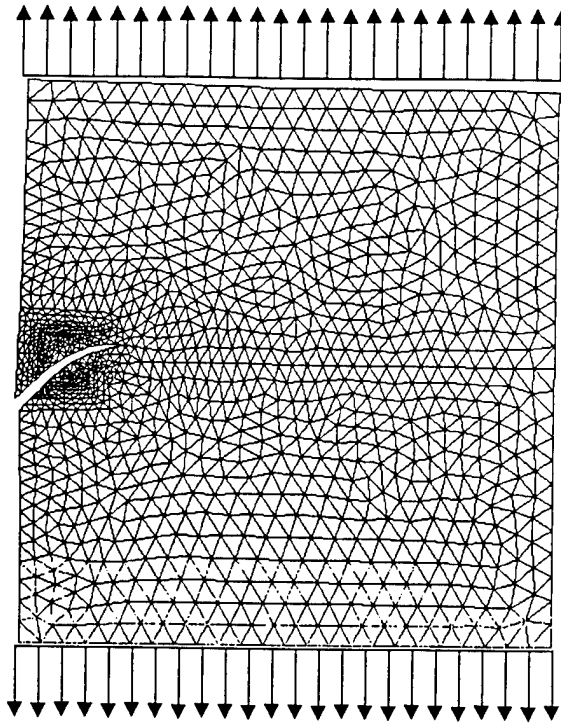
Fig. 32 A straight crack grew into a curved one under mixed mode loading.

Currently, the 2D program is being used to evaluate crack growth in fretting fatigue specimens. Using the results of fretting fatigue experiments, we are interested in determining which crack growth laws best predict the behavior of the growing crack, including the transition between a shear dominated growth and a tensile dominated growth.

For the 3D case, we are currently finishing up the automatic remeshing part of the programing. In order not to duplicate the efforts, we will be using the fracture mechanics code developed at Northwestern University (by Dr. Moran) for calculating the SIF in the simulation program.

4. FRETTING FATIGUE

Fretting fatigue is a widespread phenomenon that occurs in a vast number of engineering components where two bodies are in contact and undergo a small oscillatory slip and at least one of the bodies is experiencing a bulk cyclic loading. Fretting fatigue is a widespread problem in navel structural components and is often the root cause of fatigue crack nucleation. Some examples include fasteners such as bolted, riveted, and clamped joints; press-fit components; keyways, splines, and dovetails; steel ropes and springs. Since it is often not feasible to eliminate fretting fatigue as a failure mode, the use of sensors at critical locations ("hot spots") where fretting fatigue cracks will grow is a viable option. However, to interpret the sensor signals under these conditions requires a better fundamental understanding of the stages of fretting fatigue and how they relate the sensor signals. A model that describes this damage evolution which includes crack

nucleation and the growth of small cracks is needed for prognostics.

Fretting fatigue crack nucleation and early crack growth is characterized using both destructive and non-destructive methods to determine the stages of the fretting fatigue process. This research involves understanding the growth of small cracks under both plain (i.e., absence of fretting) and fretting fatigue conditions. These well-controlled tests are used as a test bed for emerging sensor technologies in both determining minimum damage size that can be detected as well as separation of damage from fretting and plain fatigue. This information is used to develop the next generation life prediction models for fretting fatigue crack nucleation and early crack growth. The materials under investigation include PH 13-8 Mo stainless steel and 4340 steel used in critical aerospace components (specifically in CH-46 helicopter).

An extensive literature survey of modeling methodologies that can be used to predict fretting fatigue crack nucleation and crack growth was conducted to determine the state of the art and directions for the next generation in modeling. Nucleation involves all the processes leading to the formation of a crack, typically of the order of 10 μm. The crack growth process describes the additional crack driving forces under fretting fatigue. The Fretting Fatigue Damage Parameter (Ruiz et al., 1984) is currently the most widely used model to predict fretting fatigue crack nucleation (see Fig. 33). It is an empirical model that has been shown to accurately predict the location of fretting fatigue cracks along a contact interface, but cannot account for differences in fretting fatigue behavior for different materials because of its lack of a physical basis. The mechanisms of fretting fatigue crack nucleation appear to be closely related to those of multiaxial low cycle fatigue, although occurring in a relatively smaller process volume (Neu et al., 1999). Next generation nucleation models may be based on multiaxial fatigue criteria, such as a critical plane approach (Socie, 1993), which can predict the direction of early crack growth as well as the nucleation location (see Fig. 30). These critical plane approaches can potentially bridge nucleation and fracture mechanics approaches. Detailed discussion is given in McDowell et al. (1997) and Neu et al. (1999).

Life Prediction Approach

State of the Art

Fretting Fatigue Crack Nucleation

Ruiz et al. (1984)

- predicts nucleation only

Next Generation

Multiaxial Fatigue Criteria Based on Critical Plane Approaches

- potential to predict both nucleation and direction of early crack growth

LINK

Fretting Fatigue Crack Growth

bulk

friction

a

Fracture Mechanics

$$\frac{da}{dN} = f\left(\Delta K_{bulk} + \Delta K_{friction} - \Delta K_{redristn}, K_{max}\right)$$

- based on continuum description

Microstructural Fracture Mechanics

- potential to use length scale appropriate for describing early crack growth where continuum description breaks down
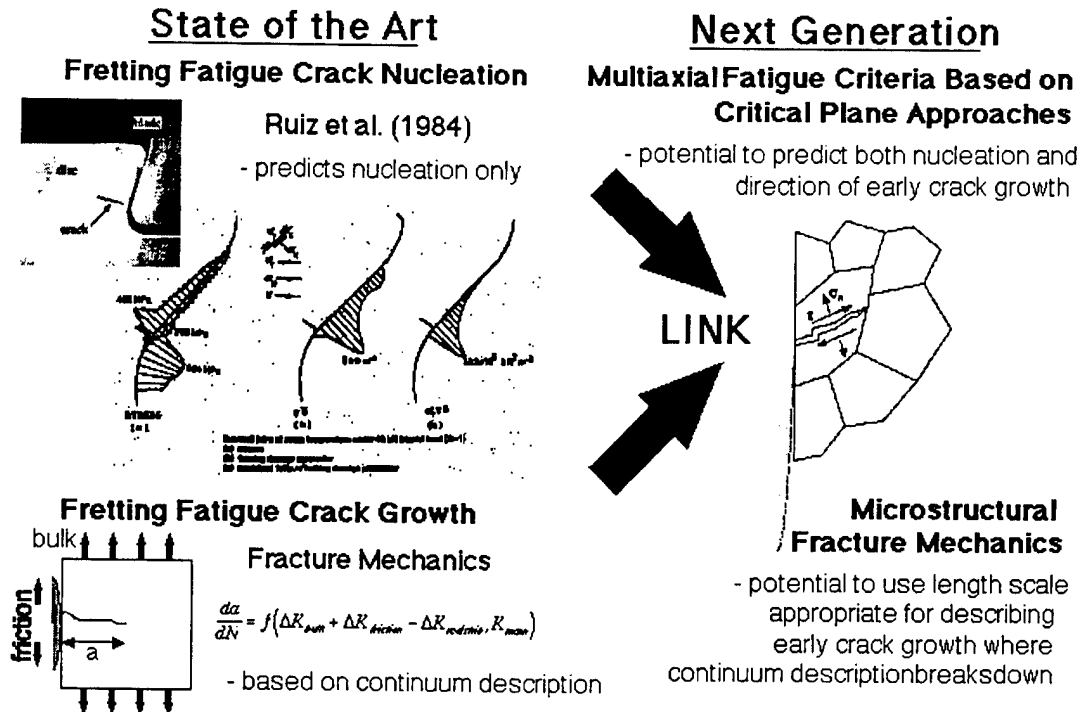
Fig. 33 Life prediction approach.

Our work has focused on validating and refining these next generation approaches to make them useful in engineering prognostic tools. This includes testing various hypotheses in applying different multiaxial fatigue criteria to clarify and validate this methodology. The idea is good but there has been no validation especially with respect to physical damage. This validation includes determining the local cyclic stress-strain response along the interface and using this response to evaluate a number of multiaxial fatigue criteria. The prediction modeling is then compared to its capability for predicting the fatigue damage observed experimentally.

The development and validation of computational methods to determine the time-varying local stress-strain response for any fretting contact situation was needed before the multiaxial criteria could be evaluated. Considering that the interfacial contact geometry between engineering components is usually complex, the finite element method (FEM) was used. It was also chosen because of widespread acceptability in industry. However, a number of issues and challenges in using FEM in this application had to be resolved. For example, how fine does the mesh need to be near the interface? Or in other words, how small is the fatigue process volume that needs to be considered? What type of contact elements work best for this application? With simple geometries such as cylindrical on flat and linear material behavior, does the solution reduce to the analytical Mindlin result? Initially, ANSYS, a general purpose commercial FEM code, was used. However, we soon realized that the contact elements in ANSYS were not ideal for the fretting problem especially in determining the local stress and strain near the contact interface. So we switched to ABAQUS, another commercial code. After exploring a

couple different contact element options, converged solutions were obtained for all our loading and contact conditions. Each fretting fatigue analysis is run to shakedown. The stress-strain response in the last cycle along the interface in the fatigue specimen is used as input to evaluate the various predictions of theories. Details on the FEM modeling are reported in Swalla-Michaud (1999).

Our fatigue specimen was modeled closely with FEM so that we could have direct experimental validation for the prognostic modeling. Elastic-plastic (using multiple linear fits to the cyclic stress-strain curve) 2-D finite element analyses of our fretting fatigue specimen configuration have been conducted to determine the local time-varying stress and strain fields in the region of fretting. The effects of mesh refinement and contact element stiffness have been explored. Near the contact, the mesh must be very fine (of the order of 10 μm) to reach converged solution. In addition, parametric studies exploring the effects of stress amplitude, mean stress, friction coefficient (e.g., 0.75, 1.0, 1.25, 1.5), relative slip (different pad spans), and geometry of interface (e.g., radii of 1.5 mm, 15 mm, and 150 mm) have been performed (Swalla-Michaud, 1999) and continue to be conducted.

Using the results of the FEM modeling, various multiaxial crack nucleation criteria were evaluated. These included the current state of the art (the maximum tangential stress and the Ruiz criterion) as well as those based on critical plane theories (in particular, Fatemi-Socie and Smith-Watson-Topper (see Socie, 1993)). A maximum shear strain range criteria was also considered. All of these nucleation criteria were critically examined in light of our new experimental results (Neu et al., 1999). Neither of the state-of-the-art nucleation criteria predict the observed oblique crack direction and early crack growth behavior. Shear-based multiaxial fatigue criteria based on critical plane theories (in particular, the Fatemi-Socie parameter) were shown to predict not only the nucleation site but also the plane of maximum damage which corresponded to the physically observed orientation of the crack nucleus.

The development of the modeling methodology also makes it possible to explore other effects that may be important to the fretting fatigue problem. For example, (1) the evolution of the *local* friction along the interface, (2) the influence of the microstructure through modeling grains with different crystallographic orientations, and (3) the size of the representative volume element (i.e., the fatigue process zone).

Experimental Program in Fretting Fatigue

The fretting fatigue test apparatus developed for this investigation is unique in that it addresses the needs of both life prediction modeling and integrated diagnostics. The fretting fatigue test method was developed (1) to validate and refine the next generation prognostic models and (2) to be used as a test bed for detecting real fatigue damage with sensors. The new fretting fatigue apparatus designed and developed for this program was based on ones previously used to study fretting fatigue behavior of materials (Attia and Waterhouse, 1992). However, our apparatus contains a number of design changes, both to improve upon the previous designs as well as for easily accepting the application of sensors. Fretting fatigue tests are performed using a flat dog-bone shaped specimen with bridge-type fretting pads attached to the edge of the specimen (see Fig. 34). The fatigue specimen with fretting apparatus attached is gripped and tested in a 90 kN servohydraulic fatigue test system. The frictional force is determined using a strain gage measure

located on the bottom of the fretting pad.

The fretting fatigue test set-up is ideally suited for evaluating sensors and other crack growth monitoring techniques, due to the large area on the fatigue specimen where sensors can be attached. Sensors are attached to either the flat side or edge of the specimen, typically after studies to determine their optimal placement. Many parameters which influence fretting fatigue behavior can be controlled, including the fatigue stress amplitude, mean fatigue stress, nominal relative slip amplitude, contact pressure distribution, normal contact load, and frequency of oscillation. Thus, this test set-up provides all of the experimental information required to evaluate current state of the art life prediction methods for crack nucleation and propagation under fretting fatigue. It is also anticipated that this investigation will impact an ASTM standard for fretting fatigue testing currently under development.
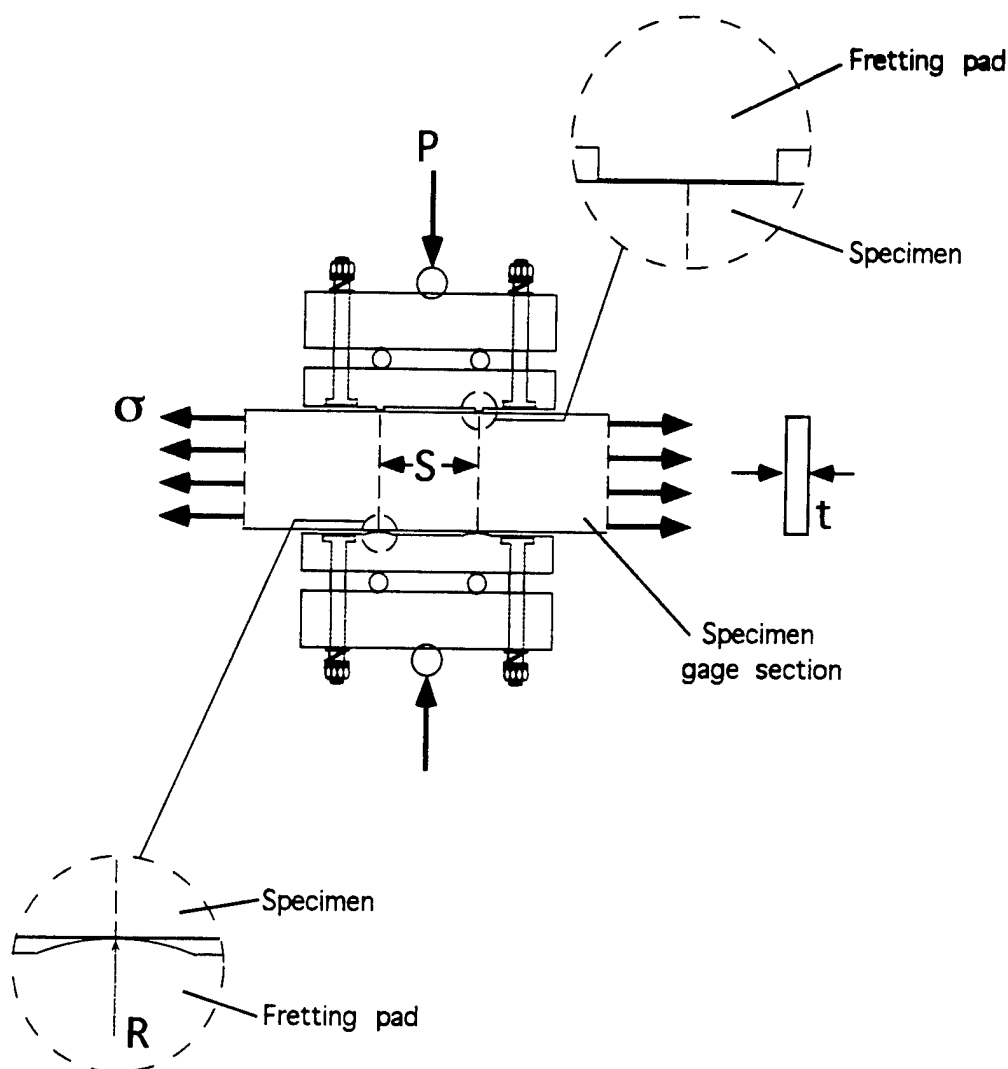

Fig. 34   Fretting fatigue apparatus.

A study of the fretting fatigue behavior of PH 13-8 Mo stainless steel has been conducted. The design and implementation of a fretting fatigue testing apparatus proved quite successful in nucleating and propagating fretting fatigue cracks. The fretting fatigue tests performed at stress levels of 40% to 50% of the fatigue limit exhibited extremely short lives. Many interesting and significant observations have been made (Pape, 1997; Pape and Neu, 1999) which will continue to stimulate further research in year 5. For example, the evolution of the frictional force between the fretting pads and the fatigue specimen was monitored throughout the fretting fatigue tests. The general trend of a relatively quick increase during the first few hundred cycles (bedding-in), followed by a gradual decrease throughout the remainder of the test, was seen in most of the tests (Fig. 35). Furthermore, a sharp drop in the range of frictional force was observed near the end of the test. This drop has been correlated with the presence of a well-defined fatigue crack in the specimen. It seems to be possible, based on the observations made, to use the frictional force evolution as a measure of the size of the fatigue cracks.
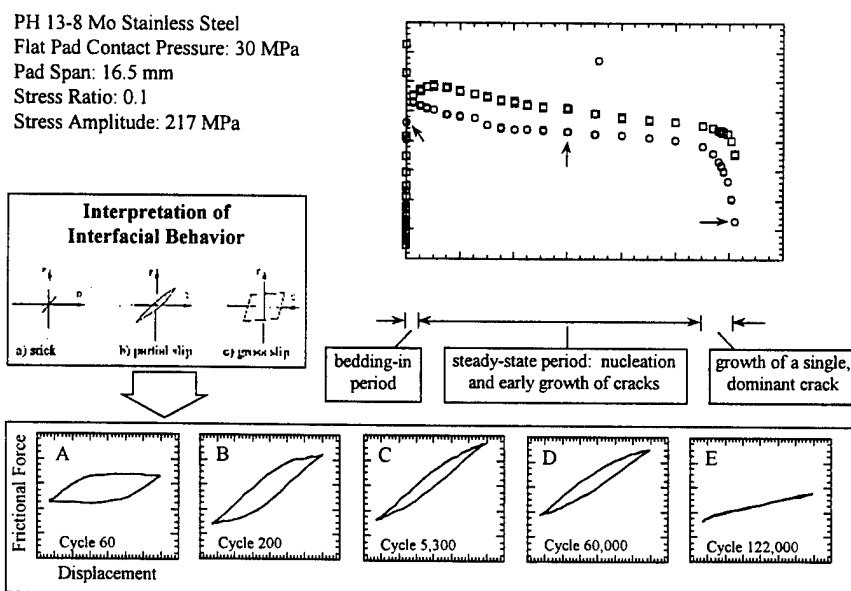
Fig. 35 Stages of fretting fatigue.

A great deal can be learned by monitoring the progression of fretting damage with sensors. Due to the extensive plastic deformation and numerous crack nuclei generated in the early stages of fretting fatigue, it may be difficult to detect the growth of very small cracks with sensors. Fortunately, the evolutionary nature of the fretting fatigue damage may be more easily detected than cracks initiating naturally under plain fatigue. A preliminary comparison of the evolution of frictional force/displacement hysteresis with the frequency of acoustic emission events (in collaboration with Jacobs/Jarzynski (GT)) suggests it is possible to detect the characteristic changes during this evolution even when the fretting fatigue damage is not very extensive such as during the early stages of fretting fatigue damage accumulation. One of the motivations for developing a fretting

fatigue method is the likely capability for sensors to pick up information as to the evolution of the interface damage. Further validation continues through a series of interrupted tests where changes in the sensor signals are directly correlated with the physical damage state.

One of our most significant contributions to the fretting fatigue testing community has been the use of different initial contact geometries in the same test (Pape and Neu, 1999). This was to address a current controversy as to the importance of the contact geometry on fretting fatigue crack nucleation. Unique tests using "flat" pads on one side of the fatigue specimen and cylindrical pads on the other side were used to assure all other parameters (e.g., fatigue loading, normal load, relative slip) were the same (see Fig. 31). Even though the maximum contact pressure at the cylindrical fretting pad was much higher than the average pressure at the flat pad, there was not a large difference (less than a factor of 2) in fatigue life between the two configurations. Clearly, this is relevant to dealing with contacts between components that may have more complex contact geometries and assuring that the new prognostic models can handle these geometric differences and be applied to components with confidence. In addition, in year 5 we plan to investigate the role of the cylindrical pressure distribution by using pads with different radii of curvature (e.g., 1.5 mm, 15 mm, and 150 mm).

The effect of the fatigue mean stress (i.e., stress ratio) on the evolution of damage leading to fatigue crack nucleation has been found to be small (Neu et al., 1999). The increase in remaining life at lower mean stress appears to be associated with the delay in the onset of crack propagation. Various fretting fatigue crack nucleation criteria have been critically examined in light of these experimental results investigating the mean stress effect (Neu et al., 1999).

A number of fretting fatigue specimens have been sectioned and cracks lengths and angles have been measured. A typical example taken from Neu et al. (1999) is shown in Fig. 36. Here, the initial crack angle is about 57° measured from a line perpendicular to the fretted surface. At about 50 μm below the surface, the angle changes to about 27°. From between 200 μm and 800 μm below the surface, the angle gradually changes from 27° to 0°, which is a crack growing normal to the remote fatigue loading. The fatigue mean stress does not seem to significantly influence these angles. These physical crack growth observations are critical for determining at what length the crack growth can be predicted using fracture mechanics methods and for evaluating different crack growth criteria for predicting the growth rate and direction for this material (in collaboration with Qu). Based on our small crack growth work specifically on PH 13-8 Mo stainless steel (Patel et al., 1999), when the fatigue crack is 50 μm or larger, its growth rate can be predicted fairly well using long crack growth models even though the crack is still physically small. However, the criterion for predicting the direction of crack growth still needs to be determined by comparing the growth direction predicted by different criteria to the experimentally observed direction (in collaboration with Qu).
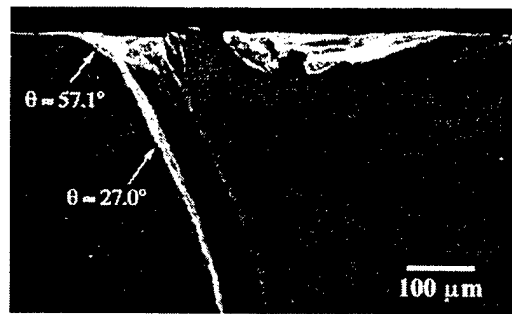
Fig. 36 Fretting fatigue crack.

References for Section 4

Attia, M.H. and Waterhouse, R.B. (eds.), *Standardization of Fretting Fatigue Test Methods and Equipment, ASTM STP 1159*, American Society for Testing and Materials, Philadelphia, 1992.

Newman, J.C., 1981, "A Crack Closure Model for Predicting Fatigue Crack Growth Under Aircraft Spectrum Loading," *Methods and Models for Predicting Fatigue Crack Growth Under Random Loading*, ASTM STP 748, pp. 53-84.

Ruiz, C., Boddington, P.H.B., and Chen, K.C., 1984, "An Investigation of Fatigue and Fretting in a Dovetail Joint," *Experimental Mechanics*, Vol. 24, No. 3, pp. 208-217.

Socie, D.F., 1993, "Critical Plane Approaches for Multiaxial Fatigue Damage Assessment," *Advances in Multiaxial Fatigue*, ASTM STP 1191, D.L. McDowell and R. Ellis, eds., pp. 7-36.

Wang, C.H., 1996, "Effect of Stress Ratio on Short Fatigue Crack Growth," *Journal of Engineering Materials and Technology*, Vol. 118, pp. 362-366.

5. ALGORITHMS FOR REMAINING LIFE PREDICTION

A fracture mechanics-based methodology for predicting remaining life of structural components based on fatigue crack growth behavior is quite well developed [1]. Figure 37 shows a classical approach to how stress analysis results can be combined with fatigue crack growth data and fracture mechanics models to predict remaining life of components subjected to cyclic loading. The emphasis of this algorithm is on hot spot locations which are identified and quantified based on a priori finite element analyses of components. The models for predicting fatigue crack growth in this methodology have been primarily developed for long fatigue cracks, i.e. > 1mm. Due to the high frequency of loading in helicopter rotor components, majority of the lifetime is expected to be spent in the regime of small cracks with dimensions in the range of 30 to 50 μm.

Even though the basic methodology for near real time diagnostics/prognostics to support condition-based maintenance is similar to that shown in Figure 37, the models used must be able to address considerations such as (i) small crack behavior including effects of interactions between small cracks and the microstructure, (ii) crack propagation under mixed-mode loading, (iii) influence of surface residual stresses, (iv)

interactions between multiple cracks (v) variable amplitude fatigue loading, and (vi) stochastic aspects of fatigue crack initiation and early growth. Moreover, the format for the "data-link" between on-board sensors and this remaining life estimation scheme is an important element of practical implementation of the scheme, which in practice would be resident in memory of an on-board processor charged with continuous updating of damage and comparison with growth rate estimates, along with evolving estimates of remaining life. Naturally, these estimates may be presented in terms of statistical bounds which reflect stochastic aspects of the crack growth behavior. A series of distributed microprocessors could be used to track hot spot damage for each critical component, or a single processor for each component could be applied with a sweeping algorithm across hot spot locations, using ROM-based look-up tables, for example, based on component-specific stress analysis for each hot spot.

For rogue flaws, the problem is fundamentally altered. Since these defects lie outside the envelope of hot spots or well-characterized critical locations, it is impractical (if not impossible) to achieve a rigorous description of their shape, driving forces for crack extension and effect on dynamical system response from an a priori analysis. By definition, these sorts of cracks occur in unanticipated locations. Accordingly, it is necessary to conceive a broader, more robust class of algorithms for estimating remaining life in this case. Input to this assessment is from a broad area array of sensors, likely involving sensors of various degrees of fidelity, resolution, and signal characteristics. Several options exist for treatment of rogue flaws, including (i) flagging for shutdown and static/manual inspection at first detection, followed by assignment of sensors for subsequent tracking, (ii) assessment of rate of degradation of dynamic component response in combination with other broad area sensor measurements to estimate rate of crack propagation and remaining life, or (iii) some combination of these. Pattern recognition of system degradation may be accomplished by a training algorithm which employs, for example, artificial neural network technology. In this manner, equivalent flaw propagation characteristics may be established. It is emphasized that this technology is most useful for broad area damage or rogue flaws, and is complementary to the hot spot remaining life assessment algorithms.

Step 1

Fracture Toughness and
Crack Growth Specimens

Tensile and Low-Cycle
Fatigue Specimens

J_{IC} (or K_{IC})

$$\frac{da}{dN} = A'\Delta K^{n1}$$

$$\epsilon = \sigma/E + D\sigma^{m}, \quad \Delta\epsilon = \frac{\Delta\sigma}{E} + D'(\Delta\sigma)^{m'}$$

Step 2

A

σ

A

Cracked Component

Sect. A-A

$$\Delta K = f_1(\Delta\sigma, a, t)$$
$$J = f_2(\sigma, a, t, \sigma_{ys}, D, m)$$
$$C = \gamma R$$

Step 3

a_0 —— Initial Crack Depth
C_0 —— Initial Half Crack Length

$$J_{IC} = f_2(\ldots a_f \ldots)$$

$$N_f = \int_{a_0}^{a_f} \frac{da}{A'[f_1(\Delta\sigma, a, t)]^{n_1}}$$

a_0

C_0

N_f

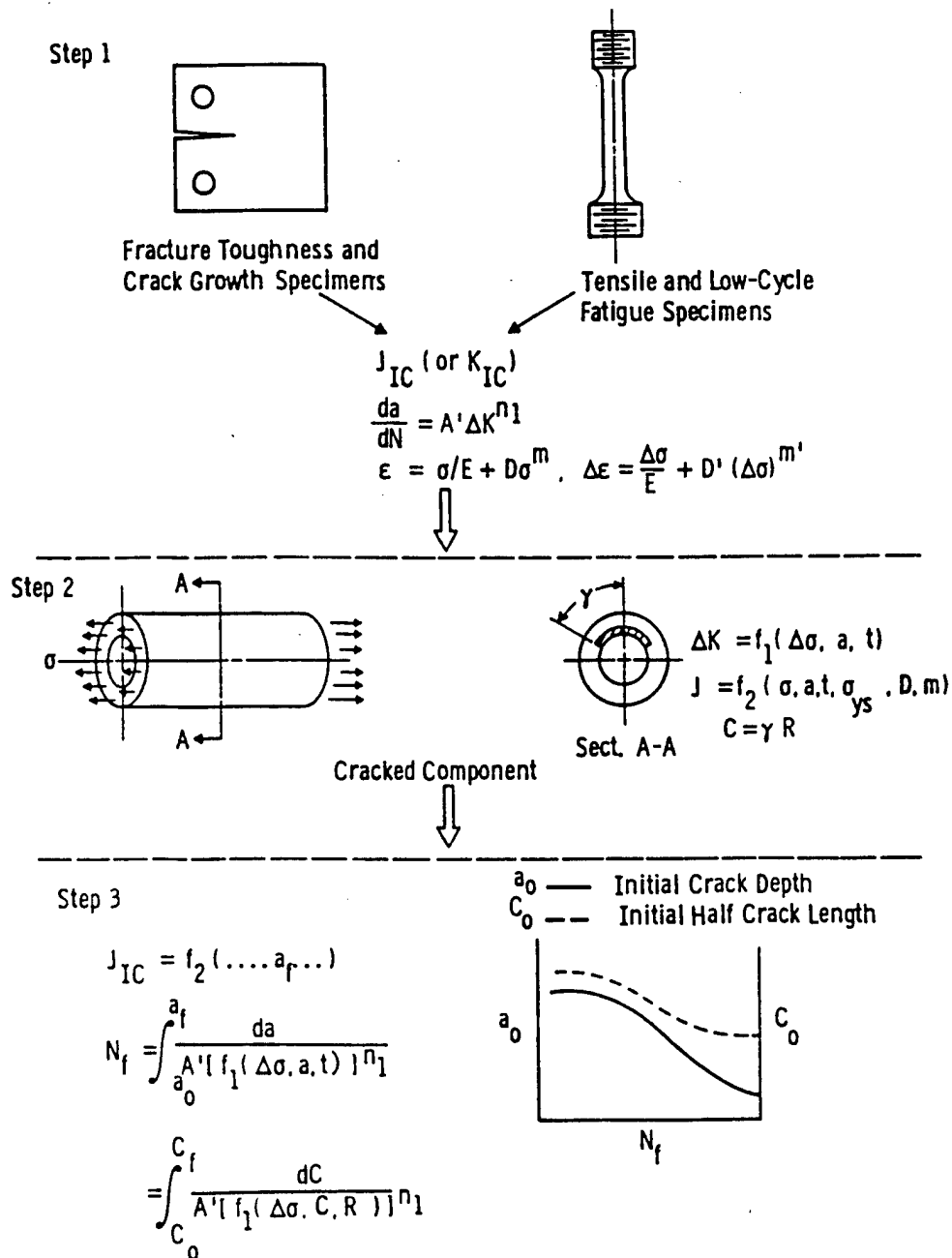$$= \int_{C_0}^{C_f} \frac{dC}{A'[f_1(\Delta\sigma, C, R)]^{n_1}}$$

Figure 37 - A schematic of the classical methodology for predicting remaining
fatigue life of components at hot spots using a fatigue crack growth
law determined from laboratory specimens.

Processing and Classification of Sensor Data

The proposed diagnostic system includes sensors on two levels of detection: focused micro-sensors and broad-band sensors. The focused sensors are embedded near "hot spot" locations where critical defects are expected to occur. These locations have been successfully identified in the H-46 rotor hub using finite element (FE) stress analysis [2]. The focused sensors include acoustic emission (AE) and eddy current (EC) devices. On the broad-band level, the overall structure is monitored for "rogue flaws" using less-focused AE and EC sensors as well as dynamic system response (DSR) measurement devices. Obviously, the uncertainty in the defect characteristics obtained from the broad-band sensors will be greater than that from the focused micro-sensors (i.e., more information is available concerning cracks at hot spots than is available for rogue flaws). This paper focuses on utilizing signals from AE sensors, either from the focused or broad-band devices. AE devices detect the elastic waves emitted from forming and progressing flaws as the material resists applied stress.

The sensors are expected to provide data that gives some measure of defect size (crack length) and location. Multiple sensors allow monitoring of numerous cracks' lengths and approximate growth rates at various locations in the structure throughout the life of the component. Local AE events corresponding to development of localized inelastic deformation or "pop-in" of cracks may be detectable using embedded sensors, and above a certain level of resolution crack length may be reliably monitored using AE data and incorporated into a life-prediction scheme based on crack propagation models [2-3]. A proposed model by McDowell [4] for use in the integrated diagnostic system divides small crack growth in polycrystalline metals into three characteristic regimes:

1. Regime I, the microstructurally small crack regime (MSC), for cracks on the order of the material grain size which are highly sensitive to microstructural features
2. Regime II, the transition region from microstructural sensitivity to relative insensitivity
3. Regime III, the physically or mechanically small (PSC) crack regime

For the system to use such a model, the crack length must be known to a limited degree in order to classify the defect into one of the three regimes. Then the estimated crack length, as well as material constants, microstructural dimensions, stress analysis results, and load histories, is incorporated by the model in order to calculate the crack growth rate, da/dN. This crack growth rate is then used, along with the loading frequency, to calculate the length of life remaining. Other models also calculate da/dN using similar information, and are valid only for certain crack lengths (e.g., conventional linear elastic fracture mechanics (LEFM) models are not valid for "small" cracks). Since the structural reliability algorithm may utilize multiple crack growth models, each of which is valid only for a certain crack length range, correct prediction of the remaining life depends on identifying the regime of crack growth of each flaw, if not its precise length, such that valid models may be selected for use in the algorithm. Due to the resolution of the AE sensors (especially the broad-band devices), precisely determining the numerical length of very small cracks (on the order of 50 μm) is probably not feasible. However, classification of the small crack into one of the three characteristic regimes may be possible using AE data, particularly that from focused micro-sensors at hot spots. Above

a certain length, the cracks may be monitored more effectively using the AE sensors, enabling more accurate predictions for remaining life. However, the proper classification of small cracks is crucial, since the cracks typically remain small for up to 90% of the life of components under HCF.

The signal conditioning and classification stage of the reliability prediction involves removing noise from the AE signals and extracting all the useful information from the AE data. The processed data may then allow, in the case of small cracks, the classification of the growth rate into one of the three characteristic regimes. This information can then be used to select appropriate crack growth models for estimating remaining life. In the case of larger cracks that may be more accurately measured with AE data, the measured crack growth rates may be compared to predictions of da/dN made by the various crack growth models, and the error between the predictions and the actual growth rates may be used to continuously update the life prediction algorithm during service.

Proposed Method of Operation for the Integrated System

A methodology for use in the proposed diagnostic system for estimating the structural reliability for components under HCF conditions is now presented. The recommended approach is intended to take advantage of the useful signal processing tools and modeling strategies presented in this paper; it incorporates wavelet analysis, a neural network, and a combination of probability- and possibility-based methods for calculating reliability. Figure 38 shows the steps involved in the recommended methodology, with steps performed by the on-board processing unit surrounded by the dotted boundary:
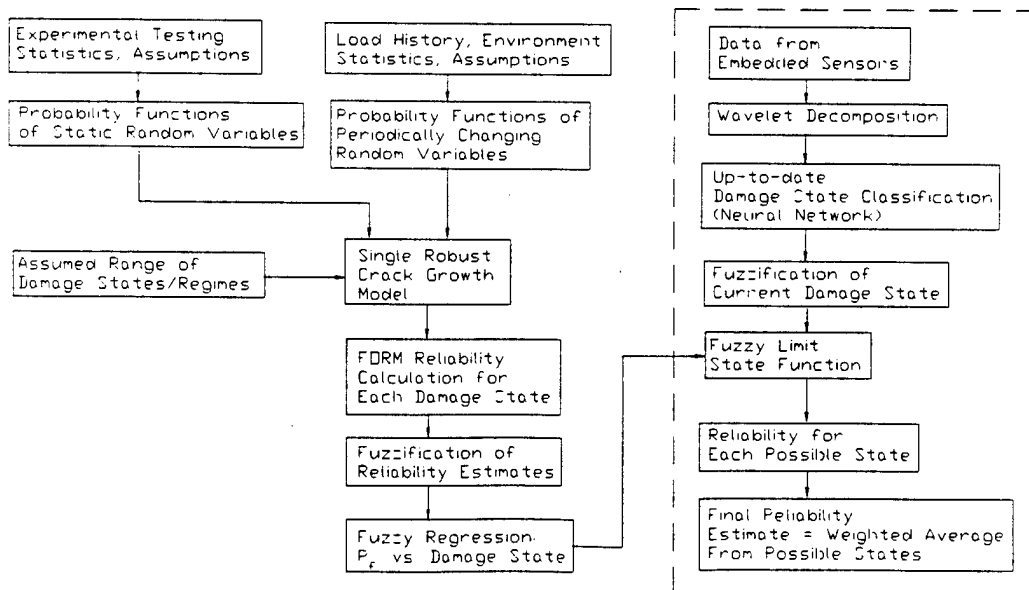

Figure 38. Proposed System Methodology

Features of Figure 38 are now discussed in more detail, beginning with those steps

outside the boundary (outside the box surrounding the right column in Figure 38) which are not directly performed by the on-board processor. The proposed method uses a single robust crack growth model, which is actually a collection of individual models, each valid at a particular crack length scale or growth regime. A robust multi-length scale regime model for growth of small fatigue cracks was developed by McDowell [4]. Inputs to the crack growth model are the following:

- The probability density functions and descriptive parameters of the static governing random variables, such as material properties and empirical constants, which may be determined from laboratory test data or assumptions and heuristic knowledge

- The probability density functions and descriptive parameters of periodically changing governing random variables, such as load amplitude and phase, mean stress, and environmental conditions; these must be updated periodically as service conditions change

- A range of assumed damage states (crack lengths, numbers, directions, etc.)

Next, the first order reliability (FORM) method is proposed to be used in conjunction with the crack growth model to calculate the reliability of the structure at each increment of the assumed damage state. FORM is recommended because of its reduced cost when compared to MCS and LSSE; however, an alternative probabilistic computational method may be used if FORM yields inaccurate results. The reliability estimates calculated using the FORM method are then fuzzified in order to account for subjective uncertainty sources such as modeling errors. In this fuzzification process, each damage state value (each crack length, for example) is assigned membership in various reliability levels; the shapes of the membership functions are chosen to reflect the degree of uncertainty in the crack growth model. A fuzzy limit state function is then generated using fuzzy regression techniques, as discussed in [5-6]. A possible form of such a state function is shown in Figure 39:
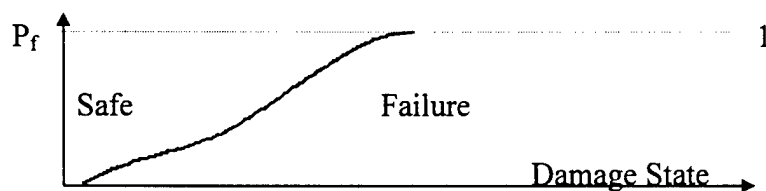

Figure 39. Fuzzy Limit State Function

Fuzzy regression is used to create a fuzzy relationship between damage state and the fuzzified reliability predictions calculated from the FORM method. Note that the boundary of the limit state surface is fuzzy; certain assumptions regarding the shape of this boundary may be required to employ the regression technique. The fuzzy regression procedure yields a direct relationship between the damage state and the reliability (or actually P_f in Figure 39), accounting for statistically quantifiable uncertainties from the FORM calculations as well as subjective uncertainties such as modeling errors. This functional regression model, once determined, is later exported to and stored in the on-

board processor for use in making real time reliability estimations. It may be updated periodically to account for changes in loading and environment, and its fuzzy membership functions may be tuned based on the performance of the system.

Now the proposed operations of the on-board components of the integrated diagnostic system are addressed. The embedded broad-band and focused sensors continuously send signals related to damage evolution to the processing unit. These signals are then decomposed using a wavelet transformation. Noise caused by fretting and other sources is filtered, while spikes in the signals corresponding to crack extension are preserved. Useful features regarding crack length, position, orientation, and growth rate are extracted from multiple sensor data. The decomposed, conditioned sensor data (perhaps in the form of wavelet coefficients at different frequencies) is then used as input to a neural network that classifies the current damage state of the material (e.g., data may be classified into crack length or growth regime). A backward-propagating neural network (BPNN) would be well-suited for this classification process. The network would have to be trained prior to use in the on-board processor via comparison of sensor data with experimentally measured crack growth data (the training set). The training, which could be lengthy, need not be done on-board; once trained, the BPNN could later classify sensor data very quickly for use in the reliability algorithm. The processor could also identify the critical flaw (perhaps the longest crack) at the current damage state.

Next, the damage state or crack length of the critical flaw is fuzzified to a degree based on the operator's confidence in the sensor data and in the neural network's performance. Membership functions for inclusion in various damage states or crack growth regimes are created based on subjective assumptions and heuristic knowledge, with broader membership functions used for more uncertain data, such as that for rogue flaws. As a simplified example, consider the membership functions shown in Figure 40:
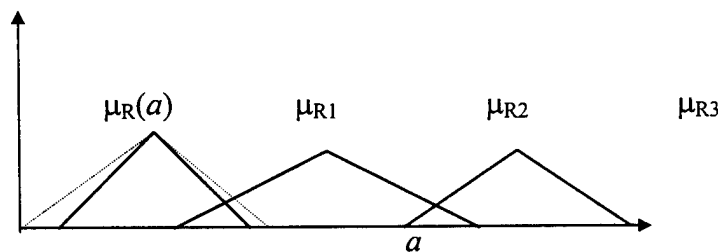

Figure 40. Example Membership Functions for Damage State

In the figure above, a is the neural network's numerical prediction of crack length, and μ_{R1}, μ_{R2}, and μ_{R3} are membership functions in Regimes I, II, and III, respectively, of small crack growth. The triangle membership function shape is commonly used, but it is not required. Note that the overlap of the membership functions permits inclusion of a given crack dimension in more than one regime. The dotted membership function illustrates a means of increasing the fuzziness or uncertainty associated with classification of rogue flaws using signals from less-focused broad-band sensors. The proposed system may implement membership functions for inclusion in various regimes by considering more than just crack length; membership in a damage set or regime may

be a function of crack number, orientation, and location, in addition to crack length a.

As a result of the fuzzification process, the current condition of the material becomes a fuzzy number having degrees of membership in one or more possible fuzzy damage states. Using the fuzzy regression model discussed previously, the reliability for each of these possible states is determined based on the functional relationship between P_f and the possible state, as indicated by the shape of the fuzzy limit state function. The current overall reliability of the component is then calculated as a weighted average of the reliabilities afforded by membership in each of the possible states. Larger weights are assigned to reliability values associated with more likely damage states (i.e., the degree of membership in each possible damage state determines the magnitude of the weight assigned to each reliability value.)

The proposed algorithm for estimating reliability has the following notable characteristics:

- Probabilities are used where available to quantify uncertainty in statistically measurable random variables.

- Possibility measures (fuzzy sets) are used to account for subjective uncertainty and modeling errors.

- Expensive, time-consuming computations (such as FORM, neural network training, fuzzy regression) need only be performed periodically to update the system, and need not be done on-board.

- Real-time reliability updates are available quickly, since all on-board operations are relatively fast: wavelet decomposition, BPNN classification, fuzzification of the damage state, and use of the pre-determined (by regression) limit state function.

References for Section 5

[1]   Liaw, P.K., Saxena, A. and Perrin, J., 1993, "Life Extension Technology from Steam Pipe Systems - Part I and II," Engineering Fracture Mechanics, Vol. 45, pp. 759 - 803.

[2]   McDowell, D.L, Winer, W.O. and Cowan, R.S., "Developing an Integrated Diagnostic System," ASME IMECE Symp. On Quantitative Nondestructive Evaluation in Integrated Diagnostics, Dallas, TX, November 17, 1997.

[3]   McDowell, D.L., Neu, R.W., Qu, J., and Saxena, A., "Prognostic Tools for Small Cracks in Structures," Emerging Technologies for Machinery Health Monitoring and Prognosis, TRIB-Vol. 7, R. Cowan, Ed., ASME, 1997, pp. 1-12.

[4]   McDowell, D.L., "Multiaxial Small Fatigue Crack Growth in Metals," Int. J. Fatigue, Vol. 19, No. 1, 1997, pp. S127-S135.

[5]   Ross, Fuzzy Logic with Engineering Applications, McGraw-Hill, 1995.

[6]   Liu and Huang, "Fatigue Reliability of Structures Based on Probability and Possibility Measures," *Computers and Structures*, Vol. 45, 1992, pp. 361-368.

6. SUMMARY OF ADVANCES IN YEARS 1-4

This report has summarized the significant advances made by Structural Fatigue Task B.4 in the development of prognostic tools to serve CBM requirements within the overall Office of Naval Research MURI program in Integrated Diagnostics (ONR N00149510539) at Georgia Tech. The problem is decomposed into treatment of a relatively small number of critical locations or hot spots in each component which require dedicated microsensors. These hot spots are defined as locations which are assigned high probability as failure sites based on preliminary component elastic stress analysis which employs realistic loading conditions. A robust model for small fatigue crack propagation is described which is applicable to dedicated hot spot microsensor algorithms. Research is described in numerous supporting areas for understanding the formation and propagation of microstructurally small, mechanically small, and long fatigue cracks. Fretting fatigue is described as a potential failure mechanism and our related research is summarized. The structure of a component remaining life estimation scheme for hot spot locations is outlined, focusing on the near- real time prognostics.

Environmental effects generally contribute to accelerated evolution of fatigue processes in components. Environmental penetration is highly sensitive to local component design details, surface exposure, surface conditions and applied loading history. Although not explicitly discussed in this work, these effects may be incorporated in the remaining life estimation schemes in terms of their influence on bounds of remaining life estimates.

7. YEAR FIVE RESEARCH

In addition to ongoing efforts in the various tasks described in this report, Task B.4 is collaborating with other tasks of the MURI to explore demonstration of concepts developed in years 1-4, focusing on selected experiments combining diagnostics and prognostic technologies.

Demonstration Projects in Year 5

A number of demonstration projects are underway. These projects involve collaboration between various groups in the MURI program to bring together the advances in sensor and prognostic technology.

Multiple "hot spots" (collaboration with Jacobs/Jarzynski (GT))

This demonstration project will highlight the integration of the sensor and remaining life technologies in year 5. The goal of the demonstration tests is to show that sensors and prognostics can capture damage that may be occurring at multiple sites. The demonstration specimen contains two types of potential hot spots: notches and two body contacts. Hot spots are sites where fatigue cracks are likely to nucleate in a component. The catastrophic fatigue crack may nucleate at either a notch or fretting location. The location where the catastrophic crack initiates will depend on the severity of the notch. Therefore, three different notch geometries each with a different stress concentration factor will be considered. In addition, preliminary tests will be conducted to verify the differences in sensor signals between those coming solely from fatigue at notches and

those solely from fretting fatigue. The preliminary tests will also provide information on the effect that notch size has on remaining life and on how the notch size influences the sensor signal. The material for this task will be PH 13-8 Mo stainless steel.

Fatigue crack detection using array of microsensors (collaboration with UM and GT)

This demonstration project involves attaching an array of microsensors developed and fabricated by UM to our notched fatigue specimens. The material for this project is 4340 steel. Ten tests are planned.

Fatigue crack detection using surface waves (collaboration with Berthelot (GT))

This demonstration project involves using surface waves to capture the size and growth of a fatigue crack initiated at a 0.5 mm diameter surface flaw. The material for this project is 4340 steel. Six tests are planned.

Other possibilities

In addition, the collaborations have led to some new ideas for using sensors to detect fatigue damage, especially focusing on smaller damage volumes. For example, it seems promising that surface and near surface (within 1 mm below the surface) flaws at our notch roots can be detected using eddy current microsensors developed by Ramalingam at UM. These eddy current microsensors may be ideal for detecting flaws as small as 10 μm in size near hot spots, which is quite a bit smaller than the current state-of-the-art technology.

REPORT DOCUMENTATION PAGE

Public reporting burden for this collection of information is estimated to average 1 hour per response, including the time for reviewing instructions, searching existing data sources, gathering and maintaining the data needed, and completing and reviewing the collection of information. Send comments regarding this burden estimate or any other aspect of this collection of information, including suggestions for reducing this burden to Washington Headquarters Services, Directorate for information Operations and Reports, 1215 Jefferson Davis Highway, Suite 1204, Arlington, VA 22202-4302, and to the Office of Management and Budget, Paperwork Reduction Project (0704-0188), Washington, DC 20503

1. AGENCY USE ONLY (Leave Blank)	2. REPORT DATE 31 May, 1999	3. REPORT TYPE AND DATES COVERED Year 4 Performance: June 1, 1998 - May 31, 1999

4. TITLE AND SUBTITLE

Integrated Diagnostics

5. FUNDING NUMBERS

G N00014-95-1-0539

6. AUTHOR(S)

Richard S. Cowan and Ward O. Winer (eds.)

7. PERFORMING ORGANIZATION NAME(S) AND ADDRESS(ES)

Georgia Institute of Technology
MULTIUNIVERSITY CENTER FOR INTEGRATED DIAGNOSTICS
G. W. Woodruff School of Mechanical Engineering
801 Ferst Drive
Atlanta, GA 30332-0405

8. PERFORMING ORGANIZATION REPORT NUMBER

9. SPONSORING/MONITORING AGENCY NAME(S) AND ADDRESS(ES)

Office of Naval Research
800 N. Quincy Street
Arlington, VA 22217-5660

10. SPONSORING/MONITORING AGENCY REPORT NUMBER

11. SUPPLEMENTARY NOTES

The information conveyed in this report does not necessarily reflect the position or the policy of the Government, and no official endorsement should be inferred.

12a. DISTRIBUTION/AVAILABILITY STATEMENT

12b. DISTRIBUTION CODE

13. ABSTRACT (Maximum 200 words) This document summarizes activity concerning the performance of basic research being conducted in the area of *Integrated Diagnostics*, a term associated with the technologies and methodologies used to determine how mechanical failures occur, and how they can be detected, predicted, and diagnosed in real-time. Objectives, set forth through a Department of Defense Multidisciplinary Research Program of the University Research Initiative (M-URI), are being addressed by faculty and staff from the Georgia Institute of Technology, Northwestern University, and the University of Minnesota. This activity is funded through the Office of Naval Research for a basic period of three years, with an option for two additional years. Fourth year accomplishments and plans are reported upon.

During this reporting period, experiments based on material, load, and vibration information from critical rotorcraft components continued so as to collect data of relevance in understanding the mechanisms of small crack growth for use in developing fatigue failure models. Such models serve as a guide in the selection and development of sensors to detect faults and pending failures. Effort has been placed on sensor development, and achieving the means to analyze and correlate reliable sensor output for operator use. Organizationally, this activity is being accomplished through (11) projects, categorized by the thrust areas of a.) Mechanical System Health Monitoring, including microsensor development and the condition monitoring of rotordynamic elements; b.) Nondestructive Examination Technology; and c.) Material Failure Characterization and Prediction Methodology.

14. SUBJECT TERMS

Integrated Diagnostics; Condition-based Maintenance
Failure Detection; Failure Prediction; Sensors; Direct Sensing

15. NUMBER OF PAGES 200

16. PRICE CODE

17. SECURITY CLASSIFICATION OF REPORT	18. SECURITY CLASSIFICATION OF THIS PAGE	19. SECURITY CLASSIFICATION OF ABSTRACT	20. LIMITATION OF ABSTRACT
Unclassified	Unclassified	Unclassified	SAR